Surface-Modified Mesoporous Transition Metal Oxide and Carbide Films with Improved Electrical Conductivities as Highly Efficient OER-Electrocatalysts

vorgelegt von
M. Sc.
Marvin Lionel Frisch

an der Fakultät II – Mathematik und Naturwissenschaften
der Technischen Universität Berlin
zur Erlangung des akademischen Grades

Doktor der Naturwissenschaften
- Dr. rer. nat. -

genehmigte Dissertation

Promotionsausschuss:

Vorsitzender: Prof. Dr. Arne Thomas
Gutachter: Dr.-Ing. habil. Ralph Krähnert
Gutachter: Prof. Dr. Peter Strasser
Gutachter: Prof. Dr. Bernd Smarsly

Tag der wissenschaftlichen Aussprache: 27. April 2022

Berlin 2022

Danksagung

Der Weg der Anfertigung einer Dissertation stellt einige Herausforderungen und Hürden, welche ohne die Zusammenarbeit und Diskussion mit einer Vielzahl an Personen kaum zu überwinden wären. Daher möchte ich mich nachfolgend ganz herzlich bei den Kolleginnen und Kollegen bedanken, die mich im Laufe meines Studiums sowie während der Erstellung der Doktorarbeit maßgeblich unterstützt haben.

Dr.-Ing. habil. Ralph Krähnert gilt mein besonderer Dank für die Aufnahme in seinen Arbeitskreis, die Betreuung während der Promotion als auch die zahlreichen fachlichen Diskussionen bei der Erarbeitung diverser Publikationen und Erfindungsmeldungen. Im Zuge des von mir bearbeiteten Projekts „ATO-KAT“ eröffneten sich vielseitige Möglichkeiten an Kooperationen sowie die Teilnahme an internationalen wissenschaftlichen Tagungen.

Prof. Dr. Peter Strasser danke ich herzlichst für die Übernahme des Gutachtens dieser Arbeit. Darüber hinaus möchte ich mich für die wissenschaftliche Zusammenarbeit und Diskussionen in den Seminaren bedanken, als auch für die Möglichkeit der Mitbenutzung der Labore und Ausstattung.

Prof Dr. Bernd Smarsly möchte ich für die Übernahme eines weiteren Gutachtens danken, *Prof. Dr. Arne Thomas* gilt ein besonderer Dank für die Übernahme des Prüfungsvorsitzes.

Wie bereits erwähnt wurden einige der in dieser Arbeit veröffentlichten Ergebnisse im Rahmen von Kooperationen mit unterschiedlichen Arbeitskreisen erarbeitet. Ich möchte ein großes Dankeschön an *Muhammad Hamid Raza* sowie *Prof. Dr. Nicola Pinna* aussprechen, die an der Humboldt-Universität zu Berlin einen wesentlichen Grundbaustein zur Oberflächen-modifikation poröser Materialien durch weiterentwickelte ALD-Verfahren legten.

Des Weiteren möchte ich ein herzliches Dankeschön an *Prof. Dr. Thomas Bredow, Joachim Laun, Anna Gomer* sowie *Katharina Bauerfeind* aussprechen. In enger Zusammenarbeit mit der Universität Bonn wurden Untersuchungen zu strukturellen und elektronischen Eigenschaften von Metalloxiden sowie –karbiden basierend auf Dichtefunktionaltheorie (DFT) getätigt.

Bei *Dr. Julien Marquardt* möchte ich mich herzlich für die Raman-Messungen an porösen Filmen und fachlichen Diskussionen bedanken.

Darüber hinaus gilt mein Dank meinen Kolleginnen und Kollegen an der Technischen Universität Berlin. Hervorheben möchte ich insbesondere *Aleks Arinchtein, Dr. Meng-Yang Ye, Dr. Denis Bernsmeier, Dr. René Sachse, Hanna Trzesniowski, Malte Klingenhof, Dr. Michael Bernicke* sowie *Dr. Cornelia Broicher*. Nicht nur für die Einführung in die Welt der Elektrochemie mit all ihren Analytikgeräten und Messtechniken, aber auch für die zahlreichen wissenschaftlichen Ratschläge und Ideen. Bei Aleks möchte ich mich ganz herzlich für die Aufnahmen am Elektronenmikroskop (TEM) bedanken, die ich sehr schätze. Meng danke ich für ihre wertvollen Ideen hinsichtlich der Darstellung und Interpretation von Daten als auch für die interessanten Diskussionen über die aktuelle Fachliteratur sowie die XPS-Messungen. In diesem Kontext gilt ein weiterer Dank an *Prof. Dr. Arne Thomas*.

Benjamin Paul danke ich in ganz besonderem Maße für seinen Rat bei unterschiedlichsten Problemstellungen im Labor. Benjamin – danke für deinen entscheidenden Beitrag bei der Errichtung des Setups zur Untersuchung der elektrischen Eigenschaften von dünnen Filmen. Danke auch für deinen Rat bei Fragen zum Rasterelektronenmikroskop (SEM) oder der Gassteuerung am Rohrofen.

Vielen Dank an *Astrid Müller-Klauke* für die Durchführung der ICP-OES-Messungen.

Herzlichen Dank an *René Gunder* vom Helmholtz-Zentrum Berlin (HZB) für die Durchführung zahlreicher GI-XRD-Messungen dünner Schichten.

Für einen regen wissenschaftlichen Austausch möchte ich mich vor allem bei *Jochen Bahner* bedanken, der mich bereits während meines Nanoscience-Studiums an der Universität Konstanz unterstützt hat.

Zuletzt möchte ich mich bei meinen engen Freunden und meiner Familie bedanken. Euer Interesse am Thema hat mich zusätzlich motiviert. Besonders hervorheben will ich meine Eltern, die mich immer unterstützt haben – ganz egal in welcher Situation. Einen erheblichen Beitrag hast auch Du, liebe Ann-Zoë, geliefert. Du hast mir gezeigt, dass alle Hürden überwunden werden können, solange man den Glauben daran nicht verliert.

Abstract

Large-scale production of hydrogen (H_2) by renewable energy powered water electrolysis represents a promising strategy to cut global carbon dioxide emissions and ease fossil fuel depletion. However, state-of-the-art electrolyzers and fuel cells employ high loadings of rare and expensive noble metals (e.g. Ir, Pt) as active electrocatalysts, hampering wide-scale adoption of industrial electrolysis and electricity generation, respectively. The design of nanostructured high-surface-area electrocatalysts with control over composition, morphology, porosity, crystallinity and surface sites can promote the overall efficiency of both processes.

In water electrolysis, the oxygen evolution reaction (OER) is considered the main bottleneck due to its sluggish kinetics and high overpotentials. This thesis contributes to an optimized utilization of OER-active species based on a rational design of surface-modified electrode coatings. A sophisticated concept is presented, which proposes transition metal oxides and carbides with template-controlled pore structures as conductive supports for both precious (IrO_x) and non-precious (NiO) metal species introduced as ultra-thin surface coatings *via* conformal atomic layer deposition (ALD). The optimized catalyst-support systems show outstanding mass-specific OER activities and outperform literature-reported catalysts as well as commercial references.

Bulk, surface-sensitive and local characterization techniques are combined for the deduction of structure-property-activity correlations that are further evaluated by theoretical calculations in order to improve the electrical properties of the support. In this context, a decisive impact of matching the interfacial properties between semiconducting, oxidic supports and the ALD surface layer is found. Employing soft-templated mesoporous tungsten carbide (mp. WC_x) films synthesized *via* an innovative approach as supports with metallic conductivity can significantly enhance the catalytic performance for both alkaline (NiO-ALD) and acidic (IrO_x-ALD) OER. The excellent conformality of ALD guarantees the formation of a dense surface layer which is shown to prevent the underlying support from oxidative dissolution and/or degradation during electrocatalysis. A basic understanding of the ALD parameters is used to adjust the properties of the deposited surface species, the morphology as well as the layer thickness, and hence serves as the bedrock in application-driven catalyst design.

The concept of improving the utilization of catalytically active species *via* conformal ALD on mesoporous metal oxides and carbides with tailored electronic properties is exemplarily proven by the successful development of highly efficient, *i.e.* active and stable, electrocatalysts for both alkaline and acidic OER.

Zusammenfassung

Die großtechnische Erzeugung von grünem Wasserstoff (H_2) mittels Wasserelektrolyse stellt eine vielversprechende Strategie zur Einsparung globaler Kohlenstoffdioxid-Emissionen sowie fossiler Brennstoffe dar. Moderne Elektrolyseur- bzw. Brennstoffzellenaufbauten benötigen derzeit jedoch hohe Beladungen an seltenen sowie teuren Edelmetallen (z. B. Ir, Pt) in den Elektroden, wodurch die großflächige H_2-Erzeugung in Elektrolyseuren bzw. die Bereitstellung von elektrischer Energie in Brennstoffzellen limitiert werden. Die Verwendung poröser, nanostrukturierter Katalysatormaterialien mit definierter Zusammensetzung, Morphologie, Porosität, Kristallinität sowie angepassten Oberflächeneigenschaften kann die Effizienz beider Prozesse steigern.

Aufgrund der trägen Kinetik und großen benötigten Überspannung gilt die Sauerstoffbildungsreaktion (OER) als begrenzend. Basierend auf einem rationalen Ansatz zur Herstellung oberflächenmodifizierter Elektrodenbeschichtungen, liefert die vorliegende Arbeit einen Beitrag für eine verbesserte Ausnutzung katalytisch aktiver Spezies. Das Konzept schlägt templatiert poröse Übergangsmetalloxide sowie –karbide als leitfähige Trägermaterialien für Edelmetall- (IrO_x) als auch Nichtedelmetall-Oberflächenspezies (NiO) vor, welche durch konforme Atomlagenabscheidung (ALD) eingeführt werden. Anhand optimierter Katalysator-Trägermaterial-Eigenschaften können hohe massenspezifische OER-Aktivitäten erreicht werden, welche die von literaturbekannten Systemen als auch kommerziellen Referenzen übertreffen.

Eine Ableitung von Struktur-Eigenschafts-Aktivitätsbeziehungen durch gezielte Kombination von volumen- als auch oberflächensensitiven Charakterisierungsmethoden wird angestrebt, um die elektrischen Eigenschaften des Trägers zu verbessern. In diesem Zusammenhang spielt die Grenzfläche zwischen halbleitendem, oxidischem Trägermaterial und ALD-Oberflächenschicht eine entscheidende Rolle. Neuartige, templatiert mesoporöse Wolframkarbidschichten (mp. WC_x) mit metallischer Leitfähigkeit können nach erfolgter Modifizierung der gesamten Oberfläche durch konforme NiO- bzw. IrO_x-ALD vor unerwünschter Volumenoxidation geschützt und zugleich mit katalytischer Aktivität versehen werden. Eine Optimierung der chemischen und strukturellen Eigenschaften der abgeschiedenen Oberflächenspezies stellt hierbei den Grundbaustein für eine anwendungsorientierte Katalysatorentwicklung dar.

Ein tiefgreifendes Verständnis des Einflusses verschiedener ALD-Parameter ermöglicht schließlich die gezielte Herstellung elektrochemisch aktiver sowie stabiler Katalysatorbeschichtungen mit gesteigerten Massenaktivitäten in der sauren als auch alkalischen OER.

Abbreviations

ADT	accelerated degradation test
AEL	alkaline (water) electrolysis
ALD	atomic layer deposition
ATO	antimony-doped tin oxide
BET	Brunauer-Emmett-Teller
ClER	chlorine evolution reaction
cac	critical aggregation concentration
CP	chronopotentiometry
cmc	critical micelle concentration
CNTs	carbon nanotubes
CV	cyclic voltammetry / cyclic voltammogram
CVD	chemical vapor deposition
DOS	density of states
ECSA	electrochemically active surface area
EDX	energy-dispersive X-ray spectroscopy
EIS	electrochemical impedance spectroscopy
EISA	evaporation-induced self-assembly
EtOH	ethanol
GC	glassy carbon (substrate)
(GI-)XRD	X-ray diffraction (in gracing incidence geometry)
H_2	hydrogen
HAADF	high-angle annular dark-field (mode)
HCl	hydrochloric acid
HER	hydrogen evolution reaction
ICP-OES	inductively coupled plasma optical emission spectrometry
IrO_x	iridium oxide
MEA	membrane electrode assembly

MOF	metal-organic framework
mp.	mesoporous
$Ni(Cp)_2$	nickelocene; *bis*(cyclopentadienyl)nickel(II)
O_2	oxygen
O_3	ozone
OER	oxygen evolution reaction
PB	poly(butadiene)
PEM	proton exchange membrane
PGM	platinum group metal
PEIS	potentiostatic electrochemical impedance spectroscopy
PEO	poly(ethylene oxide)
PMMA	poly(methyl methacrylate)
PPO	poly(propylene oxide)
PTFE	poly(tetrafluoroethylene)
RHE	reversible hydrogen electrode
SAED	selected area electron diffraction
SE	spectroscopic ellipsometry
SEM	scanning electron microscopy
Si	silicon (wafer / substrate)
SiO_2	quartz glass (substrate)
T	temperature
$T_{calc.}$	calcination temperature
TALH	titanium(IV) *bis*(ammonium lactato)dihydroxide
TEM	transmission electron microscopy
TGA	thermogravimetric analysis
Ti	titanium (substrate)
WDX	wavelength-dispersive X-ray spectroscopy
XPS	X-ray photoelectron spectroscopy

Publication List

This work is written in the form of a cumulative thesis discussing results from research carried out during my PhD. In the following, the relevant publications are listed in chronological order. Additionally, patent applications have been submitted to the European Patent Office and will be addressed in their proper context. In the appendix of this work (A-1 to A-3), the publications are reprinted with permission from the respective scientific journals.

[MF-1] M. Frisch*, J. Laun*, J. Marquardt, A. Arinchtein, K. Bauerfeind, D. Bernsmeier, M. Bernicke, T. Bredow, R. Kraehnert, *Bridging Experiment and Theory: Enhancing the Electrical Conductivities of Soft-Templated Niobium-Doped Mesoporous Titania Films*, *Physical Chemistry Chemical Physics* **2021**, *23*, 3219-3224.

https://doi.org/10.1039/d0cp06544g

[MF-2] M. Frisch*, M. H. Raza*, M.-Y. Ye, R. Sachse, B. Paul, R. Gunder, N. Pinna, R. Kraehnert, *ALD-Coated Mesoporous Iridium-Titanium Mixed Oxides: Maximizing Iridium Utilization for an Outstanding OER Performance*, *Advanced Materials Interfaces* **2022**, *9*, 2102035.

https://doi.org/10.1002/admi.202102035

[MF-3] M. Frisch*, M.-Y. Ye*, M. H. Raza, A. Arinchtein, D. Bernsmeier, A. Gomer, T. Bredow, N. Pinna, R. Kraehnert, *Mesoporous WC_x Films with NiO-Protected Surface: Highly Active Electrocatalysts for the Alkaline Oxygen Evolution Reaction*, *ChemSusChem* **2021**, *14*, 4708-4717.

https://doi.org/10.1002/cssc.202101243

*These authors contributed equally to the work.

Contents

1. Introduction

1.1 Electrochemical Water Splitting

Hydrogen (H_2) represents a highly promising energy carrier due to its exceptionally high gravimetric energy density exceeding that of any other fuel.[1,2] In order to reduce global greenhouse gas emissions and ease the depletion of fossil fuel resources, H_2 production *via* electrochemical water splitting can serve as an economically favorable alternative, as it affords high purity H_2 gas.[3] Recently, there is an ongoing growth in the established worldwide *hydrogen economy* due to the fact that H_2 can not only play a decisive role in electricity generation, but also in energy storage and transport.[4] It is anticipated that the use of H_2 as an energy carrier will support the energy transition in the next decades and aid countries worldwide to reach their climate targets.[5] In this context, energy generated from renewable energy sources can be used for H_2 generation *via* water electrolysis, rendering the overall process economically and ecologically viable.[1,3] Green H_2 produced from "green energy" can afterwards be converted into manifold valuable compounds, e.g. into ammonia (NH_3) by the addition of nitrogen (N_2) gas, or into methanol (CH_3OH) by adding carbon dioxide (CO_2) gas.[6] Alternatively, H_2 can be converted back into water (H_2O) in fuel cells for the production of electricity without any emission of greenhouse gases during operation.[6,7]

In general, electrochemical water splitting can be divided into two main reactions: The hydrogen evolution reaction (HER), producing H_2 gas at the cathode, and the oxygen evolution reaction (OER), taking place at the anode with the production of oxygen (O_2) gas.[8,9] The latter typically limits the overall efficiency of water electrolysis due to its sluggish reaction kinetics and complex reaction mechanism resulting in high anodic overpotentials.[10] Hence, the development of highly efficient electrocatalysts to promote the OER reaction kinetics is desirable for an overall increased H_2 production per energy input.

Water electrolysis can be performed at different temperatures and varying pH values. The following section will briefly summarize the advantages and disadvantages of each technology. In figure 1.1, the most important types of electrolyzers are schematically illustrated. Alkaline electrolysis (AEL) and polymer-electrolyte-membrane electrolysis (PEM-WE) operate at low temperatures between approximately 50 – 80 °C. Contrarily, much higher temperatures between 600 – 900 °C are necessary for an efficient water electrolysis using a solid-oxide

electrolyzer (SOEL).[11,12] In this thesis, the focus lies exclusively on the two former low temperature processes.

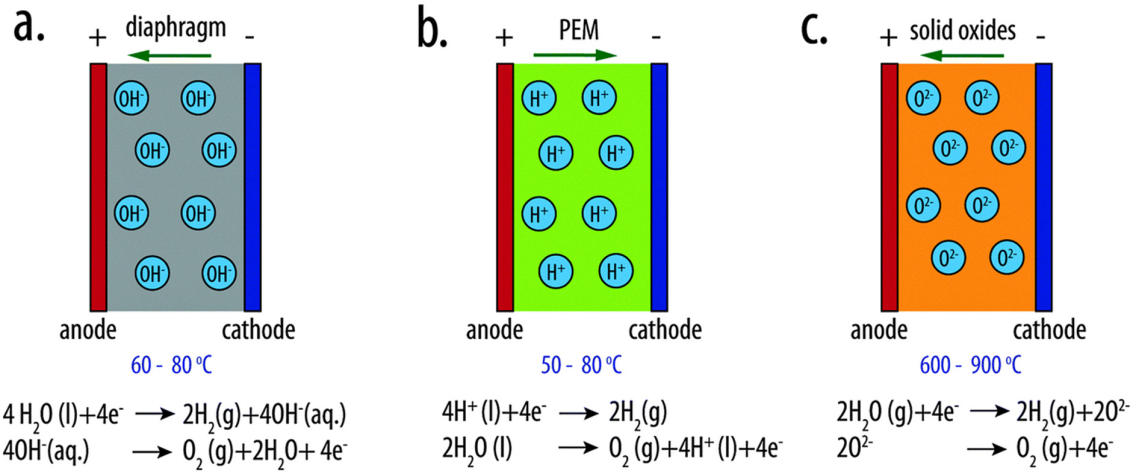

Figure 1.1: Schematic overview over the different types of water electrolyzer systems. a) illustrates an alkaline (AEL), b) a polymer-electrolyte-membrane (PEM) and c) a solid-oxide (SOEL) electrolyzer. In each of the systems, different ionic species pass through the electrically insulating membrane between the anode and the cathode. AEL and PEM usually operate at lower temperatures of about 50 – 80 °C, whereas SOEL represents a high-temperature process carried out at more than 600 °C. Reproduced from reference[11] with permission from the Royal Society of Chemistry.

1.1.1 Alkaline electrolysis (AEL)

In typical AEL, an alkaline electrolyte solution (e.g. aqueous KOH) is used as a feedstock and the electrolyzers are powered by electricity.[13] The electrodes immersed into the diluted alkaline electrolyte (typically 25–30 wt-% KOH) are separated by a porous diaphragm which serves as an ion-conducting membrane for the transport of OH^- species. During operation, solvated OH^- ions migrate through the electrolyte towards the anode, where oxidation and evolution of O_2 gas occur. The diaphragm ideally ensures a physical separation and a prevention of cross-diffusion of the evolving H_2 and O_2 gases in the cathode and the anode compartment, respectively.[3,14]

In general, the concept of AEL shows several advantages, such as the relatively low production costs, as a result of the use of non-precious metal catalysts (e.g. MoS_2 or Ni_2P[15] nanoparticles for HER, iron-nickel (oxy-)hydroxides for OER), or the production of high-purity H_2 gas. Stacks in the megawatt (MW) range were already proven efficient, hence the industrial application for large-scale H_2 generation has become a cutting-edge technology.[16,17] Starting

as early as in the 1920's, huge electrolyzer plants of up to 100 MW power were built in Canada.[17] Thus, AEL can be ranked amongst the most mature technologies in H_2 production with lifetimes in the range of ten years.[18]

Disadvantageously, the current densities are about a factor of five less than the values in PEM electrolyzers.[18] This can be explained by non-ideal gas permeability properties of the diaphragm, unfavorable interactions between the applied ionomers with the catalysts and high ohmic resistances.[15,19,20] In addition to the current losses, high-pressure operation is largely hampered by these effects due to safety concerns.[21] In this context, the coupling to fluctuating energy input sources shows a deteriorating influence on the catalyst durability. Yet, advances have recently been made concerning the use of renewable energy as energy source.[16] Despite a very high cost-effectiveness, AEL technology suffers from relatively large system dimensions.[12]

Recently, anion-exchange membrane water electrolysis (AEM-WE) has gained attraction, combining the advantages of both AEL and PEM-WE (*vide infra*). In particular, non-noble metals and steel can be used as catalysts and bipolar plates, respectively, which increases the cost efficiency of a stack. However, several years of research and development are expected to be necessary for the development of sufficiently stable and, concomitantly, conductive membranes to provide efficient anion-exchange properties during operation.[12]

1.1.2 Proton-exchange membrane water electrolysis (PEM-WE)

The overall high efficiency, especially at high current densities, alongside the production of high-purity H_2 gas represent the most important advantages of PEM-WE.[22] A differential pressure operation mode can be employed, enabling H_2 production at elevated pressure. Beyond that, a coupling to renewable energy sources becomes feasible due to a better response at fluctuating potentials and improved start-up/shutdown times.[22,23]

In contrast to AEL systems, no diaphragm is used in the cells. Instead, a relatively thin, electrically insulating membrane is used as a proton conductor and typically composed of perfluorosulfonic acid (PFSA, e.g. *Nafion*®) compounds to ensure a high chemical and mechanical stability. Typical thicknesses of PFSA-type membranes are in the range of 20 – 300 µm.[14] As a result, a lower potential drop between the electrodes compared to AEL

can be realized, thereby increasing the geometric current as well as the power densities. PEM-WE shows a rapid response to fluctuating energy inputs due to favorable H^+ transport kinetics through the *Nafion*® membrane. In brief, improved gas barrier properties of the membrane account for lower crossover rates and a higher purity of the produced H_2 in the cathode chamber. Importantly, gas crossover can lead to safety issues and decrease the overall efficiency.[14,24]

Disadvantageously, the acidic, corrosive environment in a PEM electrolyzer imposes severe restrictions to the applied electrocatalyst materials. For both the cathode as well as the anode, noble metals (*i.e.* platinum group metals, PGM) are typically used to fulfill the requirements of high activity and sufficient long-term stability under reductive or oxidative potentials, respectively.[3,14,22] Regarding the cathode, significant progress has been achieved decreasing the amount of platinum (Pt) to very low loadings at similar catalytic performance.[22] Yet, the OER half-reaction at the anode still requires high loadings of noble metals that are mainly based on iridium (Ir). The scarcity and exceptionally high costs for Ir hamper a wide-spread adoption of large-scale PEM electrolysis.[25] Therefore, innovative strategies to reduce the amounts of precious Ir in the catalysts are of uttermost importance.

The identification of stable OER catalysts and support materials that do not undergo irreversible dissolution and pronounced bulk oxidation is a highly challenging task. The design of highly efficient OER electrocatalysts represents one of the most critical factors in the improvement of the overall efficiency of electrolyzers with a leveraging effect on the economics of H_2 production.

In this thesis, a new concept for the design of nanostructured OER electrodes for both alkaline and acidic media will be described, aiming at an improved utilization of active species. In particular, for efficient OER catalysis in acid, high catalyst loadings of scarce Ir hamper a widespread industrial commercialization and up-scaling of PEM-WE for the production of green H_2. Thus, high surface area catalyst supports for active Ir species are urgently required. Yet, the oxidative and corrosive environments during OER impose several challenges and limitations to the choice of support materials. Accordingly, a highly electrically conductive and, at the same time, oxidation- and corrosion-stable material is ideally pursued. To date, no such ideal catalyst support has been found. A sophisticated concept for an improvement in catalyst durability is herein proposed, relying on the introduction of a homogeneous, conformal

surface overlay coating *via* atomic layer deposition (ALD), which is expected to protect the underlying support material from oxidation and dissolution into the surrounding electrolyte.

1.2 Support Materials with Templated Porosity

1.2.1 Porous materials

Nanostructured, porous materials show interesting properties due to their increased surface-area-to-volume ratio in manifold applications in the fields of energy conversion[26], storage (e.g. of gases[27] or charge[28]), drug delivery[29], heterogeneous catalysis[30] or gas sensing[31], amongst others. According to IUPAC, porous materials can be divided into three major classes: microporous, mesoporous and macroporous. The classification is based on the respective pore sizes of < 2 nm, 2 - 50 nm and > 50 nm, respectively.[32]

Zeolites are the most popular representatives of microporous materials with very high specific surface areas.[33,34] High-surface-area materials can lead to significantly enhanced catalytic activities, for example in heterogeneous catalysis[35,36], in charge storage[37], or in gas storage[38]. For an application in OER, microporous materials advantageously provide a very high number of accessible surface sites and are, thus, capable of promoting reaction kinetics at an electrode. However, the small diameter of the micropores can lead to mass transport limitations, manifesting for example in hampered transport of evolving reaction product gases (especially O_2) during electrocatalysis. In this context, mesoporous materials were reported to show superior characteristics due to their significantly improved mass transfer properties[39] and fast reaction product removal.[40,41]

In general, porous materials can be synthesized with various morphologies and structures, such as metal powders[42], nanoparticles[43,44], aerogels[45,46], thin films[47,48] or hybrid materials (e.g. metal-organic frameworks, MOFs[49]). The introduction of porosity into the materials can occur *via* hard templating, using e.g. silica (SiO_2) nanoparticles[50], or, alternatively, *via* soft-templating, using e.g. an amphiphilic copolymer as structure-directing agent[51,52].

1.2.2 Soft templating and evaporation-induced self-assembly (EISA)

In general, porosity can be introduced into solid materials in a controlled way using either a hard or a soft template. In the former route, the template has to be removed after the crystallization or formation of the material, e.g. *via* etching using an appropriate solvent or a mixture of solvents. A replica is obtained after the removal of the template, in which the size and dimensions of the template determines the pore structure of the formed material.[53] Often, the removal of the template involves the use of hazardous and/or toxic liquids, such as aqueous solutions of hydrofluoric acid (HF).[54,55] Porous materials derived from the so-called nano-casting often feature interesting properties due their high specific surface areas. As an illustrative example, (meso-)porous carbon monoliths can serve as electrodes in lithium ion batteries with superior capacities.[56] The key advantage of the hard templating approach is related to the absence of any complex interactions between metal precursor species undergoing hydrolysis and condensation steps with surfactant molecules serving as soft template, for instance.[57]

In the latter route, co-assembling amphiphilic compounds (e.g. surfactants) are used instead of pre-formed nanoparticles for the introduction of porosity into a material.[57,58] Brinker *et al.*[52] profoundly investigated the synthesis of ordered mesoporous structures *via* soft templating relying on *Evaporation-Induced Self-Assembly (EISA)*. Starting from soft-templated SiO_2[52,59], various other metal oxides, such as TiO_2[57], Al_2O_3[60], ZnO[61] or IrO_x[62] have been synthesized in the meantime using the EISA process. The Kraehnert group developed well-defined templated mesoporous catalytic coatings featuring significantly improved activities for applications in HER-[63], OER-[41,62] and chlorine-evolution reaction (ClER-)[64] electrocatalysis.

The synthesis concept for the different porous materials involves (a) soluble amphiphilic surfactant molecules which undergo self-assembly in an appropriate solvent (b). Often, block-copolymers are used as pore templates, which are comprised of hydrophilic head groups and hydrophobic tails.[52,65] Above a certain threshold concentration, the *critical aggregation concentration (cac)*, aggregates are formed in solution (e.g. spherical micellar structures).[66,67] Additionally, one or more metal salt(s) (c) is/are dissolved in the solution, representing the precursor(s) for the desired (mixed) metal (oxide). Electrostatic interactions between the ionic metal precursor species and the surfactant aggregates result, which undergo dynamic processes and variations during hydrolysis and subsequent condensation of the precursor species. Several factors determine the forming structures and homogeneity during the EISA process, such as[66]

- the ratio of inorganic metal precursor to surfactant,
- the concentration of the surfactant,
- the presence of H_2O,
- the temperature, and
- the relative humidity.

For the synthesis of thin films with ordered mesoporosity, the dip-coating technique represents one of the methods of choice due to its excellent reproducibility, high control over stoichiometry, pore size, and film thickness, amongst others.[66,68] Figure 1.2 provides a simplified schematic overview of the processes during dip-coating for the synthesis of templated mesoporous metal (oxide) or, for example, ordered carbon materials. When the concentration of the surfactant in the solution rises above a critical value as a consequence of the evaporation of solvent molecules, micellar structures are formed (c > cmc; note that also other structures, such as lamellar or vesicular structures, can result depending on the type of surfactant and its self-assembly behavior). These micelles serve as templating agents in the following steps. As illustrated in the schematic drawing in figure 1.2, polar, hydrophilic surfactant heads point toward the surrounding solvent, whereas the apolar, hydrophobic tails accumulate in the interior in close vicinity to each other.[66] Such behavior is characteristic for typical ionic surfactants such as sodium dodecylsulfate (SDS) in H_2O[69] or poly(ethylene oxide) – poly(propylene oxide) (PEO-PPO) block-copolymers.[70] In this context, it has to be noted that tri-block copolymers, for example, PEO-PPO-PEO copolymers, show a relatively low cmc and, thus, micellar structures already exist in the initial solution.[71]

The concomitant evaporation of other volatile compounds, such as HCl or EtOH depending on the precursors and solvent(s), leads to local variations in pH or in concentration, hence directly affecting the sol-gel kinetics of the neighboring metal precursor species.[66]

Essentially, a rapid evaporation of solvent molecules during the self-assembly of the amphiphilic compounds guarantees the build-up of a hybrid mesophase, which is further stabilized by the condensation of inorganic precursor species. Finally, after drying, a thermal treatment of the formed mesophase (e.g. *via* calcination at elevated temperature in air) leads to the crystallization of the respective metal (oxide) and the concomitant removal of the template.

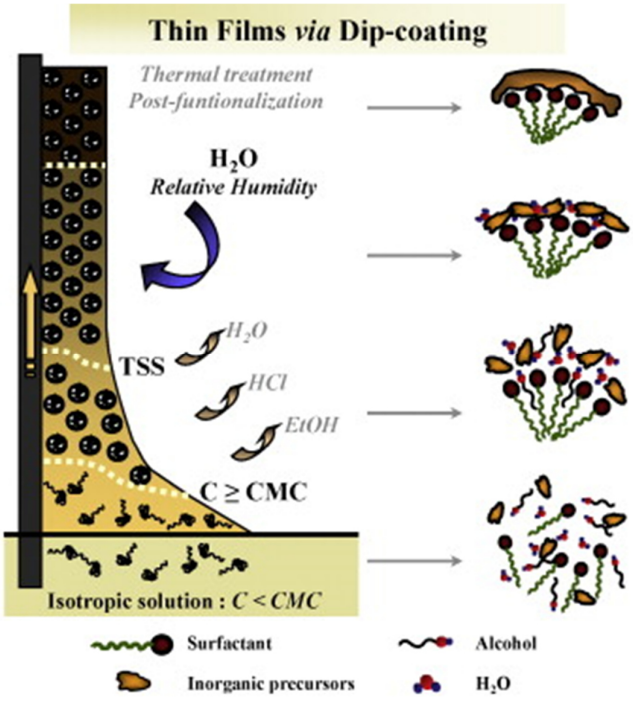

Figure 1.2: Schematic illustration of the concept of dip-coating involving the EISA process for the synthesis of thin films on planar substrates. Reproduced with permission from reference[66]*. Copyright © 2009 Elsevier Masson SAS. All rights reserved.*

The herein described concept of EISA and dip-coating offers access to the synthesis of nanostructured model systems for investigations of structure-property or structure-activity relationships.[41,72] Importantly, not only mesoporous films deposited on substrates of adjustable geometries can be prepared, but also other morphologies such as powders or fibers.[52] Different material parameters can be adjusted during the synthesis *via* dip-coating and successive thermal treatment of the deposited mesophase, such as:

- composition (by adjusting the ratio of the precursors)[41,52,62,71]
- crystallinity (by changing the temperature, duration of the thermal treatment or by using different precursors)[41,52,62,72]
- phase and crystallite size (by variations in thermal treatment)[41]
- size and shape of the pores (by changing the template)[52]
- film thickness (by tuning the withdrawal speed or viscosity of the solution)[73]
- pore wall thickness (by varying the template concentration in the solution)[71,74]

An optimization of these parameters ensures the synthesis of homogeneous, macroscopically crack-free thin films with a typical layer thickness of approximately 50 to 1000 nm.[75] Impressively, Smarsly and co-workers[76] extended the range of accessible layer thicknesses down to only a few or even one micellar monolayer. Well-ordered mesoporous titania films with a layer thickness of approximately 13-18 nm were synthesized, for instance. Modifications of the process are necessary for certain types of metal oxides, e.g. for those showing low crystallization temperatures. In case the latter is below the temperature required for the decomposition of the template, significant crystallite growth and sintering effects may impede the formation of a well-ordered mesoporous film. Exemplarily, Brezesinski *et al.*[77] found an elegant way to overcome this limitation by the choice of an appropriate polymer template with a higher thermal stability for the synthesis of mesoporous goethite films.

1.2.3 The "citrate-route"

Another approach is the addition of a stabilizing compound during the synthesis. Eckhardt *et al.*[78] found out that different anions, such as citrate anions, interact with the metal species in the precursor solution *via* electrostatic interactions and metal-ligand complexes are obtained.[78] Amongst other, oxides of zinc, cobalt and aluminum were successfully synthesized *via* this innovative "citrate-route".

In brief, the decomposing precursor complex is converted into a structurally-stable metal carbonate phase. This intermediate carbonate phase is formed at relatively low temperatures and shows very low crystallinity ("X-ray amorphous"), thereby retaining the ordered mesophase which has built during the EISA process. In the following step, a benign thermal treatment leads to the removal of the template *via* oxidative decomposition, yet without provoking a collapse of the mesopore structure. Hence, a templated mesoporous metal carbonate film with well-accessible, interconnected pores is obtained. Based on thermogravimetric analyses (TGA), insights into the material formation mechanisms were gained. Importantly, the removal of the polymer template has to occur at a lower temperature than the carbonate-to-oxide transformation. Otherwise, the template-introduced mesopore structure vanishes during the conversion of the pore wall material to the respective metal oxide. In fact, mesoporous oxide films were successfully developed by a controlled decomposition of the X-ray amorphous metal carbonate.[78]

Bernicke *et al.*[79] extended this citrate-assisted synthesis approach to the development of mesoporous nickel oxide (mp. NiO_x) catalytic coatings. A weakly crystalline character of the metal oxides combined with a high specific surface area, as a result of the introduced mesoporosity, were of particular importance to achieve high catalytic OER activities in alkaline electrolyte.

In summary, previous works provide access to various types and morphologies of porous transition metal oxides that could serve as catalyst supports with high specific surface areas. For enhanced catalytic activities, however, an optimization of the materials with respect to their bulk electrical properties, in particular conductivity, is highly desirable. This, in turn, would comprise a partial decoupling of the bulk and the surface properties of a catalyst material. The former is supposed to promote charge transfer at the electrode (electrical conductivity), whereas the latter is mainly responsible for a high catalytic turnover at the interface to the surrounding electrolyte (electrocatalytic activity). For the realization of such decoupling of bulk and surface properties of an electrocatalyst, new concepts are required, which include methods for a well-controlled surface modification of a porous support with active species.

1.3 OER Catalyst Support Materials: Metal Oxides

1.3.1 Mesoporous titanium oxide

Mesoporous titanium dioxide (mp. TiO_2) support materials are of great interest for applications in heterogeneous catalysis[80] or in photocatalysis[81,82] due to their cost-effectivity, non-toxicity, high thermal and chemical stability in combination with tunable electronic (e.g. doping) and optical properties.[83] Semiconducting TiO_2 ranks amongst the most efficient photocatalysts for solar H_2 production or light-assisted degradation of organic pollutants, for instance.[81–84] Different crystal phases were found depending on the synthesis parameters. Rutile represents the thermodynamically most stable polymorph of TiO_2, comprising a tetragonal crystal structure.[85,86] The distinct phase of TiO_2 was shown to take a significant impact on the electronic and optical properties for example in sensing applications[86] or in photocatalysis[87]. The anatase polymorph outperforms its rutile-type counterpart in terms of photocatalytic activity as a result of optimized charge carrier transport properties in the bulk. A profound study by Luttrell *et al.*[87] provides insights into the principles of light-induced exciton

generation in both rutile and anatase thin films produced *via* epitaxial growth. Notably, the photocatalytic activity can be influenced by the layer thickness of the oxide films.

Mp. TiO_2 films are also highly promising as active catalysts or support materials in electrocatalysis, particularly after improving their electronic properties.[88] Several works theoretically[88–90] and experimentally[91,92] investigated the catalytic performance of doped TiO_2 or mixed titanium-based metal oxide electrocatalysts for OER or chlorine evolution reaction (ClER). The following sections will discuss the role of doped or mixed titanium-based oxides as catalyst(s) (supports) for the acidic OER.

1.3.2 Doped titanium oxide as OER catalyst support

Due to their high mechanical and chemical stability as well as corrosion resistance, TiO_2-based materials can serve as promising catalyst supports for OER catalysis in acid.[93] Different nanostructured TiO_2-based supports have already been used for the dispersion of catalytically active Ir- or Ru-oxides, such as nanoparticles[94] or nanotubes[93,95]. Genova-Koleva *et al.*[95] reported higher catalytic OER activities for IrO_2-nanoparticles dispersed at the surface of niobium-doped (Nb-doped) TiO_x nanotubes compared to IrO_2 on bare TiO_2 nanotubes. In brief, the study revealed that n-type doping, as a result of the introduction of 3 mol-% Nb into the oxide's lattice (confirmed *via* XPS analysis), can improve the electrical properties and, hence, promote OER kinetics. Additionally, doping was shown to improve the accessibility of active sites by increasing the specific surface area of the nanotube support to up to 260 m^2/g (evaluated *via* N_2-physisorption).

Similarly, Hao *et al.*[96] dispersed small IrO_2-nanoparticles at the surface of mesoporous Nb-doped TiO_x powders prepared *via* EISA and sol-gel chemistry. In their work, the authors investigated the impact of the dopant fraction in the porous oxide support, which was surface-functionalized by 40 wt-% IrO_2 using the well-established Adam's fusion method. The latter is based on chloroiridic acid ($H_2IrCl_6 \cdot 6H_2O$) and *iso*propanol as IrO_2 precursor and polar solvent, respectively. Sodium nitrate ($NaNO_3$) is then added for the oxidation of the metal precursor salt at elevated temperatures of about 500 °C. For 20 mol-% of Nb in the support, the highest catalytic activities are found in both half-cell and single-cell PEM electrolyzer setups. Importantly, the introduction of a conductive, porous support *via* transition metal doping shows a beneficial impact on the specific surface area as well as on the surface activity

by tuning the nature of active sites. Accordingly, the OER activity of the most active catalyst consisting of IrO_2-nanoparticles (40 wt-%, < 3 nm in size) dispersed on mesoporous $Nb_{0.2}Ti_{0.8}O_2$ outperforms catalysts based on un-doped mesoporous TiO_2 or unsupported IrO_2-nanoparticles.

In brief, several works propose different concepts for the synthesis of Nb-doped titania powders and films with high specific surface areas. Even though a clear enhancement in electrical conductivity of the doped oxides with respect to bare titania was observed, most studies lack profound insights into the origin of the improved electronic properties. In this context, inconsistencies regarding the maximum in electrical conductivity and dopant fraction can be found. Hence, it would be highly desirable to combine the findings from experimental characterizations on well-defined model oxide systems with those from theoretical calculations in order to identify the composition with the highest conductivity that represents the most appropriate candidate for an application as OER catalyst support in acid. Beyond that, computation can aid in the identification of other promising dopants or host oxides and, thus, extend the range of catalyst supports. Yet, the prediction of (in)stability of these doped oxides during OER catalysis still remains a major challenge, which can only be addressed by developing more complex theoretical simulations accounting for potential-dependent dopant leaching, amongst others.

1.3.3 Doped tin oxide as OER catalyst support

Stannic oxide (SnO_2) is mainly used for the preparation of transparent conducting oxides (TCOs) due to its wide band-gap semiconducting properties.[97] Different dopants, such as Zn[97] or Sb[98], were shown to improve the electrical properties and, thus, enhance the electrocatalytic performance of SnO_x-based materials, e.g. in gas sensing[97], redox-flow batteries[99] or in OER-electrocatalysis[98].

Böhm *et al.*[98] synthesized macroporous antimony-doped tin oxide (ATO) supports *via* ultrasonic spray pyrolysis using spherical poly(methyl methacrylate) (PMMA) as hard template. By variations in the particle diameter of the polymer template, the resulting pore sizes could be adjusted. These porous ATO particles served as supports for catalytically active IrO_x nanoparticles which were finely dispersed throughout the surface of the carrier's pore walls. The last step in the multi-step synthesis involved a thermal oxidation step for the conversion

of metallic Ir- to oxidic IrO_x-nanoparticles at the surface of the well-conductive doped support. The most active OER catalyst (ATO@IrO_x) reached a high Ir-mass-specific activity of 60 A/g_{Ir} at a potential of 1.53 V_{RHE} in a typical rotating disc electrode (RDE) setup using 0.5 M H_2SO_4 as supporting electrolyte (O_2-saturated; 1600 rpm, T = 60 °C). The aim of the study was a significant reduction of the Ir volumetric packing density in the catalysts. Despite the very low Ir loadings, high catalytic activities were claimed. More precisely, a low overpotential of only 215 mV is necessary to afford a geometric current density of 1 mA/cm^2, which can be explained by the improved electrical properties of the support and a good dispersion of the highly active IrO_x-nanoparticles (mainly IrO_2). However, the authors had to admit that doped SnO_x-based materials show a rather weak long-term stability under applied oxidative potentials and usually lack sufficient corrosion resistance. According to their conclusions, Nb-doped TiO_x might represent a suitable candidate with a higher corrosion resistance.

The general issue of an application of doped SnO_x-based supports for OER catalysis has also been pointed out by Geiger *et al.*[100] recently. The authors compared the stabilities of tin oxides doped with fluorine (FTO), indium (ITO) or antimony (ATO). For all of them, leaching of the dopants into the surrounding solution in a corrosive and oxidative environment negatively affects their long-term stability. FTO was found to show the highest catalytic stability, yet with poor electrical conductivity that, in turn, negatively affects catalytic activity.

In their work entitled *"Mesoporous iridium oxide/Sb-doped SnO_2 nanostructured electrodes for polymer electrolyte membrane water electrolysis"*, Han *et al.*[101] evaluated the OER performance of ATO-supported IrO_x catalyst powders prepared *via* Adam's fusion and ball-milling for the introduction of active Ir species. The high-surface-area ATO support provides favorable mass transport as well as charge transfer properties during catalysis. Additionally, the authors stated an increased number of accessible active sites, *i.e.* of oxidic Ir sites that are surface-exposed. In a typical RDE setup, a high Ir-mass-specific activity of 193 A/g_{Ir} at a potential of 1.60 V_{RHE} was found for the most active catalyst (0.1 M $HClO_4$, T = 25 °C, catalyst loading: ~ 200 µg/cm^2). In comparison to a reference IrO_2 powder catalyst as an unsupported benchmark, enhanced activities for the ATO-supported catalyst were also reported in a single-cell PEM electrolyzer (cathode: 20 wt-% Pt/C; membrane: Nafion 117), despite the significantly reduced Ir loadings.

Summing up the results discussed in this section, doped transition metal oxides advantageously show moderate to high stabilities in oxidative and acidic conditions. However, the achieved electrical bulk conductivities often lie within the range of semiconductors and, consequently, hamper an efficient electrocatalytic process at the electrode. Hence, the identification of stable support materials with higher conductivities, such as metal-like conductive carbides, is of great importance to promote charge transfer kinetics during OER.

1.4 OER Catalyst Support Materials: Metal Carbides

1.4.1 High-surface-area metal carbides

The excellent electrical properties, primarily the metallic electrical conductivity, as well as the very high mechanical stability of metal carbides provide a good basis for an application as catalyst or catalyst support in various electrochemical reactions.[102,103] However, the formation of metal carbides often requires very high synthesis temperatures and harsh thermal treatments, which hamper the development of carbide-based materials displaying high specific surface areas.[102,104,105] Elevated temperatures promote excessive crystallite growth and sintering effects lead to drastic reductions in specific surface area. Therefore, new synthesis concepts for the design of nanostructured, high-surface-area carbides are required for an application as conductive support material in electrocatalysis, amongst others.

1.4.2 Synthesis of mesoporous tungsten carbides

Apart from applications as wear-resistant tools, e.g. for cutting or in surgical instruments, tungsten carbides were employed as electrode materials in the fields of electrocatalysis and fuel cells.[102,106] During the last two decades, innovative synthesis methods and concepts for nanostructured tungsten carbides and cemented carbides are on the rise. Several studies investigated the obtained crystal structures, deduced structure-stability correlations and improved the electronic properties.[105–107] Yet, only a few works reported concepts for the synthesis of mesoporous tungsten carbide powders.

Ma *et al.*[108] supported nanosized platinum on mesoporous tungsten carbide (Pt on mp. WC) *via* impregnation. The tungsten carbide support was of equimolar stoichiometry (WC) and

produced using ammonium metatungstate as tungsten precursor. After thermal treatment for 8 h at 750 °C in a gas mixture of methane (CH_4) and H_2 with a ratio of 3:1 and a subsequent quenching-passivation step, hollow WC spheres were yielded. WC_x materials were theoretically and experimentally found to show moderate intrinsic HER activities and, hence, are highly promising for the development of superior HER catalysts with reduced noble metal loadings and a higher resistance to poisoning by carbon monoxide, for instance.[102,108] Notably, Pt on mp. WC outperformed a highly active benchmark HER catalyst (Pt supported on carbon, Pt/C), despite the presence of residual surface carbon species after the thermal treatment in CH_4/H_2.

Ko *et al.*[103] synthesized nanostructured, well-defined mesoporous tungsten carbide nanosheets by employing a template-free synthetic route *via* tungsten nitride nanosheets as intermediate phase. Similar to the work mentioned above by Ma *et al.*, ammonium metatungstate was used as a tungsten precursor. The intermediate nitride phase was then converted to the carbide phase *via* a carburization reaction in an atmosphere of CH_4 and H_2 with a ratio of 1:4 at temperatures above 700 °C. After a comprehensive analysis of the physicochemical properties of the carbide nanosheets, electrochemical testings as oxygen reduction reaction (ORR) catalyst in alkaline electrolyte were performed. The addition of palladium species to the carbide support led to beneficial effects on both the electrocatalytic activity and stability due to enhanced metal-support interactions. The best catalyst system, Pd/WC900-m, shows a superior performance than a reference Pt/C catalyst and, hence, might serve as promising alternative for fuel cell cathodes.

1.4.3 Applications of tungsten carbides in OER catalysis

Han *et al.*[109] reported nitrogen-doped (N-doped) WC nanoarrays as active electrocatalyst for both the HER and the OER half-reaction in acidic electrolyte. The two-step synthesis involved the growth of WO_3 nanoarrays on carbon fiber paper (CFP) as a support, and a subsequent reduction-carbonization for the formation of N-doped WC on CFP by the addition of melamine in a controlled chemical vapor deposition (CVD) process at temperatures above 650 °C. Thereby, melamine served as precursor for both C and N species, *i.e.* for the carbide formation and, concomitantly, the doping. By the incorporation of N dopant atoms into the carbide lattice, an optimized electronic structure and, consequently, an excellent HER activity for a PGM-free

catalyst were obtained. Theoretical calculations suggested a favorable down-shift in the d-band center, hence leading to a decrease in hydrogen binding energy, compared to the un-doped WC counterpart whose reaction kinetics were found hampered by slow hydrogen desorption. Importantly, after doping, not only a high HER activity but also a reasonable OER activity was reported in the study. At a loading of 10 mg/cm^2, the most active N-WC nanoarray electrocatalyst outperformed a reference Ir-based electrodes of similar loadings using 0.5 M H_2SO_4 as a supporting electrolyte. However, an ongoing loss in OER activity was mentioned by the authors and is most likely the result of an irreversible oxidation starting at the carbide's surface and increasing throughout the bulk of the material over prolonged time under oxidative conditions. After 60 min, a potential of 1.54 V_{RHE} to achieve a geometric current density of 10 mA/cm^2 was recorded in the chronopotentiometric stability tests of N-WC.

More often, tungsten carbides were used as highly conductive catalyst support materials. An impressive example is recently reported by Li *et al.*[110] using single-atom catalysts based on iron and nickel species supported on tungsten carbide. Importantly, the synthesized WC_x support can aid in the stabilization of (bi-)atomic Fe, Ni and FeNi metal species. Strong interactions between the metal-like support and the surface-exposed single-atom metals ensure the formation of a highly stable and active OER electrocatalyst for alkaline OER.
As precursor for the WC_x, a dopamine-tungstate complex was synthesized, to which traces of Fe and/or Ni were introduced by precipitation. An optimized thermal treatment can lead to an excellent dispersion of catalytically active single-sites in the PGM-free catalyst.
Results from electrochemical investigations reveal a very high catalytic activity (low overpotential of 211 mV at a current density of 10 mA/cm^2). Remarkably, an unprecedented durability of ~ 1000 h was reported in the study for catalysts deposited on nickel foam as substrate. The origin of the observed excellent catalytic performance has been evaluated both experimentally and theoretically using DFT calculations. Most importantly, the former confirms the formation of weakly bound, atomically dispersed FeNi species at the surface of the WC_x crystallites without any signs for replacements of tungsten atoms in the lattice of the support. Post-OER analysis provides evidence for the formation of O-bridged FeNi moieties during catalysis, according to the results from X-ray absorption spectroscopy.
Theoretical investigations reveal distinct insights into the mechanistic OER pathways and, thus, propose explanations for the superior activities. Synergistic effects between Fe and Ni species in highly active Fe-O-Ni moieties ultimately result in very high turnover-frequencies (TOF) of almost 5 s^{-1} at a moderate potential of 1.53 V_{RHE}. The partial oxidation of the metal

Fe and Ni surface sites during OER can be claimed to show a beneficial impact on the stability, as a consequence of Coulomb repulsion.

In principal, transition metal carbides are promising candidates for an application as conductive catalyst support for many electrocatalytic reactions. Yet, the oxidative and harsh conditions during the OER half-reaction in electrochemical water splitting impose severe obstacles due to an insufficient stability against bulk oxidation and, concomitantly, dissolution of the material into the surrounding electrolyte. In addition to that, synthesis concepts for the introduction of templated porosity in well-defined metal carbide coatings *via* nanocasting have not been reported to date. The main challenge with regard to the development of high surface area metal carbides is the excessive and uncontrolled sintering of crystallites during the high temperature synthesis, which prevents the formation of an interconnected pore structure.

1.5 OER Catalysts with Templated Mesoporosity

1.5.1 Acidic OER: Mesoporous titanium-based oxides

The inherent promising corrosion resistance of TiO_2 is the main driving force in the development of titanium-based mixed oxides as efficient OER catalysts with reduced noble metal contents operating in acidic environments. Yet, the intrinsic OER activity of pristine TiO_2 is several orders of magnitude lower than that of Ir- or Ru-based oxides.[14,72] One reason for this behavior lies in the low electrical conductivity of TiO_2 due to its semiconducting properties. One strategy to improve the electrical properties and, in parallel, introduce catalytic activity, is the replacement of Ti atoms in the oxide lattice with e.g. Ir or Ru atoms.

Bernsmeier *et al.*[72] and Bernicke *et al.*[14,111] reported interesting structure-activity relationships for mesoporous Ir-Ti mixed oxides with varying compositions based on systematic investigations. For their studies, model-type mixed oxide catalyst films with template-controlled porosity and homogeneity were synthesized and electrochemically tested in a three-electrode setup (rotating disc electrode, RDE) using diluted H_2SO_4 as a supporting electrolyte. Based on an exact variation of the parameters, such as film composition, crystallinity or layer thickness, structure-activity correlations were deduced in a quantitative way, highlighting the decisive role of Ir on the morphology, but also on the electrical properties and, thus, on the activity of the coatings.

Comprehensive analyses of the material's physicochemical properties revealed important insights into the role of the noble metal species in the porous films. First, the impact of the Ir content on the morphology and porosity is relatively weak. Macroscopically crack-free thin films can be synthesized over a broad range of Ir contents (0 – 100 % Ir) using titanium(IV) *bis*(ammonium lactato)dihydroxide (TALH) and iridium(III) acetate as Ti and Ir precursor, respectively. A triblock-copolymer template comprised of 18,700 g/mol PEO and 10 000 g/mol PB (PEO_{213}-PB_{184}-PEO_{213}) leads to the formation of spherical mesopores after calcination in air, independent of the film composition. The developed synthesis route ensures good Ir dispersion and the three-dimensional mesoporous structure mitigates mass transport limitations during catalysis.[72,111]

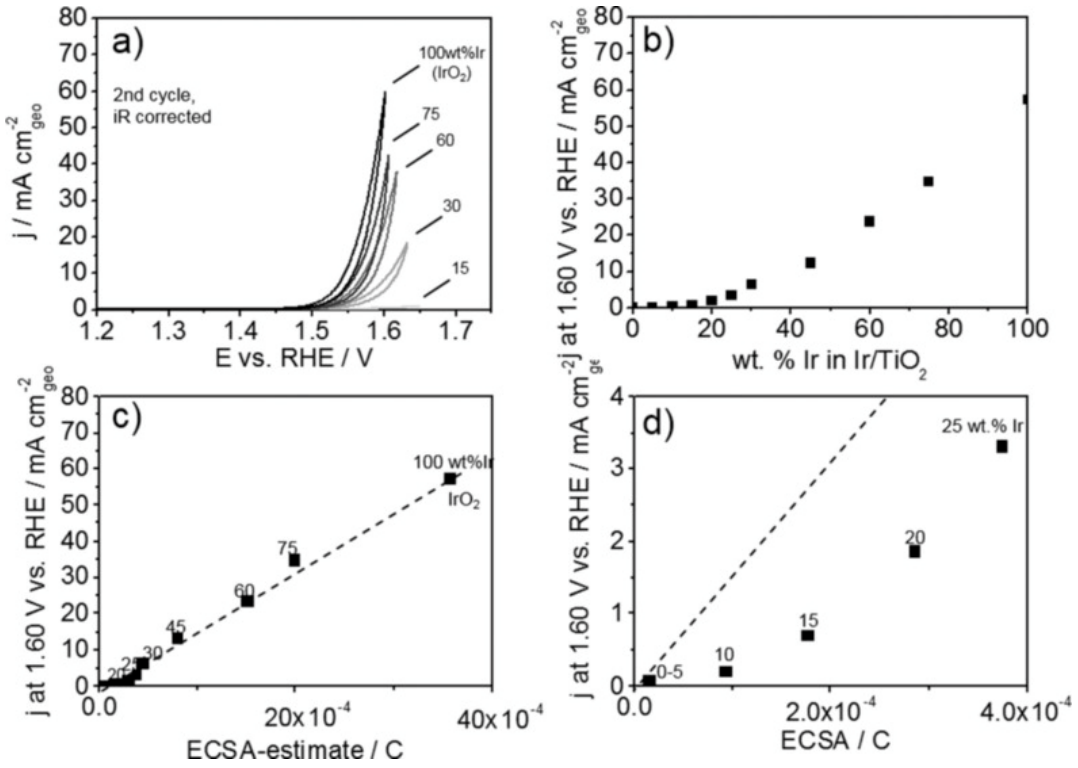

Figure 1.3: Influence of Ir content in Ir-Ti mixed oxide films on the catalytic OER activity, assessed via electrochemical testings in an RDE setup at room temperature, using N_2-purged 0.5 M H_2SO_4 as a supporting electrolyte. a) shows the geometric current densities j of the 2nd CV for each catalyst film deposited on a flat, polished titanium substrate in OER regime. b) represents a plot of OER current density j vs. Ir content at a potential of 1.60 V vs. RHE. c) & d) show estimated ECSA values as a function of Ir content. Reprinted from reference[72] with permission from John Wiley and Sons. Copyright 2018 WILEY-VCH Verlag GmbH & Co. KGaA, Weinheim.

One of the most interesting findings in the previous studies is the clear correlation of electrocatalytic activity and electrical conductivity in the mixed oxide films. In this context, the content of Ir in the mixed oxides affects the ratio of the present crystal phases of the pore walls that was found to be a mixture of a Ti-rich rutile, an Ir-rich rutile and a TiO_2-based anatase phase.[72] At moderate calcination temperatures of about 400 °C, the former two phases are of low crystallinity, which is desired to establish high catalytic activity via the formation of highly OER-active IrO_x species.

More precisely, the Ir-rich rutile phase is found to be well-dispersed within a Ti-rich rutile phase alongside a TiO_2-anatase phase. This structural model implies important consequences in order to produce sufficient conductivity throughout the bulk of the material and, thereby, promote OER kinetics. A minimum relative amount of conductive Ir species in the network is mandatory to provide conductive electron pathways which are surrounded by insulating Ti-rich phases, e.g. by TiO_2-anatase crystallites. According to Bernsmeier & Bernicke *et al.*[72] (see figure 1.3) a minimum Ir fraction of 15 mol-% (30 wt-%) in the porous Ir-Ti mixed oxide catalysts is necessary to establish OER activity by sufficient electron transport kinetics in the bulk of the catalyst.

1.5.2 Alkaline OER: Mesoporous nickel-based oxides

Bernicke *et al.*[79] developed nickel oxide coatings with templated porosity (mp. NiO_x) for alkaline OER *via* a citrate-assisted synthesis route. In the study, the impact of varying synthesis parameters, such as the calcination temperature, on the structural properties and the electrochemical activity of the films was investigated. Based on results from thermal analysis of the precursor complexes, insights into phase, crystallinity and composition in dependency of calcination temperature were received. For a high catalytic OER activity in alkaline electrolyte, a high specific surface area (assessed *via* BET measurements) along with a weakly crystalline NiO phase, that can be reversibly converted into an active NiOOH phase at oxidative potentials, are necessary. According to findings from electron microscopy, XPS and GI-XRD, the low-crystallinity NiO phase is predominantly formed at a calcination temperature of about 350 °C.

Structural properties can thus be interrelated with electrocatalytic activity. In this context, the authors have shown that a further increase in activity can be achieved by the application of

extensive anodic pre-treatments of the electrodes. During this electrochemical activation, a significant fraction of near-surface Ni species are converted to $Ni(OH)_2$ or NiOOH by partial oxidation and reconstruction.
Overall, the study highlights the importance of the identification of structure-determining factors and the deduction of structure-activity correlations in order to improve catalytic activity of a material. The synthesized homogeneous mp. NiO_x films serve as model systems, yet it can be expected that the electronic properties of the bulk phases still need to be optimized to promote OER kinetics.

The group of Tüysüz *et al.* used nickel-based oxides with templated-controlled porosity (e.g. mp. Ni-Co oxides[112] or Ni-Fe oxides[113]) as model systems to study the impact of residual Fe impurities originating from the alkaline electrolyte (e.g. KOH) on the catalytic activity. There is a general consensus in recent literature that the unintended incorporation of Fe species at the catalyst surface affects the structural and electrical properties. Notably, even very little amounts of Fe impurities (< 1 ppm) in the electrolyte were proven to alter the electrocatalytic performance, as both the nature and the amount of active sites are modified, leading to a boost in activity.[112,114] Experimental and computational approaches shed light on the most relevant effects of Fe incorporation: On the one hand, enhanced electrical conductivities result, and, on the other hand, variations in the OH^- adsorption strengths on the surface (Sabatier principle) can be calculated.[114,115] Similar effects were observed for other OER-active transition metal oxides, such as cobalt oxides[116]. Boettcher *et al.*[117] even state that pure NiOOH would represent "a very poor OER catalyst", emphasizing the beneficial impact of incorporated Fe ions at the catalyst surface which is most effective for nickel oxides. Their detailed investigations about (oxy)hydroxides of first-row transition metals reveal that a sufficient electrical conductivity of the active phase with delocalized electronic structure is required for a high OER activity. Importantly, the metal centers undergo dynamic changes during catalysis, such as redox transitions between different oxidized states, which, in turn, affects the overpotential.

As an interim summary, it can be concluded that porous, high surface area (mixed) metal oxides represent active electrocatalysts for the OER in both acidic and alkaline electrolyte. The introduction of mesoporosity was shown to increase the number of accessible active sites at the surface and, as a direct consequence, enhance the catalytic activity with respect to their un-templated counterparts of similar composition and crystallinity.

Yet, the development of a concept that allows an independent adjustment of the properties of the bulk and the surface of the catalyst material is desirable in order to optimize the mass-specific activity by an improved utilization of active species. A subsequent modification of the entire pore wall surface of a conductive support *via* ALD ideally ensures a superior utilization of the deposited active sites. Moreover, in the case of the formation of a homogeneous overlay coating of high conformality, a protection of the underlying support material can be realized. This effect can be expected to promote the overall catalyst durability during OER electrocatalysis.

1.6 Atomic Layer Deposition (ALD)

Atomic Layer Deposition (ALD) is the method of choice for a well-controlled deposition of thin films with an exceptional degree of conformality, especially on high-aspect-ratio substrates.[118,119] As a vapor-phase technique, ALD can be used for various applications, such as to improve the properties of gas sensors[120,121], batteries[120,122], fuel cells[120,123], photocatalysts[120,124] or electrocatalysts[125], amongst others. Its self-limiting reaction mechanism with alternating precursor exposure during the formation of e.g. surface metal[126], metal oxide[127] or metal carbide[128] layers enables the deposition of homogeneous structures with adjustable composition and thickness. Even though ALD has often been developed from CVD methods, the different reaction mechanism and different reaction precursor compounds affect the temperature during the reaction with the substrate's surface. Typically, ALD is performed with high stoichiometric control at lower temperatures compared to CVD processes.[118]

The following section briefly describes the underlying ALD reaction mechanism for a typical thermal ALD process. For a more detailed investigation of the working principle based on the ongoing chemical and physical processes close to the surface, the interested reader is referred to a comprehensive work by Bent *et al.*[129]. Figure 1.4 represents a simplified overview over a general ALD process, in which the thickness of the deposited surface layers can be precisely tuned by variations in cycle number. A pre-functionalization of the substrate's surface can be useful to achieve a faster nucleation of the reacting gaseous precursor species during the initial phase. In this context, the presence of hydroxy (–OH) functionalities promotes the chemisorption of the precursor molecules being pulsed into the reaction chamber *in vacuo*.

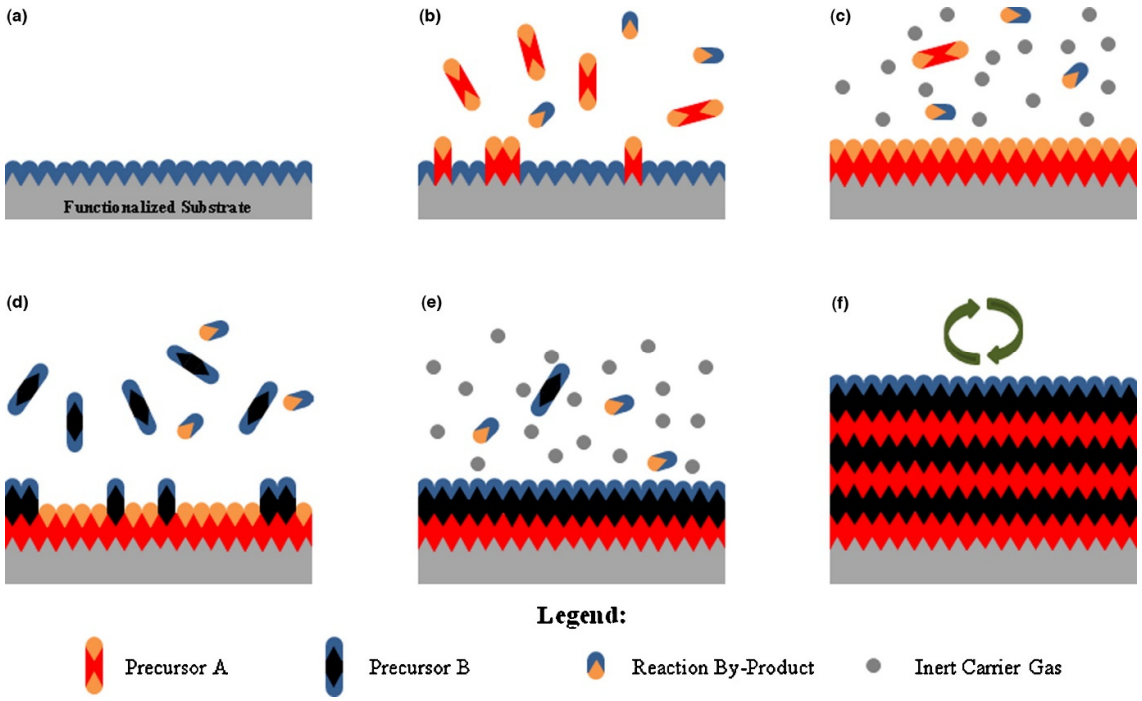

Figure 1.4: Schematic illustration of the general ALD reaction mechanism. A surface-functionalized substrate (a) is modified using thin layers of a desired material via conformal ALD. As an example, surface –OH groups can serve as nucleation sites that subsequently react with species of Precursor A in (b). After the pulse of Precursor A (b), a purge step is performed (c) to remove excess precursor species and by-products of the reaction. Typically, an inert gas such as N_2 or Ar is applied and fed into the reaction chamber. Afterwards, the second precursor (denoted as Precursor B) is introduced into the chamber and reacts with the surface (d). Again, excess precursor and forming reaction by-products are removed by purging with an inert carrier gas (e). Processes (b)-(e) represent one complete ALD cycle, which can be repeated several times to afford a certain thickness of surface-deposited layers of a desired compound (f). Note that the schematic is a simplified and idealized representation of the process. Reprinted with permission from reference[118]*. Copyright 2014 Elsevier Ltd.*

Both the duration and the temperature of the chamber of the ALD reactor depend on the chemical properties of the precursor compounds used in each half-cycle. Importantly, the aim is to yield a monolayer coverage at the substrate's entire exposed surface (*cf.* figure 1.4b). Purging with an inert gas such as N_2 or Ar aids in the removal of formed reaction by-products and excess precursor molecules (*cf.* figure 1.4c). After purging, the second half-cycle starts with the introduction of the second precursor compound into the reaction chamber (*cf.* figure 1.4d). Again, a subsequent purging step with an inert gas carrier removes un-reacted species and by-products (*cf.* figure 1.4e), thereby completing one full ALD cycle. For the adjustment of surface layer thickness of the desired material, the whole process can be iterated several times (*cf.* figure 1.4f). Based on such sequential deposition, the film thickness can be varied between a few Å to tens of nm. Comparably low temperatures (typically < 350 °C) are employed to ensure a self-limiting reaction mechanism. Depending on the respective ALD precursors, the temperature during deposition has to be adjusted to identify the optimum growth

rate with balanced reaction kinetics, which is often referred to as the "ALD temperature window".[118–120,129] In general, high temperatures promote an undesired thermal decomposition of the compounds or uncontrolled desorption processes from the surface, whereas low temperatures can lead to sluggish reaction kinetics or the condensation of precursor compounds.[119,120,129]

Summing up, the development of a new ALD process for the deposition of a desired material entails the development of a profound understanding of the precursor chemistry and chemisorption properties. Multiple parameters, such as the right choice of deposition temperature for a certain combination of precursor compounds (ligands, oxidation state of metal ion etc.) show a decisive impact on the resulting structures.
In particular, ALD represents a convenient yet complex method for the homogeneous, conformal surface modification of support materials with interconnected pore structures. In this context, a concept based on the deposition of OER-active species exposed at the surface of porous electrodes introduces an additional degree of freedom in the design of nanostructured electrocatalysts. Ultimately, an optimization of the interactions between the support and the surface layer can be expected to improve both the activity as well as the stability of the electrode coating. An improved spatial distribution of surface-exposed active species introduced *via* ALD is thus proposed to result in significantly enhanced mass-specific OER activities.

1.7 State-of-the-Art ALD-Modified OER Electrocatalysts

Recently developed OER electrocatalyst systems based on a surface modification of a catalyst support *via* ALD provide evidence for improved OER activities in terms of utilization of active species (mass activity). Importantly, a careful optimization of the experimental parameters during ALD is required in order to establish high OER activities. Depending on the pH of the surrounding electrolyte, different combinations of support and surface metal (oxide) were proven effective in literature studies (*vide infra*).

1.7.1 Alkaline OER electrocatalysis

Matienzo *et al.*[130] investigated the electrocatalytic performance of NiO-ALD as well as IrO_2-ALD surface-modified expanded Ni meshes serving as conductive substrates using a typical RDE setup (6.0 M KOH, T = 80 °C). In their study, the ALD layer thickness was rather high with values between 25 nm and 60 nm for NiO and 50 to 60 nm for IrO_2. As metal precursors, nickel(II) *bis*-2,2,6,6-tetramethyl-heptane-3,5-dionate ($Ni(tmhd)_2$) and iridium(III) acetyl-acetonate ($Ir(acac)_3$) were used for the deposition of NiO and IrO_2, respectively. O_3 was employed as oxygen source, N_2 was used as carrier gas for purging. Importantly, the deposition afforded crystalline surface oxide layers, as revealed by X-ray diffraction in gracing incidence geometry (GI-XRD). Resulting from the relatively high Ni and Ir metal loadings introduced *via* ALD, dense and homogeneous surface coatings introducing high catalytic activities under industrially relevant conditions (up to 10 kA/cm^2 current) were obtained. As already mentioned by the authors, further work has to be done in order to evaluate the catalysts' stabilities under these oxidative reaction conditions.

1.7.2 Acidic OER electrocatalysis

Due to their high corrosion resistance, nanostructured TiO_2-based materials have received great attention as suitable OER catalyst support in acid environment. Schlicht *et al.*[93] prepared ALD-surface-modified anodic TiO_2 nanotube arrays with adjustable pore lengths in the micron-size range. By well-controlled conformal ALD, metallic $Ir^{(0)}$ surface layers of varying layer thickness were deposited onto the surface of the TiO_2 tubes. The study is based on a previously established novel ALD route developed by the Bachmann group using ethylcyclopentadienyl-1,3-cyclohexadiene-iridium(I) $[(EtCp)Ir^{(I)}(CHD)]$[131] at 220 °C in combination with O_3 as oxygen source. Structure-activity correlations were deduced, revealing a minimum ALD layer thickness in the ordered porous Ir/TiO_2 electrodes. More precisely, for low ALD cycle numbers of 50 or 25 cycles, the tendency for the formation of discontinuous islands of noble metal species rather than thick, continuous surface layers was increasing. As summarized in the results from the electrocatalytic OER testings given in figure 1.5, a significant drop in activity can be observed for catalysts with low ALD cycle number, *i.e.* for 25 and 50 cycles. In contrast, an increase in cycle number to 75 cycles led to an excellent OER activity of 200 A/g at

1.57 V_{RHE} for a catalyst loading of 160 µg/cm^2 (Ir loading analyzed *via* inductively coupled plasma optical emission spectrometry, ICP-OES).

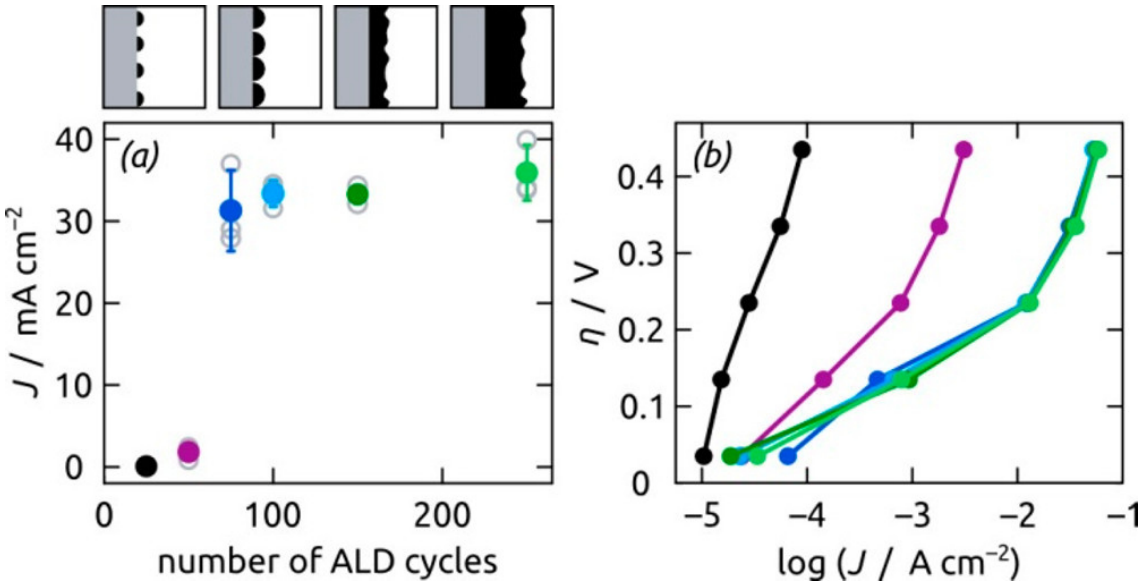

Figure 1.5: Results from steady-state electrocatalytic testings in a three-electrode setup using 0.1 M H_2SO_4 as a supporting electrolyte: (a) Correlation between geometric current density J (at 1.57 V_{RHE}) and ALD cycle number of the deposition of metallic $Ir^{(0)}$ species at the surface of TiO_2 tubes (average length: 12 µm); (b) corresponding Tafel plots (color-coded). Reprinted with permission from reference[93]. Copyright 2019 American Chemical Society.

To conclude, most studies exclusively report the surface modification of metal (oxide) supports, e.g. $Ni^{(0)}$ or TiO_2, with either metallic or oxidic species, e.g. $Ir^{(0)}$, IrO_2 or NiO. Considering the variations in structure, the surface modification of metal carbide support materials represents a highly challenging task, which will also be addressed in this thesis.

1.8 Analytical Methods: Investigation of the Electrical Properties of Thin Films

1.8.1 Impedance spectroscopy

Impedance spectroscopy is a non-destructive method for the investigation of the electronic properties of a material, e.g. of thin films of semiconductors or metals. As an AC (alternating current) technique, it represents an alternative to classical DC measurements relying on current-voltage analysis. Advantageously, not only the charge transport properties in the bulk of a material can be evaluated, but also interfacial electrochemical reactions.[132,133]

Usually, a sinusoidal excitation potential of small intensity is applied to the system and the voltage-response to this, *i.e.* an AC signal, is analyzed and used for the assessment of the electrical conductivity or, for example, the ionic conductivity.[132–134] Impedance spectroscopy can be performed over a broad range of frequencies and thus represents a routine method for the characterization of various compounds for applications in fuel cells, batteries or capacitors, for instance, revealing distinct insights into the ongoing multi-step processes. Due to the fact that every single reaction or ion/charge migration step shows a certain associated time constant, the corresponding frequency domain analysis theoretically enables a distinct separation of each individual step in the whole process.[135]

In contrast to Ohm's law *(1)*,

$$R = \frac{U}{I} \qquad (1)$$

the concept of impedance or its reciprocal, the so-called *admittance*, is not limited to an ideal resistor being the only circuit element. Rather, a frequency-dependency of the resistance is accounted for.

The time-dependent excitation potential U_t can be expressed as given in equation *(2)*,

$$U_t = U_0 \cdot \sin(\omega t) \qquad (2)$$

in which U_0 represents the amplitude and ω represents the radial frequency.

Accordingly, the time-dependent output or response signal (I_t) can be expressed as the following:

$$I_t = I_0 \cdot \sin(\omega t + \Delta) \tag{3}$$

In *(3)*, I_0 describes the amplitude of the response current signal and Δ is introduced to account for the phase shift of the signal with respect to the incoming excitation signal (for linear or pseudo-linear systems).[132,133,135]

Finally, an expression for the impedance *Z (4)* can be defined in analogy to Ohm's law:

$$Z = \frac{U_t}{I_t} = \frac{U_0 \cdot \sin(\omega t)}{I_0 \cdot \sin(\omega t + \Delta)} = Z_0 \cdot \frac{\sin(\omega t)}{\sin(\omega t + \Delta)} \tag{4}$$

Using Euler's relationship, the complex impedance $Z(\omega)$ *(5)* can be obtained as follows:

$$Z(\omega) = \frac{U_t}{I_t} = Z_0 \cdot \exp(j\Delta) = Z_0 \cdot [\cos(\Delta) + j\sin(\Delta)] \tag{5}$$

For the data evaluation and the assessment of the electrical conductivity of a dielectric material, a *Nyquist plot* can be obtained plotting the real part of the complex impedance function $Z(\omega)$, Z', on the abscissa and the imaginary part, Z'', on the ordinate. Figure 1.6 shows an example for a simplified Randles model circuit that is frequently used for characterization in electrochemical impedance spectroscopy (EIS). Different elements are used in the construction of an equivalent circuit model, such as resistors (R), capacitors (C) and inductors (L), as well as more complex elements such as constant phase elements (CPE) or Warburg impedance (W) to account for non-ideality in e.g. capacitance or diffusion, respectively.[135,136]

Real systems often show complex characteristics and phenomena as a result of multiple processes at different electrochemical interfaces. As an example, the surface roughness of an electrode can influence the electrical double-layer at an electrode-electrolyte interface.[136] It is thus important to understand the whole electrochemical system and reduce the amount of necessary components in an equivalent circuit to a minimum in order to obtain realistic results.

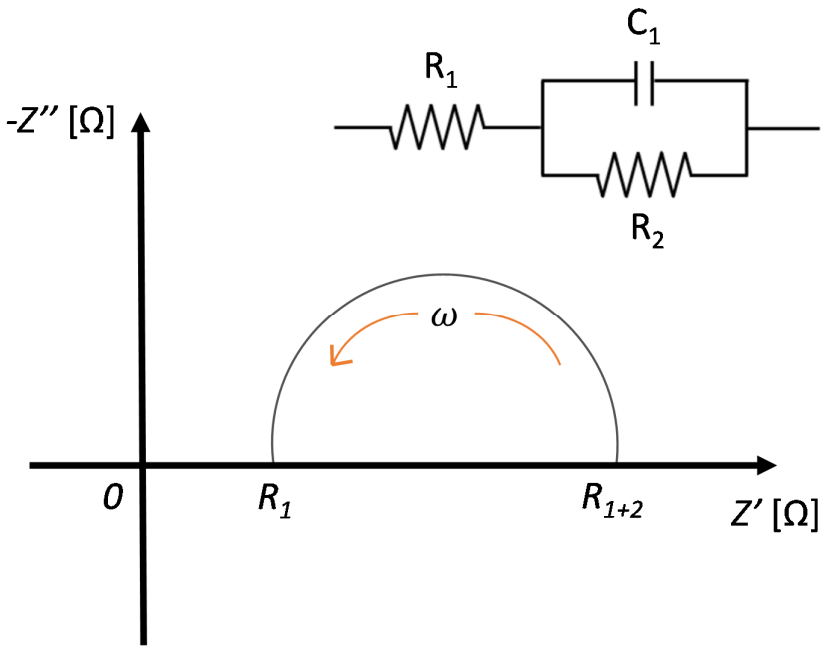

Figure 1.6: Schematic representation of a Nyquist plot of a so-called Randles-cell model circuit (upper right). The orange arrow indicates the direction of an increasing radial frequency.

Using potentiostatic EIS (PEIS), the characterization of the electrical properties of porous thin films deposited on insulating substrates is feasible.[137] From the fitted data, the sheet conductivity of the investigated material can be calculated and structure-property correlations can be deduced based on a comprehensive analysis of both electrical and structural properties. The most relevant methods for the characterization of metal oxide and carbide films deposited on planar substrates will be summarized in the following section.

1.8.2 GI-XRD and SAED analysis of thin films

X-ray diffraction in gracing incidence geometry for the incoming beam is a non-destructive technique for the phase analysis of e.g. polymer or metal (oxide) thin films of thicknesses smaller than ~500 nm.[138] In contrast to conventional XRD for bulk phase analysis of powder materials, in GI-XRD, the angle of the incoming beam of monochromatic X-rays usually is low (typically between 0.5 to 10.0°) and different from that of the diffracted beam (angles given respective to the sample surface). Such asymmetric geometry renders GI-XRD a more surface-sensitive and less bulk-sensitive method. Similar to bulk XRD analysis, the Bragg equation can

be applied and reflections occur in dependency of the lattice plane distances for specific crystallographic with *hkl* Miller indices.[139]

Based on the results from GI-XRD analysis, several parameters can be investigated, for example, the crystallinity, the lattice parameters, or the size of the crystallites (*via* the Scherrer equation). Moreover, by variations of the incoming beam angle, the thickness of an oxide layer at the surface of a metal can be estimated. Beyond that, more complex structures such as multilayered stacks of different compounds can be analyzed with high resolution, thus providing a depth profile.[139]

Obviously, GI-XRD is less sensitive for amorphous or weakly crystalline materials, for which selected area electron diffraction (SAED) in a TEM represents an important alternative characterization technique. For SAED, similar diffraction principles hold true as in (GI-)XRD analysis. Locally ordered periodic distances can be detected by the diffraction of electrons by the atoms arranged in lattice planes, which finally leads to characteristic diffraction patterns. As illustrated in figure 1.7, broad diffraction rings without any distinct spots are obtained for amorphous or very low crystalline materials, such as mesoporous IrO_x films deposited on Ti substrates at the onset of crystallization. Higher calcination temperatures of ~ 475 °C in air lead to the observation of more narrow rings in the SAED pattern, indicating the formation of crystalline IrO_2 with rutile-type crystal structure, according to the assignment of the respective *hkl* Miller indices. Even higher calcination temperatures of ~ 625 °C lead to the appearance of several distinct spots alongside narrow rings in the pattern. Accordingly, the crystallinity of the IrO_2 crystallites constituting the pore walls of the films increases with rising calcination temperature and similar duration of the thermal treatment.[41]

Another difference between GI-XRD and SAED analysis is that the latter represents a local characterization technique probing only a little volume of a material with high spatial resolution and intensity. Therefore, SAED is a highly suitable method for the analysis of phase and crystallinity of nanostructures and –materials due to its high local resolution and signal-to-noise ratio.[140]

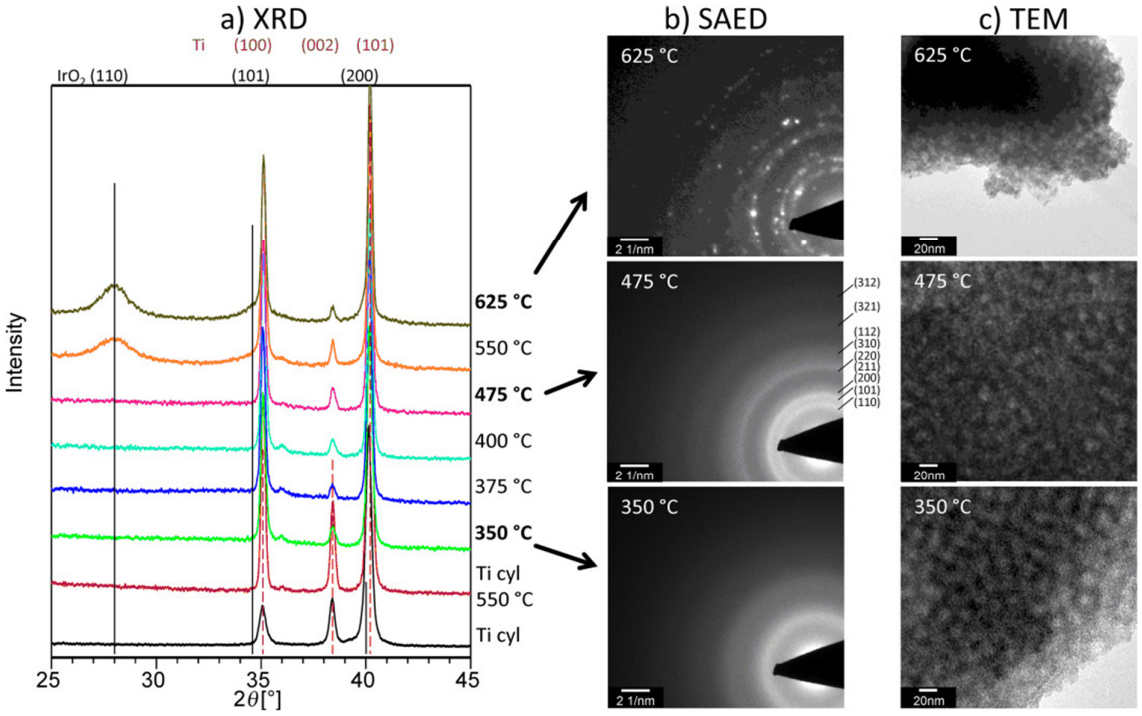

Figure 1.7: (a) GI-XRD patterns of templated mesoporous IrO_x thin films on polished titanium cylinders after calcination at different temperatures in air and (b) selected corresponding SAED patterns analyzed via TEM. In (c), TEM images are shown for the analysis of the pore structures in dependency of calcination temperature. Reprinted with permission by John Wiley and Sons from reference[41]*. Copyright 2015 WILEY-VCH Verlag GmbH & Co. KGaA, Weinheim.*

In this thesis, the deduction of structure-property and structure-activity correlations represents one of the most important aims. Based on a comprehensive physicochemical characterization of the materials prior to and after surface modification *via* ALD, distinct insights into the structural properties can be gained. Moreover, the impact of the ALD process on the morphology and crystallinity of the material can be evaluated and, afterwards, correlated with trends observed from electrochemical testings in OER regime. Impedance spectroscopy plays an important role in the assessment of the electronic properties of the catalytic coatings by revealing insights into the interactions between the surface catalyst layer and the underlying support. Favorable catalyst-support interactions were often claimed to improve not only the activity but also the stability of a catalyst system.

1.9 Aims and Structure of this Thesis

This doctoral thesis contributes to the design of novel, nanostructured catalyst support materials with templated porosity and improved electrical properties. Using conformal ALD, a subsequent surface modification of different types of mesoporous supports with metal and/or metal oxide species is proposed in order to enhance electrocatalytic OER activities by an improved utilization of active sites.

As a first step, doping of a transition metal oxide (titania) is systematically investigated from both an experimental and a theoretical point of view. This combined approach (see **[MF-1]**) is developed in order to provide a fundamental understanding of the impact of the nature and the amount of dopant on the electronic as well as on the structural properties. Model support materials, such as doped metal oxide films with templated mesopore structures, can be used for an investigation of the effects of different dopants on the crystallinity, phase or electrical conductivity, amongst others. As a central aim of this thesis, an improvement in the sheet conductivity of the support with low PGM content is pursued.

As a second step, the surface modification process *via* ALD is adjusted and adapted to titanium-based oxide support materials. The bulk properties of the mesoporous support, *i.e.* composition, crystallinity and phase, as well as the surface properties, *i.e.* texture of the pore walls and hydrophilicity of surface groups, affect the homogeneity of the deposited surface layer. Understanding the influence of the parameters and the working principle of a particular ALD process is key for tuning the surface properties of a material and, consequently, improving the electrocatalytic OER activity (see **[MF-2]**). Besides, the electronic interactions between the thin surface catalyst layer and the underlying support will be examined in order to identify suitable combinations which effectively promote charge transfer kinetics at the electrode. Due to the nanoscale dimensions of the deposited surface layers *via* ALD, sophisticated characterization tools will be necessary to evaluate the crystallinity, phase and morphology.

As a third step, a synthesis concept for highly conductive support materials is presented. As representative example, homogeneous, soft-templated tungsten carbide films are developed in **[MF-3]**, which are subsequently surface-modified with highly active NiO species *via* an adapted ALD process. The obtained results confirm the successful modification of a metal carbide support with a metal oxide surface layer. Synergistic effects between the surface

catalyst layer and the bulk support were both experimentally and theoretically shown to improve the catalytic performance, *i.e.* activity and stability, in alkaline OER.

As a last step, all findings are summarized and discussed. The main factors for an improvement in catalytic activity, in particular mass-specific OER activity, are pointed out. In brief, a high electrical conductivity of the support plays a key role. Yet, favorable electronic interactions between the bulk and the surface catalyst layer are even more important for the design of highly efficient OER electrocatalysts and electrodes with reduced contents of active species.

2. Transition-Metal-Doped Titania with Enhanced Electrical Conductivity

This chapter has been published in the peer-reviewed journal *Physical Chemistry Chemical Physics* under the title

"Bridging Experiment and Theory: Enhancing the Electrical Conductivities of Soft-Templated Niobium-Doped Mesoporous Titania Films"

by Marvin Frisch[*], Joachim Laun[*], Julien Marquardt, Aleks Arinchtein, Katharina Bauerfeind, Denis Bernsmeier, Michael Bernicke, Thomas Bredow and Ralph Kraehnert[†] (*Phys. Chem. Chem. Phys.* **2021**, *23*, 3219-3224; https://doi.org/10.1039/D0CP06544G). **[MF-1]**

[*] These authors contributed equally to the work. [†] denotes the corresponding author.

The following sections briefly summarize the most important findings from the study with the aim of improving the electrical properties of porous titania based on a combined experimental and theoretical approach. For further information, the reader is referred to the appendix of this thesis (A-1), where a reprint of the publication can be found.

2.1 Abstract

"Theoretical calculations suggest a strong dependence of electrical conductivity and doping concentration in transition-metal doped titania. Herein, we present a combined theoretical and experimental approach for the prediction of relative phase stability and electrical conductivity in niobium-doped titania as model system. Our method paves the way towards the development of materials with improved electrical properties."

2.2 Summary & Scope of the Study

Background:

A theoretical approach relying on DFT and established approximate functionals can aid in the identification of suitable dopant species to improve the electrical properties of a material, e.g. of transition metal oxides. Commonly, the segregation energy of a dopant with respect to the host lattice represents a decisive parameter in order to predict the tendency for the formation of a doped compound with a statistical distribution of dopant species. Based on a previous screening of various d-block elements, niobium (Nb) has emerged as one of the most promising dopants for titania as a result of a strongly negative segregation energy and the similar ionic radii of Ti^{4+} and Nb^{4+} / Nb^{5+}.

Concept:

Via well-controlled dip-coating and EISA, homogeneous Nb-doped titania films with templated mesoporosity are exemplarily developed and used as model systems to study structure-conductivity and structure-property relationships. In the study, the focus lies on the impact of doping on crystallinity, phase, morphology, as well as on the electrical properties.

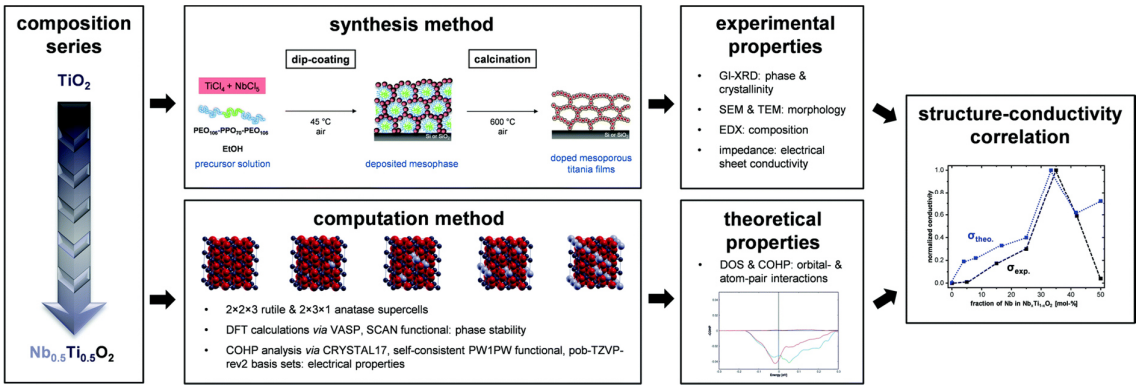

*Scheme 2.1: Schematic illustration of the combined experimental and theoretical approach for the prediction of trends in electrical and structural properties of Nb-doped titania with templated mesoporosity. Doped mesoporous (mp.) $Nb_xTi_{1-x}O_2$ ($0 \leq x \leq 0.5$) films were synthesized via dip-coating and thermal treatment in air. In parallel, theoretical calculations were performed to assess the impact of doping on the relative phase stability and the electrical properties. Finally, structure-conductivity correlations were deduced based on a comprehensive analysis of the physicochemical properties (experiment) and computed parameters such as the electronic interactions and density of states (DOS) (theory). Reproduced from **[MF-1]** with permission from the PCCP Owner Societies.*

In view of an application-driven synthesis of conductive, high-surface-area supports, the addition of a structure-directing agent, *i.e.* a block-copolymer soft-template, is used in order to obtain ordered, macroscopically crack-free titania-based films over a broad range of dopant concentrations. Theory predicts a significant increase in electrical bulk conductivity for Nb-doped titania compared to pristine TiO_2, which is expected to be highly favorable for applications in electrocatalysis[72,111]. The overall concept is illustrated in scheme 2.1.

Results & Discussion:

Calcination for 30 min at 600 °C in air leads to the formation of well-ordered doped titania films showing a similar mesoporous structure with an average pore size of 10 ± 2 nm, as confirmed by electron microscopy (SEM and TEM, see *Appendix A-1*). The corresponding fast-Fourier transform (FFT) images clearly portray an intact mesopore structure, independent of Nb-dopant fraction. However, phase analysis *via* GI-XRD and Raman spectroscopy revealed distinct differences regarding the crystallinity and phases in dependency of the latter. In good agreement with results from theoretical calculations based on DFT and VASP[141–143], predicting a higher relative phase stability for the rutile phase for higher dopant fractions of more than 25 mol-% Nb, a transition from predominantly anatase phase to the rutile-type can be observed at similar dopant fractions in experiment. Phase assignments relying on GI-XRD, Raman spectroscopy and HR-TEM (SAED) suggest the formation of a predominantly anatase-type oxide for low dopant fractions, a mixed anatase-rutile-type oxide for 25 mol-% Nb, whereas for 35 mol-% Nb the contribution of the anatase-type phase vanishes and rutile represents the predominant phase.

Beside the prediction of relative phase stability of titania-based materials depending on the amount of dopant, trends in the electrical properties, e.g. bulk conductivity in dependency of dopant fraction, can be deduced from computation. Therefore, a concept already introduced in 1993, the so-called crystal orbital Hamilton population (COHP) analysis[144], can be applied for a theoretical investigation of nearest-neighbor interactions in a crystal lattice. Based on the simplified COHP analysis combined with the calculation of the density of states (DOS) for different amounts of Nb-dopant fractions, a maximum in theoretical electrical conductivity for ~ 33 mol-% is theoretically predicted. In this context, it has to be mentioned that the theoretical calculations rely on non-porous, bulk oxides. The herein synthesized oxide films all show a similar mesoporous structure with insulating air filling the voids between the pore walls of the materials. Thus, the mesoporosity itself has no impact on the observed experimental trends in

conductivity vs. dopant fraction. Yet, the absolute electrical conductivities analyzed *via* impedance spectroscopy are reduced compared to bulk Nb-doped titania due to grain boundaries or nanocrystalline domains, amongst others. Importantly, the overall trend and maximum in conductivity can be confirmed in experiment, in which the maximum is found for ~ 35 mol-% Nb. In addition, theoretical analyses of the electrical properties provide insights into the origin of the significantly enhanced conductivity for dopant fractions of ~ 33 mol-%, which can be explained by an increase in electron density (DOS) while avoiding unfavorable Nb-Nb-interactions (COHP).

Conclusion & Outlook:

The presented combined experimental and theoretical approach can be applied for the prediction of trends in both electrical and structural properties of doped, semiconducting metal oxides. As a proof-of-concept, these trends were studied in both experiment and theory using Nb-doped titania films with varying dopant fractions and well-defined mesoporous structure as model films showing similar crystallite sizes as well as wall- and sheet-thicknesses. A good consistency between the theoretically predicted and the experimentally observed trends are found in this study. Yet, the computation of absolute values for the electrical conductivity in dependency of the amount of dopant remains a challenge and needs further optimizations. Nevertheless, the experimentally observed value of up to 10^{-3} S/cm for mp. $Nb_{0.35}Ti_{0.65}O_2$ represent the highest reported sheet conductivity for early-transition-metal-doped TiO_2 films with mesoporosity.

3. Surface-Modified Oxide-based Electrodes for Acidic OER

This chapter has been accepted for publication in the peer-reviewed journal *Advanced Materials Interfaces* as a research article entitled

"ALD-Coated Mesoporous Iridium-Titanium Mixed Oxides: Maximizing Iridium Utilization for an Outstanding OER Performance"

by Marvin Frisch[*], Muhammad Hamid Raza[*], Meng-Yang Ye, René Sachse, Benjamin Paul, René Gunder, Nicola Pinna[†] and Ralph Kraehnert[†] (*Adv. Mater. Interfaces* **2022**, *9*, 2102035; https://doi.org/10.1002/admi.202102035). **[MF-2]**

[*] These authors contributed equally to the work. [†] symbols denote the corresponding authors.

Again, the following sections summarize the most important results from this study pursuing an optimization of the ALD process for the deposition of conformal IrO_x surface layers with high intrinsic OER activities on a conductive support, *i.e.* a mixed iridium-titanium oxide with reduced PGM content. In the appendix of this thesis (A-2), a reprint of the manuscript and the SI are given.

3.1 Abstract

"With the increasing production of renewable energy and concomitant depletion of fossil resources, the demand for efficient water splitting electrocatalysts continues to grow. Iridium (Ir) and iridium oxides (IrO_x) are currently the most promising candidates for an efficient oxygen evolution reaction (OER) in acidic medium, which remains the bottleneck in water electrolysis. Yet, the extremely high costs for Ir hamper a widespread production of hydrogen (H_2) on an industrial scale. Herein, we report a concept for the synthesis of electrode coatings with template-controlled mesoporosity surface-modified with highly active Ir species. The improved utilization of noble metal species relies on the synthesis of soft-templated metal oxide supports and a subsequent shape-conformal deposition of Ir species via atomic layer deposition (ALD) at two different reaction temperatures. The study reveals that a minimum Ir

content in the mesoporous titania-based support is mandatory to provide a sufficient electrical bulk conductivity. After ALD, a significantly enhanced OER activity results in dependency of the ALD cycle number and temperature. The most active developed electrocatalyst film achieves an outstanding mass-specific activity of 2622 mA mg_{Ir}^{-1} *at 1.60* V_{RHE} *in a rotating-disc electrode (RDE) setup at 25 °C using 0.5 M* H_2SO_4 *as a supporting electrolyte."*
(Reproduced from **[MF-2]** with permission from John Wiley and Sons, Wiley-VCH, Copyright 2022.)

3.2 Summary & Scope of the Study

Background:

The concept of PEM water electrolysis provides several key advantages over H_2 generation in alkaline or neutral media. For a realization of large-scale PEM electrolysis, however, a significant reduction in noble metal loadings at the electrodes, in particular of scarce Ir at the anode, will be required. Oxides of Ir have emerged as the most suitable electrocatalysts to date, with high OER activity and sufficient stability in oxidative and acidic conditions. It is thus desirable to identify strategies to drastically reduce the required Ir contents, more precisely the geometric Ir-loadings, in the catalysts without decreasing their activity or accepting trade-offs in durability. ALD represents a promising tool for the controlled modification of the entire surface area of nanostructured, porous support materials and, thereby, modify the reactivity of the surface. Regarding the deposition of PGM species such as Ir, previous studies revealed a high tendency for the formation of metallic, nanoparticulate surface deposits. Accordingly, a profound understanding of the ongoing processes at the pore wall surface of the support during ALD is necessary in order to achieve well-conformal surface layers of intrinsically highly active Ir species (IrO_x).

Concept:

The overall concept for the development of active and acid-stable, surface-modified electrode coatings with reduced Ir contents is illustrated in scheme 3.1. A systematic variation in ALD parameters is performed using model-type titanium-based oxide films with templated pore structures. Concomitantly, the impact of the electrical properties of the support oxide (low vs. high conductivity) on the electrocatalytic OER activity is systematically examined and structure-activity correlations are deduced. The support may show moderate catalytic activity

itself, yet a significant increase in mass-specific activity is pursued by well-controlled surface modification *via* ALD, as a result of an optimized active site geometry with a maximized number of OER-active Ir^{x+} species at the interface to the surrounding electrolyte. In order to ensure a sufficient electrical conductivity, a minimum content of 15 mol-% Ir in mixed iridium titanium oxides OER catalysts with templated mesopore structure was previously reported by the Kraehnert group.[41,72] Accordingly, an application of such mp. $IrTiO_x$ films with a favorably low Ir-content in the bulk as electrically conductive catalyst supports is highly promising.

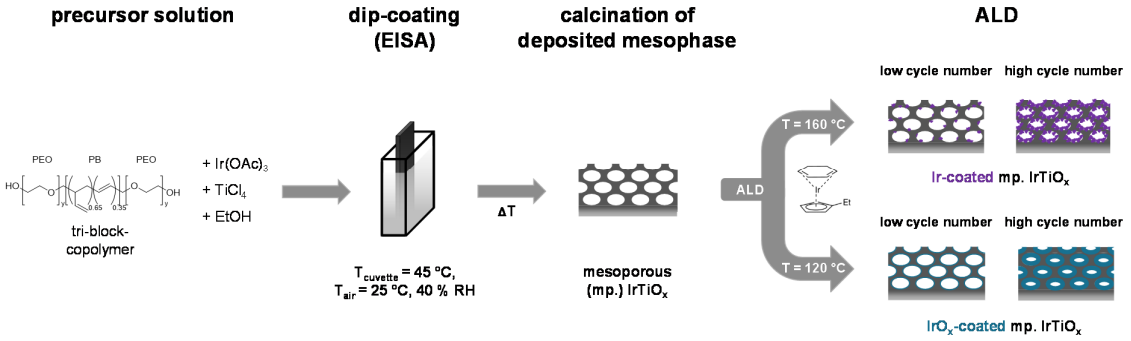

*Scheme 3.1: Schematic illustration of the proposed synthesis concept for the rational design of mixed iridium-titanium OER electrodes with high specific surface areas via conformal ALD. A previously established synthesis route[72,111] for $IrTiO_x$ films with template-controlled porosity (mp. $IrTiO_x$) and low Ir-content of 15 mol-% is adapted in a first step for the preparation of conductive support materials. Afterwards, the entire pore wall surface of the support is modified with either metallic Ir^0 or oxidic IrO_x species via ALD at 160 °C or 120 °C, respectively. The ALD process, in particular the temperature during deposition, largely affects the chemical and structural properties of the deposited surface species. Variations in ALD cycle number can be used to adjust the overall Ir-content in the coatings and play a key role in the optimization of the electrocatalytic activity as well as stability. Reproduced from **[MF-2]** with permission from John Wiley and Sons, Wiley-VCH, Copyright 2022.*

Results & Discussion:

Both temperature and cycle number during ALD play a decisive role in the adjustment of the chemical, structural and electronic properties of the deposited surface species. The temperature inside the ALD reaction chamber is found to alter the average oxidation state and morphology of the surface Ir species, whereas variations in the amount of performed ALD cycles affect the porosity and overall Ir content of the materials. The results from electron microscopy depicted in figure 3.2 provide an overview over the morphology and pore structure prior to and after different ALD treatments. In brief, ALD at higher temperature (*i.e.* 160 °C) affords nanoparticulate surface deposits that partially block the mesopores for high cycle numbers (see figure 3.2c). Contrarily, after ALD at lower temperature (*i.e.* 120 °C) well-conformal, dense surface layers distributed over the entire pore wall surface of the support are obtained. Further investigations of the average pore diameters in the direction parallel to the substrate confirm

the self-limiting character of ALD at 120 °C. The average pore size decreases from 18 nm to approximately 17, 16 and 15 nm after 20, 40 and 60 ALD cycles, respectively. This linear correlation between average pore size and cycle number results from a rise in ALD-layer thickness for increasing cycle numbers. Due to the rigidity of the $IrTiO_x$ support after calcination in air, each ALD cycle adds more material to pore wall surface, hence decreasing the average pore diameter.

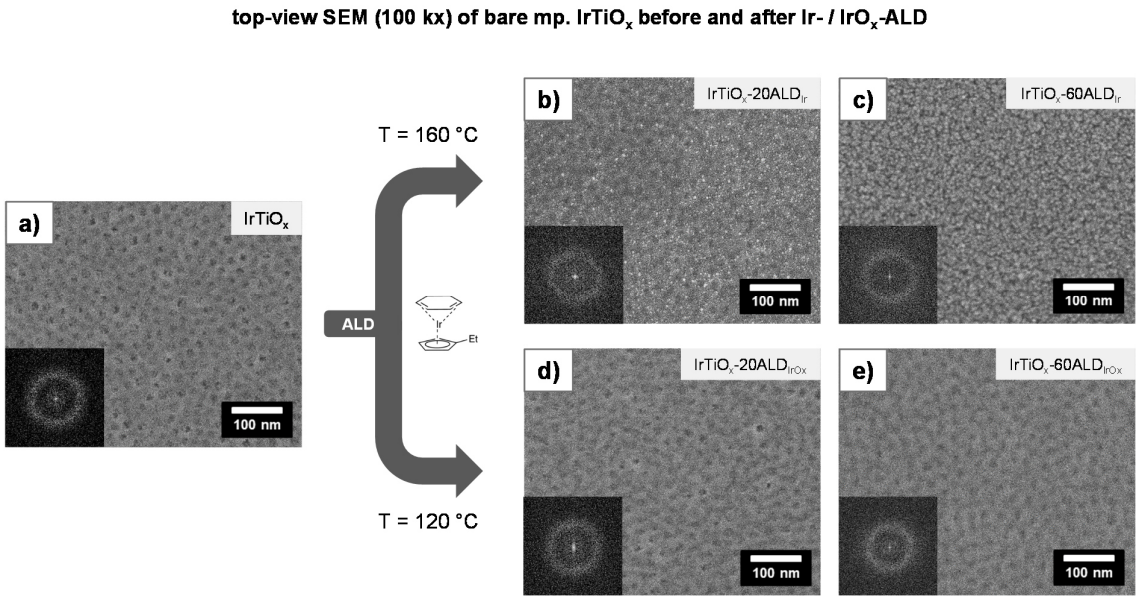

*Figure 3.2: Representative SEM images (top-view, 100 kx magnification) of the unmodified mesoporous $IrTiO_x$ support (a) and surface-modified $IrTiO_x$ electrode coatings via ALD at 160 °C (b-c) and at 120 °C (d-e). In the bottom left corner of each image, the corresponding FFT insets clearly portray a preserved mesopore structure for all materials. In b & c, bright features indicate the presence of predominantly Ir-rich species, according to differences in Z-contrast (atomic contrast) between heavy Ir and light Ti atoms. Images b & d correspond to 20, images c & e correspond to 60 ALD cycles, as denoted in the sample description (top-right corner of each image). Reproduced from **[MF-2]** with permission from John Wiley and Sons, Wiley-VCH, Copyright 2022.*

Based on the comprehensive investigations of the physicochemical properties of the surface-modified materials, structure-activity correlations can be deduced. Aiming at improved mass-specific OER activities in acid, a high intrinsic activity of the exposed surface Ir sites represents a key factor that can be tuned by the ALD temperature. For low-temperature ALD, importantly, low-crystallinity IrO_x surface species are obtained. These oxidic IrO_x species can significantly boost the OER activity compared to the unmodified mp. $IrTiO_x$ support or Ir^0-modified $IrTiO_x$ coatings obtained *via* ALD at 160 °C. It has to be noted that both types of ALD processes (affording either Ir^0 or IrO_x) lead to improved electrical sheet conductivities (see figure 3.3a).

Yet, results from electrochemical investigations in a three-electrode setup (RDE) using 0.5 M H_2SO_4 as a supporting electrolyte clearly reveal the superiority of IrO_x-modified $IrTiO_x$ catalytic coatings in terms of mass activity.

The most active catalyst, $IrTiO_x$-$60ALD_{IrOx}$, outperforms literature-reported Ir-based systems as well as commercial benchmark catalysts (see figure 3.3c & **[MF-2]** for further details). Beyond that, a remarkably improved catalyst durability can be observed after IrO_x-ALD (see the SI of **[MF-2]**).

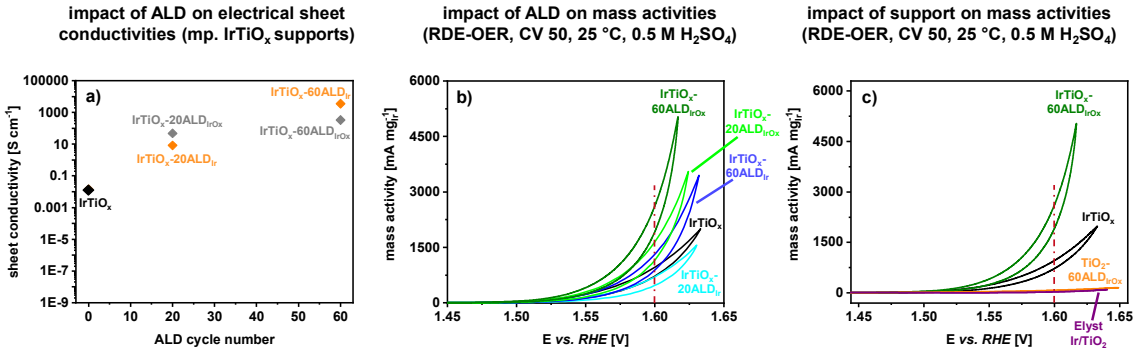

*Figure 3.3: Results from investigations of the electrical sheet conductivity assessed via impedance spectroscopy for films deposited on planar, insulating glass substrates (a), RDE-OER mass activities for surface-modified catalytic coatings on polished titanium substrates highlighting the influence of the ALD parameters (b) and the impact of the support material (c). As a reference, results for unmodified $IrTiO_x$ electrode coatings with 15 mol-% (30 wt.-%) Ir are shown. In addition, the OER performance of a commercial reference catalyst powder (ELYST Ir/TiO_2, 74.7 wt.-% Ir, Umicore) is given. Reproduced from **[MF-2]** with permission from John Wiley and Sons, Wiley-VCH, Copyright 2022.*

As thoroughly discussed in **[MF-2]**, the electronic properties of the underlying support oxide play a major role in the optimization of electrocatalytic OER activity. For n-type semi-conducting TiO_2 support films with templated porosity, similar surface modifications *via* ALD notably do not lead to high OER activities (*cf.* figure 3.3c), which can, most likely, be related to an insufficient bulk conductivity and the concomitant formation of an electronic barrier at the electrode, which ultimately hampers fast OER kinetics.

Conclusion & Outlook:

An innovative concept for the design of high-surface-area electrode coatings with reduced Ir-contents, which are both active and stable in acidic OER, is demonstrated. A systematic study on the impact of different ALD processes for the controlled deposition of low amounts of surface Ir species onto conductive metal oxide supports is presented, aiming at an improved utilization of precious Ir. Notably, low Ir-contents in the support are essential to effectively promote charge transfer during OER and prevent the formation of a *Schottky* barrier at the electrode (see also section 5.3 for further discussion). The proposed concept is promising for the design of various catalyst-support combinations and can be further extended to different PGMs as active sites in electro-, photocatalysis or heterogeneous catalysis, amongst others.

4. Surface-Modified Carbide-based Electrodes for Alkaline OER

This chapter has been published in the peer-reviewed journal *ChemSusChem* under the title

"Mesoporous WC_x Films with NiO-Protected Surface: Highly Active Electrocatalysts for the Alkaline Oxygen Evolution Reaction"

by Marvin Frisch[*], Meng-Yang Ye[*], Muhammad Hamid Raza, Aleks Arinchtein, Denis Bernsmeier, Anna Gomer, Thomas Bredow, Nicola Pinna and Ralph Kraehnert[†]
(*ChemSusChem* **2021**, *14*, 4708-4717; DOI: https://doi.org/10.1002/cssc.202101243). **[MF-3]**

[*] These authors contributed equally to the work. [†] denotes the corresponding author.

In the following sections, a brief summary and description of the most important findings from the work are given. The main targets of this study involve the improvement of the electrical properties of Ni-based OER electrocatalysts alongside the development of a concept to enhance the mass-specific OER activities of active species *via* conformal ALD on a conductive high-surface-area support. Further information can be found in section A-3, where a reprint of the publication is given.

4.1 Abstract

"Metal carbides are promising materials for electrocatalytic reactions such as water electrolysis. However, for application in catalysis for the oxygen evolution reaction (OER), protection against oxidative corrosion, a high surface area with facile electrolyte access, and control over the exposed active surface sites are highly desirable. This study concerns a new method for the synthesis of porous tungsten carbide films with template-controlled porosity that are surface-modified with thin layers of nickel oxide (NiO) to obtain active and stable OER catalysts. The method relies on the synthesis of soft-templated mesoporous tungsten oxide (mp. WO_x) films, a pseudomorphic transformation into mesoporous tungsten carbide (mp. WC_x), and a subsequent shape-conformal deposition of finely dispersed NiO species by atomic layer deposition (ALD). As theoretically predicted by density functional theory (DFT)

calculations, the highly conductive carbide support promotes the conversion of Ni^{2+} into Ni^{3+}, leading to remarkably improved utilization of OER-active sites in alkaline medium. The obtained Ni mass-specific activity is about 280 times that of mesoporous NiO_x (mp. NiO_x) films. The NiO-coated WC_x catalyst achieves an outstanding mass-specific activity of 1989 A/g_{Ni} in a rotating-disc electrode (RDE) setup at 25 °C using 0.1 M KOH as the electrolyte."
(Reproduced from **[MF-3]** with permission from John Wiley and Sons, Wiley-VCH, Copyright 2021.)

4.2 Summary & Scope of the Study

Background:

The semiconducting properties of Ni-based oxides can limit their electrocatalytic performance, e.g. in alkaline OER. On the contrary, transition metal carbides, such as earth-abundant tungsten carbide (WC_x), show very high metallic conductivity and, thus, are promising catalyst supports. However, the introduction of (meso-)porosity into carbides is considered challenging due to excessive crystallite growth and sintering effects at elevated temperatures during their preparation. Beyond that, a concept needs to be developed that prevents the carbide support from irreversible bulk oxidation as a consequence of the oxidative and corrosive conditions during OER electrocatalysis.

Concept:

An innovative concept has been developed in the context of the project that is based on (1) the synthesis of templated mesoporous WO_x *via* an adaptation of the previously established citrate-route (*cf.* section 1.2.3), (2) a subsequent pseudomorphic transformation to the corresponding metal carbide, WC_x, with well-preserved mesoporous structure, and (3) the modification of its entire pore wall surface with ultra-thin layers of NiO deposited *via* conformal ALD using $Ni(Cp)_2$ and O_3 as metal and oxygen precursor, respectively.
Scheme 4.1 illustrates the proposed concept relying on the design of nanostructured electrodes with an improved utilization of active Ni^{x+} species by employing a highly conductive mesoporous carbide support (mp. WC_x).

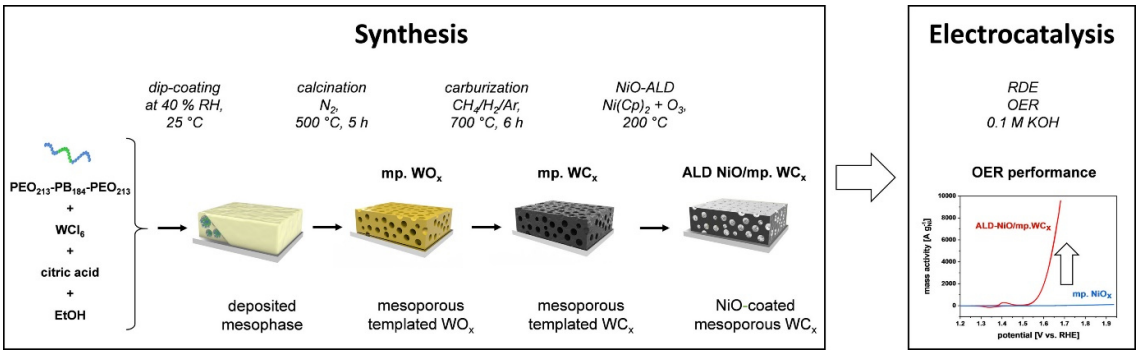

*Scheme 4.1: Schematic illustration of the developed synthetic approach for the preparation of homogeneous, templated mesoporous NiO-surface-modified WC_x films on planar substrates (left) and their application as highly efficient alkaline OER electrocatalysts (right). Reproduced from **[MF-3]** with permission from John Wiley and Sons, Wiley-VCH, Copyright 2021.*

Results & Discussion:

As a first step (1), mp. WO_x films are deposited on different planar substrates (glass, Si, Ti) *via* controlled dip-coating, subsequent removal of the template and concomitant crystallization by thermal treatment in nitrogen (N_2) atmosphere at 500 °C. In order to obtain homogeneous, macroscopically crack-free oxide films, an optimization of the synthesis was pursued, revealing a stabilizing effect by the addition of citric acid in a defined molar ratio to the tungsten precursor (WCl_6). Electron microscopy (SEM, TEM) confirms the formation of well-ordered, mesoporous WO_x films that are predominantly composed of a WO_3 phase, according to GI-XRD analysis. Importantly, the nanocrystalline character of the synthesized mp. WO_x can be expected to promote a conversion into the corresponding metal carbide *via* a carburization step using a mixture of $CH_4/H_2/Ar$ at elevated temperatures.

As a second step (2), a pseudomorphic transformation of the oxide (mp. WO_x) into the carbide (mp. WC_x) phase is evidenced by a combination of local, bulk- and surface-sensitive analytical techniques (HR-TEM, SAED, GI-XRD, XPS). Moreover, the analysis of the electrical sheet conductivities of the synthesized oxide and carbide films *via* impedance spectroscopy suggests the conversion into a highly conductive carbide phase inside the bulk of the material.

As a third step (3), the mesoporous WC_x films are surface-modified *via* conformal NiO-ALD using $Ni(Cp)_2$ and O_3 in alternating cycles at 200 °C. Again, the characterization of the modified material *via* HR-TEM, SAED, GI-XRD and XPS confirms the controlled deposition of thin surface layers of predominantly NiO. As reference systems, the same optimized ALD process is directly applied to mp. WO_x films (a), as well as to mesoporous nickel oxide

(mp. NiO_x) films (b) synthesized according to a previously established procedure reported by Bernicke *et al.*[79].

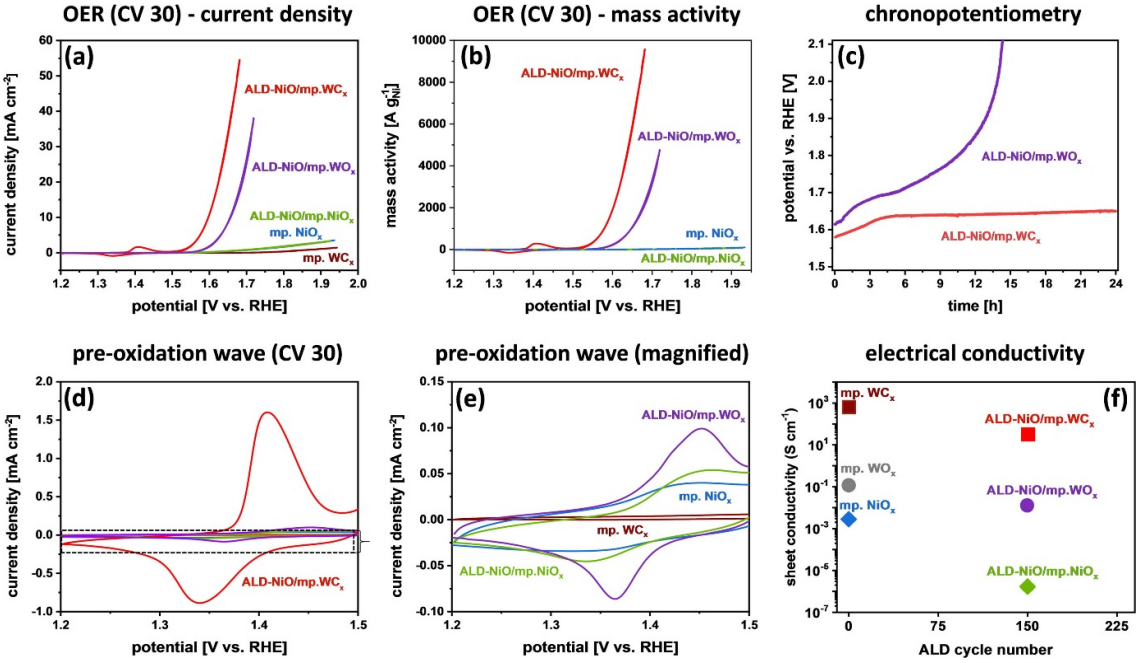

*Figure 4.2: (a-e) Results from the electrochemical testings of the different ALD-surface-modified catalyst films deposited on extensively polished Ti substrates in a typical RDE setup using 0.1 M KOH as electrolyte (1600 rpm, 25 °C). A chronopotentiometric stability test (c) reveals the improved catalytic stability of the NiO-coated WC_x electrode. A plausible explanation for its enhanced OER activity (a,b) can be provided by the significantly improved electrical properties originating from the carbide support (f). Reproduced from **[MF-3]** with permission from John Wiley and Sons, Wiley-VCH, Copyright 2021.*

Results from electrochemical tests in an RDE setup using 0.1 M KOH as electrolyte clearly portray a drastically enhanced OER performance of the NiO-coated WC_x electrocatalyst. Despite a lower geometric loading of active Ni species, significantly higher currents are reached compared to mp. NiO_x catalyst films, in which Ni atoms are distributed throughout the bulk of the material. Beyond that, cyclic voltammetry also reveals a superior catalytic performance compared to NiO-coated WO_x films with template-controlled porosity (see figure 4.2a-b). Notably, not only the catalytic activities, but also the stabilities at moderate potentials in OER regime are enhanced, according to chronopotentiometric stability (CP) tests in a typical three-electrode setup (see figure 4.2c).

Theoretical calculations (*via* DFT) provide further evidence for the experimentally observed (see figure 4.2 d-e) and strongly augmented Ni^{2+} / Ni^{3+} conversion in the case of the conductive carbide support. The interaction of the support and the catalyst surface layer leads to a beneficial impact on the adsorption of OER reaction intermediates (*OH) and, concomitantly, to a lower overpotential with respect to bare NiO with rock-salt crystal structure.

Conclusion & Outlook:

The findings in this study indicate that employing metal carbides with a template-controlled pore structure as conductive support can effectively promote charge transfer kinetics during OER. Moreover, the conformal ALD surface modification impedes pronounced oxidative corrosion during OER. As a proof-of-concept, NiO-ALD on mp. WC_x can improve catalyst stability despite the oxidative environments, and outstanding mass activities are obtained for NiO-modified WC_x in alkaline OER. Importantly, the concept is not limited to the presented catalyst-support combination and can, for example, be transferred to PGM-ALD on conductive metal carbide supports with mesoporous structure.

5. General Discussion

5.1 Overall Concept of Surface Modification

The results from the studies discussed in the previous chapters show a promising concept for the development of nanostructured, high-surface-area catalysts with a significantly improved utilization of active species, as demonstrated exemplarily for both alkaline and acidic OER. This concept relies on the surface modification of templated mesoporous transition metal oxides and carbides with tunable electrical properties *via* conformal ALD. The electrical conductivity of the support plays a key role in order to promote charge transfer at the electrode in electrocatalysis, in general. Despite its high stability in oxidative and acidic environment, bare titania (TiO_2) shows an insufficient conductivity (n-type semiconductor). Hence, the identification of suitable metal dopants into a host titanium oxide lattice represents a basic component in the overall concept toward the development of highly active electrocatalysts with reduced contents (*i.e.* geometric loadings) of active species. This issue has been addressed in **[MF-1]**, as well as in **[MF-4]** in close collaboration with the Bredow group. The results from theoretical calculations summarized in **[MF-4]** reveal Nb and Ta as the most promising PGM-free dopants for titanium oxide. The former was extensively investigated in **[MF-1]**, targeting the discovery of the most conductive, porous support with a sufficient stability in acid. Importantly, the electronic properties of the porous support can be independently adjusted prior to surface modification *via* ALD.

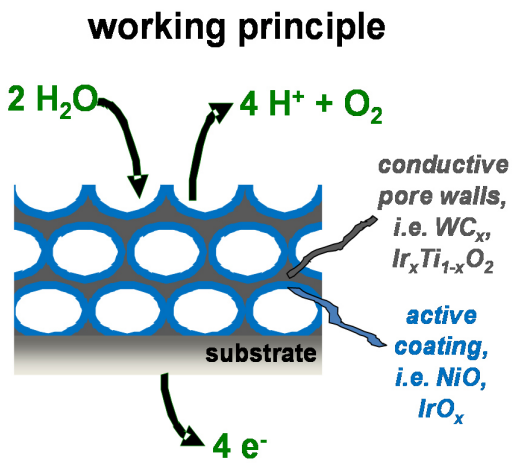

Figure 5.1: Schematic representation of the concept for the development of conductive electrode coatings with template-controlled pore structures and conformal ALD surface modifications for the introduction of OER-active surface species.

As a second step, an optimization of the ALD process was pursued in order to achieve a well-homogeneous distribution of noble metal species, such as precious Ir^{x+}, at the pore wall surface of titanium-based supports, as reported in **[MF-2]**. Notably, improved mass-specific activities in electrocatalytic OER tests after surface modification with either Ir or IrO_x species were exclusively observed for p-type semiconducting support materials (mixed Ir-Ti oxides; see also

[MF-6]). As described in the following sections, for surface-modified n-type semiconducting supports, such as Nb-doped titania (developed in **[MF-1]**), results from electrochemical testings reveal a significantly reduced OER activity in acidic electrolyte. Hence, the concept of doping titania-based supports with templated mesopore structure was extended to further promising PGM-free metal ion dopants, such as Y^{3+}, to alter the electronic properties (p-type doping), and more complex co-doped oxide systems (see section 5.2.2). The results provide clear evidence for the versatility and excellent control over composition, morphology, as well as porosity and crystallinity *via* dip-coating and EISA, also for ternary oxides. Based on physicochemical characterizations, structure-property relationships can be deduced, which aid in the fundamental understanding of the interactions between support and active surface coating. By variations in the ALD parameters, the structural and electronic properties of these surface layers can be precisely tuned and, hence, the intrinsic catalytic activity of the active species can be optimized (*cf.* **[MF-2]**, **[MF-6]**). Figure 5.1 provides a schematic illustration of the working principle of the improved catalyst design.

Albeit the properties of the support and the ALD surface layer can be independently adjusted during material synthesis, results from electrocatalytic investigations indicate the formation of interfacial charge transfer barriers *(Schottky barrier)* for certain metal-semiconductor combinations (metal-like conductive layers on n-type semiconducting support). This aspect is of great importance for the design of active electrocatalysts and will be thoroughly discussed in section 5.3.

Finally, the idea of introducing a metallic conductive high surface area carbide as a PGM-free support is extended from alkaline to acidic OER. Findings in **[MF-3]** indicate that a well-controlled surface modification of a carbide support (WC_x) with oxidic metal species (NiO) affords active and durable electrode coatings. The developed porous WC_x films, as described in **[MF-5]**, prevent the formation of an electronic barrier and, thus, are highly promising as noble-metal-free support for acidic OER after conformal surface modification *via* previously established IrO_x-ALD (*cf.* **[MF-2]**). Section 5.4.2 briefly summarizes the most important results from the characterization and the electrochemical performance of surface-modified, PGM-free supports in acid, thereby highlighting the versatility of the proposed overall concept.

5.2 Synthesis and Characterization of PGM-free p-type and co-doped Titania Films with template-controlled Porosity

5.2.1 How does non-noble-metal p-type doping of titania affect its electrical conductivity?

In **[MF-1]**, n-type doping of titania with Nb has been thoroughly investigated. Theoretical calculations suggest that p-type doping of titania, e.g. with Sc^{3+} or Y^{3+}, represents an alternative approach to alter the electronic properties and improve the electrical charge transport in the metal oxides (see **[MF-4]**[145]). Doped, nanocrystalline titania with high specific surface area is not only considered an interesting catalyst support in electrocatalysis, but also highly promising as electron transport material in the fields of photo(electro)catalysis.[146] In this context, enhanced bulk electrical conductivities are desirable in the development of more efficient catalysts or solar cells, amongst others. Importantly, the identification of doped, PGM-free titania materials with both enhanced electrical conductivity and high specific surface area can reduce the catalyst costs by improving PGM utilization and, concomitantly, enhancing mass-specific activities after surface modification. Therefore, a rational design of nanostructured and conductive support materials for OER-active Ir species with sufficient stability in oxidative as well as corrosive environments is required to control the interfacial properties and electronic catalyst-support interactions.

Based on the synthesis of doped metal oxide films with template-controlled porosity *via* dip-coating and EISA, homogeneous model systems can be obtained, which can then be applied for a profound investigation of the physicochemical properties and a deduction of structure-conductivity correlations. The aim of this study is to understand the impact of dopant fraction in p-type titania and optimize both the electronic and structural properties based on experimental and computational data.

Using $YCl_3 \cdot 6H_2O$ as Y^{3+} precursor in an ethanolic precursor solution containing titanium(IV)-ethoxide (by dissolution of $TiCl_4$ in EtOH) and a tri-block copolymer as template (already used in **[MF-1])**, p-doped titania films with well-defined mesoporous structures can be successfully prepared over a broad range of dopant fractions. As revealed by electron microscopy analysis after calcination of the deposited mesophases for 30 min at 600 °C in air (see figure 5.2a), higher fractions of 50 mol-% Y lead to a collapse of the mesopore structure. Yet, lower dopant fractions of 5, 17 and 33 mol-% Y enhance the structural and morphological stability, which is

in good consistency with the previous findings for Nb-doped titania reported in **[MF-1]**. Calcination of bare titania films at 600 °C in air results in a loss of mesoporosity due to excessive crystallite growth, whereas a thermal treatment at 475 °C in air leads to the preservation of a well-ordered mesoporous network with interconnected porosity and nanocrystalline anatase-type phase (see figure 5.2b). Hence, similar to n-doping, p-doping can improve the thermal stability of high-surface-area titania.

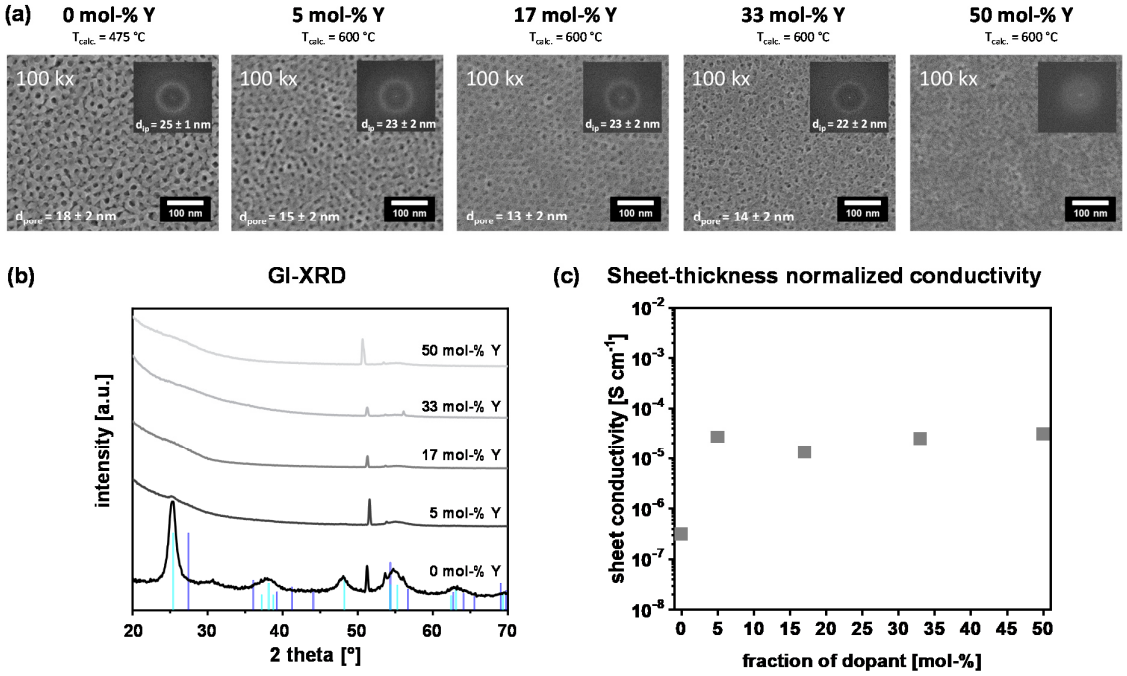

Figure 5.2: (a) Representative top-view SEM images (100 kx magnification) of templated mesoporous Y-doped titania films after thermal treatment for 30 min at 600 °C in air. The average pore diameters for each material as well as the average interpore distances, as evaluated by FFT analysis (see inset), are given. As a reference, bare mp. TiO_2 films ($T_{calc.}$ = 475 °C) were analyzed. (b) GI-XRD pattern in dependency of Y fraction, and (c) results from impedance spectroscopy analysis to assess the electrical conductivities of the films after normalization to the average layer thickness (determined via cross-sectional SEM for each material).

Even though a decrease in crystallinity can be observed for the doped oxides compared to bare TiO_2 (*cf.* GI-XRD analysis, figure 5.2b), increased sheet conductivities are found *via* impedance spectroscopy for films deposited on insulating glass substrates (figure 5.2c). In contrast to the Nb-system described in **[MF-1]**, no clear correlation can be deduced from the experimental data after doping with different concentrations of Y^{3+}. Here, doping seems to prevent crystallization of the material in the pore walls of the porous films, as further revealed by SAED analysis (see figure 5.3, top insets). For bare TiO_2, sharp diffraction spots alongside narrow rings can be found, indicating a highly crystalline character, which is decreasing with increasing dopant fraction. For 17 and 33 mol-% Y, broad rings dominate the pattern, which is

evidence for the formation of a weakly crystalline material, in accordance with results from GI-XRD analysis shown above (figure 5.2b). For the Nb-system (**[MF-1]**), an emerging rutile-type phase of high crystallinity has been observed for dopant fractions of ~ 25 mol-%, which is expected to favor high bulk conductivity. High Nb fractions of 50 mol-% lead to a lower experimental conductivity than theoretically predicted. On the one hand, this likely relates to an increase in unfavorable Nb-Nb nearest-neighbor interactions, as proposed by mechanistic considerations (for more details see **[MF-1]**). On the other hand, the reduced crystallinity of the material may hamper efficient charge transport throughout the bulk.

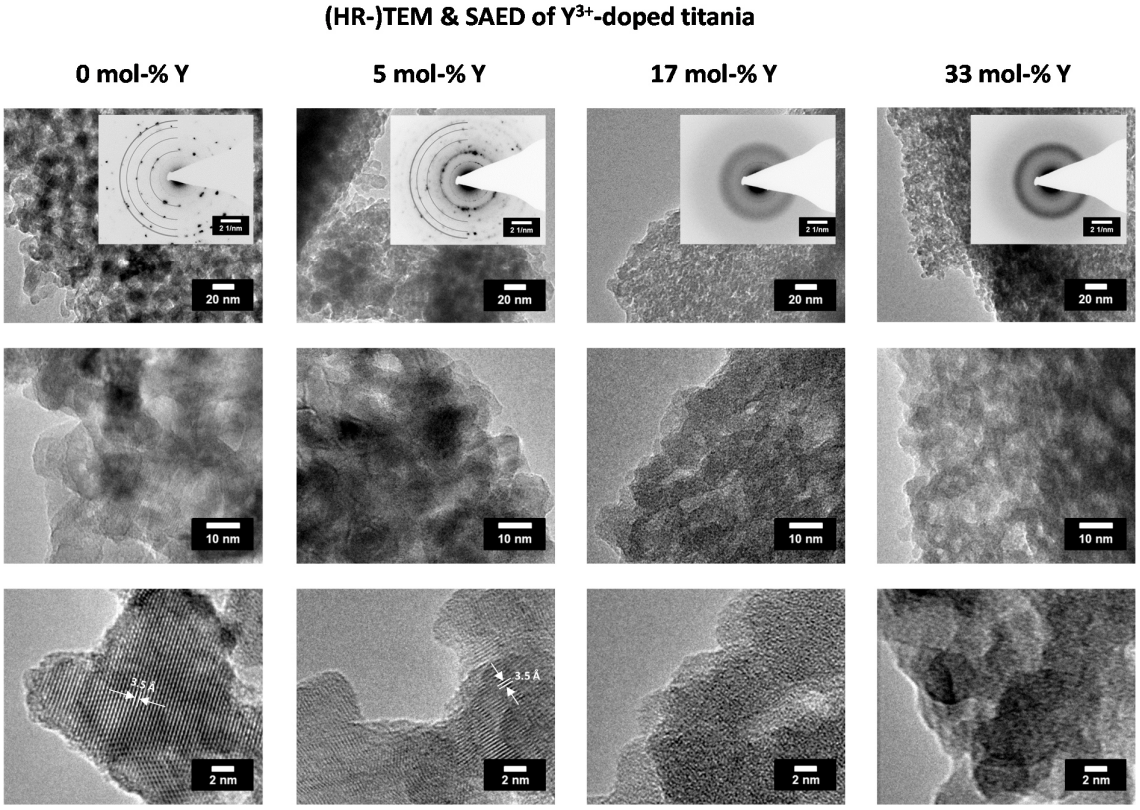

Figure 5.3: Representative (HR-)TEM images for bare mp. TiO_2 and Y-doped titania with template-controlled pore structures and increasing Y fraction. For bare TiO_2 (0 mol-% Y) and low concentrations of Y (5 mol-% Y), the SAED patterns (insets in top row) can be assigned to a polycrystalline anatase-type phase showing corresponding lattice fringes of ~ 3.5 Å in HR-TEM images (bottom). For higher Y fractions (17, 33 mol-%), the illustrated HR-TEM images provide further evidence for a reduced crystallinity. Film segments were analyzed after scraping-off from films deposited on Si substrates using a diamond-scraper tool.

Pronounced segregation into Y-rich and Ti-rich domains in the pore walls of the films could be an important factor affecting the electrical properties. COMPO (Z-contrast) analysis *via* SEM can provide useful information about the homogeneity in composition on the micron-scale. Results from the composition mode electron microscopy suggest the formation of a

homogeneous oxide material without larger segregated domains, as evidenced by representative SEM/COMPO images in figure 5.4 (bottom).

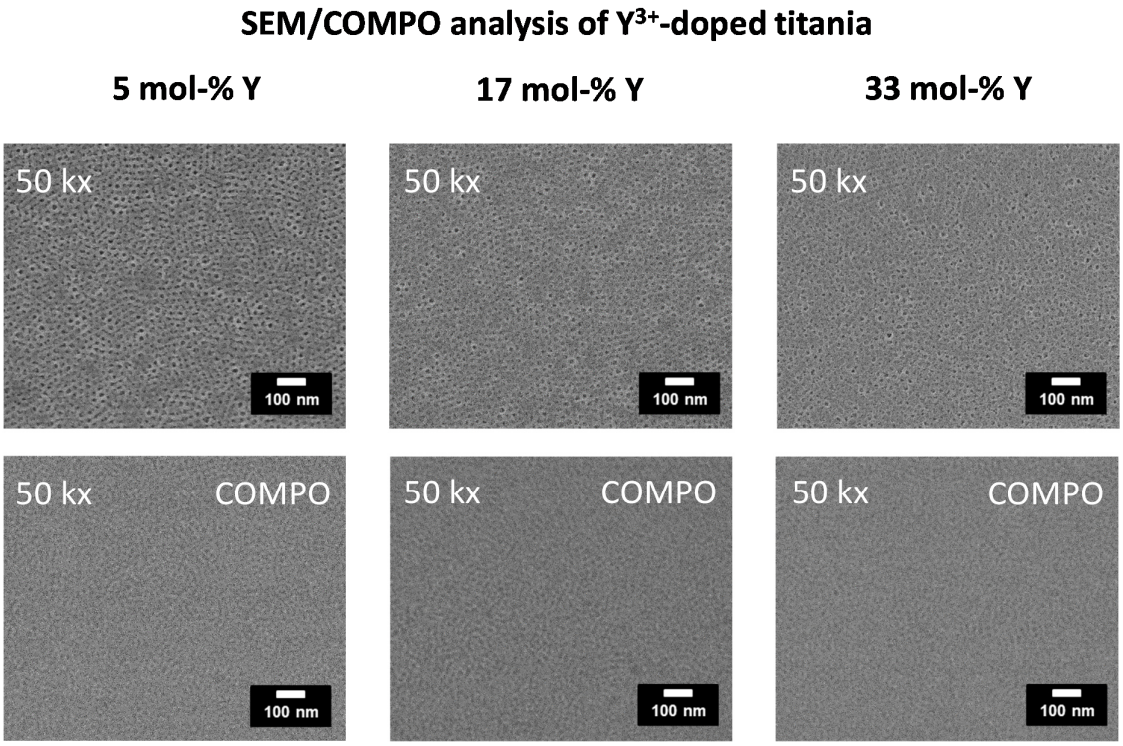

Figure 5.4: Lower magnification (50 kx) SEM images (top) in dependency of Y fraction for films calcined for 30 min at 600 °C in air on flat Si substrates. The lower row represents corresponding COMPO images with an enhanced material contrast, which suggest a high degree of intermixing of Y and Ti species in the oxides due to the absence of areas with varying contrast (on the investigated length scale).

In good consistency with the theoretical results from DFT calculations summarized in **[MF-4]**, p-type metal ion doping of titania is considered less effective than n-doping in terms of enhanced electrical bulk conductivities. This can only be achieved for p-type doping with PGM elements (e.g. Ir) leading to strongly increased conductivities for relatively high amounts of PGM species. It has to be noted that the observed enhanced electrical properties may originate from the formation of conductive island-like pathways (PGM-rich) throughout the bulk of the PGM-doped titania materials. For non-noble metals, however, segregation has an opposite effect, as the corresponding oxide phases in the segregated domains often show insulating electrical properties (see **[MF-4]** for further explanations). In the context of the aim of this thesis, doping of the support with PGM is not desirable, in particular for relatively high PGM contents. Accordingly, further approaches to improve the electrical properties of titanium-based oxides were pursued.

5.2.2 Is it possible to reach higher bulk conductivities by the introduction of another dopant in Nb-doped titania, *i.e. via* co-doping?

Based on the findings from the investigations of different metal ion n- and p-doped titania model systems, Nb-doped titania with high dopant fractions of about 33 mol-% shows the most promising electrical bulk conductivity. In this section, the additional substitution of a small amount of Ti atoms in conductive Nb-doped titania and the influence of the introduction of a second dopant ion on the electronic and structural properties will be discussed.

Ternary metal oxides with a composition of $TM_4Nb_{0.28}Ti_{0.68}O_2$ and well-defined mesoporous structure were successfully synthesized *via* dip-coating and EISA, followed by thermal calcination at 600 °C in air. Due to their similar ionic radii with respect to Ti^{4+} and results from theoretical calculations (negative or near-zero segregation energy), Sc, Y, and Fe were selected as most promising non-noble metal candidates. For all co-dopants, homogeneous films with controlled mesoporosity and similar average pore sizes can be obtained, providing further evidence for the versatility of the developed synthesis approach. The co-doping of titania with different metal species has been shown to improve the optical properties and, hence, the photocatalytic activity[147], for instance. Consequently, potential applications of the herein developed titania-based materials with template-controlled mesoporosity in e.g. photo(electro)catalysis might be interesting.

Exemplarily, ternary oxide films with a molar fraction of 28 mol-% Nb are discussed in this section. Both, top-view and cross-section SEM images reveal the formation of porous films with homogeneous mesoporous structure and interconnected porosity, independent of the co-doping element. Based on the estimations of the average sheet thickness *via* cross-sectional SEM, normalized electrical sheet conductivities can be calculated for each material. The results from impedance spectroscopy measurements reveal a distinct impact of the co-dopant on both the electrical properties and the crystallinity. A correlation between an increasing crystallinity in the ternary oxides (assessed *via* GI-XRD) and sheet conductivity can be found, according to the data summarized in figure 5.5. While an addition of 4 mol-% Y seems to prevent the crystallization of the titania-based compound and an X-ray amorphous material is obtained, an increasing crystallinity can be observed for similar amounts of Fe and Sc. As expected, co-doping with low amounts of non-noble metals can improve the electrical conductivity respective to pristine mp. TiO_2, particularly for Sc co-dopants.

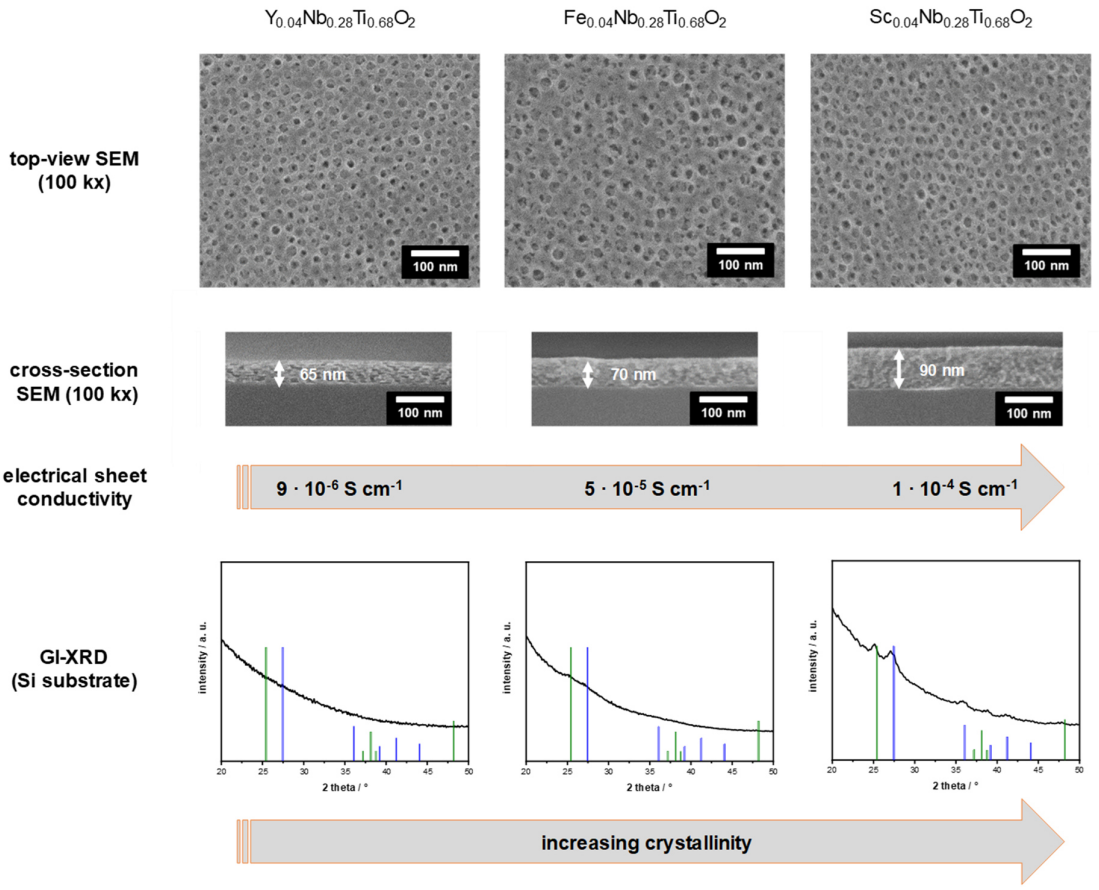

Figure 5.5: Results from the physicochemical characterizations of ternary, co-doped titania materials with template-controlled porosity and $TM_{0.04}Nb_{0.28}Ti_{0.68}O_2$ stoichiometry (TM = Y, Fe, Sc) via electron microscopy for the analysis of the pore structure and layer thickness, as well as impedance spectroscopy and GI-XRD for information about the electrical conductivity and crystallinity, respectively. A correlation between an increasing sheet conductivity for an increasing crystallinity of the oxide phases can be found. In the bottom row, green and blue vertical bars represent reference XRD pattern for anatase-type and rutile-type TiO_2, respectively.

Yet, further enhancements of the reported maximum conductivity value of up to 10^{-3} S/cm for Nb-doped titania (*cf.* **[MF-1]**) are not achieved and require further work to identify other suitable candidates or oxide compositions. In this context, anion doping of titania might represent a viable alternative to improve the electrical properties.

For all herein discussed materials, increasing the calcination temperature (e.g. up to 700 °C) led to an increased crystallinity of the pore walls. However, the templated pore structures could not be fully preserved due to crystallite growth and sintering effects.

5.3 Investigation of Catalyst-Support Interactions and their Influence on Catalytic OER Activity

5.3.1 Despite being sufficiently conductive, what are the main reasons for the observed low OER activities for surface-modified Nb-doped titania films?

As a starting point for the synthesis of titania-based metal oxides with template-controlled mesoporosity, theoretical DFT screenings (results summarized in publication **[MF-4]**) suggest Nb to be one of the most promising PGM-free dopants in order to improve the electrical conductivity and structural stability of the catalyst support material. As already mentioned, TiO_2 has emerged as the only oxidation-stable support material for acidic OER, so far.[148] Yet, its unfavorable electronic properties, especially the very low conductivity, hamper a direct application as catalyst support for OER-active Ir species. Moreover, by the introduction of a nanostructure aiming for an increased specific surface area, the electrical conductivity decreases even further with respect to single-crystalline TiO_2. In **[MF-1]**, an optimized synthesis concept for Nb-doped titania films with well-defined mesopore structure is described. Both, computational and experimental methods are applied in order to improve the electrical conductivities of titania based on a profound understanding of the doping process. Importantly, the evaluated maximum sheet conductivity of ~ 10^{-3} S/cm for a fraction of 35 mol-% Nb should, in theory, promote OER activity after the surface modification with OER-active species, e.g. IrO_x species deposited *via* ALD. The reason for this lies in the previous findings by Bernicke & Bernsmeier *et al.*[14,72,111] stating a minimum required conductivity of ~ 0.1 S/m (≈ 10^{-3} S/cm) to provide efficient charge transfer during OER for mixed iridium-titanium oxides as templated mesoporous model catalysts. Ir contents < 15 mol-% in the mixed oxide films lead to very low catalytic activities in acidic OER using 0.5 M H_2SO_4 as a supporting electrolyte, despite the formation of homogeneous coatings with well-accessible pore structures.

The developed Nb-doped titania films in **[MF-1]** feature a high surface area, as well as a sufficient sheet conductivity and are thus applied as promising porous, PGM-free catalyst support for nanocrystalline IrO_x species introduced *via* ALD. In brief, low currents in OER regime have been observed, independent of the ALD layer thickness and geometric Ir loadings. Different precursor combinations for the coating of the doped oxide pore walls were evaluated regarding their structural and electronic properties, as well as their impact on the catalytic activity in acidic electrolyte. For low loadings of Ir and thin layers of IrO_x produced *via* the

previously established ALD process at low temperature using (EtCp)Ir^{I}CHD as metal precursor in combination with O_3 (as described in **[MF-2]**), very low OER currents can be found. Increasing the temperature of the electrolyte during the RDE testings to 60 °C or increasing the potential of up to 2.2 V_{RHE} does not lead to any significant OER currents for films on polished Ti substrates.

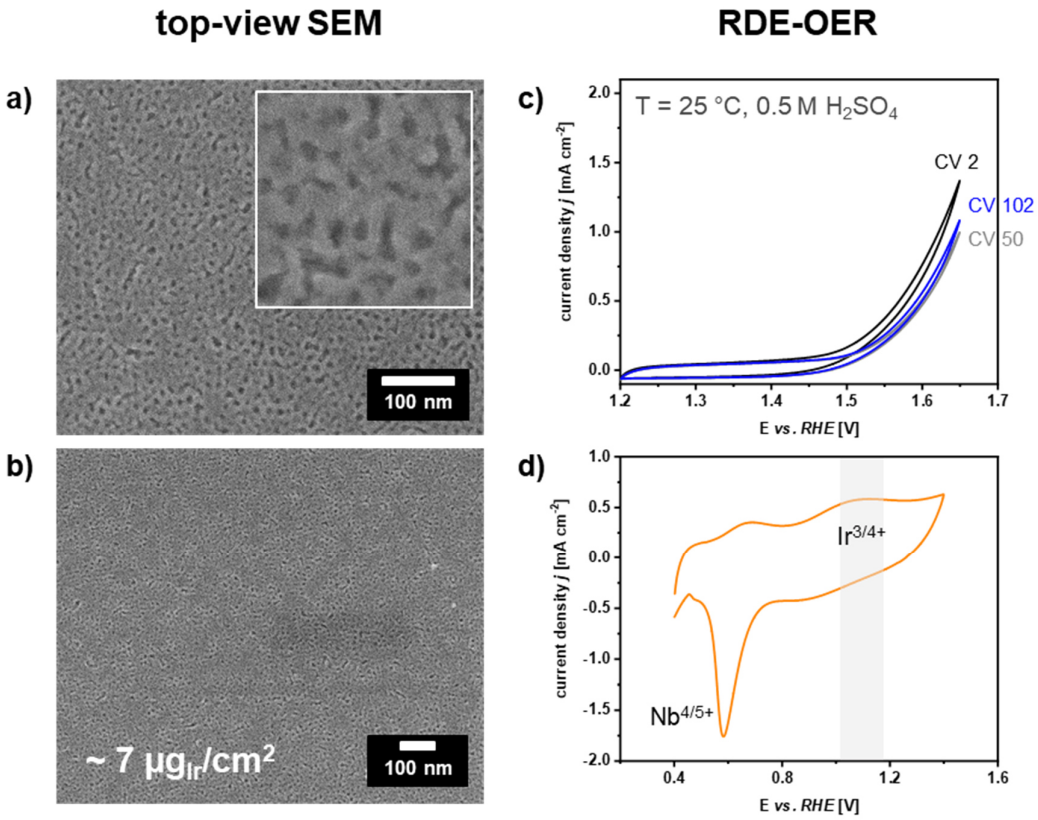

Figure 5.6: Results from physicochemical characterizations (a-b) and electrocatalytic testings (c-d) for ALD-surface-modified Nb-doped titania electrode coatings. 100 cycles of ALD using Ir(acac)$_3$ and O_3 as metal and oxygen precursor, respectively, were performed to modify the entire pore wall surface of mesoporous $Nb_{0.35}Ti_{0.65}O_2$ films deposited via dip-coating on flat Ti substrates. In the base voltammogram in (d), corresponding redox transitions for Nb and Ir species were assigned.

For a more detailed investigation of the unfavorable interactions between the Nb species in the titania host lattice (support) and the surface IrO_x species (catalyst), electrode coatings with higher geometric Ir loadings were produced and electrochemically tested. Therefore, the ALD metal precursor has been varied. The combination of Ir(acac)$_3$ and O_3 at 200 °C has been reported[149] to afford homogeneous IrO_2 surface coatings. Relatively thick noble metal oxide layers can ensure a high degree of conformality. Figure 5.6 shows the most important results from the physicochemical and electrocatalytic investigations for an ALD-surface-modified mp.

$Nb_{0.35}Ti_{0.65}O_2$ support after 100 cycles at 200 °C. Top-view SEM images (figure 5.6a-b) suggest a well-preserved mesoporous structure after ALD. A post-thermal treatment of the films for 10 min at 375 °C in air ensures a sufficiently high electrical sheet conductivity. Remarkably, the observed sheet conductivity is almost three order of magnitude higher than the empirically determined minimum mentioned above. This is in good consistency with the relatively high Ir loading of ~ 7 µg/cm^2 and, more importantly, has not yet been observed for surface-modified Nb-doped titania films with lower geometric Ir loadings, independent of the ALD precursor. Nevertheless, as shown in figure 5.6c, low currents are found in OER regime in acidic electrolyte. In base voltammetry (figure 5.6d), features corresponding to redox transitions of Nb species can be observed.

Additional investigations indicate that an undesired electronic interaction between an n-type semiconductor, *i.e.* Nb-doped titania, and a metal, *i.e.* IrO_x, may lead to the formation of a so-called Schottky barrier that hampers OER kinetics under applied oxidative potentials. The following factors provide further evidence for the formation of such interfacial barrier between n-type semiconductor and metal layer:

- For thick Ir-based surface layers, surface-conductive pathways that effectively promote electron transport, and hence catalytic OER activity, at the electrode are built, which is in accordance with previous literature works.[93,131,150]
- Intrinsically, bare TiO_2 reveals n-type semiconducting properties and surface modification *via* Ir-/IrO_x-ALD leads to low OER (mass) activities, despite the deposition of relatively thick surface layers and drastically enhanced electrical conductivities, as reported in **[MF-2]**.
- The observed reduced catalytic activity can also be found for other n-doped titania supports, such as W-doped titania, coated with IrO_x surface layers.
- The effect is not only limited to doped titania supports. Strikingly, for IrO_x-modified mp. WO_x films deposited on Ti substrates, a similar performance loss can be claimed. Yet, employing a different porous support with improved electrical conductivity, *i.e.* metallic conductivity in the case of mp. WC_x films, can prevent the formation of such Schottky barrier.

In summary, the formation of a Schottky barrier at the interface between a semiconducting oxidic support and a metal-like surface coating seems to hamper OER kinetics, even at elevated oxidative potentials and temperatures. The native oxide layer on the Ti substrates, on which the surface-modified films are deposited, grows during thermal treatment in the preparation of the supports and, consequently, may give rise to the formation of another Schottky junction at the surface of the substrate. As an outlook, the addition of a conductive (*i.e.* metallic) interlayer is proposed to prevent a pronounced surface oxidation of the Ti substrate and mitigate the formation of a potential energy barrier. Prior to the deposition of the porous films, passivating coatings in the range of several tens to hundreds of nanometers of gold (Au) or platinum (Pt) might represent a promising strategy and, beyond that, improve the overall reaction kinetics due to an enhanced charge transfer at the electrode. Alternatively, highly conductive, carbide-based supports can alter the electronic situation and positively affect both the reaction and charge transfer kinetics, as will be discussed in the following.

5.4 Porous Metal Carbides as Catalyst Supports for both Alkaline and Acidic OER

5.4.1 Which main issues need to be solved in order to develop carbide-based OER catalysts?

There are only few reports about an application of porous transition metal carbides as support materials for OER electrocatalysis, despite their excellent electrical properties.[110,151–154] The main issue is the limited stability under oxidative potentials in OER regime, leading to an irreversible bulk oxidation of the carbide phase and a concomitant drop in electrical conductivity. In this thesis, well-controlled surface modifications with both PGM and non-noble metals are reported by the concept of conformal ALD on high-surface-area transition metal carbides, as an innovative approach for the rational design of next-generation electrode coatings with improved utilization of active species. Advantageously, the metallic conductivity of the support prevents the formation of an undesirable Schottky barrier at the interface to the surface layer comprised of OER-active species.

Exemplarily, results from electrochemical testings in alkaline electrolyte in publication **[MF-3]** provide strong evidence for synergistic effects between a highly conductive carbide support (WC_x) and semiconducting surface oxide layers (NiO). The synthesized material shows a significantly higher bulk conductivity compared to porous NiO_x catalyst films. Moreover, as a result of the optimized synthesis concept *via* conformal ALD on a porous support, an improved spatial distribution of the active Ni^{x+} ($x \geq 3$) sites can be achieved. Yet, the observed enhancement in catalytic OER mass activity for the NiO-coated WC_x electrocatalyst of a factor of ~ 280 can not only be explained by an optimized utilization of active Ni species. In contrast to mesoporous NiO_x films, redox and charge transfer processes during OER are drastically accelerated in the presence of a highly conductive support. Results from reference experiments applying the same NiO-ALD process to weakly conductive NiO_x supports, underline the decisive role of the electrical conductivity of the support for enhanced catalytic activities and reduced overpotentials. Similarly, in the case of porous WO_x supports, reduced OER activities and stabilities were found. Accordingly, the issue of a pronounced bulk oxidation of the carbide support has to be carefully addressed a) during the synthesis of the surface-modified catalyst *via* ALD, and b) during the electrocatalytic reactions in oxidative and corrosive environments. Concerning a), mild reaction conditions, such as a moderate temperature of 200 °C in the ALD chamber and reduced pulses of highly oxidizing O_3 have been established using $Ni(Cp)_2$ as

metal precursor. An optimization of the ALD parameters plays a decisive role in order to ensure a structural and morphological integrity of the support. Concerning b), a high degree of conformality in the ALD surface layer is very important. Beyond that, a good adhesion of the surface catalyst layer to the pore wall surface is required. In this context, a slight surface oxidation of the metal carbide support as a result of an intended passivation in air, can promote the adhesion of the deposited oxide species to the underlying support. Further explanations will be given in the following in section 5.5.

5.4.2 Can the concept of improving oxidation resistance of carbide supports by conformal ALD be transferred to acidic environments?

The excellent conductivity of the synthesized templated mesoporous carbide films renders them highly promising candidates for an application in acidic OER after surface modification with conductive IrO_x layers. The optimized ALD process reported in work **[MF-2]** for the deposition of conformal surface layers of predominantly oxidic Ir^{x+} ($x \geq 3$) species is thus applied on porous WC_x films.

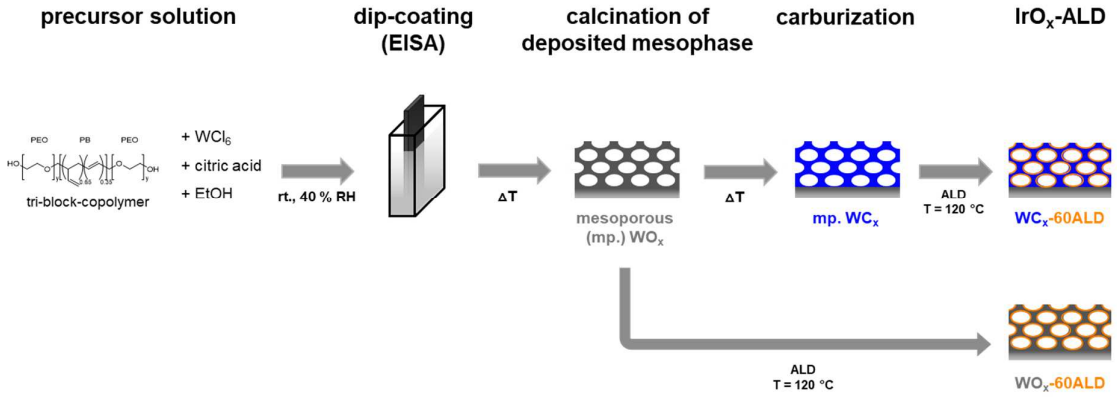

*Figure 5.7: Schematic illustration of the developed synthesis route for IrO_x-coated mesoporous WO_x and WC_x films on flat substrates (glass, Si, Ti) via dip-coating (EISA) and subsequent conformal IrO_x-ALD. The exact experimental details for the preparation of mp. WO_x and mp. WC_x films can be found in section D in the appendix of this thesis and are similar to the descriptions stated in **[MF-3]**. The ALD parameters for the surface modification are described in publication **[MF-2]**.*

As shown in figure 5.7, reference catalytic coatings with porous WO_x as a less conductive support were prepared for an elucidation of structure-activity relationships. Physicochemical analysis of the obtained materials *via* electron microscopy and EDX (see figure 5.8) confirm a successful surface modification for both the oxide and the carbide support with thin IrO_x layers

after 60 ALD-cycles at 120 °C using similar parameters as reported in publication **[MF-2]**. GI-XRD analysis reveals a preservation of the nanocrystalline W_2C phase and no indications for any pronounced bulk oxidation of the carbide support by the oxidative conditions during ALD can be found. Results from both SEM and TEM (see figure 5.8a-I & b-I) analyses suggest a well-preserved mesoporous structure after modification of the pore wall surfaces. HAADF-STEM images with corresponding elemental mappings (EDX analysis) underline a fine distribution of the deposited Ir species. Moreover, data from impedance spectroscopy for surface-modified films on insulating glass substrates show very high electrical conductivities for IrO_x-coated WC_x that are in the range of those observed for bare mp. WC_x films (~ 10^3 S/cm). For IrO_x-coated WO_x, a slight increase in conductivity with respect to the bare oxide support is found, leading to a value that is approximately two orders of magnitude higher (≈ 10^{-1} S/cm) than the estimated conductivity limit[72] for efficient charge transport during OER.

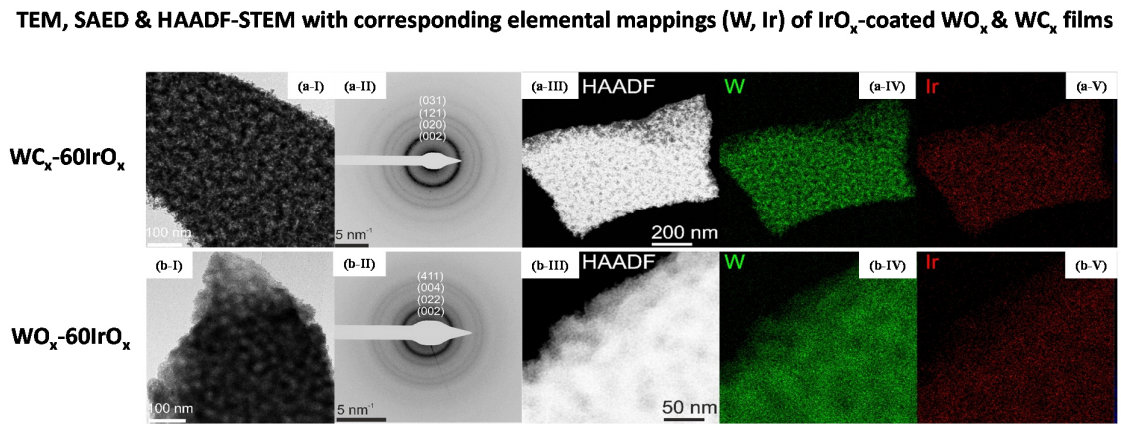

Figure 5.8: TEM, SAED, as well as HAADF-STEM images with corresponding elemental mappings for IrO_x-coated WC_x (top) and WO_x (bottom) films with template-controlled porosity. 60 ALD cycles at a low temperature of 120 °C were performed for the surface modification of both supports. Both films show a preserved mesopore structure after ALD (I, III-V). The elemental mappings (V) indicate the presence of well-distributed Ir species after ALD. The SAED patterns (II) are assigned according to the reference card numbers COD 96-591-0042 and COD 96-152-08916 for WO_3 (γ-WO_3, monoclinic) and W_2C (trigonal, hexagonal axis), respectively.

The obtained results from electrocatalytic OER testings in acidic electrolyte (0.5 M H_2SO_4) provide further evidence for the Schottky barrier formation hypothesis mentioned in previous sections. WO_x, mainly composed of the WO_3 phase, intrinsically shows n-type semiconducting properties.[155] Hence, the deposition of pseudo-metallic IrO_x surface layers, leads to hampered OER reaction kinetics and, consequently, low catalytic activities are found (see figure 5.9a). In stark contrast, by employing a highly conductive metal carbide as support for active Ir species, high currents in OER regime result and excellent mass-specific activities of up to

~ 1750 mA/mg_{Ir} at a potential of 1.60 V_{RHE} can be calculated in the 50th CV (scan rate: 6 mV/s). This value is lower than the reported mass activity for the most active IrO_x-coated $IrTiO_x$ support assessed under similar measurement conditions (**[MF-2]**). Further optimizations of the ALD process, such as a variation of cycle number to adjust the surface layer thickness, might improve the catalytic performance. Nevertheless, this study serves as another proof-of-concept for a maximization of surface-exposed, highly active sites introduced *via* conformal ALD on porous supports. Outstanding mass activities can be achieved in both alkaline (NiO-ALD, see **[MF-3]**), as well as in acidic (IrO_x-ALD, see **[MF-2]**) OER by the application of surface-modified, highly conductive metal carbide supports with interconnected mesopore structures.

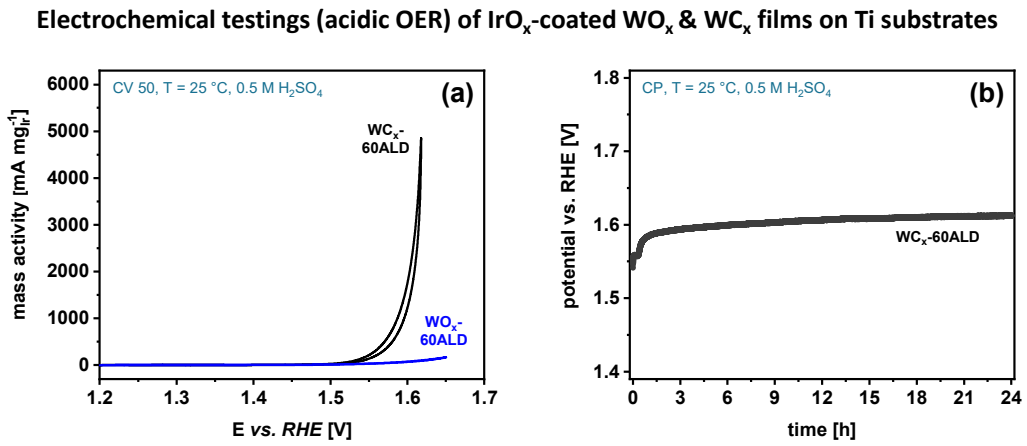

Figure 5.9: Results from electrocatalytic OER testings for IrO_x-coated mp. WC_x films in an RDE setup using 0.5 M H_2SO_4 as a supporting electrolyte (T = 25 °C; 1600 rpm). A Pt-mesh (Chempur, 1024 mesh/cm²) was used as counter electrode. In (a), the 50th CV for IrO_x-coated WC_x as well as IrO_x-coated WO_x films deposited on conductive Ti substrates are plotted. In (b), results from a chronopotentiometric stability test of the surface-modified WC_x electrode coating is shown. A constant current density of j = 1 mA/cm² was set.

The findings summarized in this section provide further evidence for the formation of an undesired Schottky barrier at the electrode in the case of n-type semiconducting supports. To overcome this limitation and boost catalytic OER activities, the previously established concept of surface-protected transition metal carbides for alkaline OER has been transferred to acidic environments. Again, an optimization of the ALD process is the basis for an improved durability during static electrochemical tests at the RDE level. For this, homogeneous and uniform IrO_x surface layers were deposited onto the entire external and internal pore wall surfaces of a WC_x support with metal-like electrical properties. Overall, the concept of improving oxidation resistance of carbide supports *via* conformal ALD can be extended to acidic OER.

5.5 Hypotheses for the Improved Catalyst Durability after Surface Modification *via* conformal ALD

5.5.1 What are the main reasons for an improvement in catalytic stability after ALD?

In this thesis, a significantly enhanced catalytic stability is described for different ALD-modified electrocatalysts in both alkaline and acidic electrolytes. By optimized ALD procedures, the concept of the formation of a protective oxide surface layer that prevents the underlying porous support from pronounced irreversible bulk oxidation and corrosion is discussed in publications **[MF-2]** and **[MF-3]**.

In **[MF-3]**, XPS depth-profiling analysis of the spent NiO-coated WC_x electrocatalysts after electrochemical testing in alkaline electrolyte revealed the oxidation of the near-surface atoms (W, C) of the support. Yet, the bulk phase was still dominated by highly conductive carbide species. In reference experiments for unmodified mp. WC_x electrode coatings, rapid bulk oxidation and concomitant dissolution into the surrounding electrolyte can be observed.
Similar conclusion can be drawn based on the results reported in **[MF-2]**. The spent IrO_x-coated $Ir_{0.15}Ti_{0.85}O_2$ electrocatalyst for acidic OER was much better protected from undesired corrosion and dissolution after conformal ALD, compared to the unmodified mixed oxide support. The mp. $Ir_{0.15}Ti_{0.85}O_2$ electrode coatings provide an insufficient durability, according to chronopotentiometric stability testings, which suggest a drastic loss of active material after several hours at low current densities in acid, as confirmed *via* quantitative EDX analysis and ICP-OES of the electrolyte solution.

The most important benefits from ALD surface modifications reported in recent literature works are briefly explained in the following. The concept of an enhanced material stability at elevated temperatures after well-controlled surface modifications on an atomic level *via* conformal ALD has been highlighted before. As an illustrative example, mesoporous iron oxide films can be effectively stabilized against undesired crystallite growth and phase transitions, that would eventually lead to a collapse in the porous structure after exposure to high temperatures, *via* SiO_x-ALD.[156] For ultra-thin AlO_x layers deposited *via* ALD, similar effects were found, yet with an inferior stabilizing effect. Based on the oxo-basicity concept[157], an explanation for the stronger or weaker interactions strengths between the SiO_x and AlO_x surface layers and the underlying iron oxide carrier can be provided, respectively. Several other interesting works reveal improved catalyst integrities and performances after surface

modification *via* ALD for the formation of uniform films (*i.a.* NbO_x[158], TiO_2[159], or ZrO_2[160]) as protective and/or functional catalyst overcoat, drastically reducing sintering, leaching or degradation of active metal species.

Moreover, the concept was transferred to electrocatalytic OER applications aiming for an enhanced catalyst durability in oxidative environments. Exemplarily, findings from a previous work[161] on NiO-ALD-modified high-aspect-ratio carbon supports indicate a high stability of the surface NiO layers during catalysis. The conductive carbon nanotube (CNT) support particles were totally wrapped by the stable, nanoparticulate-like NiO species introduced *via* an optimized ALD process. Both the entire inner and outer CNT walls are homogeneously covered. For higher ALD cycle numbers (~ 200 cycles), the NiO surface deposits start overlapping. Remarkably, the composite catalyst prepared using only 100 cycles NiO-ALD shows an excellent stability in 1.0 M KOH and analyses of the spent catalyst reveal a well-preserved morphology. Accordingly, the study provides evidence for an enhanced catalyst durability by controlled ALD surface modification on a carbonaceous support that is prone to oxidation and concomitant degradation.

Recently, both effects were successfully combined in a study by Lei *et al.*[162], demonstrating the protective role of ALD-deposited Al_2O_3 nanolayers for both the structure as well as the electrocatalytic performance of MOF-derived NiFe-based OER catalysts. On the one hand, the surface Al_2O_3 ALD layer is reported to prevent a structural collapse of the well-defined metal-organic framework during pyrolysis. On the other hand, a high OER activity alongside a drastically increased stability in alkaline electrolyte with respect to the unmodified MOF-derived catalyst can be found after ALD modification. The authors provide reasonable explanations for the observed increase in catalytic performance, which mainly relies on the integrity of the nanostructure ensuring high specific surface areas, as well as on reduced etching of active NiFe species by the electrolyte due to the confined structure.

The findings discussed in this thesis provide further insights into an improved catalytic stability of ALD-modified catalyst systems, which is essentially independent of the pH of the surrounding electrolyte. Durable electrode coatings with high surface areas were developed by optimized ALD methods and variations in ALD layer thickness. The most important requirement for an enhanced stability and protection from excessive dissolution during OER is a high degree of conformality to ensure the formation of a dense surface layer. For precious metals, this is known to be particularly difficult.[118,163] Hence, a careful investigation of the

relevant factors affecting the nucleation and growth of the surface layers is critical. Based on an understanding of the mechanisms, optimized reaction parameters and precursor combinations can be identified. As shown in **[MF-2]**, significantly improved OER activities and stabilities can be achieved, finally leading to highly efficient catalysts with strongly reduced noble metal contents.

Concerning the assessment of electrocatalytic stability, results obtained from RDE testing setups are to be taken with caution, especially when investigated under *static* operation (*i.e.* CP or CA measurements). In fact, accelerated degradation tests (ADTs) with *transient* cycling over a broad potential range were shown to significantly affect the morphology and integrity of Ir-based OER catalysts in acid.[164] To gain further insights into catalyst activity and stability under realistic conditions, the fabrication of catalyst-coated membranes (CCMs) and the integration into commercially relevant PEM electrolyzer setups will be required. Recent studies by Bernt *et al.*[165] point out that RDE measurements are appropriate for the determination of catalytic activity, yet for an evaluation of stability, ADTs on the MEA level would be necessary.

Nevertheless, the findings in this thesis underline the importance of a high degree of conformality and homogeneity during the surface modification step. ALD represents the method of choice for the formation of thin yet dense surface layers of metal or metal oxides at the entire surface of porous materials. In addition, beside a high intrinsic activity, a sufficient stability of the deposited surface species is a key requirement in order to ensure an improved electrode durability in oxidative and corrosive environments.

6. Conclusion & Outlook

In the following, the most important findings from chapters 2 – 4 are summarized considering the addressed issues and challenges in the design of highly efficient OER electrocatalysts discussed in chapter 5. The main targets of the developed synthesis concept are:

I enhanced electrical conductivity,
II maximization of the number of active sites,
III control over the exposed surface sites,
IV improvements in mass-specific catalytic activity, and
V in catalyst durability during OER.

For a successful optimization of each of the five targets, a profound understanding of the structural and electrical properties of the catalyst material is necessary to promote the reaction kinetics at the electrode. In this context, it is desirable to adjust chemical and physical properties on multiple length scales, ranging from macroscopic (electrode geometry) over microscopic (mesopore structure) to atomic (deposition of ultra-thin surface layers *via* ALD). Figure 6.1 schematically illustrates the overall concept, highlighting the most important features in the design of highly active and durable OER electrodes *via* ALD-based surface modification of electrically conductive, porous metal oxide and carbide supports.

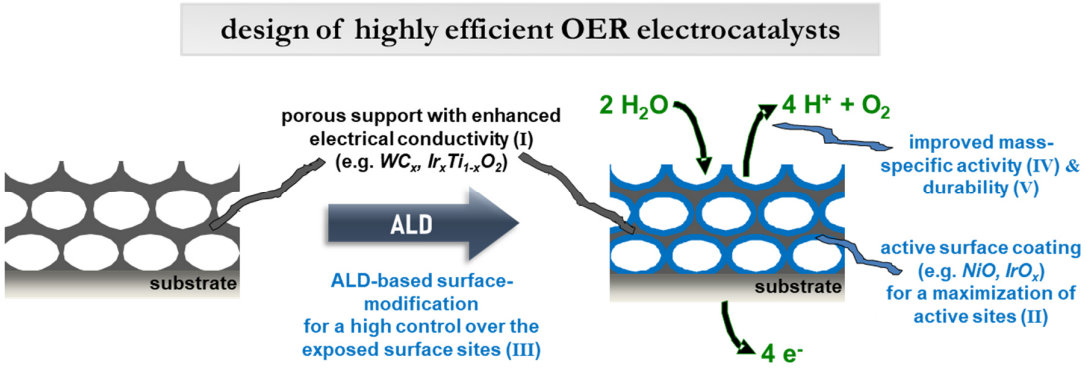

Figure 6.1: Concept for the design of active and durable OER electrodes based on the surface modification of porous metal oxides and carbides via conformal ALD.

The concept relies on the rational design of surface-modified electrode coatings with template-controlled porosity. Dip-coating and EISA with subsequent thermal treatments were applied for the synthesis of homogeneous templated mesoporous films composed of (doped) transition metal oxides and carbides, serving as model systems for the elucidation of structure-property correlations. In **[MF-1]**, doping of titania with Nb species could significantly improve the electrical sheet conductivities without negatively affecting the porosity. As such, mp. $Nb_{0.35}Ti_{0.65}O_2$ films were identified as a highly promising catalyst supports for acidic OER, taking into account the high stability of titanium-based oxides in acidic and oxidative environments, according to target **I**.

In order to address targets **II** and **III**, optimizations in the surface modification process *via* ALD finally led an excellent conformality of the deposited layers for both nanocrystalline NiO and weakly crystalline IrO_x. In **[MF-3]**, a previously established ALD process for nanoparticulate-like NiO based on $Ni(Cp)_2$ and O_3 as metal and oxygen precursor, respectively, was adapted to porous tungsten carbide support films on different substrates. Importantly, no evidence for an undesired pronounced oxidation of the bulk carbide phase was observed after ALD, despite the presence of oxidizing agents at elevated temperature. The nanostructured and highly conductive carbide support synergistically interacts with the surface NiO layers during OER, as further outlined by theoretical considerations discussed in **[MF-3]**. Regarding target **III**, the results in **[MF-2]** provide straightforward insights into the impact of the ALD parameters on the structural and chemical properties of the introduced surface sites. A good control over the exposed surface sites is essential for both an improved utilization of active species and an enhanced catalyst durability in oxidative conditions.

To reach target **IV**, the interfacial properties between the support and the introduced surface layers have to be evaluated and, finally, optimized. In the previous chapter, the formation of a *Schottky barrier* is pointed out for n-type semiconductor supports (e.g. Nb-doped TiO_x, WO_x) and metal-type surface layers (e.g. IrO_x). In electrochemical testings, mesoporous Nb-doped TiO_x and WO_x films deposited on Ti substrates and subsequently surface-modified *via* IrO_x-ALD show low currents in OER regime. Contrarily, for Ir-doped TiO_x and highly conductive WC_x excellent OER activities are found in RDE testings in acidic electrolyte. Compared to state-of-the-art reference catalysts, similar current densities in OER regime are achieved at significantly reduced geometric loadings of precious Ir.

The main reason for the observed improvements in catalyst durability during both alkaline and acidic OER after ALD (target **V**) lies in the formation of a dense, homogeneous surface layer covering the entire pore wall surface of the support. The kinetics for the oxidation of H_2O molecules in spatial proximity to the exposed surface sites in the ALD layer are strongly promoted and can be expected to prevail over the oxidation of the bulk phase of the support. Besides, the deposited conformal ALD surface layer hampers the direct contact of electrolyte species (e.g. OH^-, H^+ or SO_4^{2-}) with the lattice of the support, and, as such, features a protective role.

As an outlook, future work is suggested to further explore the range of oxidation- and corrosion-resistant oxide-based support materials with high specific surface areas and sufficient electrical conductivities. In this context, theoretical *ab-initio* screenings might aid in the identification of promising materials with p-type semiconducting properties, hence preventing the formation of a Schottky barrier at the interface to the active surface IrO_x layer. Beyond that, the developed catalyst systems should be tested in industrially relevant PEM or AEL/AEM setups to assess both activity and stability under more realistic conditions and higher currents. Therefore, the synthesis of MEAs has to be established, in which the herein developed materials serve as electrocatalysts at the anode of the cells. Systematic investigations of the impact of fluctuating potentials or shut-downs of the electrolyzers will provide further relevant insights into the stability of the catalysts in realistic operation conditions. In general, the introduced surface modification concept *via* ALD is not limited to OER electrocatalysis, but might also be applied to improve the performance of catalyst systems for different reactions in the field of heterogeneous catalysis.

References

(1) Mazloomi, K.; Gomes, C. Hydrogen as an Energy Carrier: Prospects and Challenges. *Renew. Sustain. Energy Rev.* **2012**, *16* (5), 3024–3033. https://doi.org/10.1016/j.rser.2012.02.028.

(2) Hirscher, M. Hydrogen Storage by Cryoadsorption in Ultrahigh-Porosity Metal-Organic Frameworks. *Angew. Chemie Int. Ed.* **2011**, *50* (3), 581–582. https://doi.org/10.1002/anie.201006913.

(3) Carmo, M.; Fritz, D. L.; Mergel, J.; Stolten, D. A Comprehensive Review on PEM Water Electrolysis. *Int. J. Hydrogen Energy* **2013**, *38* (12), 4901–4934. https://doi.org/10.1016/j.ijhydene.2013.01.151.

(4) Brandon, N. P.; Kurban, Z. Clean Energy and the Hydrogen Economy. *Philos. Trans. R. Soc. A Math. Phys. Eng. Sci.* **2017**, *375* (2098), 20160400. https://doi.org/10.1098/rsta.2016.0400.

(5) van Renssen, S. The Hydrogen Solution? *Nat. Clim. Chang.* **2020**, *10* (9), 799–801. https://doi.org/10.1038/s41558-020-0891-0.

(6) Wulf, C.; Zapp, P.; Schreiber, A. Review of Power-to-X Demonstration Projects in Europe. *Front. Energy Res.* **2020**, *8*. https://doi.org/10.3389/fenrg.2020.00191.

(7) Staffell, I.; Scamman, D.; Velazquez Abad, A.; Balcombe, P.; Dodds, P. E.; Ekins, P.; Shah, N.; Ward, K. R. The Role of Hydrogen and Fuel Cells in the Global Energy System. *Energy Environ. Sci.* **2019**, *12* (2), 463–491. https://doi.org/10.1039/C8EE01157E.

(8) Suryanto, B. H. R.; Wang, Y.; Hocking, R. K.; Adamson, W.; Zhao, C. Overall Electrochemical Splitting of Water at the Heterogeneous Interface of Nickel and Iron Oxide. *Nat. Commun.* **2019**, *10* (1), 5599. https://doi.org/10.1038/s41467-019-13415-8.

(9) Anantharaj, S.; Ede, S. R.; Sakthikumar, K.; Karthick, K.; Mishra, S.; Kundu, S. Recent Trends and Perspectives in Electrochemical Water Splitting with an Emphasis on Sulfide, Selenide, and Phosphide Catalysts of Fe, Co, and Ni: A Review. *ACS Catal.* **2016**, *6* (12), 8069–8097. https://doi.org/10.1021/acscatal.6b02479.

(10) Schuler, T.; Kimura, T.; Schmidt, T. J.; Büchi, F. N. Towards a Generic Understanding of Oxygen Evolution Reaction Kinetics in Polymer Electrolyte Water Electrolysis. *Energy Environ. Sci.* **2020**, *13* (7), 2153–2166. https://doi.org/10.1039/D0EE00673D.

(11) Xiang, C.; Papadantonakis, K. M.; Lewis, N. S. Principles and Implementations of Electrolysis Systems for Water Splitting. *Mater. Horizons* **2016**, *3* (3), 169–173. https://doi.org/10.1039/C6MH00016A.

(12) Pham, C. Van; Escalera-López, D.; Mayrhofer, K.; Cherevko, S.; Thiele, S. Essentials of High Performance Water Electrolyzers – From Catalyst Layer Materials to Electrode Engineering. *Adv. Energy Mater.* **2021**, *11* (44), 2101998. https://doi.org/10.1002/aenm.202101998.

(13) David, M.; Ocampo-Martínez, C.; Sánchez-Peña, R. Advances in Alkaline Water Electrolyzers: A Review. *J. Energy Storage* **2019**, *23*, 392–403. https://doi.org/10.1016/j.est.2019.03.001.

(14) Bernicke, M. Dissertation: "Mesoporous Oxides as Efficient Catalysts for the Electrocatalytic Oxygen Evolution Reaction (OER)", Technische Universität Berlin, 2016.

(15) You, B.; Sun, Y. Chalcogenide and Phosphide Solid-State Electrocatalysts for Hydrogen Generation. *Chempluschem* **2016**, *81* (10), 1045–1055. https://doi.org/10.1002/cplu.201600029.

(16) Brauns, J.; Turek, T. Alkaline Water Electrolysis Powered by Renewable Energy: A Review. *Processes* **2020**, *8* (2), 248. https://doi.org/10.3390/pr8020248.

(17) Zeng, K.; Zhang, D. Recent Progress in Alkaline Water Electrolysis for Hydrogen Production and Applications. *Prog. Energy Combust. Sci.* **2010**, *36* (3), 307–326. https://doi.org/10.1016/j.pecs.2009.11.002.

(18) Guo, Y.; Li, G.; Zhou, J.; Liu, Y. Comparison between Hydrogen Production by Alkaline Water Electrolysis and Hydrogen Production by PEM Electrolysis. *IOP Conf. Ser. Earth Environ. Sci.* **2019**, *371*, 042022. https://doi.org/10.1088/1755-1315/371/4/042022.

(19) Maurya, S.; Noh, S.; Matanovic, I.; Park, E. J.; Narvaez Villarrubia, C.; Martinez, U.; Han, J.; Bae, C.; Kim, Y. S. Rational Design of Polyaromatic Ionomers for Alkaline Membrane Fuel Cells with >1 W Cm −2 Power Density. *Energy Environ. Sci.* **2018**, *11* (11), 3283–3291. https://doi.org/10.1039/C8EE02192A.

(20) Yan, X.; Biemolt, J.; Zhao, K.; Zhao, Y.; Cao, X.; Yang, Y.; Wu, X.; Rothenberg, G.; Yan, N. A Membrane-Free Flow Electrolyzer Operating at High Current Density Using Earth-Abundant Catalysts for Water Splitting. *Nat. Commun.* **2021**, *12* (1), 4143. https://doi.org/10.1038/s41467-021-24284-5.

(21) Schalenbach, M.; Lueke, W.; Stolten, D. Hydrogen Diffusivity and Electrolyte Permeability of the Zirfon PERL Separator for Alkaline Water Electrolysis. *J. Electrochem. Soc.* **2016**, *163* (14), F1480–F1488. https://doi.org/10.1149/2.1251613jes.

(22) Hartig-Weiss, A.; Miller, M.; Beyer, H.; Schmitt, A.; Siebel, A.; Freiberg, A. T. S.; Gasteiger, H. A.; El-Sayed, H. A. Iridium Oxide Catalyst Supported on Antimony-Doped Tin Oxide for High Oxygen Evolution Reaction Activity in Acidic Media. *ACS Appl. Nano Mater.* **2020**, *3* (3), 2185–2196. https://doi.org/10.1021/acsanm.9b02230.

(23) Barbir, F. PEM Electrolysis for Production of Hydrogen from Renewable Energy Sources. *Sol. Energy* **2005**, *78* (5), 661–669. https://doi.org/10.1016/j.solener.2004.09.003.

(24) Schalenbach, M.; Carmo, M.; Fritz, D. L.; Mergel, J.; Stolten, D. Pressurized PEM Water Electrolysis: Efficiency and Gas Crossover. *Int. J. Hydrogen Energy* **2013**, *38* (35), 14921–14933. https://doi.org/10.1016/j.ijhydene.2013.09.013.

(25) Minke, C.; Suermann, M.; Bensmann, B.; Hanke-Rauschenbach, R. Is Iridium Demand a Potential Bottleneck in the Realization of Large-Scale PEM Water Electrolysis? *Int. J. Hydrogen Energy* **2021**, *46* (46), 23581–23590. https://doi.org/10.1016/j.ijhydene.2021.04.174.

(26) Li, Y.; Fu, Z.-Y.; Su, B.-L. Hierarchically Structured Porous Materials for Energy Conversion and Storage. *Adv. Funct. Mater.* **2012**, *22* (22), 4634–4667. https://doi.org/10.1002/adfm.201200591.

(27) Morris, R. E.; Wheatley, P. S. Gas Storage in Nanoporous Materials. *Angew. Chemie Int. Ed.* **2008**, *47* (27), 4966–4981. https://doi.org/10.1002/anie.200703934.

(28) Liu, Z.; Yuan, X.; Zhang, S.; Wang, J.; Huang, Q.; Yu, N.; Zhu, Y.; Fu, L.; Wang, F.; Chen, Y.; Wu, Y. Three-Dimensional Ordered Porous Electrode Materials for Electrochemical Energy Storage. *NPG Asia Mater.* **2019**, *11* (1), 12. https://doi.org/10.1038/s41427-019-0112-3.

(29) Arruebo, M. Drug Delivery from Structured Porous Inorganic Materials. *WIREs Nanomedicine and Nanobiotechnology* **2012**, *4* (1), 16–30. https://doi.org/10.1002/wnan.132.

(30) Liang, J.; Liang, Z.; Zou, R.; Zhao, Y. Heterogeneous Catalysis in Zeolites, Mesoporous Silica, and Metal-Organic Frameworks. *Adv. Mater.* **2017**, *29* (30), 1701139. https://doi.org/10.1002/adma.201701139.

(31) Wales, D. J.; Grand, J.; Ting, V. P.; Burke, R. D.; Edler, K. J.; Bowen, C. R.; Mintova, S.; Burrows, A. D. Gas Sensing Using Porous Materials for Automotive Applications. *Chem. Soc. Rev.* **2015**, *44* (13), 4290–4321. https://doi.org/10.1039/C5CS00040H.

(32) Sing, K. S. W. Reporting Physisorption Data for Gas/Solid Systems with Special Reference to the Determination of Surface Area and Porosity (Recommendations 1984). *Pure Appl. Chem.* **1985**, *57* (4), 603–619. https://doi.org/10.1351/pac198557040603.

(33) Ma, Z.; Kyotani, T.; Tomita, A. Preparation of a High Surface Area Microporous Carbon Having the Structural Regularity of Y Zeolite. *Chem. Commun.* **2000**, No. 23, 2365–2366. https://doi.org/10.1039/b006295m.

(34) Na, K.; Somorjai, G. A. Hierarchically Nanoporous Zeolites and Their Heterogeneous Catalysis: Current Status and Future Perspectives. *Catal. Letters* **2015**, *145* (1), 193–213. https://doi.org/10.1007/s10562-014-1411-5.

(35) Ledoux, M. J.; Huu, C. P.; Guille, J.; Dunlop, H. Compared Activities of Platinum and High Specific Surface Area Mo2C and WC Catalysts for Reforming ReactionsI. Catalyst Activation and Stabilization: Reaction of n-Hexane. *J. Catal.* **1992**, *134* (2), 383–398. https://doi.org/10.1016/0021-9517(92)90329-G.

(36) Rioux, R. M.; Song, H.; Hoefelmeyer, J. D.; Yang, P.; Somorjai, G. A. High-Surface-Area Catalyst Design: Synthesis, Characterization, and Reaction Studies of Platinum Nanoparticles in Mesoporous SBA-15 Silica. *J. Phys. Chem. B* **2005**, *109* (6), 2192–2202. https://doi.org/10.1021/jp048867x.

(37) Salanne, M.; Rotenberg, B.; Naoi, K.; Kaneko, K.; Taberna, P.-L.; Grey, C. P.; Dunn, B.; Simon, P. Efficient Storage Mechanisms for Building Better Supercapacitors. *Nat. Energy* **2016**, *1* (6), 16070. https://doi.org/10.1038/nenergy.2016.70.

(38) Klechikov, A.; Mercier, G.; Sharifi, T.; Baburin, I. A.; Seifert, G.; Talyzin, A. V. Hydrogen Storage in High Surface Area Graphene Scaffolds. *Chem. Commun.* **2015**, *51* (83), 15280–15283. https://doi.org/10.1039/C5CC05474E.

(39) Li, S.; Zhao, Z.; Ma, T.; Pachfule, P.; Thomas, A. Superstructures of Organic–Polyoxometalate Co-crystals as Precursors for Hydrogen Evolution Electrocatalysts. *Angew. Chemie Int. Ed.* **2021**. https://doi.org/10.1002/anie.202112298.

(40) Han, L.; Dong, C.; Zhang, C.; Gao, Y.; Zhang, J.; Gao, H.; Wang, Y.; Zhang, Z. Dealloying-Directed Synthesis of Efficient Mesoporous CoFe-Based Catalysts towards the Oxygen Evolution Reaction and Overall Water Splitting. *Nanoscale* **2017**, *9* (42), 16467–16475. https://doi.org/10.1039/C7NR06254K.

(41) Bernicke, M.; Ortel, E.; Reier, T.; Bergmann, A.; Ferreira de Araujo, J.; Strasser, P.; Kraehnert, R. Iridium Oxide Coatings with Templated Porosity as Highly Active Oxygen Evolution Catalysts: Structure-Activity Relationships. *ChemSusChem* **2015**, *8* (11), 1908–1915. https://doi.org/10.1002/cssc.201402988.

(42) Oh, I.-H.; Nomura, N.; Masahashi, N.; Hanada, S. Mechanical Properties of Porous Titanium Compacts Prepared by Powder Sintering. *Scr. Mater.* **2003**, *49* (12), 1197–1202. https://doi.org/10.1016/j.scriptamat.2003.08.018.

(43) Baeza, A.; Ruiz-Molina, D.; Vallet-Regí, M. Recent Advances in Porous Nanoparticles for Drug Delivery in Antitumoral Applications: Inorganic Nanoparticles and Nanoscale Metal-Organic Frameworks. *Expert Opin. Drug Deliv.* **2017**, *14* (6), 783–796. https://doi.org/10.1080/17425247.2016.1229298.

(44) Hu, J.; Jiang, R.; Zhang, H.; Guo, Y.; Wang, J.; Wang, J. Colloidal Porous Gold Nanoparticles. *Nanoscale* **2018**, *10* (39), 18473–18481. https://doi.org/10.1039/C8NR06149A.

(45) Cui, S.; Cheng, W.; Shen, X.; Fan, M.; Russell, A. (Ted); Wu, Z.; Yi, X. Mesoporous Amine-Modified SiO2 Aerogel: A Potential CO2 Sorbent. *Energy Environ. Sci.* **2011**, *4* (6), 2070. https://doi.org/10.1039/c0ee00442a.

(46) Mu, P.; Bai, W.; Zhang, Z.; He, J.; Sun, H.; Zhu, Z.; Liang, W.; Li, A. Robust Aerogels Based on Conjugated Microporous Polymer Nanotubes with Exceptional Mechanical Strength for Efficient Solar Steam Generation. *J. Mater. Chem. A* **2018**, *6* (37), 18183–18190. https://doi.org/10.1039/C8TA05698F.

(47) Shpigel, N.; Sigalov, S.; Malchik, F.; Levi, M. D.; Girshevitz, O.; Khalfin, R. L.; Aurbach, D. Quantification of Porosity in Extensively Nanoporous Thin Films in Contact with Gases and Liquids. *Nat. Commun.* **2019**, *10* (1), 4394. https://doi.org/10.1038/s41467-019-12277-4.

(48) Kumar, P.; Kim, K.-H.; Vellingiri, K.; Samaddar, P.; Kumar, P.; Deep, A.; Kumar, N. Hybrid Porous Thin Films: Opportunities and Challenges for Sensing Applications. *Biosens. Bioelectron.* **2018**, *104*, 120–137. https://doi.org/10.1016/j.bios.2018.01.006.

(49) Baumann, A. E.; Burns, D. A.; Liu, B.; Thoi, V. S. Metal-Organic Framework Functionalization and Design Strategies for Advanced Electrochemical Energy Storage Devices. *Commun. Chem.* **2019**, *2* (1), 86. https://doi.org/10.1038/s42004-019-0184-6.

(50) Xia, Y.; Yang, Z.; Mokaya, R. Templated Nanoscale Porous Carbons. *Nanoscale* **2010**, *2* (5), 639. https://doi.org/10.1039/b9nr00207c.

(51) Mahoney, L.; Koodali, R. Versatility of Evaporation-Induced Self-Assembly (EISA) Method for Preparation of Mesoporous TiO2 for Energy and Environmental Applications. *Materials (Basel).* **2014**, *7* (4), 2697–2746. https://doi.org/10.3390/ma7042697.

(52) Brinker, C. J.; Lu, Y.; Sellinger, A.; Fan, H. Evaporation-Induced Self-Assembly: Nanostructures Made Easy. *Adv. Mater.* **1999**, *11* (7), 579–585. https://doi.org/10.1002/(SICI)1521-4095(199905)11:7<579::AID-ADMA579>3.0.CO;2-R.

(53) Rumplecker, A.; Kleitz, F.; Salabas, E.-L.; Schüth, F. Hard Templating Pathways for the Synthesis of Nanostructured Porous Co3O4. *Chem. Mater.* **2007**, *19* (3), 485–496. https://doi.org/10.1021/cm0610635.

(54) Janson, C.; Palmqvist, A. E. C. Improved Oxygen Reduction Activity of Transition Metal-Chelating Ordered Mesoporous Carbon Fuel Cell Catalysts by Milder Template Removal. *Catal. Letters* **2019**, *149* (5), 1297–1304. https://doi.org/10.1007/s10562-019-02694-x.

(55) Zhou, X.-L.; Zhang, H.; Shao, L.-M.; Lü, F.; He, P.-J. Preparation and Application of Hierarchical Porous Carbon Materials from Waste and Biomass: A Review. *Waste and Biomass Valorization* **2021**, *12* (4), 1699–1724. https://doi.org/10.1007/s12649-020-01109-y.

(56) Roberts, A. D.; Li, X.; Zhang, H. Porous Carbon Spheres and Monoliths: Morphology Control, Pore Size Tuning and Their Applications as Li-Ion Battery Anode Materials. *Chem. Soc. Rev.* **2014**, *43* (13), 4341–4356. https://doi.org/10.1039/C4CS00071D.

(57) Niu, B.; Wang, X.; Wu, K.; He, X.; Zhang, R. Mesoporous Titanium Dioxide: Synthesis and Applications in Photocatalysis, Energy and Biology. *Materials (Basel).* **2018**, *11* (10), 1910. https://doi.org/10.3390/ma11101910.

(58) Marcos-Hernández, M.; Villagrán, D. Mesoporous Composite Nanomaterials for Dye Removal and Other Applications. In *Composite Nanoadsorbents*; Elsevier, 2019; pp 265–293. https://doi.org/10.1016/B978-0-12-814132-8.00012-5.

(59) Brinker, C. J. Evaporation-Induced Self-Assembly: Functional Nanostructures Made Easy. *MRS Bull.* **2004**, *29* (9), 631–640. https://doi.org/10.1557/mrs2004.183.

(60) Hartmann, S.; Sachse, A.; Galarneau, A. Challenges and Strategies in the Synthesis of Mesoporous Alumina Powders and Hierarchical Alumina Monoliths. *Materials (Basel).* **2012**, *5* (12), 336–349. https://doi.org/10.3390/ma5020336.

(61) Zhou, X.; Zhu, Y.; Luo, W.; Ren, Y.; Xu, P.; Elzatahry, A. A.; Cheng, X.; Alghamdi, A.; Deng, Y.; Zhao, D. Chelation-Assisted Soft-Template Synthesis of Ordered Mesoporous Zinc Oxides for Low Concentration Gas Sensing. *J. Mater. Chem. A* **2016**, *4* (39), 15064–15071. https://doi.org/10.1039/C6TA05687C.

(62) Ortel, E.; Reier, T.; Strasser, P.; Kraehnert, R. Mesoporous IrO2 Films Templated by PEO-PB-PEO Block-Copolymers: Self-Assembly, Crystallization Behavior, and Electrocatalytic Performance. *Chem. Mater.* **2011**, *23* (13), 3201–3209. https://doi.org/10.1021/cm200761f.

(63) Bernsmeier, D.; Sachse, R.; Bernicke, M.; Schmack, R.; Kettemann, F.; Polte, J.; Kraehnert, R. Outstanding Hydrogen Evolution Performance of Supported Pt Nanoparticles: Incorporation of Preformed Colloids into Mesoporous Carbon Films. *J. Catal.* **2019**, *369*, 181–189. https://doi.org/10.1016/j.jcat.2018.11.006.

(64) Menzel, N.; Ortel, E.; Mette, K.; Kraehnert, R.; Strasser, P. Dimensionally Stable Ru/Ir/TiO2 - Anodes with Tailored Mesoporosity for Efficient Electrochemical Chlorine Evolution. *ACS Catal.* **2013**, *3* (6), 1324–1333. https://doi.org/10.1021/cs4000238.

(65) De, S.; Malik, S.; Ghosh, A.; Saha, R.; Saha, B. A Review on Natural Surfactants. *RSC Adv.* **2015**, *5* (81), 65757–65767. https://doi.org/10.1039/C5RA11101C.

(66) Sanchez, C.; Rozes, L.; Ribot, F.; Laberty-Robert, C.; Grosso, D.; Sassoye, C.; Boissiere, C.; Nicole, L. "Chimie Douce": A Land of Opportunities for the Designed Construction of Functional Inorganic and Hybrid Organic-Inorganic Nanomaterials. *Comptes Rendus Chim.* **2010**, *13* (1–2), 3–39. https://doi.org/10.1016/j.crci.2009.06.001.

(67) Jain, N.; Trabelsi, S.; Guillot, S.; McLoughlin, D.; Langevin, D.; Letellier, P.; Turmine, M. Critical Aggregation Concentration in Mixed Solutions of Anionic Polyelectrolytes and Cationic Surfactants. *Langmuir* **2004**, *20* (20), 8496–8503. https://doi.org/10.1021/la0489918.

(68) Scarpelli, F.; Mastropietro, T. F.; Poerio, T.; Godbert, N. Mesoporous TiO2 Thin Films: State of the Art. In *Titanium Dioxide - Material for a Sustainable Environment*; InTech, 2018. https://doi.org/10.5772/intechopen.74244.

(69) Hammouda, B. Temperature Effect on the Nanostructureof SDS Micelles in Water. *J. Res. Natl. Inst. Stand. Technol.* **2013**, *118*, 151. https://doi.org/10.6028/jres.118.008.

(70) Nagarajan, R.; Ganesh, K. Comparison of Solubilization of Hydrocarbons in (PEO–PPO) Diblock versus (PEO–PPO–PEO) Triblock Copolymer Micelles. *J. Colloid Interface Sci.* **1996**, *184* (2), 489–499. https://doi.org/10.1006/jcis.1996.0644.

(71) Ortel, E.; Fischer, A.; Chuenchom, L.; Polte, J.; Emmerling, F.; Smarsly, B.; Kraehnert, R. New Triblock Copolymer Templates, PEO-PB-PEO, for the Synthesis of Titania Films with Controlled Mesopore Size, Wall Thickness, and Bimodal Porosity. *Small* **2012**, *8* (2), 298–309. https://doi.org/10.1002/smll.201101520.

(72) Bernsmeier, D.; Bernicke, M.; Schmack, R.; Sachse, R.; Paul, B.; Bergmann, A.; Strasser, P.; Ortel, E.; Kraehnert, R. Oxygen Evolution Catalysts Based on Ir-Ti Mixed Oxides with Templated Mesopore Structure: Impact of Ir on Activity and Conductivity. *ChemSusChem* **2018**, *11* (14), 2367–2374. https://doi.org/10.1002/cssc.201800932.

(73) Grosso, D. How to Exploit the Full Potential of the Dip-Coating Process to Better Control Film Formation. *J. Mater. Chem.* **2011**, *21* (43), 17033. https://doi.org/10.1039/c1jm12837j.

(74) Wei, J.; Li, Y.; Wang, M.; Yue, Q.; Sun, Z.; Wang, C.; Zhao, Y.; Deng, Y.; Zhao, D. A Systematic Investigation of the Formation of Ordered Mesoporous Silicas Using Poly(Ethylene Oxide)-b-Poly(Methyl Methacrylate) as the Template. *J. Mater. Chem. A* **2013**, *1* (31), 8819. https://doi.org/10.1039/c3ta11469d.

(75) Yang, P.; Zhao, D.; Margolese, D. I.; Chmelka, B. F.; Stucky, G. D. Generalized Syntheses of Large-Pore Mesoporous Metal Oxides with Semicrystalline Frameworks. *Nature* **1998**, *396* (6707), 152–155. https://doi.org/10.1038/24132.

(76) Brezesinski, T.; Groenewolt, M.; Gibaud, A.; Pinna, N.; Antonietti, M.; Smarsly, B. Evaporation-Induced Self-Assembly (EISA) at Its Limit: Ultrathin, Crystalline Patterns by Templating of Micellar Monolayers. *Adv. Mater.* **2006**, *18* (17), 2260–2263. https://doi.org/10.1002/adma.200600258.

(77) Brezesinski, T.; Groenewolt, M.; Antonietti, M.; Smarsly, B. Crystal-to-Crystal Phase Transition in Self-Assembled Mesoporous Iron Oxide Films. *Angew. Chemie Int. Ed.* **2006**, *45* (5), 781–784. https://doi.org/10.1002/anie.200502332.

(78) Eckhardt, B.; Ortel, E.; Bernsmeier, D.; Polte, J.; Strasser, P.; Vainio, U.; Emmerling, F.; Kraehnert, R. Micelle-Templated Oxides and Carbonates of Zinc, Cobalt, and Aluminum and a Generalized Strategy for Their Synthesis. *Chem. Mater.* **2013**, *25* (14), 2749–2758. https://doi.org/10.1021/cm400535d.

(79) Bernicke, M.; Eckhardt, B.; Lippitz, A.; Ortel, E.; Bernsmeier, D.; Schmack, R.; Kraehnert, R. Synthesis and OER Activity of NiO Coatings with Micelle-Templated Mesopore Structure. *ChemistrySelect* **2016**, *1* (3), 482–489. https://doi.org/10.1002/slct.201600110.

(80) Bagheri, S.; Muhd Julkapli, N.; Bee Abd Hamid, S. Titanium Dioxide as a Catalyst Support in Heterogeneous Catalysis. *Sci. World J.* **2014**, *2014*, 1–21. https://doi.org/10.1155/2014/727496.

(81) Hoffmann, M. R.; Martin, S. T.; Choi, W.; Bahnemann, D. W. Environmental Applications of Semiconductor Photocatalysis. *Chem. Rev.* **1995**, *95* (1), 69–96. https://doi.org/10.1021/cr00033a004.

(82) Carboni, D.; Marongiu, D.; Rassu, P.; Pinna, A.; Amenitsch, H.; Casula, M.; Marcelli, A.; Cibin, G.; Falcaro, P.; Malfatti, L.; Innocenzi, P. Enhanced Photocatalytic Activity in Low-Temperature Processed Titania Mesoporous Films. *J. Phys. Chem. C* **2014**, *118* (22), 12000–12009. https://doi.org/10.1021/jp501653x.

(83) Li, W.; Wu, Z.; Wang, J.; Elzatahry, A. A.; Zhao, D. A Perspective on Mesoporous TiO2 Materials. *Chem. Mater.* **2014**, *26* (1), 287–298. https://doi.org/10.1021/cm4014859.

(84) Zhou, W.; Li, W.; Wang, J.-Q.; Qu, Y.; Yang, Y.; Xie, Y.; Zhang, K.; Wang, L.; Fu, H.; Zhao, D. Ordered Mesoporous Black TiO2 as Highly Efficient Hydrogen Evolution Photocatalyst. *J. Am. Chem. Soc.* **2014**, *136* (26), 9280–9283. https://doi.org/10.1021/ja504802q.

(85) Srivastava, A.; Deepa, M.; Bhandari, S.; Fuess, H. Tunable Nanostructures and Crystal Structures in Titanium Oxide Films. *Nanoscale Res. Lett.* **2009**, *4* (1), 54. https://doi.org/10.1007/s11671-008-9202-9.

(86) Bai, J.; Zhou, B. Titanium Dioxide Nanomaterials for Sensor Applications. *Chem. Rev.* **2014**, *114* (19), 10131–10176. https://doi.org/10.1021/cr400625j.

(87) Luttrell, T.; Halpegamage, S.; Tao, J.; Kramer, A.; Sutter, E.; Batzill, M. Why Is Anatase a Better Photocatalyst than Rutile? - Model Studies on Epitaxial TiO2 Films. *Sci. Rep.* **2015**, *4* (1), 4043. https://doi.org/10.1038/srep04043.

(88) Karlsson, R. K. B.; Cornell, A.; Pettersson, L. G. M. The Electrocatalytic Properties of Doped TiO2. *Electrochim. Acta* **2015**, *180*, 514–527. https://doi.org/10.1016/j.electacta.2015.08.101.

(89) Karlsson, R. K. B.; Hansen, H. A.; Bligaard, T.; Cornell, A.; Pettersson, L. G. M. Ti Atoms in Ru0.3Ti0.7O2 Mixed Oxides Form Active and Selective Sites for Electrochemical Chlorine Evolution. *Electrochim. Acta* **2014**, *146*, 733–740. https://doi.org/10.1016/j.electacta.2014.09.056.

(90) Hansen, H. A.; Man, I. C.; Studt, F.; Abild-Pedersen, F.; Bligaard, T.; Rossmeisl, J. Electrochemical Chlorine Evolution at Rutile Oxide (110) Surfaces. *Phys. Chem. Chem. Phys.* **2010**, *12* (1), 283–290. https://doi.org/10.1039/B917459A.

(91) Chang, J.-H.; Wang, Y.-L.; Dong, C.-D.; Shen, S.-Y. Electrocatalytic Degradation of Azo Dye by Vanadium-Doped TiO2 Nanocatalyst. *Catalysts* **2020**, *10* (5), 482. https://doi.org/10.3390/catal10050482.

(92) Li, B.; Zhu, X.; Wang, J.; Xing, R.; Liu, Q.; Shi, X.; Luo, Y.; Liu, S.; Niu, X.; Sun, X. Ti3+ Self-Doped TiO2−x Nanowires for Efficient Electrocatalytic N2 Reduction to NH3. *Chem. Commun.* **2020**, *56* (7), 1074–1077. https://doi.org/10.1039/C9CC08971C.

(93) Schlicht, S.; Büttner, P.; Bachmann, J. Highly Active Ir/TiO2 Electrodes for the Oxygen Evolution Reaction Using Atomic Layer Deposition on Ordered Porous Substrates. *ACS Appl. Energy Mater.* **2019**, *2* (3), 2344–2349. https://doi.org/10.1021/acsaem.9b00402.

(94) Hu, W.; Chen, S.; Xia, Q. IrO2/Nb–TiO2 Electrocatalyst for Oxygen Evolution Reaction in Acidic Medium. *Int. J. Hydrogen Energy* **2014**, *39* (13), 6967–6976. https://doi.org/10.1016/j.ijhydene.2014.02.114.

(95) Genova-Koleva, R. V.; Alcaide, F.; Álvarez, G.; Cabot, P. L.; Grande, H.-J.; Martínez-Huerta, M. V.; Miguel, O. Supporting IrO2 and IrRuOx Nanoparticles on TiO2 and Nb-Doped TiO2 Nanotubes as Electrocatalysts for the Oxygen Evolution Reaction. *J. Energy Chem.* **2019**, *34*, 227–239. https://doi.org/10.1016/j.jechem.2019.03.008.

(96) Hao, C.; Lv, H.; Mi, C.; Song, Y.; Ma, J. Investigation of Mesoporous Niobium-Doped TiO2 as an Oxygen Evolution Catalyst Support in an SPE Water Electrolyzer. *ACS Sustain. Chem. Eng.* **2016**, *4* (3), 746–756. https://doi.org/10.1021/acssuschemeng.5b00531.

(97) Jiang, Y.; Sun, W.; Xu, B.; Yan, M.; Bahlawane, N. Unusual Enhancement in Electrical Conductivity of Tin Oxide Thin Films with Zinc Doping. *Phys. Chem. Chem. Phys.* **2011**, *13* (13), 5760. https://doi.org/10.1039/c0cp00816h.

(98) Böhm, D.; Beetz, M.; Schuster, M.; Peters, K.; Hufnagel, A. G.; Döblinger, M.; Böller, B.; Bein, T.; Fattakhova-Rohlfing, D. Efficient OER Catalyst with Low Ir Volume Density Obtained by Homogeneous Deposition of Iridium Oxide Nanoparticles on Macroporous Antimony-Doped Tin Oxide Support. *Adv. Funct. Mater.* **2020**, *30* (1), 1906670. https://doi.org/10.1002/adfm.201906670.

(99) Lv, Y.; Yang, C.; Wang, H.; Zhang, J.; Xiang, Y.; Lu, S. Antimony-Doped Tin Oxide as an Efficient Electrocatalyst toward the VO 2+ / VO2 + Redox Couple of the Vanadium Redox Flow Battery. *Catal. Sci. Technol.* **2020**, *10* (8), 2484–2490. https://doi.org/10.1039/C9CY01793C.

(100) Geiger, S.; Kasian, O.; Mingers, A. M.; Mayrhofer, K. J. J.; Cherevko, S. Stability Limits of Tin-Based Electrocatalyst Supports. *Sci. Rep.* **2017**, *7* (1), 4595. https://doi.org/10.1038/s41598-017-04079-9.

(101) Han, S.-B.; Mo, Y.-H.; Lee, Y.-S.; Lee, S.-G.; Park, D.-H.; Park, K.-W. Mesoporous Iridium Oxide/Sb-Doped SnO2 Nanostructured Electrodes for Polymer Electrolyte Membrane Water Electrolysis. *Int. J. Hydrogen Energy* **2020**, *45* (3), 1409–1416. https://doi.org/10.1016/j.ijhydene.2019.11.109.

(102) Chen, W.-F.; Muckerman, J. T.; Fujita, E. Recent Developments in Transition Metal Carbides and Nitrides as Hydrogen Evolution Electrocatalysts. *Chem. Commun.* **2013**, *49* (79), 8896. https://doi.org/10.1039/c3cc44076a.

(103) Ko, A.-R.; Lee, Y.-W.; Moon, J.-S.; Han, S.-B.; Cao, G.; Park, K.-W. Ordered Mesoporous Tungsten Carbide Nanoplates as Non-Pt Catalysts for Oxygen Reduction Reaction. *Appl. Catal. A Gen.* **2014**, *477*, 102–108. https://doi.org/10.1016/j.apcata.2014.02.034.

(104) Gotoh, Y.; Fujimura, K.; Koike, M.; Ohkoshi, Y.; Nagura, M.; Akamatsu, K.; Deki, S. Synthesis of Titanium Carbide from a Composite of TiO2 Nanoparticles/Methyl Cellulose by Carbothermal Reduction. *Mater. Res. Bull.* **2001**, *36* (13–14), 2263–2275. https://doi.org/10.1016/S0025-5408(01)00713-9.

(105) Shanmugam, S.; Jacob, D. S.; Gedanken, A. Solid State Synthesis of Tungsten Carbide Nanorods and Nanoplatelets by a Single-Step Pyrolysis. *J. Phys. Chem. B* **2005**, *109* (41), 19056–19059. https://doi.org/10.1021/jp0540003.

(106) Kurlov, A. S.; Gusev, A. I. *Tungsten Carbides*; Springer Series in Materials Science; Springer International Publishing: Cham, 2013; Vol. 184. https://doi.org/10.1007/978-3-319-00524-9.

(107) Yan, Z.; Cai, M.; Shen, P. K. Nanosized Tungsten Carbide Synthesized by a Novel Route at Low Temperature for High Performance Electrocatalysis. *Sci. Rep.* **2013**, *3* (1), 1646. https://doi.org/10.1038/srep01646.

(108) Ma, C.; Sheng, J.; Brandon, N.; Zhang, C.; Li, G. Preparation of Tungsten Carbide-Supported Nano Platinum Catalyst and Its Electrocatalytic Activity for Hydrogen Evolution. *Int. J. Hydrogen Energy* **2007**, *32* (14), 2824–2829. https://doi.org/10.1016/j.ijhydene.2006.12.022.

(109) Han, N.; Yang, K. R.; Lu, Z.; Li, Y.; Xu, W.; Gao, T.; Cai, Z.; Zhang, Y.; Batista, V. S.; Liu, W.; Sun, X. Nitrogen-Doped Tungsten Carbide Nanoarray as an Efficient Bifunctional Electrocatalyst for Water Splitting in Acid. *Nat. Commun.* **2018**, *9* (1), 924. https://doi.org/10.1038/s41467-018-03429-z.

(110) Li, S.; Chen, B.; Wang, Y.; Ye, M.-Y.; van Aken, P. A.; Cheng, C.; Thomas, A. Oxygen-Evolving Catalytic Atoms on Metal Carbides. *Nat. Mater.* **2021**, *20* (9), 1240–1247. https://doi.org/10.1038/s41563-021-01006-2.

(111) Bernicke, M.; Bernsmeier, D.; Paul, B.; Schmack, R.; Bergmann, A.; Strasser, P.; Ortel, E.; Kraehnert, R. Tailored Mesoporous Ir/TiOx: Identification of Structure-Activity Relationships for an Efficient Oxygen Evolution Reaction. *J. Catal.* **2019**, *376*, 209–218. https://doi.org/10.1016/j.jcat.2019.06.044.

(112) Deng, X.; Öztürk, S.; Weidenthaler, C.; Tüysüz, H. Iron-Induced Activation of Ordered Mesoporous Nickel Cobalt Oxide Electrocatalyst for the Oxygen Evolution Reaction. *ACS Appl. Mater. Interfaces* **2017**, *9* (25), 21225–21233. https://doi.org/10.1021/acsami.7b02571.

(113) Yu, M.; Moon, G.; Bill, E.; Tüysüz, H. Optimizing Ni–Fe Oxide Electrocatalysts for Oxygen Evolution Reaction by Using Hard Templating as a Toolbox. *ACS Appl. Energy Mater.* **2019**, *2* (2), 1199–1209. https://doi.org/10.1021/acsaem.8b01769.

(114) Trotochaud, L.; Young, S. L.; Ranney, J. K.; Boettcher, S. W. Nickel–Iron Oxyhydroxide Oxygen-Evolution Electrocatalysts: The Role of Intentional and Incidental Iron Incorporation. *J. Am. Chem. Soc.* **2014**, *136* (18), 6744–6753. https://doi.org/10.1021/ja502379c.

(115) Spanos, I.; Masa, J.; Zeradjanin, A.; Schlögl, R. The Effect of Iron Impurities on Transition Metal Catalysts for the Oxygen Evolution Reaction in Alkaline Environment: Activity Mediators or Active Sites? *Catal. Letters* **2021**, *151* (7), 1843–1856. https://doi.org/10.1007/s10562-020-03478-4.

(116) Dionigi, F.; Zhu, J.; Zeng, Z.; Merzdorf, T.; Sarodnik, H.; Gliech, M.; Pan, L.; Li, W.; Greeley, J.; Strasser, P. Intrinsic Electrocatalytic Activity for Oxygen Evolution of Crystalline 3d-Transition Metal Layered Double Hydroxides. *Angew. Chemie* **2021**, *133* (26), 14567–14578. https://doi.org/10.1002/ange.202100631.

(117) Burke, M. S.; Zou, S.; Enman, L. J.; Kellon, J. E.; Gabor, C. A.; Pledger, E.; Boettcher, S. W. Revised Oxygen Evolution Reaction Activity Trends for First-Row Transition-Metal (Oxy)Hydroxides in Alkaline Media. *J. Phys. Chem. Lett.* **2015**, *6* (18), 3737–3742. https://doi.org/10.1021/acs.jpclett.5b01650.

(118) Johnson, R. W.; Hultqvist, A.; Bent, S. F. A Brief Review of Atomic Layer Deposition: From Fundamentals to Applications. *Mater. Today* **2014**, *17* (5), 236–246. https://doi.org/10.1016/j.mattod.2014.04.026.

(119) George, S. M. Atomic Layer Deposition: An Overview. *Chem. Rev.* **2010**, *110* (1), 111–131. https://doi.org/10.1021/cr900056b.

(120) Marichy, C.; Bechelany, M.; Pinna, N. Atomic Layer Deposition of Nanostructured Materials for Energy and Environmental Applications. *Adv. Mater.* **2012**, *24* (8), 1017–1032. https://doi.org/10.1002/adma.201104129.

(121) Marichy, C.; Pinna, N. Atomic Layer Deposition to Materials for Gas Sensing Applications. *Adv. Mater. Interfaces* **2016**, *3* (21), 1600335. https://doi.org/10.1002/admi.201600335.

(122) Li, X.; Liu, J.; Banis, M. N.; Lushington, A.; Li, R.; Cai, M.; Sun, X. Atomic Layer Deposition of Solid-State Electrolyte Coated Cathode Materials with Superior High-Voltage Cycling Behavior for Lithium Ion Battery Application. *Energy Environ. Sci.* **2014**, *7* (2), 768–778. https://doi.org/10.1039/C3EE42704H.

(123) Christensen, S. T.; Feng, H.; Libera, J. L.; Guo, N.; Miller, J. T.; Stair, P. C.; Elam, J. W. Supported Ru−Pt Bimetallic Nanoparticle Catalysts Prepared by Atomic Layer Deposition. *Nano Lett.* **2010**, *10* (8), 3047–3051. https://doi.org/10.1021/nl101567m.

(124) Liu, R.; Lin, Y.; Chou, L.-Y.; Sheehan, S. W.; He, W.; Zhang, F.; Hou, H. J. M.; Wang, D. Water Splitting by Tungsten Oxide Prepared by Atomic Layer Deposition and Decorated with an Oxygen-Evolving Catalyst. *Angew. Chemie Int. Ed.* **2011**, *50* (2), 499–502. https://doi.org/10.1002/anie.201004801.

(125) Yang, H.; Chen, Y.; Qin, Y. Application of Atomic Layer Deposition in Fabricating High-Efficiency Electrocatalysts. *Chinese J. Catal.* **2020**, *41* (2), 227–241. https://doi.org/10.1016/S1872-2067(19)63440-6.

(126) Clancey, J. W.; Cavanagh, A. S.; Kukreja, R. S.; Kongkanand, A.; George, S. M. Atomic Layer Deposition of Ultrathin Platinum Films on Tungsten Atomic Layer Deposition Adhesion Layers: Application to High Surface Area Substrates. *J. Vac. Sci. Technol. A Vacuum, Surfaces, Film.* **2015**, *33* (1), 01A130. https://doi.org/10.1116/1.4901459.

(127) Seo, E. K.; Lee, J. W.; Sung-Suh, H. M.; Sung, M. M. Atomic Layer Deposition of Titanium Oxide on Self-Assembled-Monolayer-Coated Gold. *Chem. Mater.* **2004**, *16* (10), 1878–1883. https://doi.org/10.1021/cm035140x.

(128) Kim, D.-H.; Kim, Y. J.; Song, Y. S.; Lee, B.-T.; Kim, J. H.; Suh, S.; Gordon, R. Characteristics of Tungsten Carbide Films Prepared by Plasma-Assisted ALD Using Bis(Tert-Butylimido)Bis(Dimethylamido)Tungsten. *J. Electrochem. Soc.* **2003**, *150* (10), C740. https://doi.org/10.1149/1.1610000.

(129) Richey, N. E.; de Paula, C.; Bent, S. F. Understanding Chemical and Physical Mechanisms in Atomic Layer Deposition. *J. Chem. Phys.* **2020**, *152* (4), 040902. https://doi.org/10.1063/1.5133390.

(130) Matienzo, D. D.; Settipani, D.; Instuli, E.; Kallio, T. Active IrO2 and NiO Thin Films Prepared by Atomic Layer Deposition for Oxygen Evolution Reaction. *Catalysts* **2020**, *10* (1), 92. https://doi.org/10.3390/catal10010092.

(131) Schlicht, S.; Haschke, S.; Mikhailovskii, V.; Manshina, A.; Bachmann, J. Highly Reversible Water Oxidation at Ordered Nanoporous Iridium Electrodes Based on an Original Atomic Layer Deposition. *ChemElectroChem* **2018**, *5* (9), 1259–1264. https://doi.org/10.1002/celc.201800152.

(132) Wang, S.; Zhang, J.; Gharbi, O.; Vivier, V.; Gao, M.; Orazem, M. E. Electrochemical Impedance Spectroscopy. *Nat. Rev. Methods Prim.* **2021**, *1* (1), 41. https://doi.org/10.1038/s43586-021-00039-w.

(133) Chang, B.-Y.; Park, S.-M. Electrochemical Impedance Spectroscopy. *Annu. Rev. Anal. Chem.* **2010**, *3* (1), 207–229. https://doi.org/10.1146/annurev.anchem.012809.102211.

(134) Lanfredi, S.; Rodrigues, A. C. M. Impedance Spectroscopy Study of the Electrical Conductivity and Dielectric Constant of Polycrystalline LiNbO3. *J. Appl. Phys.* **1999**, *86* (4), 2215–2219. https://doi.org/10.1063/1.371033.

(135) Raistrick, I. D.; Franceschetti, D. R.; Macdonald, J. R. *Impedance Spectroscopy: Theory, Experiment, and Applications*; Macdonald, J. R., Barsoukov, E., Eds.; Wiley-VCH, New-York, 2005. https://doi.org/10.1002/0471716243.ch2.

(136) Choi, W.; Shin, H.-C.; Kim, J. M.; Choi, J.-Y.; Yoon, W.-S. Modeling and Applications of Electrochemical Impedance Spectroscopy (EIS) for Lithium-Ion Batteries. *J. Electrochem. Sci. Technol.* **2020**, *11* (1), 1–13. https://doi.org/10.33961/jecst.2019.00528.

(137) Cesiulis, H.; Tsyntsaru, N.; Ramanavicius, A.; Ragoisha, G. *The Study of Thin Films by Electrochemical Impedance Spectroscopy, in: Tiginyanu I., Topala P., Ursaki V. (Eds) Nanostructures and Thin Films for Multifunctional Applications*; Springer, Cham, 2016. https://doi.org/10.1007/978-3-319-30198-3_1.

(138) Ishige, R. Precise Structural Analysis of Polymer Materials Using Synchrotron X-Ray Scattering and Spectroscopic Methods. *Polym. J.* **2020**, *52* (9), 1013–1026. https://doi.org/10.1038/s41428-020-0357-2.

(139) Bouroushian, M.; Kosanovic, T. Characterization of Thin Films by Low Incidence X-Ray Diffraction. *Cryst. Struct. Theory Appl.* **2012**, *01* (03), 35–39. https://doi.org/10.4236/csta.2012.13007.

(140) Schamp, C. T.; Jesser, W. A. On the Measurement of Lattice Parameters in a Collection of Nanoparticles by Transmission Electron Diffraction. *Ultramicroscopy* **2005**, *103* (2), 165–172. https://doi.org/10.1016/j.ultramic.2004.11.007.

(141) Kresse, G.; Joubert, D. From Ultrasoft Pseudopotentials to the Projector Augmented-Wave Method. *Phys. Rev. B* **1999**, *59* (3), 1758–1775. https://doi.org/10.1103/PhysRevB.59.1758.

(142) Kresse, G.; Hafner, J. Ab Initio Molecular Dynamics for Liquid Metals. *Phys. Rev. B* **1993**, *47* (1), 558–561. https://doi.org/10.1103/PhysRevB.47.558.

(143) Kresse, G.; Furthmüller, J. Efficient Iterative Schemes for Ab Initio Total-Energy Calculations Using a Plane-Wave Basis Set. *Phys. Rev. B* **1996**, *54* (16), 11169–11186. https://doi.org/10.1103/PhysRevB.54.11169.

(144) Deringer, V. L.; Tchougréeff, A. L.; Dronskowski, R. Crystal Orbital Hamilton Population (COHP) Analysis As Projected from Plane-Wave Basis Sets. *J. Phys. Chem. A* **2011**, *115* (21), 5461–5466. https://doi.org/10.1021/jp202489s.

(145) Bauerfeind, K. C. L.; Laun, J.; Frisch, M.; Kraehnert, R.; Bredow, T. Metal Substitution in Rutile TiO2: Segregation Energy and Conductivity. *J. Electron. Mater.* **2021**. https://doi.org/10.1007/s11664-021-09318-4.

(146) Carey, J. J.; McKenna, K. P. Screening Doping Strategies To Mitigate Electron Trapping at Anatase TiO2 Surfaces. *J. Phys. Chem. C* **2019**, *123* (36), 22358–22367. https://doi.org/10.1021/acs.jpcc.9b05840.

(147) Estrellan, C. R.; Salim, C.; Hinode, H. Photocatalytic Decomposition of Perfluorooctanoic Acid by Iron and Niobium Co-Doped Titanium Dioxide. *J. Hazard. Mater.* **2010**, *179* (1–3), 79–83. https://doi.org/10.1016/j.jhazmat.2010.02.060.

(148) Böhm, D.; Beetz, M.; Gebauer, C.; Bernt, M.; Schröter, J.; Kornherr, M.; Zoller, F.; Bein, T.; Fattakhova-Rohlfing, D. Highly Conductive Titania Supported Iridium Oxide Nanoparticles with Low Overall Iridium Density as OER Catalyst for Large-Scale PEM Electrolysis. *Appl. Mater. Today* **2021**, *24*, 101134. https://doi.org/10.1016/j.apmt.2021.101134.

(149) Hämäläinen, J.; Kemell, M.; Munnik, F.; Kreissig, U.; Ritala, M.; Leskelä, M. Atomic Layer Deposition of Iridium Oxide Thin Films from Ir(Acac)3 and Ozone. *Chem. Mater.* **2008**, *20* (9), 2903–2907. https://doi.org/10.1021/cm7030224.

(150) Oakton, E.; Lebedev, D.; Povia, M.; Abbott, D. F.; Fabbri, E.; Fedorov, A.; Nachtegaal, M.; Copéret, C.; Schmidt, T. J. IrO2-TiO2 : A High-Surface-Area, Active, and Stable Electrocatalyst for the Oxygen Evolution Reaction. *ACS Catal.* **2017**, *7* (4), 2346–2352. https://doi.org/10.1021/acscatal.6b03246.

(151) Esposito, D. V.; Hunt, S. T.; Kimmel, Y. C.; Chen, J. G. A New Class of Electrocatalysts for Hydrogen Production from Water Electrolysis: Metal Monolayers Supported on Low-Cost Transition Metal Carbides. *J. Am. Chem. Soc.* **2012**, *134* (6), 3025–3033. https://doi.org/10.1021/ja208656v.

(152) Wang, H.; Zhu, S.; Deng, J.; Zhang, W.; Feng, Y.; Ma, J. Transition Metal Carbides in Electrocatalytic Oxygen Evolution Reaction. *Chinese Chem. Lett.* **2021**, *32* (1), 291–298. https://doi.org/10.1016/j.cclet.2020.02.018.

(153) Karimi, F.; Peppley, B. A. Metal Carbide and Oxide Supports for Iridium-Based Oxygen Evolution Reaction Electrocatalysts for Polymer-Electrolyte-Membrane Water Electrolysis. *Electrochim. Acta* **2017**, *246*, 654–670. https://doi.org/10.1016/j.electacta.2017.06.048.

(154) Liu, Y.; Kelly, T. G.; Chen, J. G.; Mustain, W. E. Metal Carbides as Alternative Electrocatalyst Supports. *ACS Catal.* **2013**, *3* (6), 1184–1194. https://doi.org/10.1021/cs4001249.

(155) Wang, S.-J.; Wang, M.-C.; Chen, S.-F.; Li, Y.-H.; Shen, T.-S.; Bor, H.-Y.; Wei, C.-N. Electrical and Physical Characteristics of WO3/Ag/WO3 Sandwich Structure Fabricated with Magnetic-Control Sputtering Metrology †. *Sensors* **2018**, *18* (9), 2803. https://doi.org/10.3390/s18092803.

(156) Kraffert, K.; Karg, M.; Schmack, R.; Clavel, G.; Boissiere, C.; Wirth, T.; Pinna, N.; Kraehnert, R. Stabilization of Mesoporous Iron Oxide Films against Sintering and Phase Transformations via Atomic Layer Deposition of Alumina and Silica. *Adv. Mater. Interfaces* **2018**, *5* (14), 1800360. https://doi.org/10.1002/admi.201800360.

(157) Flood, H.; Förland, T.; Sillén, L. G.; Linnasalmi, A.; Laukkanen, P. The Acidic and Basic Properties of Oxides. *Acta Chem. Scand.* **1947**, *1*, 592–604. https://doi.org/10.3891/acta.chem.scand.01-0592.

(158) Pagán-Torres, Y. J.; Gallo, J. M. R.; Wang, D.; Pham, H. N.; Libera, J. A.; Marshall, C. L.; Elam, J. W.; Datye, A. K.; Dumesic, J. A. Synthesis of Highly Ordered Hydrothermally Stable Mesoporous Niobia Catalysts by Atomic Layer Deposition. *ACS Catal.* **2011**, *1* (10), 1234–1245. https://doi.org/10.1021/cs200367t.

(159) Hu, S.; Shaner, M. R.; Beardslee, J. A.; Lichterman, M.; Brunschwig, B. S.; Lewis, N. S. Amorphous TiO2 Coatings Stabilize Si, GaAs, and GaP Photoanodes for Efficient Water Oxidation. *Science* **2014**, *344* (6187), 1005–1009. https://doi.org/10.1126/science.1251428.

(160) Gong, Y.; Palacio, D.; Song, X.; Patel, R. L.; Liang, X.; Zhao, X.; Goodenough, J. B.; Huang, K. Stabilizing Nanostructured Solid Oxide Fuel Cell Cathode with Atomic Layer Deposition. *Nano Lett.* **2013**, *13* (9), 4340–4345. https://doi.org/10.1021/nl402138w.

(161) Fan, Y.; Wu, Y.; Clavel, G.; Raza, M. H.; Amsalem, P.; Koch, N.; Pinna, N. Optimization of the Activity of Ni-Based Nanostructures for the Oxygen Evolution Reaction. *ACS Appl. Energy Mater.* **2018**, *1* (9), 4554–4563. https://doi.org/10.1021/acsaem.8b00666.

(162) Lei, H.; Liang, Y.; Cen, G.; Liu, B.; Tan, S.; Wang, Z.; Mai, W. Atomic Layer Deposited Al2O3 Layer Confinement: An Efficient Strategy to Synthesize Durable MOF-Derived Catalysts toward the Oxygen Evolution Reaction. *Inorg. Chem. Front.* **2021**, *8* (6), 1432–1438. https://doi.org/10.1039/D0QI01317J.

(163) Mattinen, M.; Hämäläinen, J.; Gao, F.; Jalkanen, P.; Mizohata, K.; Räisänen, J.; Puurunen, R. L.; Ritala, M.; Leskelä, M. Nucleation and Conformality of Iridium and Iridium Oxide Thin Films Grown by Atomic Layer Deposition. *Langmuir* **2016**, *32* (41), 10559–10569. https://doi.org/10.1021/acs.langmuir.6b03007.

(164) Spöri, C.; Brand, C.; Kroschel, M.; Strasser, P. Accelerated Degradation Protocols for Iridium-Based Oxygen Evolving Catalysts in Water Splitting Devices. *J. Electrochem. Soc.* **2021**, *168* (3), 034508. https://doi.org/10.1149/1945-7111/abeb61.

(165) Bernt, M.; Hartig-Weiß, A.; Tovini, M. F.; El-Sayed, H. A.; Schramm, C.; Schröter, J.; Gebauer, C.; Gasteiger, H. A. Current Challenges in Catalyst Development for PEM Water Electrolyzers. *Chemie Ing. Tech.* **2020**, *92* (1–2), 31–39. https://doi.org/10.1002/cite.201900101.

A Publication Reprints

A-1 Reprinted Publication [MF-1]:

Bridging Experiment and Theory: Enhancing the Electrical Conductivities of Soft Templated Niobium-Doped Mesoporous Titania Films

M. Frisch*, J. Laun*, J. Marquardt, A. Arinchtein, K. Bauerfeind, D. Bernsmeier, M. Bernicke, T. Bredow, R. Kraehnert

Physical Chemistry Chemical Physics **2021**, *23*, 3219-3224.

https://doi.org/10.1039/d0cp06544g

PCCP

COMMUNICATION

View Article Online
View Journal | View Issue

Cite this: *Phys. Chem. Chem. Phys.*, 2021, **23**, 3219

Received 18th December 2020,
Accepted 29th January 2021

DOI: 10.1039/d0cp06544g

rsc.li/pccp

Bridging experiment and theory: enhancing the electrical conductivities of soft-templated niobium-doped mesoporous titania films†

Marvin Frisch, *[a] Joachim Laun,*[b] Julien Marquardt,[c] Aleks Arinchtein,[a] Katharina Bauerfeind,[b] Denis Bernsmeier,[a] Michael Bernicke,[a] Thomas Bredow[b] and Ralph Kraehnert ‡*[a]

Theoretical calculations suggest a strong dependence of electrical conductivity and doping concentration in transition-metal doped titania. Herein, we present a combined theoretical and experimental approach for the prediction of relative phase stability and electrical conductivity in niobium-doped titania as model system. Our method paves the way towards the development of materials with improved electrical properties.

1. Introduction

The optical and electronic properties of various transition metal oxides have been investigated for decades due to their broad applicability in photo-,[1,2] electro-catalysis,[3–5] photovoltaics[6] and, amongst others, sensing.[7] The oxides of titanium, primarily TiO_2, are of particular importance as a result of their excellent efficiencies in photocatalytic processes, *e.g.* water splitting,[8] water purification[9] or as support materials in electro-catalytic reactions.[10] For TiO_2, the rutile phase is the most stable modification under atmospheric conditions.[11] Different ways to obtain TiO_2 materials in the thermodynamically less stable anatase or brookite phase have been developed and shown to have superior photocatalytic properties compared to rutile, for instance.[12–14]

The semiconducting properties of bare TiO_2 limit its application as support material in electro-catalytic reactions.[10] Aliovalent doping is an important concept to significantly enhance the conductivity of a material. In the case of TiO_2, both n- and p-type doping have been reported in literature.[15,16] The impact of different dopant atoms and concentrations on the photocatalytic activity were theoretically simulated.[15,16] Niobium-doped TiO_2 was shown to exhibit higher activities compared to bare rutile TiO_2 or other transition-metal-doped TiO_2 photo-catalysts.[11,17] By photoemission spectroscopic techniques, the oxidation states of the transition metals were analyzed and correlations with the electrical conductivity of the oxide materials were found.[18,19] Moreover, there is a clear correlation between electrical conductivity and electrochemical activity due to improved charge carrier kinetics lowering the activation barriers of redox reactions at an electrode.[10]

Beside a high electrical conductivity, many applications, *e.g.* as support materials[20] or energy storage materials,[21] demand for nanostructured materials with large surface areas. Mesoporous materials offer high surface-to-volume ratios[22] and are able to promote mass transfer kinetics.[23] Mesoporous doped TiO_2 materials show superior activities as a consequence of their enhanced surface areas and nanostructure.[24,25] Importantly, a fully accessible, interconnected pore network is desirable for catalytic applications. The evaporation-induced self-assembly (EISA) process using an appropriate soft template, *e.g.* a block-copolymer, is a well-established method to produce mesoporous transition metal oxide films of varying thicknesses from several nanometers to micrometers with excellent reproducibility and stoichiometric control.[26] Liu *et al.*[19] synthesized mesoporous Nb-doped TiO_2 films from the assembly of pre-formed nanoparticles. Such inexpensive nanostructured transparent conductive oxides (TCO) were previously shown to improve the photovoltaic performance when applied as photo-anode in dye-sensitized solar cells (DSSCs).[27] Advantageously, an improved electrical conductivity combined with a controlled mesoporosity not only affects the application of titania-based electrodes in photovoltaics,[27] but also in photo-,[28] electro-catalysis[29] and charge storage.[30,31]

Our theoretical studies suggest Nb to be the most promising dopant for improving the electrical conductivity of TiO_2. Even though there are several reports about the synthesis of high surface area Nb-doped TiO_2 nanomaterials with enhanced

[a] *Department of Chemistry, Technische Universität Berlin, Strasse des 17. Juni 124, Berlin D-10623, Germany. E-mail: ralph.kraehnert@tu-berlin.de*
[b] *Mulliken Center for Theoretical Chemistry, Institute of Physical and Theoretical Chemistry, University of Bonn, Beringstr. 4, Bonn D-53115, Germany*
[c] *Federal Institute for Materials Research and Testing (BAM), Richard-Willstätter-Straße 11, Berlin D-12489, Germany*

† Electronic supplementary information (ESI) available. See DOI: 10.1039/d0cp06544g

‡ M. Frisch and J. Laun contributed equally to this work.

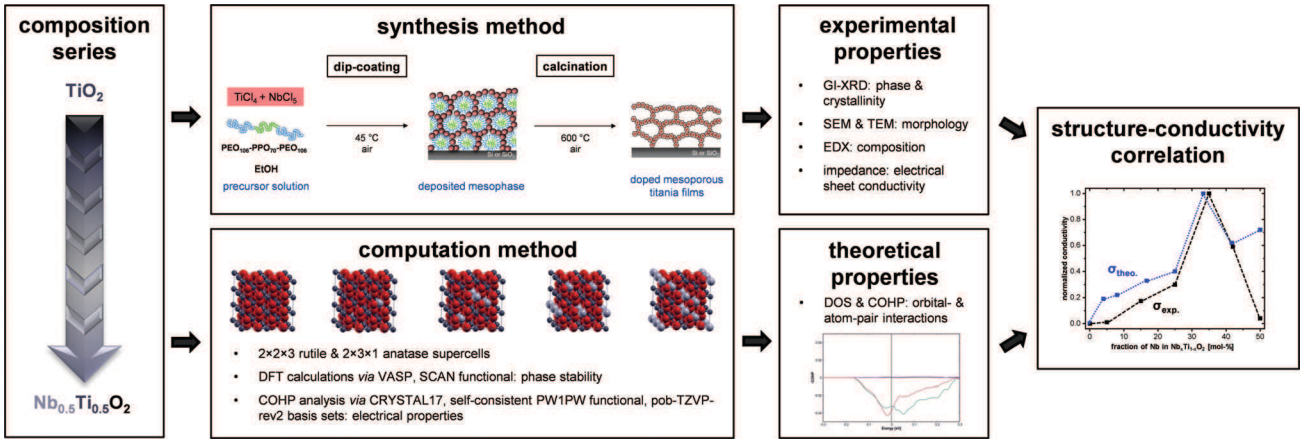

Scheme 1 Combined experimental and computational approach for the analysis of stable phases and electrical conductivity in model-type doped metal oxide systems. Synthesis route for mesoporous $Nb_xTi_{1-x}O_2$ films *via* dip-coating in a controlled atmosphere. The deposited micelle-structured mesophase is converted to a mesoporous $Nb_xTi_{1-x}O_2$ film after calcination and concomitant removal of the soft-template for 30 min at 600 °C in air. The computation method relies on two different approaches. Relative phase stabilities were calculated using VASP/900 eV/SCAN. For the calculation of the electrical properties, a self-consistent hybrid approach with CRYSTAL17/pob-TZVP-rev2/sc-PW1PW was used.

conductivities to date, inconsistent results regarding the exact influence of the dopant ion concentration on phase and electrical conductivity can be found.[31,32]

Herein, we elucidate structure–property relationships based on calculated and experimental results to highlight the correlation between Nb-dopant fraction and electrical conductivity. Scheme 1 provides an overview on the proposed combined experimental and computational approach. In order to establish a model system with systematically varied properties, a composition series of $Nb_xTi_{1-x}O_2$ with Nb-fraction between 0 and 50 mol% was defined. The respective materials were synthesized *via* dip-coating because of its high reproducibility, control of layer thickness and atmosphere during deposition based on evaporation-induced self-assembly. Using such model-type oxides allows the deduction of structure–activity correlations, *e.g.* the impact of electrical conductivity on the electrocatalytic performance in the oxygen evolution reaction,[33,34] as well as fundamental phase formation and transition processes.[35] Herein, we modified a previously reported synthesis route[26] to obtain Nb-doped titania with controlled nanostructure. As precursors, $TiCl_4$ and $NbCl_5$ were dissolved in EtOH, leading to the formation of the corresponding metal ethoxides. A commercially available tri-*block*-copolymer, PEO–PPO–PEO (Pluronic F127), was used as soft-template for the introduction of mesoporosity after oxidative removal *via* calcination at 600 °C. The materials were analyzed *via* electron microscopy (SEM, TEM, EDX), X-ray diffraction (GI-XRD), Raman and impedance spectroscopy to derive physicochemical and electrical properties, in particular the formed crystal phases and the electrical conductivity. For the prediction of phase stability and electrical conductivity *via* DFT calculations, rutile and anatase supercells were proposed, in which Ti atoms were partially replaced by defined numbers of Nb atoms. As explained in the section *Theoretical Calculations* in the **SI**, the relative phase stabilities were calculated using VASP,[36–38] a high energy cut-off of 900 eV and the SCAN[39] functional. The electrical properties were calculated applying a self-consistent hybrid approach using CRYSTAL17[40,41] with pob-TZVP-rev2 basis sets[42,43] and the PW1PW[44] functional (see section *Sheet conductivity* in the **SI** for further explanations). Finally, experimental and theoretical values were compared. The maximum conductivity of the synthesized mesoporous films amounts to 0.0014 S cm^{-1} at 25 °C for 35 mol% Nb in $Nb_xTi_{1-x}O_2$ after calcination of a stabilized mesophase at 600 °C in air. Theoretical calculations suggest a maximum in conductivity for 33 mol% Nb.

2. Results and discussion

2.1. Synthesis of mesoporous $Nb_xTi_{1-x}O_2$ films

The synthesis route schematically illustrated in Scheme 1 affords mp. $Nb_xTi_{1-x}O_2$ materials with macroscopically crack-free, templated porosity extending throughout the entire film volume. Fig. 1 illustrates scanning electron microscopy (SEM) images of a concentration series of mp. $Nb_xTi_{1-x}O_2$ films. The dopant ion concentration can be precisely adjusted by the ratio of the metal precursors. Cross-sectional SEM images (see **SI-1**) reveal the formation of an interconnected pore network and layer thickness between 280 and 320 nm. There is no collapse of the micelle-templated mesoporous structure prior to the crystallization of the oxide materials. The organic block-copolymer template can be successfully removed *via* calcination for 30 min at 600 °C. Energy-dispersive X-ray spectroscopy (EDX) revealed the successful synthesis of mp. $Nb_xTi_{1-x}O_2$ materials with different Nb fractions (see **SI-2**). Notably, the incorporation of Nb atoms into the titania lattice stabilizes the morphology of the templated oxide films.

As representative example, electron microscopic analysis of 35 mol% Nb in $Nb_xTi_{1-x}O_2$ is shown in more detail in Fig. 1. The average pore diameter amounts to 10 ± 2 nm (Fig. 1a) with a local order indicated by a periodic distance of 15 ± 1 nm (fast Fourier transform (FFT); inset Fig. 1a). Cross-section SEM (Fig. 1c and d) indicates a layer thickness of approximately 320 nm and the formation of a homogeneous mesoporous structure which is further corroborated by TEM images (Fig. 1e).

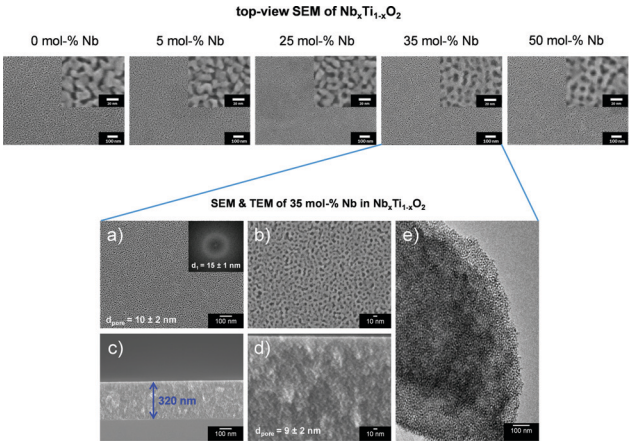

Fig. 1 Top: Electron microscopy of mesoporous $Nb_xTi_{1-x}O_2$ films. Bottom: Electron microscopy of a selected mesoporous film containing 35 mol% Nb; (a and b) Top-view SEM images at different magnifications with corresponding FFT (inset, a). (c and d) Cross-sectional SEM images at different magnifications. A film thickness of 320 nm was evaluated using *ImageJ* software (c). (e) TEM image clearly indicating the mesoporous structure.

2.2. Relative phase stability rutile *vs.* anatase

Experimental results indicate a higher relative phase stability of the rutile phase for increasing Nb fractions >25 mol%, which is evidenced by gracing-incidence X-ray diffraction (GI-XRD) and Raman spectroscopy (see Fig. 2a and b). Due to the polycrystallinity and small crystallite size, broad reflexes were obtained for all $Nb_xTi_{1-x}O_2$ films (*cf.* Fig. 2a). For bare TiO_2, the metastable anatase phase is found in experiment. The diffraction pattern corresponds well to that for anatase TiO_2 and no reflections of rutile TiO_2 can be observed (Fig. 2a). With an increase in Nb fraction, the B_{1g} bands of the anatase phase shift to lower wavenumbers, as already observed by Yue *et al.*[21] This can be explained by the formation of Nb–O–Ti bonds.[21,45] For Nb fractions ≥25 mol%, both Raman and GI-XRD indicate the coexistence of anatase and rutile phases, which is in excellent accordance with theory. For 35 mol%, the rutile phase becomes predominant (*cf.* Fig. 2a and b). A further increase in Nb fraction to 50 mol% leads to a significant decrease in crystallinity, as shown in the corresponding GI-XRD pattern. Raman spectroscopy suggests the predominance of the rutile phase, which, accordingly, is X-ray amorphous. X-ray photoelectron spectroscopy (XPS) was used to investigate the surface composition of the synthesized $Nb_xTi_{1-x}O_2$ materials. As shown in the results in **SI-3**, Nb atoms tend to segregate toward the surface of the nanocrystalline $Nb_xTi_{1-x}O_2$ materials. This surface-segregation is particularly pronounced for 35 mol% Nb in $Nb_xTi_{1-x}O_2$ and leads to an increase in the relative fraction of Ti^{3+} species compared to the other $Nb_xTi_{1-x}O_2$ materials. The stable phases predicted by the computation strongly depend on the dopant fraction, as shown in Fig. 2c. For small fractions <25 mol% Nb, the metastable anatase phase is favored, whereas for increasing Nb fractions, the rutile phase starts to emerge. For a fraction of 33 mol% Nb, the rutile phase is favored by 2.02 kJ mol^{-1} over the anatase phase. Fig. 2d illustrates an overview over the obtained experimental and calculated results regarding phase stability in dependency of dopant fraction. Therein, a very high consistency between experiment and theory is indicated, validating our simplified theoretical DFT approach *via* VASP and SCAN functional (further information given in the Experimental section in the ESI†).

2.3. Impact of Nb fraction on electrical properties of $Nb_xTi_{1-x}O_2$

Significant variations in the electronic properties are expected considering the distinct structural differences for an increasing fraction of Nb. Both theoretical and experimental results show a strong correlation of phase and electrical conductivity of the doped transition metal oxides. A clear trend can be deduced from the data shown in Fig. 3. Bare TiO_2 shows the lowest electrical sheet conductivity (Fig. 3a). Up to a fraction of 35 mol% Nb in $Nb_xTi_{1-x}O_2$, an increase in conductivity of more than three orders of magnitude was experimentally determined, which is in agreement with theoretical calculations based on a substitutional incorporation of Nb ions into the titania lattice. A detailed discussion for the general trend from a theoretical point of view is given in **SI-9**. Mulliken population analyses reveal an increasing occupation of Ti 3d-orbitals, in particular $3d_{z^2}$, $3d_{x^2-y^2}$ and $3d_{xy}$, for increasing Nb-fraction (*cf.* **SI-9**). For a high fraction of 50 mol% Nb, a decreased sheet conductivity was observed, which can be explained by the lower crystallinity and the formation of a solid solution rather than a doped titanium oxide (*cf.* Fig. 2a; **SI-4**). Accordingly, the crystal phase shows a pronounced impact on the electronic properties and a high material's crystallinity is of pivotal importance for high electrical conductivities.

Notably, the mesoporous structure is kept intact at high temperatures up to 600 °C, *i.e.* the incorporation of Nb ions into the titania lattice has a beneficial impact on the morphological stability of the porous network. For bare titania, crystallite growth and sintering effects become pronounced at high temperatures, leading to a loss of templated pore structure. Comparing the experimentally determined values with the theoretical data calculated applying a self-consistent hybrid approach (for further details see section *Sheet conductivity* in the **SI**), the impact of Nb fraction on conductivity is well in line. A maximum conductivity is predicted for a fraction of 33 mol% Nb and rutile phase. The correlation between high crystallinity and electrical conductivity becomes evident for high fractions of 50 mol% Nb. Experimental results show a significantly reduced conductivity compared to theoretical calculations assuming high crystallinity at high Nb fractions up to 50 mol%. In this context, the deviation between experiment and theory for large Nb fractions of 50 mol% (*cf.* Fig. 3a and b) can be explained by the differences in crystallinity. For fractions ≤42 mol% Nb, consistent results between experimental and theoretical conductivities were obtained.

The herein obtained values of more than 10^{-3} S cm^{-1} for mp. $Nb_xTi_{1-x}O_2$ with 35 mol% Nb are, to the best of our knowledge, the highest electrical sheet conductivities for

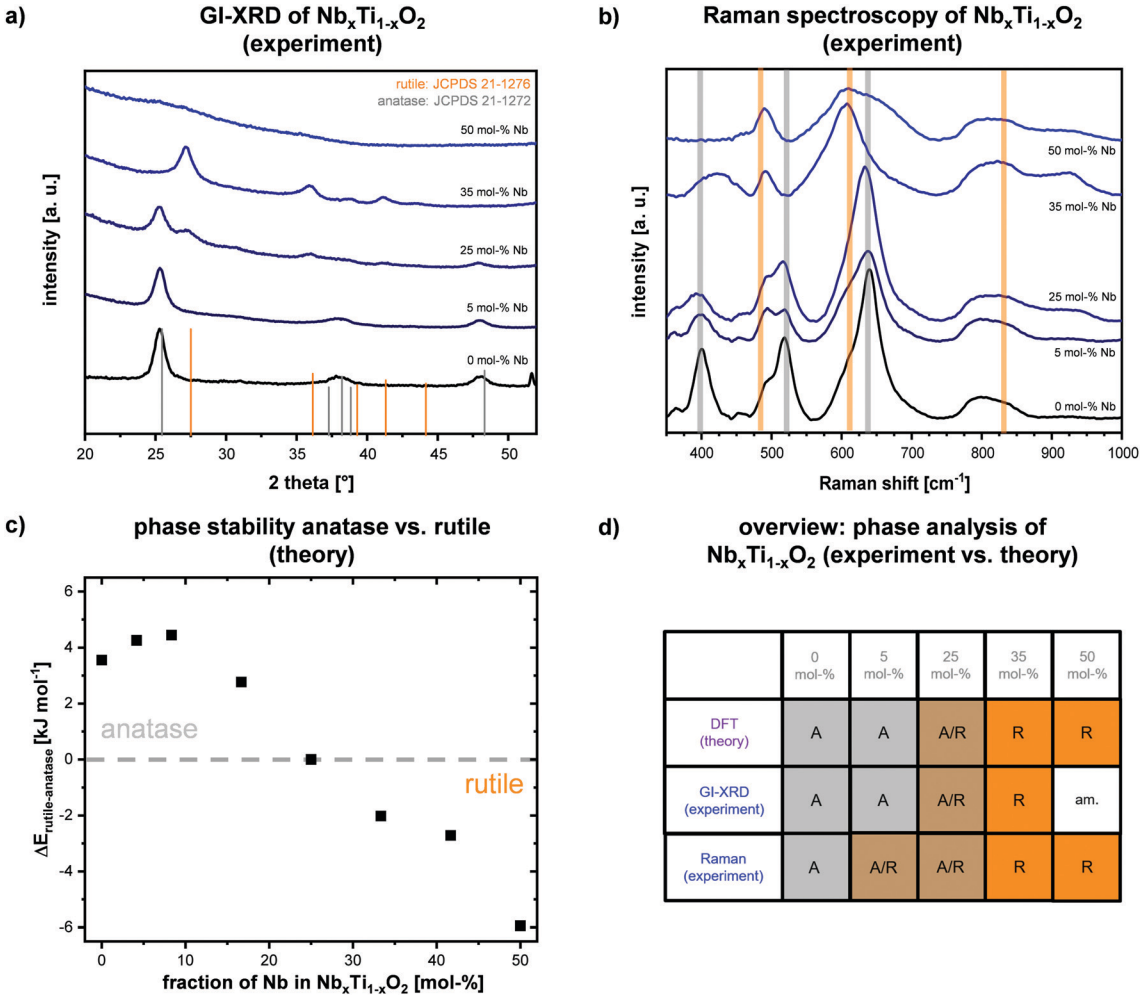

	0 mol-%	5 mol-%	25 mol-%	35 mol-%	50 mol-%
DFT (theory)	A	A	A/R	R	R
GI-XRD (experiment)	A	A	A/R	R	am.
Raman (experiment)	A	A/R	A/R	R	R

Fig. 2 Experimental GI-XRD patterns (a) and Raman spectra (b) of synthesized templated $Nb_xTi_{1-x}O_2$ films in dependency of Nb fraction. Calculated relative phase stabilities of rutile and anatase phase in dependency of Nb fraction (c). Clear indications for an ongoing phase transition from anatase to rutile for Nb >25 mol% in $Nb_xTi_{1-x}O_2$ are given in both experimental and theoretical data in (a–c). In (b), calculated active Raman modes for the rutile (orange) and anatase (grey) phase are illustrated as vertical bars (absolute values are given in **SI-5**). The dotted grey line in (c) represents a guideline to the eye. In (d), an overview over experimentally observed and theoretically calculated phases is given, revealing good consistency of experiment and theory (A = anatase, R = rutile, A/R = mixed phase of anatase and rutile, am. = X-ray amorphous).

mesoporous early-transition-metal doped TiO_2 films. It has to be noted that grain boundaries and the mesoporous structure decrease the electrical conductivity of a material. Similar observations were previously reported by Liu *et al.*[19] who assembled pre-synthesized nanoparticles into mesoporous films *via* dip-coating. Compared to their study showing a maximum in sheet conductivity of 3×10^{-4} S cm^{-1} for a fraction of 20 mol%, our results suggest a maximum electrical conductivity for a higher Nb fraction of 35 mol%. Liu *et al.* found decreased conductivity values for Nb fractions of more than 20 mol%. Importantly, no observations of an emerging rutile phase for higher Nb fractions were reported. A more detailed discussion and comparison with previous reports in literature can be found in **SI-3** in the ESI.† Even though the herein presented DFT results exclusively refer to the bulk properties of the doped oxides, the theoretical calculations coincide well with the observed trends in both relative conductivity and relative phase stability without any consideration of (*meso*-)porosity in the theoretical models. The high crystallinity of the oxides, the independence of the pore size and the interface with insulating air filling the pores underline the dominance of bulk properties (for further explanations see **SI-10**). The herein presented system enables a systematic investigation of structure–property relations. For small fractions of Nb dopants (<10 mol%), theoretical calculations suggest a stronger increase in electrical conductivity (*cf.* Fig. 3b), yet, the general trend is in good agreement. Particularly, the theoretically predicted maximum in conductivity was corroborated by our experimental data and our calculations provide reasonable explanations for the observed behavior, *e.g.* the highest electrical conductivity resulting from a combination of increasing electron density while avoiding Nb–Nb interactions, which can be deduced from quantum chemical calculations (see **SI-9**).

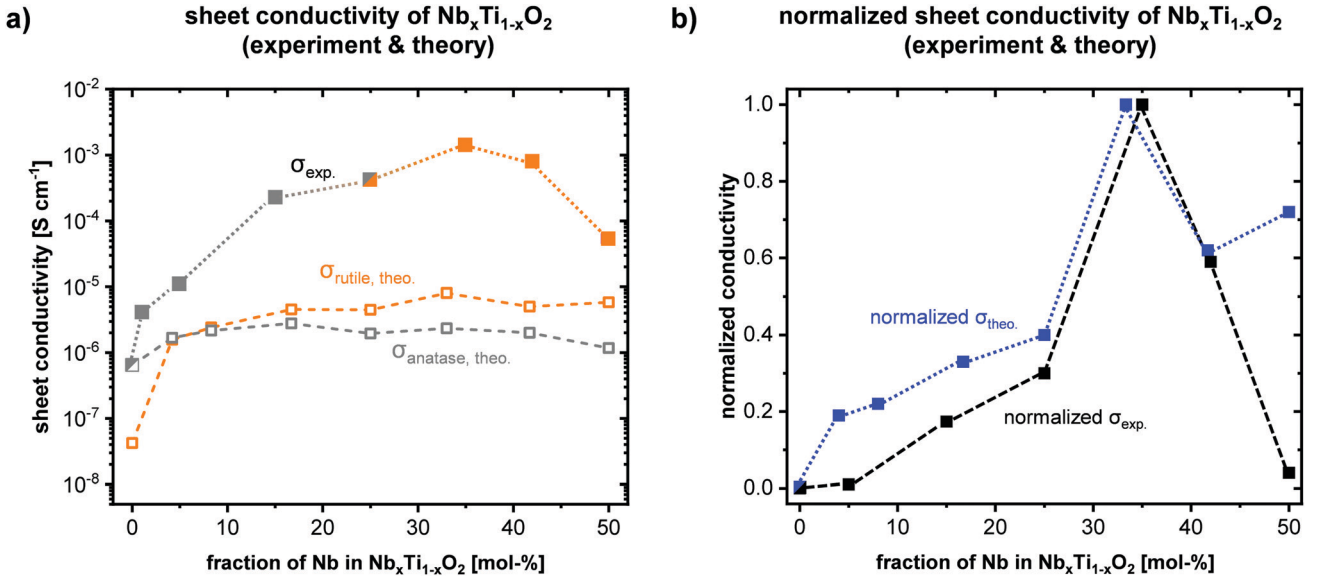

Fig. 3 Calculated and experimental electrical sheet conductivities in dependency of Nb fraction in mp. $Nb_xTi_{1-x}O_2$ films (filled squares: experimentally determined sheet conductivities *via* impedance spectroscopy, open grey squares: calculated values for anatase, open orange squares: calculated values for rutile) (a); normalized calculated and experimental conductivities as function of Nb fraction (b). All values in (a) are given in S cm^{-1}. To ensure comparability between theory and experiment, the calculated conductivity of the bare anatase was set to the experimentally determined sheet conductivity of $6.40 \cdot 10^{-7}$ S cm^{-1} and all calculated conductivities are stated relative to this value. The absolute values of the calculated conductivities are given in **SI-6**. The color code for the experimental data in (a) represents an indication of the respective phase.

3. Conclusions

The herein presented combined experimental and computational approach for the analysis of stable phases and electrical conductivity in model-type doped metal oxide systems synthesized *via* template-assisted dip-coating highlights the most relevant factors to tune the electrical properties of a semiconducting material. As a model system, the impact of Nb fraction on the phase, crystallinity and electrical conductivity of mesoporous titanium oxide films was experimentally and theoretically investigated. Advantageously, the herein presented synthesis concept enables a detailed investigation by the variation of a single parameter, *i.e.* doping concentration. A profound understanding of the correlations between doping concentration, phase stability and electronic properties lead to the synthesis of a high surface area support material which can find promising applications in electro- or photo-catalysis, in which high electrical conductivities and stability are key factors for achieving a superior performance. Importantly, our model system is not limited to Nb-doped titania, but can also be extended to other dopants such as Y^{3+}, for instance. As such, a new highly effective screening method is presented which may help to identify suitable materials for applications in electro- or photo-(electro-)catalysis.

Author contributions

M. Frisch* and J. Laun* contributed equally to this work. M. F. contributed to all experimental aspects of data analysis and interpretation. J. L. contributed to all theoretical aspects, simulations and interpretation of the calculated data. M. F. & J. L. contributed to the writing and editing of the manuscript. J. M. performed Raman spectroscopic measurements and evaluated the data. A. A., D. B. and M. B. aided in the design of synthesis protocols of the templated mesoporous films. A. A. contributed to GI-XRD analyses. K. B. contributed to the calculations of relative phase stability and Raman spectra. T. B. & R. K. conceived the study, contributed to the writing and editing of the manuscript.

Conflicts of interest

There are no conflicts to declare.

Acknowledgements

The authors thank ZELMI (TU Berlin) for access to TEM and SAED analyses and gratefully acknowledge financial support by BMBF (Bundesministerium für Bildung und Forschung) *ATO-KAT: Atomar dünn beschichtete poröse Elektroden als neuartige Katalysatoren für die Wasser-Elektrolyse* (03EK3052A). Jörg Radnik (BAM, Berlin) is thankfully acknowledged for XPS analyses. The authors acknowledge also preliminary tests by Paulina Kalle at TU Berlin and the support of Benjamin Paul (TU Berlin) in the building of a setup for impedance spectroscopy measurements of thin films in the dark.

Notes and references

1 A. Fujishima, X. Zhang and D. Tryk, *Surf. Sci. Rep.*, 2008, **63**, 515–582.
2 S.-Y. Lee and S.-J. Park, *J. Ind. Eng. Chem.*, 2013, **19**, 1761–1769.

3 J. M. Macak, P. J. Barczuk, H. Tsuchiya, M. Z. Nowakowska, A. Ghicov, M. Chojak, S. Bauer, S. Virtanen, P. J. Kulesza and P. Schmuki, *Electrochem. Commun.*, 2005, **7**, 1417–1422.
4 S. Shanmugam and A. Gedanken, *Small*, 2007, **3**, 1189–1193.
5 H.-J. Kim, D.-Y. Kim, H. Han and Y.-G. Shul, *J. Power Sources*, 2006, **159**, 484–490.
6 W. M. Campbell, A. K. Burrell, D. L. Officer and K. W. Jolley, *Coord. Chem. Rev.*, 2004, **248**, 1363–1379.
7 H.-M. Lin, C.-H. Keng and C.-Y. Tung, *Nanostruct. Mater.*, 1997, **9**, 747–750.
8 M. Ni, M. K. H. Leung, D. Y. C. Leung and K. Sumathy, *Renewable Sustainable Energy Rev.*, 2007, **11**, 401–425.
9 R. W. Matthews, *Sol. Energy*, 1987, **38**, 405–413.
10 Z.-X. Lu, Y. Shi, C.-F. Yan, C.-Q. Guo and Z.-D. Wang, *Int. J. Hydrogen Energy*, 2017, **42**, 3572–3578.
11 W. Yan and X. Liu, *Inorg. Chem.*, 2019, **58**, 3090–3098.
12 S. C. Pillai, P. Periyat, R. George, D. E. McCormack, M. K. Seery, H. Hayden, J. Colreavy, D. Corr and S. J. Hinder, *J. Phys. Chem. C*, 2007, **111**, 1605–1611.
13 K. Lv, J. Yu, L. Cui, S. Chen and M. Li, *J. Alloys Compd.*, 2011, **509**, 4557–4562.
14 A. Di Paola, M. Bellardita and L. Palmisano, *Catalysts*, 2013, **3**, 36–73.
15 M. V. Dozzi and E. Selli, *J. Photochem. Photobiol., C*, 2013, **14**, 13–28.
16 G. Liu, Y. Zhao, C. Sun, F. Li, G. Q. Lu and H.-M. Cheng, *Angew. Chem., Int. Ed.*, 2008, **47**, 4516–4520.
17 L. Kong, C. Wang, H. Zheng, X. Zhang and Y. Liu, *J. Phys. Chem. C*, 2015, **119**, 16623–16632.
18 M. S. Dabney, M. F. A. M. van Hest, C. W. Teplin, S. P. Arenkiel, J. D. Perkins and D. S. Ginley, *Thin Solid Films*, 2008, **516**, 4133–4138.
19 Y. Liu, J. M. Szeifert, J. M. Feckl, B. Mandlmeier, J. Rathousky, O. Hayden, D. Fattakhova-Rohlfing and T. Bein, *ACS Nano*, 2010, **4**, 5373–5381.
20 F. Hu, F. Ding, S. Song and P. K. Shen, *J. Power Sources*, 2006, **163**, 415–419.
21 J. Yue, C. Suchomski, P. Voepel, R. Ellinghaus, M. Rohnke, T. Leichtweiss, M. T. Elm and B. M. Smarsly, *J. Mater. Chem. A*, 2017, **5**, 1978–1988.
22 M. Vallet-Regí, F. Balas and D. Arcos, *Angew. Chem., Int. Ed.*, 2007, **46**, 7548–7558.
23 J. Kärger and D. Freude, *Chem. Eng. Technol.*, 2002, **25**, 769–778.
24 X. Fan, X. Chen, S. Zhu, Z. Li, T. Yu, J. Ye and Z. Zou, *J. Mol. Catal. A: Chem.*, 2008, **284**, 155–160.
25 J. B. Yin and X. P. Zhao, *Chem. Mater.*, 2002, **14**, 4633–4640.
26 E. Ortel, A. Fischer, L. Chuenchom, J. Polte, F. Emmerling, B. Smarsly and R. Kraehnert, *Small*, 2012, **8**, 298–309.
27 X. Lü, X. Mou, J. Wu, D. Zhang, L. Zhang, F. Huang, F. Xu and S. Huang, *Adv. Funct. Mater.*, 2010, **20**, 509–515.
28 H. Liu, H. Gong, M. Zou, H. Jiang, R. S. Abolaji, A. K. Tareen, B. V. Hakala and M. Yang, *Mater. Res. Bull.*, 2017, **96**, 10–17.
29 L. Chevallier, A. Bauer, S. Cavaliere, R. Hui, J. Rozière and D. J. Jones, *ACS Appl. Mater. Interfaces*, 2012, **4**, 1752–1759.
30 Y. Tanaka, H. Usui, Y. Domi, M. Ohtani, K. Kobiro and H. Sakaguchi, *ACS Appl. Energy Mater.*, 2019, **2**, 636–643.
31 Y. Wang, B. M. Smarsly and I. Djerdj, *Chem. Mater.*, 2010, **22**, 6624–6631.
32 C. Hao, H. Lv, C. Mi, Y. Song and J. Ma, *ACS Sustainable Chem. Eng.*, 2016, **4**, 746–756.
33 M. Bernicke, D. Bernsmeier, B. Paul, R. Schmack, A. Bergmann, P. Strasser, E. Ortel and R. Kraehnert, *J. Catal.*, 2019, **376**, 209–218.
34 M. Bernicke, E. Ortel, T. Reier, A. Bergmann, J. Ferreira de Araujo, P. Strasser and R. Kraehnert, *ChemSusChem*, 2015, **8**, 1908–1915.
35 K. Schulz, R. Schmack, H. W. Klemm, A. Kabelitz, T. Schmidt, F. Emmerling and R. Kraehnert, *Chem. Mater.*, 2017, **29**, 1724–1734.
36 G. Kresse and D. Joubert, *Phys. Rev. B: Condens. Matter Mater. Phys.*, 1999, **59**, 1758–1775.
37 G. Kresse and J. Furthmüller, *Phys. Rev. B: Condens. Matter Mater. Phys.*, 1996, **54**, 11169–11186.
38 G. Kresse and J. Hafner, *Phys. Rev. B: Condens. Matter Mater. Phys.*, 1993, **47**, 558–561.
39 J. Sun, A. Ruzsinszky and J. P. Perdew, *Phys. Rev. Lett.*, 2015, **115**, 036402.
40 R. Dovesi, A. Erba, R. Orlando, C. M. Zicovich-Wilson, B. Civalleri, L. Maschio, M. Rérat, S. Casassa, J. Baima, S. Salustro and B. Kirtman, *Wiley Interdiscip. Rev.: Comput. Mol. Sci.*, 2018, **8**, 1360.
41 S. C. R. Dovesi, V. R. Saunders, C. Roetti, R. Orlando, C. M. Zicovich-Wilson, F. Pascale, B. Civalleri, K. Doll, N. M. Harrison, I. J. Bush, P. D'Arco, M. Llunell, M. Causà, Y. Noël, L. Maschio, A. Erba and M. Rerat, *CRYSTAL17 User's Manual*, University of Torino, 2017.
42 D. Vilela Oliveira, J. Laun, M. F. Peintinger and T. Bredow, *J. Comput. Chem.*, 2019, **40**, 2364–2376.
43 J. Laun, D. Vilela Oliveira and T. Bredow, *J. Comput. Chem.*, 2018, **39**, 1285–1290.
44 T. Bredow and A. R. Gerson, *Phys. Rev. B: Condens. Matter Mater. Phys.*, 2000, **61**, 5194–5201.
45 L. De Trizio, R. Buonsanti, A. M. Schimpf, A. Llordes, D. R. Gamelin, R. Simonutti and D. J. Milliron, *Chem. Mater.*, 2013, **25**, 3383–3390.

Bridging Experiment and Theory: Enhancing the Electrical Conductivities of Soft-Templated Niobium-doped Mesoporous Titania Films

Marvin Frisch[a], Joachim Laun*[b], Julien Marquardt[c], Aleks Arinchtein[a], Katharina Bauerfeind[b], Denis Bernsmeier[a], Michael Bernicke[a], Thomas Bredow[b] and Ralph Kraehnert†[a]*

[a]Department of Chemistry
Technical University of Berlin
Strasse des 17. Juni 124, D-10623 Berlin, Germany
†E-mail: ralph.kraehnert@tu-berlin.de

[b]Mulliken Center for Theoretical Chemistry, Institute of Physical and Theoretical Chemistry, University of Bonn
Beringstr. 4, D-53115 Bonn, Germany
E-mail: bredow@thch.uni-bonn.de

[c]Federal Institute for Materials Research and Testing (BAM)
Richard-Willstätter-Straße 11, D-12489 Berlin

Table of Contents

Experimental Section

Theoretical Calculations

For the presented DFT calculations, we applied two different approaches. On the one hand, relative phase stabilities were calculated using VASP[1–3]/900 eV/SCAN[4]. SCAN is a reasonable choice to calculate highly accurate thermodynamic and structural properties. On the other hand, meta-GGA functionals are not able to accurately describe the electronic structure, in particular the electronic band gap and the resulting electrical conductivity. For this reason, we have chosen a self-consistent hybrid approach with CRYSTAL17[5,6] based on the hybrid functional PW1PW[7] for the calculation of these properties, on the other hand. All computational details of both approaches are explicitly described in the following chapters.

To obtain the relative phase stability and the corresponding electronic sheet conductivity, 2×2×3 rutile and 2×3×1 anatase supercells were simulated. Each supercell was comprised of 24 stoichiometric units and Ti atoms were partially substituted by 1, 2, 4, 6, 8, 10 or 12 Nb atoms. All configurations show a maximum distribution of the substitute and are given in **SI-7&8**.

Relative phase stability

The density functional theory (DFT) calculations for the relative phase stabilities of rutile and anatase phase were performed with the Vienna *ab initio* program (VASP)[1–3] version 5.4.4 using the projector-augmented wave (PAW) approach of Joubert and Kresse.[8,9] The respective POTCAR files containing the PAW parameters were extracted from the VASP library. The PAWs with the largest valence-space available denoted as Ti_sv_GW (12 valence electrons (VE), $3s^2 3p^6 4s^2 4d^2$), Nb_sv_GW (13 VE, $3s^2 3p^6 4s^2 4d^3$) and O_GW (6 VE, $2s^2 3p^4$), which include the semi-core *s* and *p* shells, were applied. While keeping the symmetry, full structure relaxations were performed using the strongly constrained and appropriately normed (SCAN) functional[4], a *k*-spacing of 0.2 A^{-1} and a 900 eV energy cutoff to expand the Kohn-Sham

orbitals into plane wave basis sets. In the DFT calculations, most exchange-correlation functionals significantly over-stabilize the anatase phase compared to the rutile phase. Computationally expensive methods such as the random phase approximation (RPA)[10] or Diffusion Monte Carlo (DMC)[11] are able the predict the experimental phase stability[12] of rutile with respect to anatase of -2.61 ± 0.41 kJ mol^{-1} but are not feasible due to their prohibitive cost scaling. It is well-known that *meta*-GGA functionals such as SCAN systematically underestimate the electronic band gap for TiO_2 phases.[13] Nevertheless, SCAN is a reasonable choice to predict highly accurate thermodynamic and structural properties especially for semiconducting materials with reasonable computational effort.[14–16] The calculated relative phase stability of rutile vs. anatase of 3.56 kJ mol^{-1} per formula is in excellent agreement with the former DFT study of Sun *et al.*[13] showing values of 2.5 kJ mol^{-1} (SCAN), 9.1 kJ mol^{-1} (PBE) and 8.4 kJ mol^{-1} (HSE).

Sheet conductivity

To calculate the electrical sheet conductivities in dependency of Nb fraction in $Nb_xTi_{1-x}O_2$, DFT calculations were performed with the CRYSTAL17 program package version 1.0.2.[5,6] For global hybrid functional calculations the electronic band structure and the resulting electronic conductivity strongly depend on the system-independent Fock exchange fraction. Previous work[17–20] has shown that the dielectric-dependent self-consistent hybrid methods[21] provide high accuracy for electronic band gaps and absolute band positions. Therefore, we used the fully-automated algorithm[22] for the determination of the system-specific optimal Fock exchange for the PW1PW functional[7] as implemented in CRYSTAL17. The resulting Fock exchange is given as 15.1 % for the pure rutile, 18.0 % for the pure anatase phase and 0 % for all substituted phases. For undoped titania, this follows previous results[17] showing that the use of hybrid functionals is necessary for semiconducting oxides in order to obtain an accurate description of electronic band gaps. Since all substituted phases have a metallic ground state as

a consequence of n-type doping, the dielectric constant increases to large values during the self-consistent procedure and results in the pure PWGGA functional.

While keeping the respective symmetry, full structural relaxations were carried out using the self-consistent PW1PW functional, all-electron Gaussian-type basis sets for Ti and O[23], and ECP basis set[24] for Nb of triple-zeta with polarization quality. To reach SCF convergence for all conducting states we used a 8×8×8 Monkhorst-Pack grid and a denser 16×16×16 Gilat net for all optimizations. The truncation criteria for bi-electronic integrals were set to 10^{-7} for the overlap and penetration threshold for the Coulomb integrals and for the overlap threshold for HF exchange integrals. For the pseudo overlap in the HF exchange series, the truncation criteria were set to 10^{-14} and 10^{-42}. The SCF accuracy was set to 10^{-7} a. u. for optimizations of geometry.

To estimate the electrical conductivity, we used the Boltzmann transport equation in relaxation time approximation as implemented as BOLTZTRA[6] in CRYSTAL17. We used a denser 12×12×12 Monkhorst-Pack grid, a 24×24×24 Gilat net and a relaxation time parameter of 10 fs to calculate the electrical conductivity at the Fermi level at 25 °C. The calculated conductivity is by definition a 3×3 tensor for a three-dimensional system, so we averaged the diagonal elements and discarded the small off-diagonal elements.

We have noticed that the calculated absolute conductivities are very sensitive to the density of the applied *k*-point grid. However, it was not possible to reach convergence due to computational effort. A reliable indicator to evaluate the electronic structure and the resulting conductivity is the fundamental band gap. With the applied method, the calculated fundamental band gaps of rutile (3.1 eV) and anatase (3.7 eV) are in good agreement with experimental results for rutile, 3.3-3.6 eV[25,26], and for anatase, 3.7-3.9 eV[27–29].

To gain a deeper insight in the electronic structure and the qualitative dependency of the electrical conductivity, we have additionally performed density of state (DOS) calculations as well as crystal orbital Hamiltonian population (COHP)[30] analyses, which provide a straightforward view into orbital- or atom-pair interactions such as bonding and antibonding

states and interaction strengths. These methods require a local description of the electronic structure in terms of atom-centered orbitals, which then allow the formation of the Hamiltonian matrix. For this reason, CRYSTAL17 is the perfect choice for COHP analyses, as it expands crystalline orbitals from atom-centered contracted Gaussian basis functions.[31] For the electrical conductivity, the bands near the Fermi level are of special interest, which are for the given substituted rutile phases primarily dominated by the metal *d*-orbitals or, more precisely, the $d_{x^2-y^2}$-orbitals showing a major contribution. Thus, we calculated the DOS and, additionally, the projected DOS (PDOS), as a Mulliken population weighted DOS, projected on the elements and all *d*-orbitals. For the COHP analyses, the interactions within the nearest neighbor atom-pairs Nb-Nb, Ti-Ti and Nb-Ti, as well as their corresponding $d_{x^2-y^2}$-orbitals, were computed, respectively. By convention, all COHP plots showing bonding (stabilizing) contributions show positive signs and antibonding (destabilizing) contributions show negative signs and are further denoted as -COHP. All PDOS and COHP calculations were performed in a range of ± 0.3 eV around the Fermi energy with identical settings as for the conductivity. The resulting plots are given in **SI-9**.

Raman Spectroscopy

In order to predict Raman spectra of bulk rutile and anatase phases, we performed vibrational frequency calculations (FREQCALC) using the CRYSTAL17 code with the PW1PW functional and the mentioned basis sets and truncation criteria. Hybrid DFT calculations have shown to predict highly accurate vibrational frequencies and corresponding Raman intensities for crystalline compounds.[32–35] For the calculated Raman intensities, the effects of the temperature at 25 °C and the wavelength of the incident beam of 633 nm were taken into account *via* RAMEXP. The calculated active Raman modes are illustrated as vertical bars in **Figure 2b** in the manuscript and the calculated values can be found in **SI-5** in the Supporting Information.

Experimental Details

Synthesis of soft-templated mesoporous $Nb_xTi_{1-x}O_2$ films

For the synthesis of mesoporous $Nb_xTi_{1-x}O_2$ films, niobium(V)chloride ($NbCl_5$, 99%) was purchased from *Alfa Aesar*, titanium(IV)chloride ($TiCl_4$, 99.9 %) and ethanol p. a. (EtOH, ≥ 99.8 %) were purchased from *VWR Chemicals*. Pluronic F-127 (PEO_{106}–PPO_{70}–PEO_{106}, M_w = 12 600 g mol^{-1}) was purchased from *Sigma-Aldrich*. All chemicals were used as received without any further purification. In a typical synthesis, 0.158 mL $TiCl_4$ were carefully dissolved in 2.50 mL EtOH (Ar) affording a clear solution (**I**). 0.451 g F-127 were dissolved in 3.00 mL EtOH (air) under stirring at 55 °C for 2 h (**II**). When a clear solution was obtained, 1.56 mL of (**II**) were added to 0.149 g $NbCl_5$ under stirring, affording a clear solution (**III**). After that, 1.79 mL of (**I**) were added to (**III**) and stirred for further 30 min at 55 °C in an oil bath (air). Dip-coating was performed in a controlled atmosphere in air (T = 25 °C, RH = 35 – 40 %) on various substrates. The films were dried for at least 10 min in the controlled atmosphere.

Substrate pre-treatment

$Nb_xTi_{1-x}O_2$ films were deposited on different substrates. Single-side polished Si-wafers were obtained from University Wafers showing a (100) orientation and cleaned with ethanol and heated in air for 2 h at 600 °C prior to film deposition. Si-wafers were used for SEM, TEM, GI-XRD and XPS. For the electrical conductivity measurements *via* impedance spectroscopy and Raman spectroscopy, SiO_2 substrates (Science Services GmbH) were used and cleaned using a mixture of KOH and *iso*propanol prior to film deposition.

Physicochemical characterization

SEM images were recorded at 10 kV on a JEOL 7401F. For EDX analysis, Quantax 400 from Bruker was used as spectroscopic device. EDX spectra were obtained at 20 kV. TEM images were taken using a FEI Tecnai G2 20 S-TWIN transmission electron microscope at 200 kV acceleration voltage on scraped off film-fragments deposited on carbon-coated copper grids. Images were evaluated with *ImageJ* freeware, version 1.48 (www.imagej.nih.gov/ij/). XRD

analysis was conducted using a Bruker D8 advance instrument using Cu-K_α radiation, grazing incidence mode and a Goebel mirror.

XPS measurements were performed with an AXIS Ultra DLD photoelectron spectrometer manufactured by Kratos Analytical (Manchester, UK). XPS spectra were recorded using monochromatic Al-K_α radiation for excitation, at a pressure of approximately $5 \cdot 10^{-9}$ mbar. The electron emission angle was 0° and the source-to-analyzer angle was 60°. The binding energy scale of the instrument was calibrated following a Kratos Analytical procedure using ISO15472 binding energy data. Spectra were taken by setting the instrument to the hybrid lens mode and the slot mode providing approximately a 300 × 700 μm² analysis area. Furthermore, the charge neutralizer was used. Survey spectra were recorded with a step size of 1 eV and a pass energy of 80 eV, high resolution spectra were recorded with a step size of 0.1 eV and a pass energy of 20 eV. Quantification was performed with Unifit 2021 using Scofield factor, the inelastic mean free pathway and the transmission function for the normalization of the peak area. For peak fitting a sum Gaussian-Lorentzian function was used. As background, a modified Tougaard background was used. Two independent areas for each $Nb_xTi_{1-x}O_2$ film on a polished silicon wafer as substrate were measured and an average value was calculated and reported in this work. Sheet conductivity measurements *via* impedance spectroscopy were performed using a 8×8 gold pin array as probe head with an altering polarity sequence. All measurements were conducted in the dark in a home-built setup to prevent any influence on electronic properties induced by the photoactivity of (doped) TiO_2 materials leading to the generation of excited charge carriers. A SP-200 potentiostat (Biologic) was used in a range between 100 mHz and 1 kHz. The obtained spectra (Nyquist impedance) were fitted using EIS Zfit software (EC-Lab version 11.33, Biologic). The Raman spectra were acquired by using a LabRam HR 800 instrument (Horiba Jobin Yvon) coupled to a BX41 microscope (Olympus). For both excitation and collection of the scattered light, a 100x/NA = 0.90 objective lens was employed. The system is equipped with a helium neon (HeNe) laser with a wavelength of 633 nm and 300 mm^{-1}

grating. The spectra were acquired with a liquid N_2-cooled (-126 °C operating temperature) charge-coupled device (CCD) camera (Symphony CCD, Horiba Jobin Yvon). Each spectrum was accumulated over six individual measurements, each with a measuring time of 20 seconds. In order to verify the homogeneity of the layers, at least five different positions were examined on each sample. The spectrometer entrance slit was 100 μm wide and the confocal pinhole was in the fully open position (1000 μm). Prior to the Raman experiment, the laser was allowed to stabilize for at least 2 h and the spectrometer was recalibrated against the most prominent mode of silicon at 520.7 cm^{-1}.

SI-1: Cross-section SEM images of mesoporous $Nb_xTi_{1-x}O_2$ films. Scale bar = 100 nm.

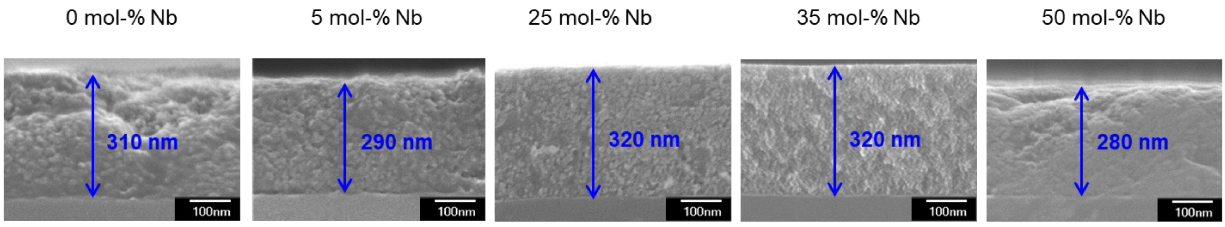

SI-2: EDX spectra of $Nb_xTi_{1-x}O_2$ films with templated mesoporosity on silicon substrates

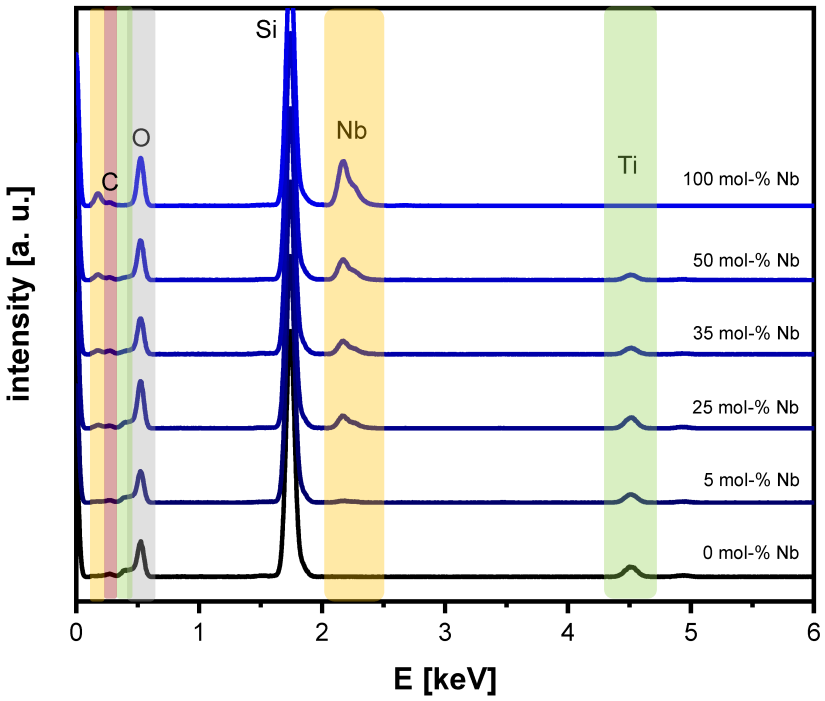

The obtained EDX spectra reveal the successful synthesis of templated mp. $Nb_xTi_{1-x}O_2$ films with varying molar Nb fraction. A quantification of the results from the spectra reveals only minor deviations between nominal and experimentally determined Nb fraction. At least three independent measurements on different areas of each film were performed and an average value for the Nb fraction was calculated and stated in the table below. As a reference, a mesoporous film containing 100 mol-% Nb was synthesized and investigated.

nominal Nb fraction [mol-%]	**Nb fraction (EDX) [mol-%]**
0.0	0.0
5.0	5.5
25.0	23.6
35.0	34.8
50.0	48.4
100.0	100.0

SI-3 Evaluation of XPS measurements of $Nb_xTi_{1-x}O_2$ films with templated mesoporosity on silicon substrates and discussion about the origin of the observed electrical conductivities in the context of literature reports

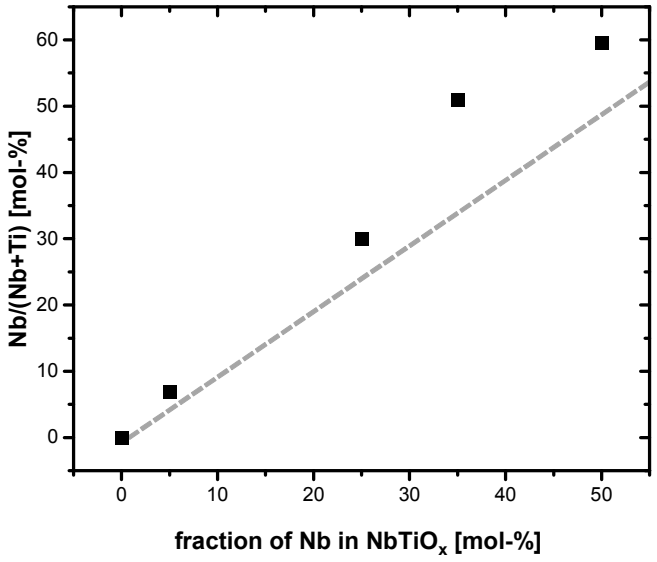

The parity plot of the relative fraction of Nb^{5+} species in mp. $Nb_xTi_{1-x}O_2$ indicates an increasing surface segregation for Nb fractions up to 35 mol-%. For 50 mol-% Nb, a less pronounced surface segregation becomes evident from surface analysis *via* XPS.

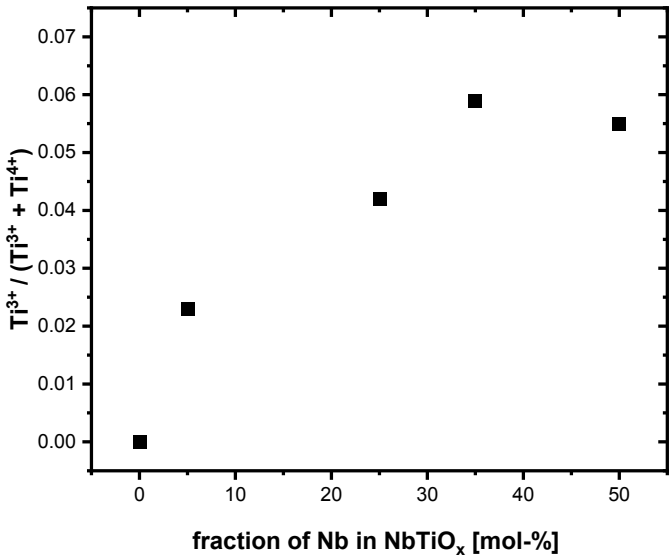

The XPS spectra of mp. $Nb_xTi_{1-x}O_2$ films show an increase in relative Ti^{3+} fraction with increasing incorporation of Nb atoms. The substitution of titanium with niobium atoms in the

lattice of the doped oxides induces charge imbalance. Hence, Ti^{3+} species are formed to counterbalance the Nb^{5+} species in the substituted lattice. For 35 mol-% Nb in $Nb_xTi_{1-x}O_2$, the relative amount of reduced Ti^{3+} species appears particularly high. In literature[36,37], two different charge compensation mechanisms by the substitutional incorporation of Nb^{5+} into the titania lattice (primarily Ti^{4+} species) are discussed. In the first, for every Nb^{5+} incorporated into the lattice, one Ti^{4+} is reduced to one Ti^{3+}. In the second, per four Nb^{5+} one Ti vacancy is formed.[38] Based on their XPS data on mp. $Nb_xTi_{1-x}O_2$ films, Yue *et al.*[36] reported that for lower fractions of Nb^{5+}, *i. e.* lower fractions of Nb in $Nb_xTi_{1-x}O_2$, charge compensation occurs *via* generation of Ti vacancies, whereas, for higher fractions of Nb^{5+}, free electrons lead to a higher electrical conductivity. In this context, however, it has to be mentioned that in their study, Yue *et al.* found the maximum in electrical conductivity for only 5 mol-% Nb in $Nb_xTi_{1-x}O_2$. For 10 mol-% Nb, the authors reported declined electrical conductivities, as a result of electron trapping at Ti^{4+} sites and, thus, reduced ionization efficiencies. Furthermore, the herein examined phase transition from anatase toward rutile phase was not observed at all in their previous study.

SI-4: GI-XRD pattern for synthesized mp. $Nb_xTi_{1-x}O_2$ films with Nb fraction > 35 mol-%

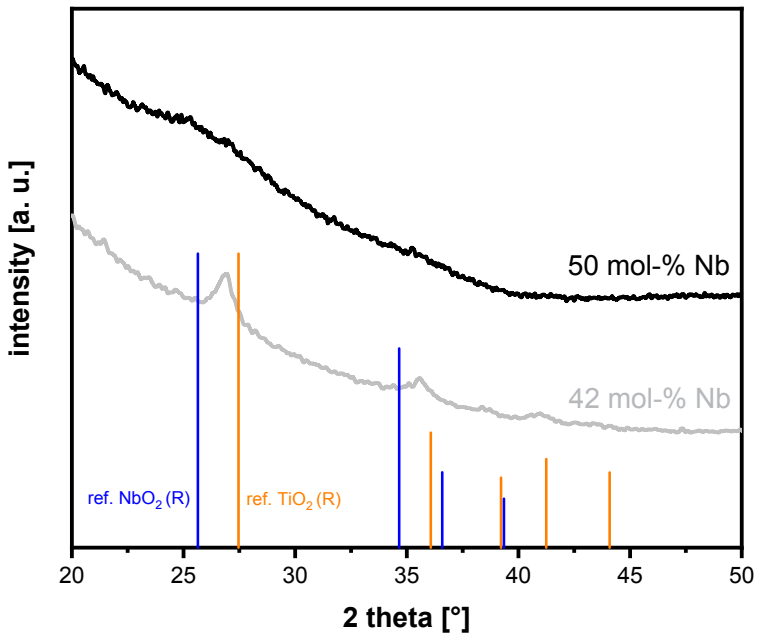

For Nb fractions of 42 mol-% Nb, distinct shifts of the reflections to lower 2 theta values can be observed compared to bare rutile TiO_2. According to the GI-XRD measurements shown in the above figure, the reflections are shifted to values between those of rutile TiO_2 (orange pattern) and rutile NbO_2 (blue pattern). This leads to the conclusion that a nanocrystalline material was obtained, in which Nb ions partially substitute Ti ions in the lattice with predominantly rutile phase. For an increasing fraction of Nb, *i. e.* for 50 mol-% Nb, a significant decrease in crystallinity can be deduced from the diffraction pattern. Accordingly, it seems more appropriate to describe this X-ray amorphous system as a solid solution, rather than a doped titanium oxide.

SI-5: Calculated rutile and anatase Raman active modes with the given symmetry indicated by the Mulliken notation. All intensities are stated relative to the highest intensity in arbitrary units.

rutile				
symmetry	B_{1g}	E_g	A_{1g}	B_{2g}
frequency [cm $^{-1}$]	140	460	611	830
intensity [a. u.]	7.2	742.3	1000.0	0

anatase					
symmetry	E_g	B_{1g}	A_{1g}	B_{1g}	E_g
frequency [cm $^{-1}$]	137	399	519	520	641
intensity [a. u.]	1000.0	98.9	18.6	82.7	197.0

SI-6: Calculated relative electrical conductivities σ in dependency of molar Nb fraction in $Nb_xTi_{1-x}O_2$. Values for σ are given in S cm^{-1}.

fraction of Nb [mol-%]	**calc. σ_{rutile} [S cm^{-1}]**	**calc. $\sigma_{anatase}$ [S cm^{-1}]**
0.0	4.22E-08	6.40E-07
4.2	1.58E-06	1.69E-06
8.3	2.42E-06	2.18E-06
16.7	4.55E-06	2.80E-06
25.0	4.50E-06	1.96E-06
33.3	8.04E-06	2.35E-06
41.7	5.03E-06	2.01E-06
50.0	5.84E-06	1.18E-06

SI-7: Fractional coordinates of the rutile 2×2×3 and the anatase 2×3×1 supercells.

The lattice parameters are given as a = 4.587 Å and c = 2.954 Å in $P4_2/mnm$ for rutile[39] and as a' = 3.782 Å and c' = 9.502 Å in $I4_1/amd$ for anatase[39].

			rutile			**anatase**	
#	**atom**	**x/*a***	**y/*b***	**z/*c***	**x/*a*'**	**y/*b*'**	**z/*c*'**
1	Ti	0.0000	0.0000	0.0000	0.0000	-0.1667	0.2500
2	Ti	0.0000	0.0000	0.3333	0.2500	0.0000	-0.2500
3	Ti	0.0000	0.0000	-0.3333	-0.5000	0.1667	0.2500
4	Ti	0.0000	-0.5000	0.0000	-0.2500	0.3333	-0.2500
5	Ti	0.0000	-0.5000	0.3333	0.0000	-0.5000	0.2500
6	Ti	0.0000	-0.5000	-0.3333	0.2500	-0.3333	-0.2500
7	Ti	-0.5000	0.0000	0.0000	-0.5000	-0.1667	0.2500
8	Ti	-0.5000	0.0000	0.3333	-0.2500	0.0000	-0.2500
9	Ti	-0.5000	0.0000	-0.3333	0.0000	0.1667	0.2500
10	Ti	-0.5000	-0.5000	0.0000	0.2500	0.3333	-0.2500
11	Ti	-0.5000	-0.5000	0.3333	-0.5000	-0.5000	0.2500
12	Ti	-0.5000	-0.5000	-0.3333	-0.2500	-0.3333	-0.2500
13	Ti	-0.2500	-0.2500	-0.1667	0.0000	0.0000	-0.5000
14	Ti	-0.2500	-0.2500	0.1667	0.2500	0.1667	0.0000
15	Ti	-0.2500	-0.2500	-0.5000	-0.5000	0.3333	-0.5000
16	Ti	-0.2500	0.2500	-0.1667	-0.2500	-0.5000	0.0000
17	Ti	-0.2500	0.2500	0.1667	0.0000	-0.3333	-0.5000
18	Ti	-0.2500	0.2500	-0.5000	0.2500	-0.1667	0.0000
19	Ti	0.2500	-0.2500	-0.1667	-0.5000	0.0000	-0.5000
20	Ti	0.2500	-0.2500	0.1667	-0.2500	0.1667	0.0000
21	Ti	0.2500	-0.2500	-0.5000	0.0000	0.3333	-0.5000
22	Ti	0.2500	0.2500	-0.1667	0.2500	-0.5000	0.0000
23	Ti	0.2500	0.2500	0.1667	-0.5000	-0.3333	-0.5000
24	Ti	0.2500	0.2500	-0.5000	-0.2500	-0.1667	0.0000
25	O	0.1521	0.1521	0.0000	0.2500	0.0000	-0.4582
26	O	0.1521	0.1521	0.3333	-0.5000	0.1667	0.0418
27	O	0.1521	0.1521	-0.3333	-0.2500	0.3333	-0.4582
28	O	0.1521	-0.3480	0.0000	0.0000	-0.5000	0.0418
29	O	0.1521	-0.3480	0.3333	0.2500	-0.3333	-0.4582
30	O	0.1521	-0.3480	-0.3333	-0.5000	-0.1667	0.0418
31	O	-0.3480	0.1521	0.0000	-0.2500	0.0000	-0.4582
32	O	-0.3480	0.1521	0.3333	0.0000	0.1667	0.0418
33	O	-0.3480	0.1521	-0.3333	0.2500	0.3333	-0.4582
34	O	-0.3480	-0.3480	0.0000	-0.5000	-0.5000	0.0418
35	O	-0.3480	-0.3480	0.3333	-0.2500	-0.3333	-0.4582
36	O	-0.3480	-0.3480	-0.3333	0.0000	-0.1667	0.0418
37	O	-0.1521	-0.1521	0.0000	0.2500	-0.1667	0.2082
38	O	-0.1521	-0.1521	0.3333	-0.5000	0.0000	-0.2918
39	O	-0.1521	-0.1521	-0.3333	-0.2500	0.1667	0.2082
40	O	-0.1521	0.3480	0.0000	0.0000	0.3333	-0.2918
41	O	-0.1521	0.3480	0.3333	0.2500	-0.5000	0.2082
42	O	-0.1521	0.3480	-0.3333	-0.5000	-0.3333	-0.2918

43	O	0.3480	-0.1521	0.0000	-0.2500	-0.1667	0.2082
44	O	0.3480	-0.1521	0.3333	0.0000	0.0000	-0.2918
45	O	0.3480	-0.1521	-0.3333	0.2500	0.1667	0.2082
46	O	0.3480	0.3480	0.0000	-0.5000	0.3333	-0.2918
47	O	0.3480	0.3480	0.3333	-0.2500	-0.5000	0.2082
48	O	0.3480	0.3480	-0.3333	0.0000	-0.3333	-0.2918
49	O	-0.0980	0.0980	-0.1667	0.0000	-0.1667	0.4582
50	O	-0.0980	0.0980	0.1667	0.2500	0.0000	-0.0418
51	O	-0.0980	0.0980	-0.5000	-0.5000	0.1667	0.4582
52	O	-0.0980	-0.4021	-0.1667	-0.2500	0.3333	-0.0418
53	O	-0.0980	-0.4021	0.1667	0.0000	-0.5000	0.4582
54	O	-0.0980	-0.4021	-0.5000	0.2500	-0.3333	-0.0418
55	O	0.4021	0.0980	-0.1667	-0.5000	-0.1667	0.4582
56	O	0.4021	0.0980	0.1667	-0.2500	0.0000	-0.0418
57	O	0.4021	0.0980	-0.5000	0.0000	0.1667	0.4582
58	O	0.4021	-0.4021	-0.1667	0.2500	0.3333	-0.0418
59	O	0.4021	-0.4021	0.1667	-0.5000	-0.5000	0.4582
60	O	0.4021	-0.4021	-0.5000	-0.2500	-0.3333	-0.0418
61	O	0.0980	-0.0980	-0.1667	0.0000	0.0000	0.2918
62	O	0.0980	-0.0980	0.1667	0.2500	0.1667	-0.2082
63	O	0.0980	-0.0980	-0.5000	-0.5000	0.3333	0.2918
64	O	0.0980	0.4021	-0.1667	-0.2500	-0.5000	-0.2082
65	O	0.0980	0.4021	0.1667	0.0000	-0.3333	0.2918
66	O	0.0980	0.4021	-0.5000	0.2500	-0.1667	-0.2082
67	O	-0.4021	-0.0980	-0.1667	-0.5000	0.0000	0.2918
68	O	-0.4021	-0.0980	0.1667	-0.2500	0.1667	-0.2082
69	O	-0.4021	-0.0980	-0.5000	0.0000	0.3333	0.2918
70	O	-0.4021	0.4021	-0.1667	0.2500	-0.5000	-0.2082
71	O	-0.4021	0.4021	0.1667	-0.5000	-0.3333	0.2918
72	O	-0.4021	0.4021	-0.5000	-0.2500	-0.1667	-0.2082

SI-8: Configurations of Nb-substituted rutile and anatase supercells. The indices of the substituted atoms refer to the labeling in **SI-7**.

fraction of Nb [mol-%]	**number of Nb atoms**	**index$_{rutile}$**	**index$_{anatase}$**
4.2	**1**	15	1
8.3	**2**	15,22	1,15
16.7	**4**	15,16,19,24	1,8,15,16
25.0	**6**	8,11,15,18,19,22	1,2,3,15,20,22
33.3	**8**	3,6,9,12,14,17,20,23	2,7,9,12,15,17,20,22
41.7	**10**	1,4,8,9,11,13,16,18,20,23	1,2,7,9,12,15,17,19,20,22
50.0	**12**	1,4,8,9,11,12,13,15,16,18,20,23	1,2,3,7,9,12,15,17,19,20,22,24

SI-9: Projected density of states (PDOS) (a), crystal orbital Hamiltonian population (-COHP) of the nearest neighbor atom (b) and orbital (c) interactions for all substituted rutile supercells. PDOS are given in states per eV, and -COHP are given per eV. By convention, all -COHP plots showing bonding (stabilizing) contributions are positive and antibonding (destabilizing) contributions are negative in sign. All energies are shown relative to the Fermi level $\varepsilon_F = 0$.

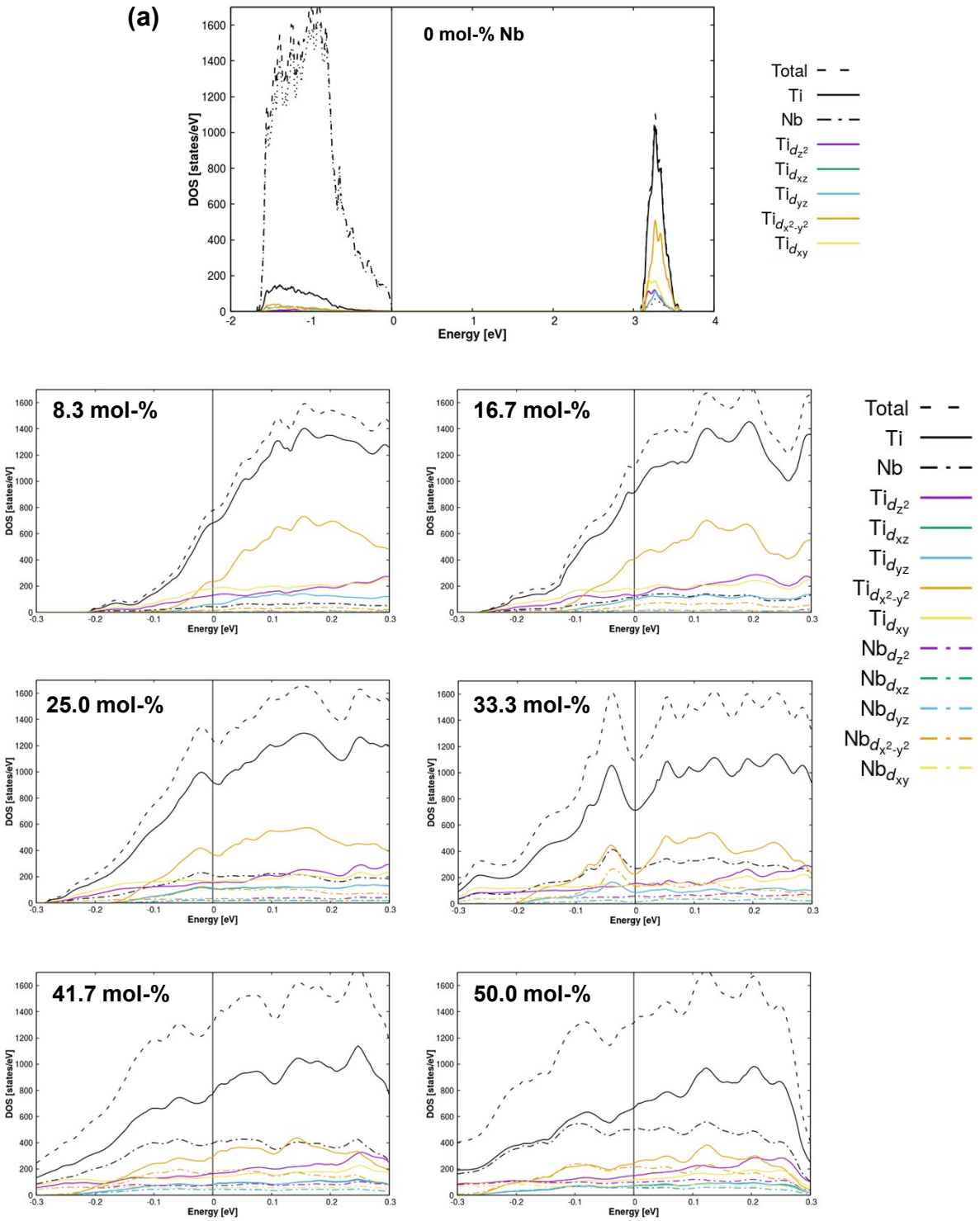

(b)

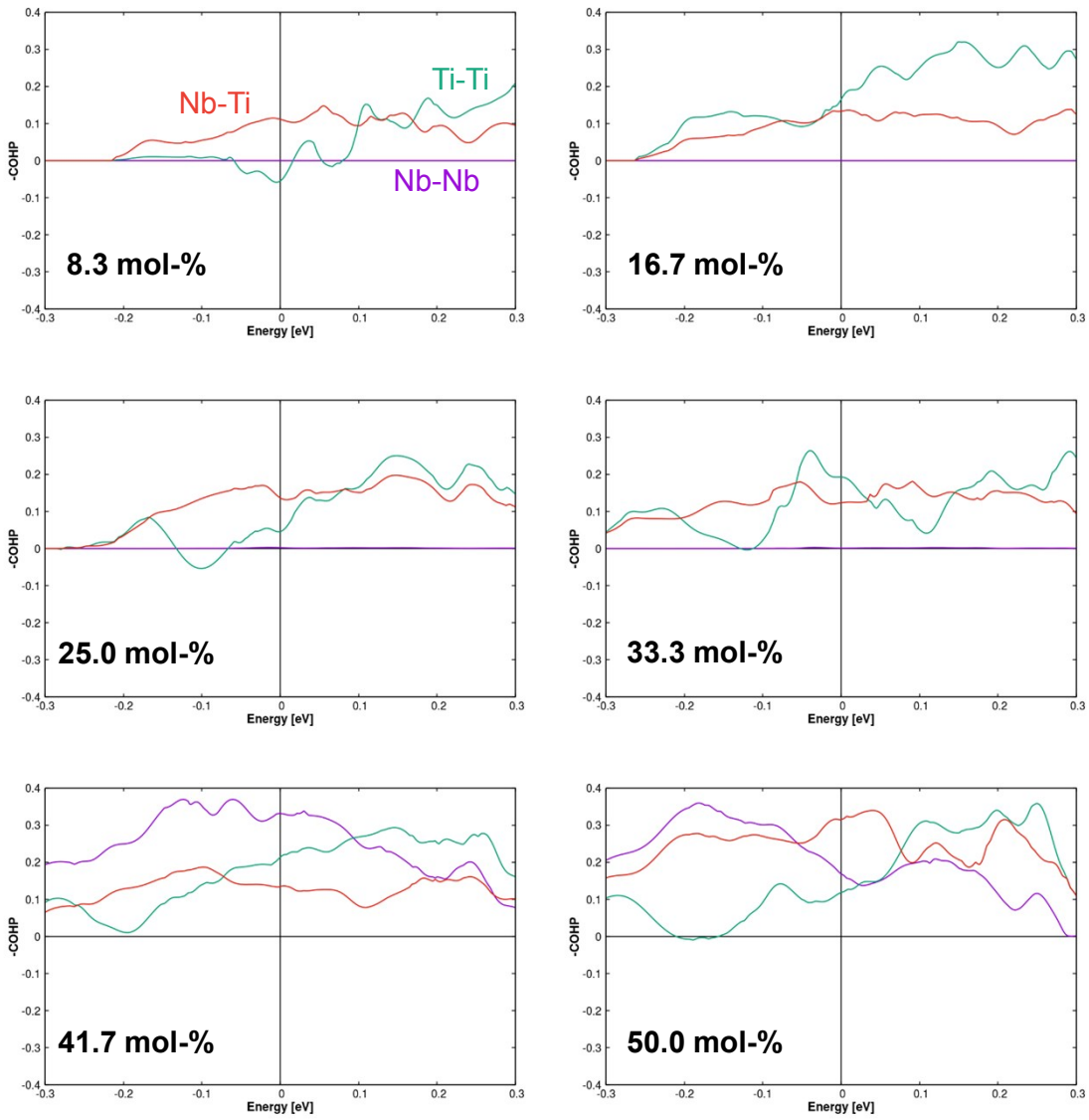
Nb-Ti
Ti-Ti
Nb-Nb
8.3 mol-%
16.7 mol-%
25.0 mol-%
33.3 mol-%
41.7 mol-%
50.0 mol-%
-COHP
Energy [eV]

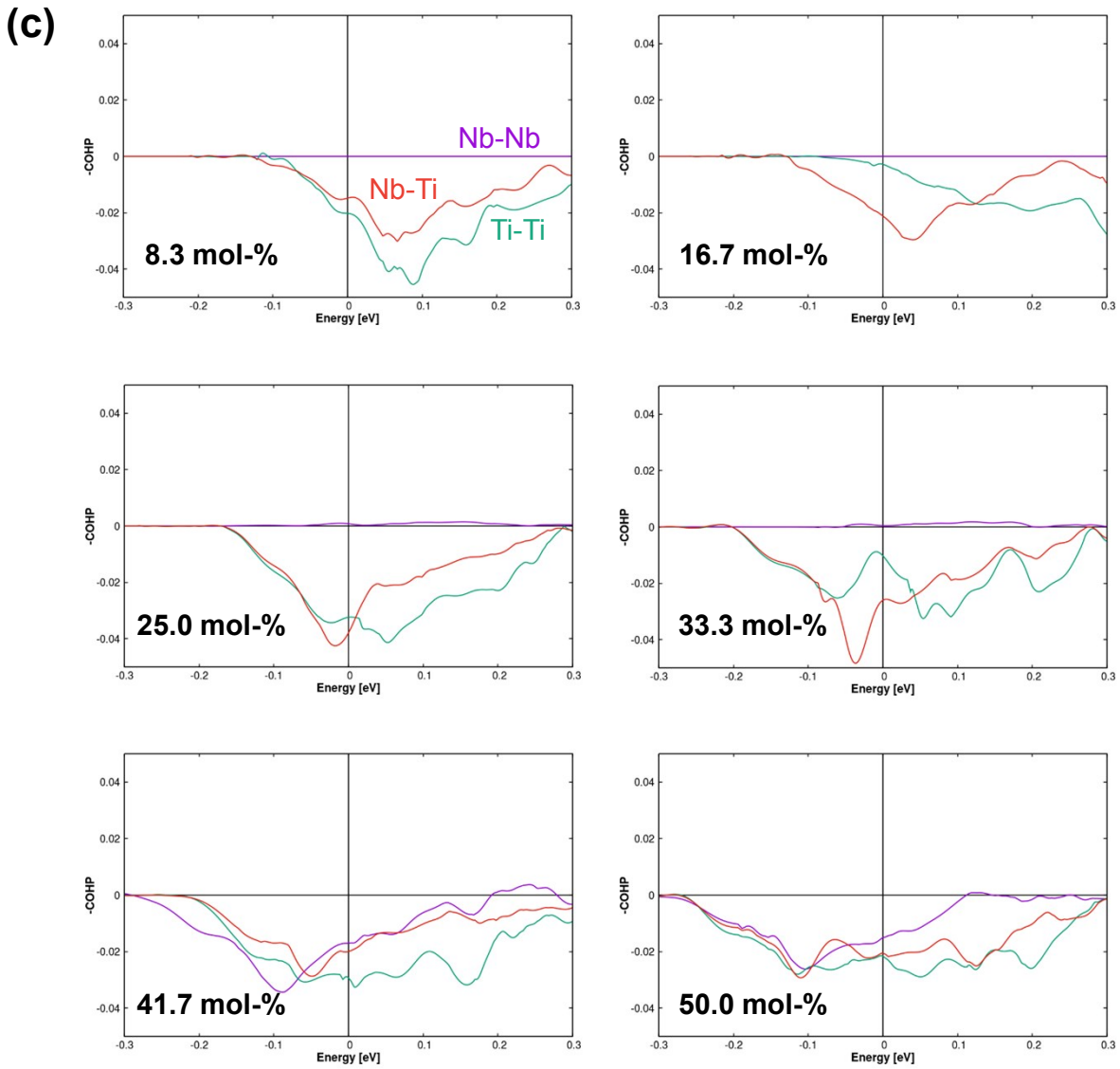

The general observed trend of the calculated electrical conductivity in dependency of molar Nb fraction is discussed by the PDOS and -COHP analyses for the substituted rutile supercells. Increasing the Nb fraction up to 25 mol-% leads to a systematic increase of the states at the Fermi level. This behavior seems reasonable due to the fact that n-type doping increases the electron density and, thus, shifts the Fermi level to higher energies.

Mulliken population analyses confirm this trend, as the occupation of Ti 3*d*-orbitals, in particular $3d_{z^2}$, $3d_{x2-y2}$ and $3d_{xy}$, increases with increasing Nb content. This is of particular importance, as these orbitals dominate the states around the Fermi level and significantly

contribute to the conductivity of the substituted phases. We do not observe a localization of charge density on particular Ti atoms, not even for small Nb fractions. This can be due to the application of a GGA method which, in general, tends to delocalize electron density.

For 33 mol-% Nb, the number of states at the Fermi level is lower than for smaller dopant fractions. Yet, there is a larger amount of states just below the Fermi level. Up to 33 mol-% of Nb, no Nb-Nb interactions occur, while bonding Nb-Ti interactions systematically increase and thus explain the rise in electrical conductivity. For 41.7 and 50.0 mol-% Nb, strong stabilizing Nb-Nb interactions appear resulting in decreasing conductivities due to more localized electrons. Overall, the maximum conductivity can be explained by a combination of increasing electron density while avoiding Nb-Nb interactions.

SI-10: Investigations on the impact of mesoporosity on the observed electrical properties for films synthesized with different polymer templates with 35 mol-% Nb in $Nb_xTi_{1-x}O_2$ as an illustrative example.

top-view SEM (100 kx)	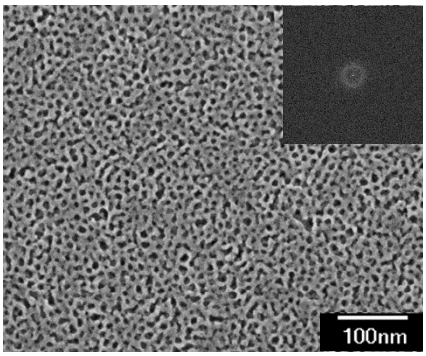	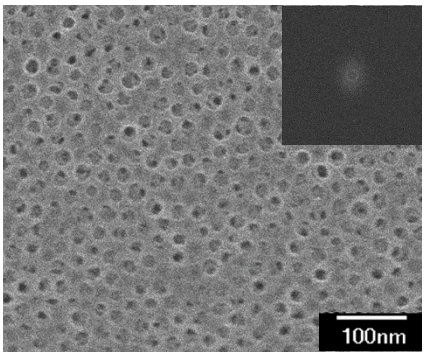
d_{pore}	10 ± 2 nm	22 ± 2 nm
d_1	15 ± 1 nm	34 ± 3 nm
sheet conductivity	0.0014 S cm^{-1}	0.0010 S cm^{-1}

Due to the fact that all herein presented theoretical models and calculations do not consider any (meso-)porosity, as this lies beyond the scope of our study, additional experiments were performed. As illustrative example, a different tri-block copolymer template was used in the synthesis of 35 mol-% Nb in $Nb_xTi_{1-x}O_2$ and compared to the F-127 templated film with the same dopant fraction.

As illustrated in the figure above, the films synthesized using PEO_{213}-PB_{184}-PEO_{213} as structure-directing agent (right) show larger pore sizes and thicker pore walls compared to the F-127-templated films (left). A larger average inter-pore distance for the PEO_{213}-PB_{184}-PEO_{213}-templated films can be confirmed by comparing the respective FFT (insets in both SEM images). Accordingly, PEO_{213}-PB_{184}-PEO_{213} forms larger spherical micelles and, hence, leads to larger pores and inter-pore distances after calcination. For both films, similar electrical sheet conductivities were found in experiment.

In general, our experimental results coincide well with the calculated data providing bulk properties, as surface effects seem to play only a minor role. One of the main advantages of our synthesis method for niobium-doped titania *via* dip-coating and the addition of a structure-directing agent is the high homogeneity of the resulting materials. Comparable wall- and sheet-thicknesses of the synthesized films enable a systematic study of their electronic properties in dependency of a single parameter which can be precisely adjusted, for example, the dopant fraction. The experimentally observed high crystallinity of the solids, the independence of the pore size and the interface with insulating air inside the pores confirm the dominance of the bulk properties in our systems.

References

[1] G. Kresse, J. Hafner, *Phys. Rev. B* **1993**, *47*, 558–561.

[2] G. Kresse, J. Furthmüller, *Comput. Mater. Sci.* **1996**, *6*, 15–50.

[3] G. Kresse, J. Furthmüller, *Phys. Rev. B* **1996**, *54*, 11169–11186.

[4] J. Sun, A. Ruzsinszky, J. P. Perdew, *Phys. Rev. Lett.* **2015**, *115*, 036402.

[5] R. Dovesi, A. Erba, R. Orlando, C. M. Zicovich-Wilson, B. Civalleri, L. Maschio, M. Rérat, S. Casassa, J. Baima, S. Salustro, B. Kirtman, *Wiley Interdiscip. Rev. Comput. Mol. Sci.* **2018**, *8*, 1360.

[6] S. C. R. Dovesi, V. R. Saunders, C. Roetti, R. Orlando, C. M. Zicovich-Wilson, F. Pascale, B. Civalleri, K. Doll, N. M. Harrison, I. J. Bush, P. D'Arco, M. Llunell, M. Causà, Y. Noël, L. Maschio, A. Erba, M. Rerat, *CRYSTAL17 User's Manual*, University of Torino, **2017**.

[7] T. Bredow, A. R. Gerson, *Phys. Rev. B* **2000**, *61*, 5194–5201.

[8] P. E. Blöchl, *Phys. Rev. B* **1994**, *50*, 17953–17979.

[9] G. Kresse, D. Joubert, *Phys. Rev. B* **1999**, *59*, 1758–1775.

[10] Z.-H. Cui, F. Wu, H. Jiang, *Phys. Chem. Chem. Phys.* **2016**, *18*, 29914–29922.

[11] Y. Luo, A. Benali, L. Shulenburger, J. T. Krogel, O. Heinonen, P. R. C. Kent, *New J. Phys.* **2016**, *18*, 113049.

[12] M. R. Ranade, A. Navrotsky, H. Z. Zhang, J. F. Banfield, S. H. Elder, A. Zaban, P. H. Borse, S. K. Kulkarni, G. S. Doran, H. J. Whitfield, *Proc. Natl. Acad. Sci.* **2002**, *99*, 6476–6481.

[13] Y. Zhang, J. W. Furness, B. Xiao, J. Sun, *J. Chem. Phys.* **2019**, *150*, 014105.

[14] Y. Hinuma, H. Hayashi, Y. Kumagai, I. Tanaka, F. Oba, *Phys. Rev. B* **2017**, *96*, 094102.

[15] Y. Zhang, D. A. Kitchaev, J. Yang, T. Chen, S. T. Dacek, R. A. Sarmiento-Pérez, M. A. L. Marques, H. Peng, G. Ceder, J. P. Perdew, J. Sun, *npj Comput. Mater.* **2018**, *4*, 9.

[16] C. Shahi, J. Sun, J. P. Perdew, *Phys. Rev. B* **2018**, *97*, 094111.

[17] J. He, C. Franchini, *J. Phys. Condens. Matter* **2017**, *29*, 454004.

[18] D. Fritsch, B. J. Morgan, A. Walsh, *Nanoscale Res. Lett.* **2017**, *12*, 19.

[19] Y. Hinuma, Y. Kumagai, I. Tanaka, F. Oba, *Phys. Rev. B* **2017**, *95*, 075302.

[20] M. Hochheim, T. Bredow, *Phys. Rev. B* **2018**, *97*, 235447.

[21] J. H. Skone, M. Govoni, G. Galli, *Phys. Rev. B* **2014**, *89*, 195112.

[22] A. Erba, *J. Phys. Condens. Matter* **2017**, *29*, 314001.

[23] D. Vilela Oliveira, J. Laun, M. F. Peintinger, T. Bredow, *J. Comput. Chem.* **2019**, *40*, 2364–2376.

[24] J. Laun, D. Vilela Oliveira, T. Bredow, *J. Comput. Chem.* **2018**, *39*, 1285–1290.

[25] Y. Tezuka, S. Shin, T. Ishii, T. Ejima, S. Suzuki, S. Sato, *J. Phys. Soc. Japan* **1994**, *63*, 347–357.

[26] S. Rangan, S. Katalinic, R. Thorpe, R. A. Bartynski, J. Rochford, E. Galoppini, *J. Phys. Chem. C* **2010**, *114*, 1139–1147.

[27] Z. Wang, U. Helmersson, P.-O. Käll, *Thin Solid Films* **2002**, *405*, 50–54.

[28] B. Liu, L. Wen, X. Zhao, *Mater. Chem. Phys.* **2007**, *106*, 350–353.

[29] M. M. Hasan, A. S. M. A. Haseeb, R. Saidur, H. H. Masjuki, M. Hamdi, *Opt. Mater. (Amst).* **2010**, *32*, 690–695.

[30] R. Dronskowski, P. E. Bloechl, *J. Phys. Chem.* **1993**, *97*, 8617–8624.

[31] M. T. Ruggiero, A. Erba, R. Orlando, T. M. Korter, *Phys. Chem. Chem. Phys.* **2015**, *17*, 31023–31029.

[32] L. Valenzano, F. J. Torres, K. Doll, F. Pascale, C. M. Zicovich-Wilson, R. Dovesi, *Zeitschrift für Phys. Chemie* **2006**, *220*, 893–912.

[33] F. Pascale, C. M. Zicovich-Wilson, F. López Gejo, B. Civalleri, R. Orlando, R. Dovesi, *J. Comput. Chem.* **2004**, *25*, 888–897.

[34] F. Pascale, C. M. Zicovich-Wilson, R. Orlando, C. Roetti, P. Ugliengo, R. Dovesi, *J.*

Phys. Chem. B **2005**, *109*, 6146–6152.

[35] B. Montanari, B. Civalleri, C. M. Zicovich-Wilson, R. Dovesi, *Int. J. Quantum Chem.* **2006**, *106*, 1703–1714.

[36] J. Yue, C. Suchomski, P. Voepel, R. Ellinghaus, M. Rohnke, T. Leichtweiss, M. T. Elm, B. M. Smarsly, *J. Mater. Chem. A* **2017**, *5*, 1978–1988.

[37] L. De Trizio, R. Buonsanti, A. M. Schimpf, A. Llordes, D. R. Gamelin, R. Simonutti, D. J. Milliron, *Chem. Mater.* **2013**, *25*, 3383–3390.

[38] X. Lü, X. Mou, J. Wu, D. Zhang, L. Zhang, F. Huang, F. Xu, S. Huang, *Adv. Funct. Mater.* **2010**, *20*, 509–515.

[39] J. K. Burdett, T. Hughbanks, G. J. Miller, J. W. Richardson, J. V. Smith, *J. Am. Chem. Soc.* **1987**, *109*, 3639–3646.

A-2 Reprinted Publication [MF-2]:

ALD-Coated Mesoporous Iridium-Titanium Mixed Oxides: Maximizing Iridium Utilization for an Outstanding OER Performance

M. Frisch‡, M. H. Raza‡, M.-Y. Ye, R. Sachse, B. Paul, R. Gunder, N. Pinna, R. Kraehnert**

Advanced Materials Interfaces **2022**, *9*, 2102035.

https://doi.org/10.1002/admi.202102035

ADVANCED MATERIALS INTERFACES
www.advmatinterfaces.de

ALD-Coated Mesoporous Iridium-Titanium Mixed Oxides: Maximizing Iridium Utilization for an Outstanding OER Performance

Marvin Frisch, Muhammad Hamid Raza, Meng-Yang Ye, René Sachse, Benjamin Paul, René Gunder, Nicola Pinna, and Ralph Kraehnert**

Dedicated to Prof. Dr. Jürgen Caro on the occasion of his 70th birthday

With the increasing production of renewable energy and concomitant depletion of fossil resources, the demand for efficient water splitting electrocatalysts continues to grow. Iridium (Ir) and iridium oxides (IrO_x) are currently the most promising candidates for an efficient oxygen evolution reaction (OER) in acidic medium, which remains the bottleneck in water electrolysis. Yet, the extremely high costs for Ir hamper a widespread production of hydrogen (H_2) on an industrial scale. Herein, the authors report a concept for the synthesis of electrode coatings with template-controlled mesoporosity surface-modified with highly active Ir species. The improved utilization of noble metal species relies on the synthesis of soft-templated metal oxide supports and a subsequent shape-conformal deposition of Ir species via atomic layer deposition (ALD) at two different reaction temperatures. The study reveals that a minimum Ir content in the mesoporous titania-based support is mandatory to provide a sufficient electrical bulk conductivity. After ALD, a significantly enhanced OER activity results in dependency of the ALD cycle number and temperature. The most active developed electrocatalyst film achieves an outstanding mass-specific activity of 2622 mA mg_{Ir}^{-1} at 1.60 V_{RHE} in a rotating-disc electrode (RDE) setup at 25 °C using 0.5 M H_2SO_4 as a supporting electrolyte.

1. Introduction

The generation of H_2 by water electrolysis represents an attractive way to obtain clean energy and reduce the excessive consumption of fossil resources.[1–3] For a combination with intermittent power supplies from renewables, PEM water electrolysis using a polymer electrolyte membrane (PEM) is highly promising.[4,5] Disadvantageously, the oxygen evolution reaction (OER) occurring at the anode shows sluggish kinetics and, thus, hampers an efficient overall electrochemical water splitting.[5,6] Large-scale electrolysis demands for affordable and active electrocatalysts.[7] Ir-[8–10] and Ru-based[11,12] materials were identified to show the highest catalytic OER activities in acidic electrolytes. Due to their higher stabilities, Ir-based catalysts represent the state-of-the-art anode materials.[8,13,14] To improve the utilization of the active noble metal, different approaches have been made, e.g., alloying IrO_x with earth-abundant metal oxides (TiO_2,[15] Ta_2O_5,[16] SnO_2[17]), dispersing IrO_x in the form of nanocrystals on high-surface area support materials (Sb-doped SnO_2[18]), or the introduction of well-defined nanostructures by templating processes.[10,19] Yet, declined electrical conductivities were frequently reported after the addition of insulating transition metal oxides such as TiO_2[20] or Ta_2O_5.[21] Regarding the stability of the support materials, doping was shown to enhance corrosion resistance, yet, most support materials show low stabilities in acid.[22] The interested reader is referred to a comprehensive review by Maillard and co-workers.[23]

M. Frisch, M.-Y. Ye, B. Paul, R. Kraehnert
Department of Chemistry
Technische Universität Berlin
Strasse des 17. Juni 124, 10623 Berlin, Germany
E-mail: ralph.kraehnert@tu-berlin.de

The ORCID identification number(s) for the author(s) of this article can be found under https://doi.org/10.1002/admi.202102035.

DOI: 10.1002/admi.202102035

M. H. Raza, N. Pinna
Institut für Chemie and IRIS Adlershof
Humboldt-Universität zu Berlin
Brook-Taylor-Strasse 2, 12489 Berlin, Germany
E-mail: nicola.pinna@hu-berlin.de

R. Sachse
Federal Institute for Materials Research and Testing (BAM)
Unter den Eichen 44-46, 12203 Berlin, Germany

R. Gunder
Helmholtz-Zentrum Berlin für Materialien und Energie
Hahn-Meitner-Platz 1, 14109 Berlin, Germany

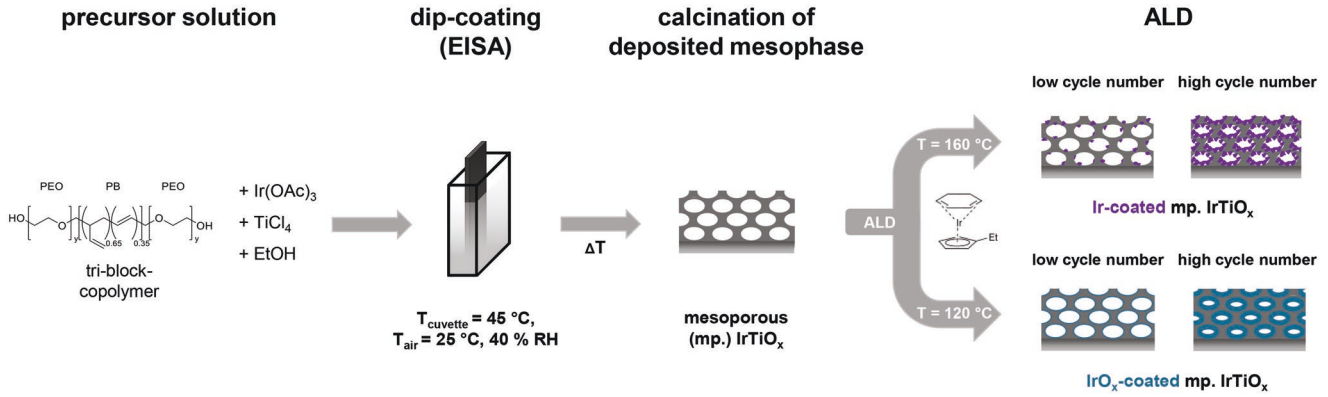

Scheme 1. Developed synthesis route for Ir- and IrO_x-coated mixed iridium titania catalysts in the form of mesoporous (mp.) films deposited on different planar substrates (Si, Ti, and glass). As a first step, a solution containing the metal precursors and a micelle-forming block-copolymer is deposited onto a substrate, dried and then calcined for 10 min at 375 °C in air to produce mesoporous iridium titania (mp. $Ir_{0.15}Ti_{0.85}O_2$, further denoted as mp. $IrTiO_x$). The obtained porous oxide support is subsequently exposed in alternating cycles to the ALD precursors (EtCp)Ir^{I}CHD and ozone (O_3) for the deposition of iridium (Ir) ($T_{Ir\text{-}ALD}$ = 160 °C) or iridium oxide (IrO_x) ($T_{IrOx\text{-}ALD}$ = 120 °C) over the entire external and internal surface of the oxides' pore systems. The obtained catalyst films show varying Ir loadings as a consequence of varying numbers of ALD cycles between 20 (low cycle number) and 60 (high cycle number).

For the design of superior electrocatalysts several key features are desirable, such as 1) a large number of active surface sites with 2) a good accessibility as well as 3) a sufficient electrical conductivity to promote charge transfer at the electrode interfaces, and 4) a sufficient stability of the catalyst against corrosion in OER regime.[24,25] As it is highly challenging to reach all of those requirements in a single catalyst material, we propose electrically conductive porous materials that fulfill requirements 2 and 3, surface-modified with thin, shape-conformal layers of a catalytically active and stable material to address requirements 1 and 4.

Mechanically stable and electrically conductive electrode coatings can be achieved by a method called evaporation-induced self-assembly (EISA).[26,27] The general synthesis concept relies on the application of a soft template, e.g., an amphiphilic block-copolymer, as a porogen to produce fully interconnected pore networks with adjustable pore diameters.[26–28] The EISA method is well-established and has been previously used to synthesize various mesoporous metal oxides such as SiO_2,[26] TiO_2,[29] IrO_x,[10] mixed metal oxides such as $IrTiO_x$[20,30] or Nb-doped TiO_x,[31] and composite materials such as Pd/TiO_2,[32] among others.

Atomic layer deposition (ALD) represents one of the most efficient ways to modify the entire surface of porous materials in a shape-conformal way, since ALD can ensure a highly conformal deposition of thin surface layers due to a self-limiting reaction mechanism.[33–37] The amount and surface layer thickness of the deposited species can be tuned by changing the number of ALD cycles.[34,38–40]

We illustrate the proposed concept for the example of mixed iridium titania films with template-controlled mesoporosity (mp. $IrTiO_x$) as a support material for IrO_x species deposited via ALD.

Summing up, we herein present the production of nanostructured acidic OER catalysts, in which the bulk consists of a sufficiently conductive iridium titanium mixed oxide support with the entire surface uniformly coated with an ultrathin layer of IrO_x deposited via conformal ALD. **Scheme 1** outlines the overall concept of the study. Based on our previous report,[30] we synthesized templated mesoporous $IrTiO_x$ films (15 mol%/30 wt% Ir content in the mixed oxide) on different flat substrates via dip-coating and EISA using titanium(IV)chloride ($TiCl_4$) and iridium(III)acetate ($Ir(OAc)_3$) as metal precursors and ethanol as a polar solvent. Subsequently, ALD was used to coat the entire internal and external surfaces of the conductive support with Ir species via alternating cycles of 1-ethylcyclopentadienyl-1,3-cyclohexadieneiridium(I) [(EtCp)Ir^{I}CHD] and ozone (O_3) pulses at two different temperatures (120 °C/160 °C). By tuning the temperature during ALD, the nature of the deposited Ir species was adjusted.[41,42]

In this work, we systematically investigate also fundamental aspects of the synthesis and electrochemical performance of IrO_x surface-modified electrode coatings. In particular, these are (a) the impact of the temperature at which ALD is performed (120 °C vs 160 °C), b) the role of the number of respective ALD cycles (0, 20, 40 and 60) and (c) the impact of ALD on the electrical properties of the mesoporous support.

2. Results and Discussion

2.1. Impact of ALD-Temperature and Cycle Number on the Morphology

As shown by representative top-view SEM images in **Figure 1**a, micelle-templated $IrTiO_x$ films were obtained via dip-coating and EISA. The corresponding fast Fourier transform (FFT, inset in Figure 1a) reveals an isotropic ring, thus indicating a locally-ordered mesoporous structure and a well-preserved template-controlled porosity in the films after calcination at 375 °C in air. These mp. $IrTiO_x$ films were then surface-modified using two different ALD processes at two different reaction temperatures. Pronounced differences become visible depending on the temperature during ALD. In brief, ALD at 160 °C leads to the formation of finely dispersed nanoparticles on the surface of the pore walls, whereas ALD at 120 °C affords dense surface Ir-rich layers covering the entire pore wall surface of the $IrTiO_x$ support. The influence of the ALD temperature and cycle number can be examined via SEM analysis. For low cycle numbers, i.e., 20 cycles, ALD at 160 °C leads to the presence of small Ir-rich nanoparticles

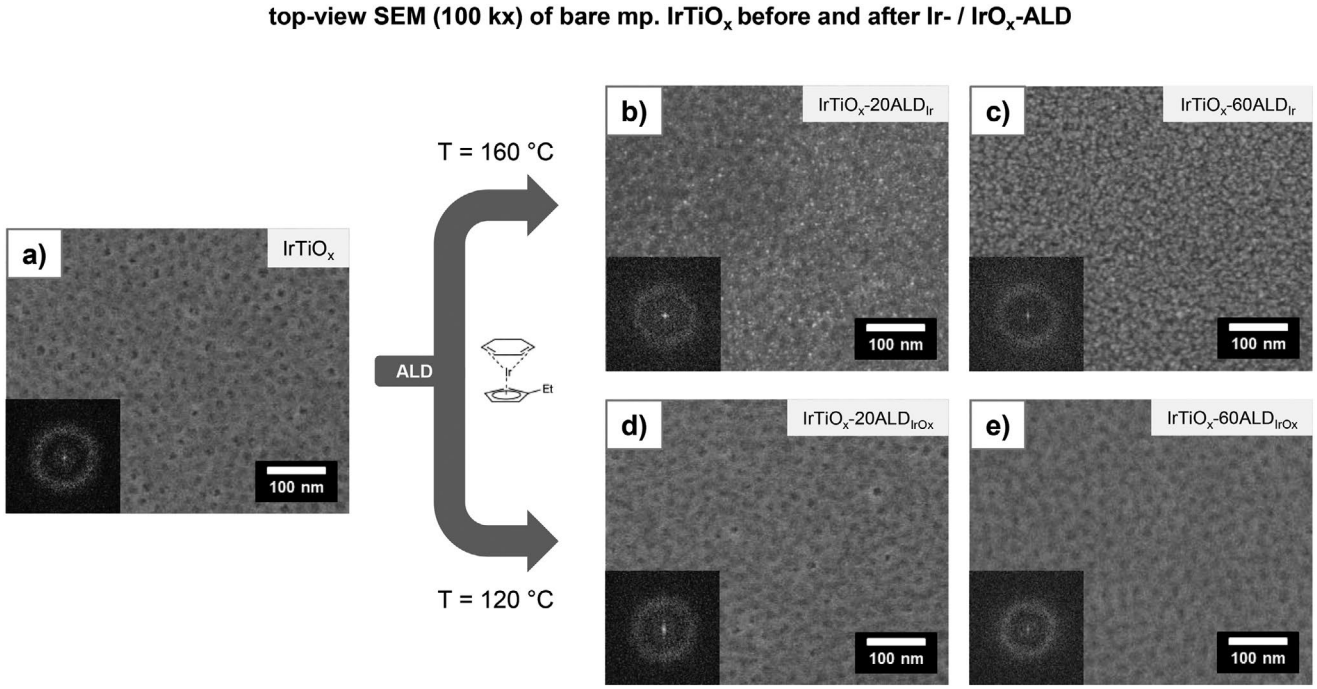

Figure 1. Representative top-view SEM images of mp. IrTiO$_x$ prior to a) and after surface-modification using ALD at b,c) 160 °C and at d,e) 120 °C. The corresponding ALD cycle number is denoted in the sample description. Insets on the bottom left corner of each image show the corresponding FFT. A diffuse ring in the FFT indicates the presence of a mesoporous structure, which is well-preserved after ALD. Distinct structural differences are visible depending on the temperature during the ALD process. High temperatures of 160 °C lead to the occurrence of nanoparticle-like deposits with bright contrast on the images, whereas lower temperatures of 120 °C lead to the formation of a homogeneous surface layer-type coating on the pore walls of the support.

of bright contrast, as evidenced by SEM images in Figure 1b. Still, the mesoporous structure remains essentially preserved, since the corresponding FFT reveals a diffuse ring (inset in Figure 1b).

With a higher cycle number of 60 ALD cycles at 160 °C, the structure of the pore walls has apparently changed and the mesopores appear partially blocked by the ALD deposits, according to SEM images depicted in Figure 1c. Nevertheless, the corresponding FFT inset provides evidence for a preserved mesoporous structure. A lower ALD temperature (120 °C) was applied, aiming at more layer-like structures rather than the formation of nanoparticulate surface species.[41,42] Apparently, SEM analysis nicely confirms the preservation of the template-introduced mesoporous structures after ALD at 120 °C (Figure 1d,e).

As reference support materials, bare TiO_2 films with template-controlled porosity were simultaneously modified via ALD at both 120 °C and 160 °C. Similar observations regarding the impact of temperature and cycle number of the ALD process on the resulting morphologies of the coatings were found (see Section I in the Supporting Information). Importantly, lower magnification SEM images suggest the formation of homogeneous films and the absence of larger, ill-defined aggregates for all investigated areas of samples (see Section II in the Supporting Information).

Our investigations clearly point out that the temperature during the ALD process is a key parameter to control the morphology of the deposited species. More specifically, ALD at 120 °C was found to be most suitable for the deposition of highly conformal, layer-like surface deposits. In the following section, the impact of the number of ALD cycles at 120 °C will be investigated in order to gain more insights into properties such as the layer thickness of the deposited surface layer.

2.2. ALD at 120 °C: Impact of Cycle Number on ALD-Layer Thickness and Pore Size

To further investigate the impact of ALD at 120 °C on the pore structure, the average pore diameters were analyzed and plotted as a function of the corresponding ALD cycle number (**Figure 2**b). IrTiO$_x$ films show spherical mesopores with an average pore diameter of 18 nm. After 20, 40, and 60 ALD cycles at 120 °C, decreasing average pore diameters of approximately 17, 16, and 15 nm were found, respectively. The observed linear correlation between the average pore diameter and the ALD cycle number results from an increase in ALD-layer thickness with an increasing number of ALD cycles, as further evidenced by results from spectroscopic ellipsometry (Figure 2a) with a calculated growth per cycle (GPC) of 0.7 ± 0.006 Å cycle^{-1} on flat silicon (Si) substrates. Vice versa, the average pore wall thickness rises for increasing cycle numbers, assuming a rigid porous framework obtained via calcination at elevated temperature.[43] Indeed, such a linear correlation is characteristic for ALD processes based on self-limiting surface reactions affording homogeneous surface coatings with high conformality and has been reported before.[41,44–46]

2.3. Impact of the Different ALD Processes at 120 °C and 160 °C on Phase and Crystallinity

To gain more insights into the structural properties such as the morphology, crystallinity, and phases prior to and after ALD, TEM, SAED, and GI-XRD analyses were performed. Calcination

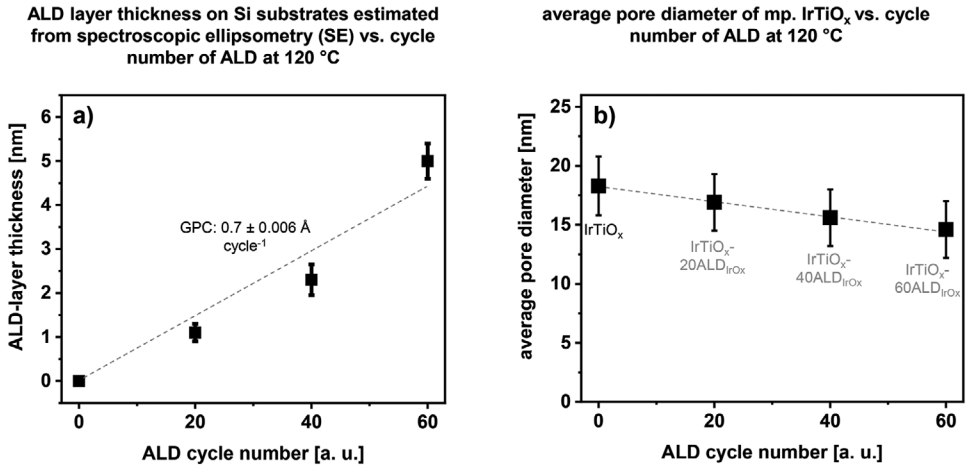

Figure 2. Plot showing the estimated layer thickness on Si substrates based on the results from spectroscopic ellipsometry (SE) versus ALD cycle number at a) 120 °C. Vertical bars indicate the respective standard deviations. A linear regression corresponding to a GPC of 0.7 Å cycle^{-1} was obtained after fitting of the data. In b), results from the pore size evaluations of mp. $IrTiO_x$ prior to and after ALD at 120 °C based on the SEM images shown in Figure 1 are given. Vertical bars indicate the respective error bars. The dashed gray lines were added to show a linear correlation between the average pore size and ALD cycle number.

of the mp. $IrTiO_x$ support for 10 min at 375 °C leads to a low crystalline oxide (**Figure 3**a,IV, SAED pattern) with template-controlled mesoporous structure, as indicated by the TEM images shown in Figure 3aI,II. EDX analysis and elemental mappings (Section IV in the Supporting Information) reveal a homogeneous distribution of Ir throughout the support.

Again, the temperature during ALD is found to show a distinct impact on the morphology, phase, and crystallinity of the deposited surface layers. In this context, ALD at 160 °C affords small, nanoparticulate Ir surface species, according to the HRTEM image depicted in Figure 3b-III.

The lattice fringes in the inset of the HRTEM image, the power spectrum (PS) of the selected region in Figure 3b-III as well as the SAED pattern in Figure 3b-IV suggest the presence of lattice fringes corresponding to metallic Ir^0 crystallites introduced via ALD. Similarly, XRD analysis in gracing-incidence geometry provides further evidence for the deposition of Ir^0 species via ALD at 160 °C, since additional reflections appear that match well with a nanocrystalline, metallic Ir phase (see Section VII in the Supporting Information). This observation is corroborated by SEM (see Figure 1a,b, right) and XPS analyses. Surface-sensitive XPS analysis reveals a significantly increased fraction of metallic Ir^0 species after ALD at 160 °C (see Section V in the Supporting Information for more details). In this context, the relative fraction of Ir^0 species (respective to the total amount of surface Ir) rises from ≈8 at% in mp. $IrTiO_x$ to ≈75 at% after 60 cycles ALD at 160 °C. For the mp. TiO_2 support films, similar results were obtained from TEM (Section III in the Supporting Information) and XPS (Section V in the Supporting Information) analyses, which underlines the predominance of mainly metallic Ir^0 deposits after ALD at 160 °C independent of the support material.

Contrarily, after ALD at 120 °C, weak signals corresponding to the onset of crystallization of rutile-type IrO_2 can be identified in the SAED pattern of ALD-coated $IrTiO_x$ (Figure 3c-IV). In addition, the low crystallinity of the ALD deposits is confirmed by GI-XRD analysis which did not reveal the appearance of additional reflections (Section VII in the Supporting Information). According to XPS results, prior to ALD, the predominant surface species can be assigned to Ir^{3+} (see Ir 4f spectrum of mp. $IrTiO_x$ in Figure S5a, Supporting Information, top) with a minor contribution of metallic Ir^0.[47,48] The latter completely vanishes after only 20 cycles ALD due to the observation that the Ir 4f spectrum of $IrTiO_x$-$20ALD_{IrOx}$ is dominated by Ir^{3+} species at its surface (see Figure S6b, Supporting Information, top). For 60 cycles of ALD at 120 °C, the ratio of surface Ir/Ti increases, as expected for higher loadings of IrO_x for higher cycle numbers (Table S2, Supporting Information). Hence, for $IrTiO_x$ support films modified via ALD at 120 °C, a structural model based on a mesoporous mixed iridium titanium oxide with low Ir content inside the bulk and high Ir concentration at the pore wall surface due to a homogeneous coating with predominantly oxidic Ir^{3+} species can be deduced. For TiO_2 supports modified via ALD at 120 °C, a similar structure with a noble-metal free bulk can be claimed. This nanostructure enables a maximized exposure of active Ir sites for electrochemical applications with the aim of improving the mass-specific OER activity. Importantly, the mesoporous structure remains well-preserved even after high ALD cycle numbers, thus avoiding mass-transfer limitations during catalysis.

2.4. Impact of ALD Temperature and Cycle Number on the Electrical Properties and OER Activity

Impedance spectroscopy is a powerful tool to assess the electrical conductivities of thin films deposited on insulating substrates.[31,49] In accordance with our previous results[20,30] for as-prepared mesoporous films prior to catalytic testing, the addition of 15 mol% Ir to TiO_x leads to well-conductive materials (≈10^{-2} S cm^{-1} for mp. $IrTiO_x$), which enables efficient charge transfer kinetics at the electrode during OER catalysis.[20] According to the results given in **Figure 4**a and **Table 1**, both ALD processes lead to a rise in conductivity for increasing ALD cycle numbers. The impact of the number of ALD cycles on the electrical conductivity is significantly more pronounced than the influence of the ALD temperature in the case of the mp. TiO_2 supported films (see Section VIII in the

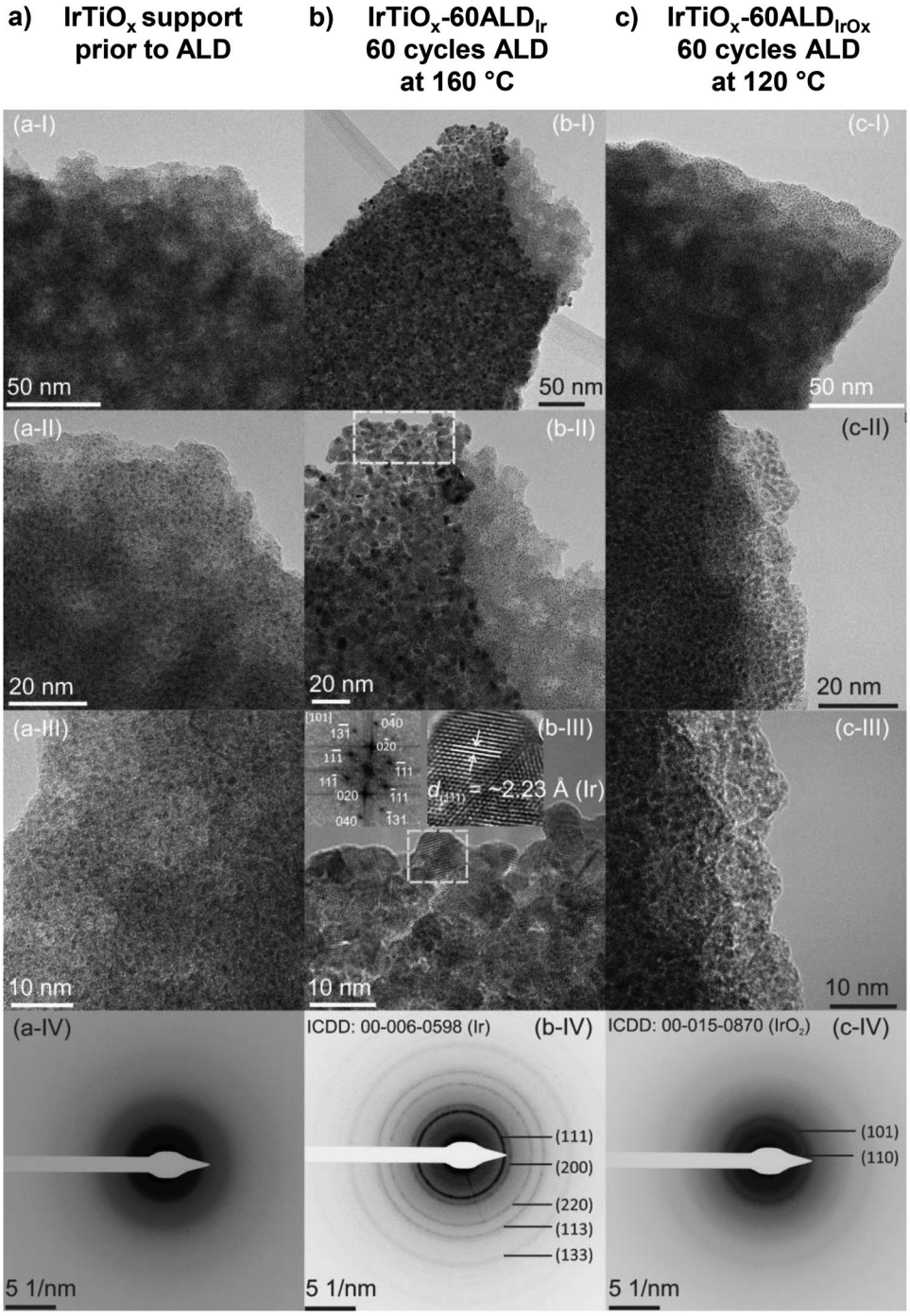

Figure 3. BF-HRTEM images (I–III) and SAED patterns (IV) for a) the mp. IrTiO$_x$ support, b) after 60 cycles of ALD at 160 °C (IrTiO$_x$-60ALD$_{Ir}$) and c) after 60 cycles ALD at 120 °C (IrTiO$_x$-60ALD$_{IrOx}$). In b-III) the upper left inset shows the obtained power spectrum (PS) of the area in the HRTEM image highlighted by the white frame. The patterns in IV are assigned according to the reference ICDD card numbers 00-006-0598 for Ir^0 (cubic) and 00-015-0870 for IrO_2 (tetragonal), respectively.

Supporting Information for further discussion). Notably, after 60 cycles of ALD at both 120 °C and 160 °C, well-conductive coatings were obtained showing similar sheet conductivities between ≈10^1 to ≈10^3 S cm^{-1}, independent of the support. These findings are in good agreement with the high conductivities of both metallic and oxidic Ir phases. Due to the fact that the evaluated sheet conductivity values for high cycle numbers of Ir- and IrO$_x$–ALD lie within a similar range (taking minor measurement errors into account), both types of surface modifications clearly improve the electrical properties of the TiO_2- and IrTiO$_x$-based materials by several orders of magnitude.

To assess the impact of both temperature and number of ALD cycles on the catalytic OER activity, RDE measurements were conducted in N_2-purged 0.5 M sulfuric acid at

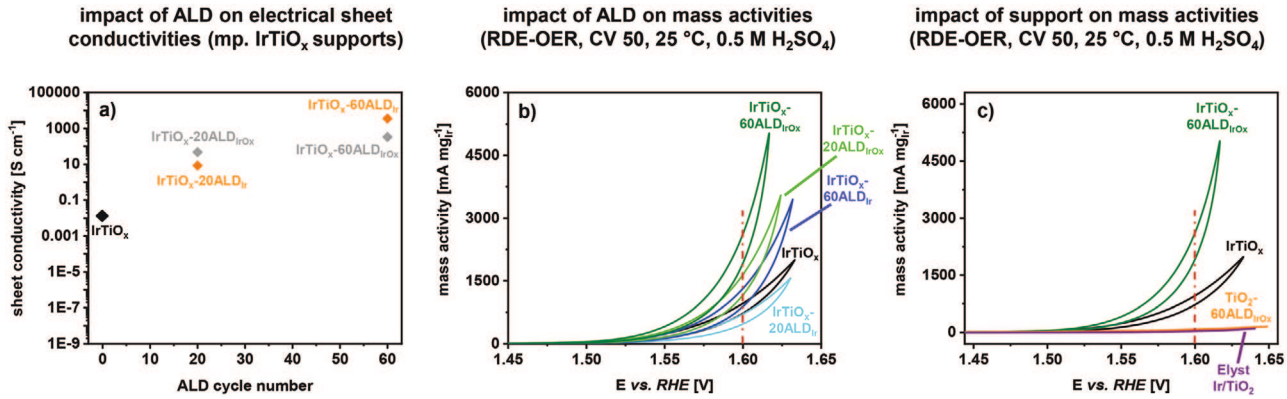

Figure 4. a) Electrical sheet conductivities assessed via impedance spectroscopy of mp. $IrTiO_x$ (black rhomb) as well as $IrTiO_x$ supports modified via ALD at 160 °C (orange) and at 120 °C (gray). All investigated films were deposited on insulating glass substrates. b) Ir mass-normalized activities of the bare mp. $IrTiO_x$ support (black) in comparison with the ALD-modified $IrTiO_x$ supports. Light and dark green curves represent supports modified via IrO_x–ALD at 120 °C with 20 and 60 ALD cycles, respectively. Light and dark blue curves represent supports modified via Ir–ALD at 160 °C with 20 and 60 cycles, respectively. c) Mass activities of the most active catalyst film $IrTiO_x$–$60ALD_{IrOx}$ (dark green) and the bare mp. $IrTiO_x$ support (black) in comparison with the commercial reference Elyst Ir75 (purple) and TiO_2-$60ALD_{IrOx}$ produced via 60 cycles ALD at 120 °C on a mp. TiO_2 support (orange). All electrochemical testings were conducted in an RDE setup and N_2-purged 0.5 M H_2SO_4 at 25 °C. The 50th CV is plotted for each catalyst film deposited on polished Ti substrates. It has to be noted that Nafion binder was added for the measurement of the reference catalyst powder. The dashed vertical red lines in (b–c) serve as a guideline to the eye.

room temperature for all films listed in Table 1. From the electrochemical testings, values for the Tafel slopes, Ir mass-normalized activities and the relative numbers of accessible active surface Ir sites (determination based on voltammetric charge using a previously established method described elsewhere[20,50]) of the catalysts were derived. Table 1 provides an overview of the electrical properties and the electrochemical performance data prior to and after ALD. Figure 4b shows the Ir-mass based activity plots of the 50th CVs for $IrTiO_x$ and ALD-modified $IrTiO_x$ films. Both, ALD temperature and cycle number affect the calculated Ir mass-normalized catalytic activities. With respect to the bare mp. $IrTiO_x$ support, improved mass activities can be achieved after the optimization of the ALD temperature and cycle number. In this context, ALD at 120 °C affords more active catalyst films than those produced via ALD at 160 °C.

At a potential of 1.60 V_{RHE}, mp. $IrTiO_x$ achieves a mass-normalized OER activity of 962 mA mg_{Ir}^{-1}, which can be explained by the presence of highly active Ir domains in a TiO_2 matrix produced via calcination at benign temperatures.[30] After 20 cycles of Ir-ALD at 160 °C, a slight drop in mass activity to 706 mA mg_{Ir}^{-1} can be observed. Importantly, deposition via ALD produces different types of Ir species compared to thermal treatments. In this context, our previous works[19,20,30,51] revealed a strong correlation between activity and calcination temperature for mesoporous Ir-based OER catalyst model

Table 1. Overview over the electrical properties and electrocatalytic RDE-OER performance in 0.5 M H_2SO_4 (25 °C) of mp. $IrTiO_x$ prior to and after ALD at 120 °C and 160 °C. As references, catalysts supported using low conductive mp. TiO_2 and the commercial Ir/TiO_2 powder (Elyst, Umicore) are given.

Catalyst	ALD cycle number	ALD temperature [°C]	Ir loading[a)] [µg cm^{-2} geom. area]	Conductivity[b)] [S cm^{-1}]	Charge $q_{(a+c)/2}$[c)] [mC]	η (1 mA cm^{-2}, CV 50) [mV]	η (10 mA cm^{-2}, CV 50) [mV]	Mass activity (1.60 V, CV 50) [A g_{Ir}^{-1}]	Tafel slope[d)] (CV 50) [mV dec^{-1}]
$IrTiO_x$	0	–	3.9	≈10^{-2}	0.30	323	414	962	69
$IrTiO_x$–$20ALD_{Ir}$	20	160	6.3	≈10^{1}	0.71	323	402	706	64
$IrTiO_x$–$60ALD_{Ir}$	60	160	9.2	≈10^{3}	0.78	302	364	1318	57
$IrTiO_x$–$20ALD_{IrOx}$	20	120	5.5	≈10^{2}	0.43	308	373	1651	59
$IrTiO_x$-$60ALD_{IrOx}$	60	120	7.0	≈10^{3}	0.93	296	353	2622	55
TiO_2-$60ALD_{IrOx}$	60	120	5.9	≈10^{2}	0.43	424	*	79	139
Ref. Elyst Ir/TiO_2 (powder)	0	–	≈80	–	0.42	344	421	30	65

[a)]Average geometric Ir loading determined via quantitative SEM-EDX measurements on Ti substrates, except for the reference catalyst powder Elyst (nominal loading). For the unmodified supports, ICP-OES measurements were performed to confirm the EDX-derived geometric Ir loadings (see Experimental Section); [b)]Electrical conductivity investigated via impedance spectroscopy in the dark; [c)]Voltammetric charge assessed via base voltammetry in a lower potential range between 0.4 to 1.4 V_{RHE} (see Section IX in the Supporting Information) as an estimate for the electrochemically active surface Ir species; [d)]Tafel plots are given in Figure S11 in the Supporting Information. An asterisk (*) indicates that the respective current density was not reached within the investigated potential range.

systems. Our previous findings indicate a deposition of predominantly metallic Ir^0 species via ALD at 160 °C. Due to the fact that the voltammetric charge (see Table 1) is more than two-fold higher for $IrTiO_x$-$20ALD_{Ir}$ than that of the $IrTiO_x$ support, a lower intrinsic activity of the ALD-deposited Ir^0 species can be claimed. After 60 ALD cycles at 160 °C, a higher mass activity of 1318 mA mg_{Ir}^{-1} is achieved, which can be explained by the larger number of nanoparticulate Ir^0 deposits providing more active surface Ir sites overall. As suggested from investigations of the electrical conductivities, neighboring crystallites are in close contact to each other and provide additional electron paths at the surface and, thereby, promote OER activity.[44,45,52]

Yet, ALD at 120 °C affords significantly more active catalysts. $IrTiO_x$-$60ALD_{IrOx}$ achieves the highest OER activity of 2622 mA mg_{Ir}^{-1} at 1.60 V_{RHE}, which is more than 2.7-fold higher than that of the unmodified mp. $IrTiO_x$ support (see Figure 4b,c). The outstanding Ir mass-specific activities of the ALD-modified $IrTiO_x$ catalysts can be deduced from the ultra-low loading and high accessibility of the well-dispersed IrO_x active centers at the surface of the porous support. The optimization of the ALD process is primordial to achieve a highly conformal and homogeneous deposition of oxidic Ir^{x+} species of low crystallinity. Notably, XPS analyses of the oxidation states of the surface Ir species for the spent catalysts modified via Ir-ALD at 160 °C indicate a significant fraction of unoxidized Ir^0 (see Section V in the Supporting Information), highlighting the necessity to adjust the ALD parameters in order to improve the intrinsic activities of the active sites. Moreover, all herein developed catalyst coatings are binder-free films which have been shown to be more active than Nafion-containing catalyst films.[53]

Amongst state-of-the-art Ir–Ti-based electrocatalysts, all herein developed ALD-modified $IrTiO_x$ films achieve a significantly improved OER performance with outstanding Ir mass-specific activities in acidic electrolyte (**Table 2**). Remarkably, despite the ultralow Ir loadings, an exceptionally high mass activity of 178 mA mg_{Ir}^{-1} at 1.53 V_{RHE} can be achieved for the most active binder-free coating, i.e., $IrTiO_x$-$60ALD_{IrOx}$, that is even higher than that of the "stellar" $IrO_x/SrIrO_3$ catalyst.[9,61,62] With respect to mp. IrO_x films calcined for 10 min at 375 °C in air,[19] a ≈1.8-fold higher mass activity reflects the superior noble metal utilization as a result from our proposed concept relying on a combination of EISA and ALD processes for the synthesis of a conductive support and post-modification of its surface with highly active species, respectively.

Importantly, our results from chronopotentiometric stability tests (see Section XIII in the Supporting Information) in acidic electrolyte indicate a remarkably improved durability after IrO_x–ALD. Compared to the unmodified $IrTiO_x$ support, $IrTiO_x$–$60ALD_{IrOx}$ shows a higher stability in acid and better protection from undesired dissolution into the surrounding electrolyte at moderate potentials and static operation as a result of the highly conformal ALD. Post-OER analysis of the

Table 2. Comparison of the most active catalysts in this work with RDE-OER activities of literature-reported Ir-based electrocatalysts (acidic electrolyte, 25 °C).

Catalyst	Ir content	Electrolyte	Electrode	Binder	η [V] (1 mA cm^{-2})	η [V] (10 mA cm^{-2})	Mass activity[a] [A g_{Ir}^{-1}]	Refs.
$IrTiO_x$–$60ALD_{IrOx}$	25 mol%	0.5 M H_2SO_4	Ti chip	Binder free	0.30	0.35	2622	This work
mp. $IrTiO_x$	15 mol% (30 wt%)	0.5 M H_2SO_4	Ti chip	Binder free	0.32	0.41	962	This work
mp. IrO_x (375 °C air)	100 mol%	0.5 M H_2SO_4	Ti chip	Binder free	0.25	0.29	1410	This work
Thermally decomposed Ir/TiO_x	30 mol%	1.0 M $HClO_4$	Ti	Binder free	n. a.	n. a.	39	[54]
ALD–IrO_2/NTO	8 wt%	0.5 M H_2SO_4	Ti foil	Binder free	0.25	n. a.	654 (at 1.69 V)	[55]
ALD-Ir/TiO_2-NTs[b]	n. a.	0.1 M H_2SO_4	TiO_2–NTs	Binder free	n. a.	0.24	200 (at 1.57 V)	[45]
IrO_2@TiO_2	26 mol%	0.1 M $HClO_4$	GC[c]	Nafion binder	n. a.	n. a.	364	[56]
IrO_2/Nb-doped TiO_2	26 wt%	0.5 M H_2SO_4	GC	Nafion binder	0.27	n. a.	≈ 550	[57]
IrO_2–TiO_2-245	40 mol%	0.1 M $HClO_4$	GC	Nafion binder	n. a.	n. a.	≈70 (at 1.53 V)	[58]
IrO_2/ATO	25 wt%	0.5 M H_2SO_4	GC	Nafion binder	0.22	n. a.	≈1100	[59]
$IrNiO_x$/Meso-ATO	19 wt%	0.05 M H_2SO_4	GC	Nafion binder	0.28	n. a.	≈90 (at 1.51 V)	[60]
6H-$SrIrO_3$	59 mol%	0.5 M H_2SO_4	GC	Nafion binder	n. a.	0.25	≈75 (at 1.53 V)	[61]
β-H_xIrO_3	79 mol%	1.0 M H_2SO_4	GC	Nafion binder	n. a.	0.35	≈150 (at 1.58 V)	[62]
Ir-nano 99.8-P	100 mol%	0.5 M H_2SO_4	GC	Nafion binder	n. a.	n. a.	≈580 (at 1.56 V)	[63]

[a]Mass activities calculated based on the loading amounts of active species in the catalysts at a potential of 1.60 V_{RHE} (unless otherwise stated). For the herein developed catalysts, geometric Ir loadings were analyzed via quantitative SEM-EDX measurements. Moreover, the Ir-normalized mass activities were derived from the current densities of the 50th CV in an RDE setup at 1.60 V_{RHE}; [b]NTs, nanotubes; [c]GC, glassy carbon.

spent catalysts via SEM-EDX revealed a significant loss (≈90%) of Ir species for bare mp. $IrTiO_x$, whereas the geometric Ir loading was essentially unaltered for $IrTiO_x$–$60ALD_{IrO_x}$. It has to be noted that further investigations will be necessary in order to assess the electrode durability at fluctuating potentials over a broad current range and dynamic operation (see Section XIII in the Supporting Information for discussion).

2.5. Impact of Support Material on OER Activity

According to the results from the electrochemical studies, not only the temperature and cycle number of the ALD process emerge as decisive parameters for high catalytic activities but also the presence of a minimum of Ir in the bulk phase of the mesoporous support is required to promote fast charge transfer kinetics at the electrode. ALD-modified TiO_2-supported catalysts show significantly lower OER activities than their $IrTiO_x$-supported counterparts, despite the formation of conductive surface electron pathways, indicated by steeply rising sheet conductivities after 60 cycles ALD (cf. Section VIII in the Supporting Information).

Evidently, a high electrical conductivity in the bulk of the catalyst is essential to promote charge carrier kinetics and, beyond that, balance the overall charge of the material during OER by reversible proton insertion.[62] Our results suggest that the incorporation of 15 mol% of Ir into the titania-based support improves both the bulk electrical conductivity and the proton diffusivity and, thus, boosts catalytic activity after surface-modification with IrO_x via ALD at 120 °C. Analyses of the Tafel slopes summarized in Table 1 further corroborate the impact of the support on the catalytic activities. For TiO_2-supported catalysts, large values of more than 100 mV dec^{-1} were found (see also Section XI in the Supporting Information). Contrarily, $IrTiO_x$-supported catalysts show smaller values between 69 and 55 mV dec^{-1} with decreasing slopes for higher ALD cycle numbers, indicating faster reaction kinetics. Accordingly, a high electrical conductivity of the support material for ALD-deposited active sites plays an essential role in the design of active electrocatalysts with strong interactions between the surface metal (oxide) species and the support.

3. Conclusion

A sophisticated concept for the design of highly efficient OER catalyst coatings based on electrically conductive porous supports surface-modified with thin, shape-conformal layers of a catalytically active species was successfully developed. Therein, an optimized ALD process was used to ensure the deposition of layer-like oxidic Ir^{x+} surface species on a well-conductive mixed iridium-titanium oxide support with template-controlled mesoporosity (mp. $IrTiO_x$). A sufficient electrical bulk conductivity of the mesoporous support is a key prerequisite to reach high OER activities. The most active system, $IrTiO_x$–$60ALD_{IrO_x}$, achieves an outstanding mass-specific OER activity of 2622 A g_{Ir}^{-1} at 1.60 V_{RHE} in a typical RDE setup at 25 °C and 0.5 M H_2SO_4 as a supporting electrolyte, which can be explained by the predominance of well-accessible, active oxidic Ir^{x+} sites. Highly conformal ALD at 120 °C paves the way toward a maximized utilization of these homogeneously distributed Ir species, culminating in a 2.7-fold higher Ir mass-specific activity than that of the unmodified mp. $IrTiO_x$ support.

As an outlook, our proposed concept can be principally transferred to other support materials and surface-exposed active species introduced via conformal ALD. As such, we expect the concept as highly promising for the future development of highly efficient (electro-)catalysts with an improved utilization of active sites.

4. Experimental Section

Material Synthesis: Substrate Pretreatments: For the deposition of the soft-templated mesoporous support films, different substrates were used. Single-side polished silicon (Si) wafers were obtained from University Wafers with (100) orientation and cleaned with EtOH after a thermal treatment for 2 h at 600 °C in air prior to the deposition of the support films. For the electrical sheet conductivity measurements, quartz glass (SiO_2) substrates bought from Science Services GmbH were used and etched prior to film deposition using a mixture of KOH and ^{i}PrOH in an ultrasonic bath. Electrochemical measurements were conducted on films deposited on electrically conductive titanium (Ti) substrates, polished with a colloidal silica suspension (amorphous, 0.02 µm, Buehler, MasterMet 2) and subsequently cleaned using a mixture of EtOH and ^{i}PrOH (1:1).

Material Synthesis: Synthesis of Soft-Templated Mesoporous TiO_2 Films: For the synthesis of mesoporous TiO_2 films, titanium(IV)chloride ($TiCl_4$, > 99.9%) was purchased from Sigma–Aldrich. Ethanol p. a. (EtOH, ≥99.8%) was purchased from VWR Chemicals. As structure-directing agent, a triblock copolymer PEO-PB-PEO, comprised of 20 400 g mol^{-1} polyethylene oxide (PEO) and 10 000 g mol^{-1} polybutadiene (PB), was purchased from Polymer Service Merseburg GmbH.[10] All chemicals were used as received without any further purification.

In a typical synthesis, the PEO-PB-PEO polymer template (75 mg) was dissolved in EtOH (2.00 mL) under stirring at 40 °C in air (I). $TiCl_4$ (232 µL) was dissolved in a closed vial in EtOH (2.00 mL) in an Ar-filled glovebox and added to solution (I). The obtained clear solution (II) was stirred for a further 30 min at 40 °C. Dip-coating was performed in air at 25 °C ambient temperature, 40% relative humidity (RH) and 300 mm min^{-1} withdrawal rate. The cuvette (PTFE) containing the clear precursor solution (II) was constantly heated to $T_{cuvette}$ = 45 °C. After drying for at least 10 min in a controlled atmosphere inside the dip-coating setup, crack-free colored films were obtained on different substrates. After drying for at least 1 h at 80 °C in air, all samples were calcined for 20 min at 475 °C in air with a heating ramp of 2 K min^{-1} in a muffle furnace.

Material Synthesis: Synthesis of Soft-Templated Mesoporous $IrTiO_x$ Films: The PEO-PB-PEO polymer template (60 mg) was dissolved in EtOH (1.50 mL) under stirring at 40 °C in air (III). $TiCl_4$ (114 µL) was dissolved in a closed vial in EtOH (1.50 mL) in an Ar-filled glovebox and added to solution (**III**). The obtained clear solution (**IV**) was stirred for a further 20 min at 40 °C. Then, iridium acetate (68 mg, $Ir(OAc)_3$, Heraeus, 48.76% Ir content) was added under stirring to (IV). A dark green, clear solution (V) was obtained after stirring for a further 30 min at 40 °C. Dip-coating was performed in air at 25 °C ambient temperature, 40% RH and 250 mm min^{-1} withdrawal rate. The cuvette was constantly heated to $T_{cuvette}$ = 45 °C. After drying for at least 10 min in a controlled atmosphere inside the dip-coating setup, crack-free colored films were obtained on different substrates. Calcination was conducted for 10 min at 375 °C in air in a preheated muffle furnace.

Material Synthesis: ALD on Different Mesoporous Supports: 1-Ethylcyclopentadienyl-1,3-cyclohexadieneiridium(I) [(EtCp)Ir^{l}CHD, 99%] was purchased from abcr GmbH. Ozone (O_3) was produced from oxygen (O_2, 99%) in an AC-2025 ozone generator-2000, Teledyne API. Nitrogen (N_2), argon (Ar), and O_2 were supplied by Air Liquide (99.9%).

Ir/IrO_x species were deposited on mesoporous films, i.e., mp. TiO_2, mp. $IrTiO_x$ on flat Ti, Si or quartz substrates. Additionally, pre-cleaned single-side polished Si-wafers (Siegert Wafer B014002) with a native SiO_2 layer (≈ 1.2–1.8 nm) were also added into the ALD chamber for calibration of the Ir/IrO_x layer thicknesses via spectroscopic ellipsometry (SE). ALD was performed in a thermal ALD system by ARRADIANCE (GEMStar-XT).

[(EtCp)Ir^{I}CHD] (at 90 °C) and O_3 (as-generated at rt.) were used as metal precursor and oxygen source, respectively. The Ir precursor and the O_2 source were supplied to the reaction chamber using two separate manifolds that were maintained at 110 °C and 100 °C, respectively. N_2 was used as a carrier gas (at 50 sccm) for the precursors into the reaction chamber, and also as a purging gas (at 100 sccm) for excess of reactants and by-products. The ALD system was evacuated (≈7 mTorr) and the temperature of the ALD reaction chamber was stabilized at 160 °C or 120 °C before starting the deposition. Prior to ALD, all samples were in situ treated with O_3 (10 cycles of 0.2 s O_3 pulse/30 s exposure/15 s purge, total exposure time of 300 s) to remove any residual organic surface impurities and to functionalize the surface. The pulse/exposure/purge time for one ALD cycle was set to 0.8 s/40 s/20 s and 0.25 s/45 s /30 s for Ir precursor and O_3, respectively. For the Ir precursor, the pulse/exposure/purge time was repeated two times within one ALD cycle. The loading of the deposited Ir/IrO_x species on the mesoporous films was controlled by varying the number of ALD cycles from 20 to 60.

Physicochemical Characterization: SEM and EDX: SEM images were recorded at 10 kV on a JEOL JSM-7401F instrument. The acquired images were then evaluated using ImageJ freeware (v. 1.48; www.imagej.nih.gov/ij/), which was also applied for the generation of the corresponding FFT images. For the estimation of the Ir mass loadings per cm^2 geometric area, SEM-EDX measurements were conducted using a Quantax 400 (Bruker) energy-dispersive X-ray spectrometer coupled with an electrometer model 6517B (Keithley) to determine the probe currents. For the latter, a Faraday cup was used to catch back-scattered, secondary and Auger electrons. An average value for the probe current was calculated based on the acquired values prior to and after the acquisition of an EDX spectrum of a material. For each sample, at least three different areas were analyzed via EDX analysis at a magnification of 1 kx. The measurement duration was set to at least 120 s. For the evaluation of the acquired EDX spectra, the software Esprit (Bruker) was used. A charge-and time-normalized signal intensity was obtained by dividing the average value of the Ir-Mα_1 and -M$_\beta$ lines by the average probe current and measurement duration. Quantitative Ir mass loadings were finally calculated by using a previously determined calibration factor evaluated from reference measurements of samples with Ir loadings validated via StrataGem analysis.[64,65] K-values were estimated from measurements of Ir metal (99.8%). Measurement errors were found negligible with only between 1% to 2% relative error.

ICP-OES: As an alternative method to analyze the geometric Ir loadings of the catalyst support films prior to ALD, ICP-OES measurements of the uncalcined mesophases deposited on flat Ti substrates were performed. Measurements were conducted on a Varian ICP-OES 715 ES (radial configuration, CCD detector). For calibration, aqueous solutions with different Ir concentrations (Carl Roth) were prepared. For the calculation of the geometric Ir loading, the geometric area of each film was calculated using ImageJ software prior to dissolution of the sample. For the dissolution of the samples via acid digestion, a solution of HCl (3.0 mL, Carl Roth, 37%), HNO_3 (1.0 mL, Carl Roth, 69%), H_2SO_4 (1.0 mL, Carl Roth, 96%) and $NaClO_3$ (20.0 mg, Alfa Aesar, 99.0%) was prepared. After 2 h at 30 °C in an ultrasonic bath, a clear solution was obtained and analyzed via ICP-OES to estimate the Ir content. For the TiO_2 support, essentially no Ir was found (0.0 μg_{Ir} cm^{-2}) and for $IrTiO_x$ a loading of 3.8 ± 0.3 μg_{Ir} cm^{-2} was obtained, which is in good agreement with EDX-derived geometric Ir loadings.

PTEM, EDX, and SAED: TEM images were acquired on a FEI Talos transmission electron microscope with 200 kV acceleration voltage on scraped-off film fragments which were deposited on carbon-coated copper grids. A FEI Talos EDX detector was used for the analysis of the elemental distributions via elemental mappings. The TEM data and EDX mappings were analyzed using FEI Velox software (v. 2.6).

XPS: X-ray photoelectron spectra (XPS) were obtained on a Thermo Fisher Scientific ESCALAB 250Xi with 400 µm spot size, K_α-X-rays. The peak position of adventitious carbon species at the surface (at a BE of 284.80 eV) was applied for correction of the binding energies of the obtained spectra. Data fitting and quantification to calculate the elemental composition were done using the software Avantage.

GI-XRD: XRD measurements were conducted using a Bruker D8 Advance instrument (Cu-K-α) in grazing-incidence geometry applying a Goebel mirror.

Electrical Sheet Conductivity: The electrical sheet conductivities were analyzed via impedance spectroscopy in a home-built setup in the dark. All measurements were carried out applying a 8 × 8 gold pin array as a probe head showing an altering polarity sequence. A SP-200 potentiostat (Biologic) was used (range from 100 mHz to 1 kHz). The obtained spectra (Nyquist impedance) were fitted using EIS Zfit software (EC-Lab version 11.33, Biologic). All given values were normalized to the average film thickness, estimated from cross-sectional SEM images of films deposited on Si substrates. For the impedance spectroscopy measurements, all films were deposited on planar, insulating quartz glass substrates.

Electrochemical Testing Procedure: OER Performance: All catalysts were tested in acidic OER via cyclic voltammetry (CV) performed using a rotating disc electrode setup (RDE). A reversible hydrogen electrode (Gaskatel, HydroFlex) was applied as a reference electrode and a Pt-gauze (Chempur, 1024 mesh cm^{-2}, wire diameter 0.06 mm, 99.9% purity) was used as counter electrode at 25 °C. All potentials are referred to the reversible hydrogen electrode (RHE) scale and were *iR*-corrected to account for Ohmic losses. All films were coated on a spherical Ti chip of 5 mm diameter and mounted on a rotating disc shaft serving as a working electrode. Due to the fact that all electrocatalysts were directly synthesized as porous films on polished Ti substrates, the addition of Nafion binder was not necessary. A rotation of 1600 rpm was set. 0.5 M H_2SO_4 was used as a supporting electrolyte (Fixanal, Fluka Analytical) and a SP-200 (Biologic) was used as a potentiostat. The electrolyte solution was purged with N_2 for at least 20 min prior to catalytic testing. The OER activity was assessed by cyclic voltammetry (CV) in a potential window ranging between 1.20 and 1.65 V versus RHE (V_{RHE}) at a scan rate of 6 mV s^{-1}. Chronopotentiometry was performed in an RDE setup in 0.5 M H_2SO_4 over 24 h at 25 °C. The potential (vs RHE) was recorded at a current density *j* of 1.0 mA cm^{-2}, considering the ultra-low Ir loadings in the catalyst films.

Base Voltammetry for ECSA Estimation: After 100 CVs in OER regime, a base voltammetry measurement was performed in a lower potential range between 0.40 to 1.40 V_{RHE} at 25 °C for an estimation of the ECSA with a scan rate of 50 mV s^{-1}, according to a previously published method.[20,30] In brief, the calculated average value of the integrated anodic and cathodic scan of the recorded *iR*-corrected CVs ($q_{(a+c)/2}$) can be used to estimate the amount of accessible iridium sites for each catalyst film. This method relies on Faradaic currents of different Ir^{x+} redox active sites correlating with their abundancy and accessibility to the electrolyte.[30,66]

Preparation of a Homogeneous Ink for RDE Measurements of a Commercial Reference (Elyst, Umicore): To investigate the OER performance of the industrially relevant and commercially available Ir/TiO_2 catalyst powder (74.7 wt.-% Ir in TiO_2, Elyst Ir 75 0480, Umicore), a dispersion was prepared by suspending the black powder (5.4 mg) in a mixture of MilliQ-H_2O (2.49 mL), ^{i}PrOH (2.49 mL, > 99.5%, Carl Roth) and Nafion perfluorinated resin (20 µL, 5 wt-% in lower aliphatic alcohols and H_2O, Sigma Aldrich, 15–20% H_2O). A homogeneous ink of dark black color was obtained after the application of ultrasound for 10 min using an ultrasonic tip (Bandelin, Sonopuls). 5 µL of the ink were subsequently drop-casted at room temperature onto an extensively polished Ti cylinder with a geometric surface area of 0.1963 cm^{-2} and dried at 65 °C in a preheated drying oven in air for 10 min. This step was repeated between one to five times to afford nominal Ir loadings of

≈20 to 100 µg cm^{-2}. The assessment of catalytic OER activity in an RDE setup revealed a linear dependence of nominal Ir loading and current density *j* at a potential of 1.60 V_{RHE}.

Supporting Information

Supporting Information is available from the Wiley Online Library or from the author.

Acknowledgements

M.F. and M.H.R. contributed equally to this work. The authors acknowledge preliminary studies by Michael Bernicke (TU Berlin) on the synthesis of the mesoporous support films and subsequent ALD modifications. Arne Thomas (TU Berlin) is thankfully acknowledged for granting access to a setup for XPS analysis. Christoph Erdmann (HU Berlin) is acknowledged for TEM measurements. Leyla Kotil (TU Berlin) is thankfully acknowledged for the assistance in the calibration of the SEM-EDX measurements for the estimation of the geometric Ir loadings. The authors gratefully acknowledge financial support by BMBF (Bundesministerium für Bildung und Forschung) ATO-KAT: Atomar dünn beschichtete poröse Elektroden als neuartige Katalysatoren für die Wasser-Elektrolyse (03EK3052A). R.S. acknowledges generous funding from the project ATMOC (20IND04, Traceable metrology of soft X-ray to IR optical constants and nanofilms for advanced manufacturing). R.K. gratefully acknowledges funding through the DFG SPP 2080 priority program (KR 3920/4-1).

Open access funding enabled and organized by Projekt DEAL.

Conflict of Interest

The authors declare no conflict of interest.

Data Availability Statement

The data that support the findings of this study are available from the corresponding author upon reasonable request.

Keywords

acidic oxygen evolution reaction, atomic layer deposition, electrocatalysis, iridium oxide, soft-templated mesoporous films

Received: October 18, 2021
Revised: December 15, 2021
Published online: January 27, 2022

[1] I. Dincer, *Int. J. Hydrogen Energy* **2012**, *37*, 1954.
[2] R. Bhandari, C. A. Trudewind, P. Zapp, *J. Cleaner Prod.* **2014**, *85*, 151.
[3] K. Mazloomi, C. Gomes, *Renewable Sustainable Energy Rev.* **2012**, *16*, 3024.
[4] G. Glenk, S. Reichelstein, *Nat. Energy* **2019**, *4*, 216.
[5] F. Barbir, *Sol. Energy* **2005**, *78*, 661.
[6] S. Cobo, J. Heidkamp, P.-A. Jacques, J. Fize, V. Fourmond, L. Guetaz, B. Jousselme, V. Ivanova, H. Dau, S. Palacin, M. Fontecave, V. Artero, *Nat. Mater.* **2012**, *11*, 802.
[7] M. Carmo, D. L. Fritz, J. Mergel, D. Stolten, *Int. J. Hydrogen Energy* **2013**, *38*, 4901.
[8] A. L. Strickler, R. A. Flores, L. A. King, J. K. Nørskov, M. Bajdich, T. F. Jaramillo, *ACS Appl. Mater. Interfaces* **2019**, *11*, 34059.
[9] L. C. Seitz, C. F. Dickens, K. Nishio, Y. Hikita, J. Montoya, A. Doyle, C. Kirk, A. Vojvodic, H. Y. Hwang, J. K. Norskov, T. F. Jaramillo, *Science* **2016**, *353*, 1011.
[10] E. Ortel, T. Reier, P. Strasser, R. Kraehnert, *Chem. Mater.* **2011**, *23*, 3201.
[11] N. Mamaca, E. Mayousse, S. Arrii-Clacens, T. W. Napporn, K. Servat, N. Guillet, K. B. Kokoh, *Appl. Catal., B* **2012**, *111-112*, 376.
[12] M. A. Hubert, A. M. Patel, A. Gallo, Y. Liu, E. Valle, M. Ben-Naim, J. Sanchez, D. Sokaras, R. Sinclair, J. K. Nørskov, L. A. King, M. Bajdich, T. F. Jaramillo, *ACS Catal.* **2020**, *10*, 12182.
[13] Z. Shi, X. Wang, J. Ge, C. Liu, W. Xing, *Nanoscale* **2020**, *12*, 13249.
[14] R. A. Flores, C. Paolucci, K. T. Winther, A. Jain, J. A. G. Torres, M. Aykol, J. Montoya, J. K. Nørskov, M. Bajdich, T. Bligaard, *Chem. Mater.* **2020**, *32*, 5854.
[15] V. V. Panić, A. B. Dekanski, M. Mitrić, S. K. Milonjić, V. B. Mišković-Stanković, B. Ž. Nikolić, *Phys. Chem. Chem. Phys.* **2010**, *12*, 7521.
[16] A. Marshall, S. Sunde, M. Tsypkin, R. Tunold, *Int. J. Hydrogen Energy* **2007**, *32*, 2320.
[17] A. Marshall, B. Børresen, G. Hagen, M. Tsypkin, R. Tunold, *Electrochim. Acta* **2006**, *51*, 3161.
[18] A. Hartig-Weiss, M. Miller, H. Beyer, A. Schmitt, A. Siebel, A. T. S. Freiberg, H. A. Gasteiger, H. A. El-Sayed, *ACS Appl. Nano Mater.* **2020**, *3*, 2185.
[19] M. Bernicke, E. Ortel, T. Reier, A. Bergmann, J. Ferreira de Araujo, P. Strasser, R. Kraehnert, *ChemSusChem* **2015**, *8*, 1908.
[20] D. Bernsmeier, M. Bernicke, R. Schmack, R. Sachse, B. Paul, A. Bergmann, P. Strasser, E. Ortel, R. Kraehnert, *ChemSusChem* **2018**, *11*, 2367.
[21] C. Comninellis, G. P. Vercesi, *J. Appl. Electrochem.* **1991**, *21*, 335.
[22] S. Geiger, O. Kasian, A. M. Mingers, K. J. J. Mayrhofer, S. Cherevko, *Sci. Rep.* **2017**, *7*, 4595.
[23] C. Daiane Ferreira da Silva, F. Claudel, V. Martin, R. Chattot, S. Abbou, K. Kumar, I. Jiménez-Morales, S. Cavaliere, D. Jones, J. Rozière, L. Solà-Hernandez, C. Beauger, M. Faustini, J. Peron, B. Gilles, T. Encinas, L. Piccolo, F. H. Barros de Lima, L. Dubau, F. Maillard, *ACS Catal.* **2021**, *11*, 4107.
[24] M. Shao, Q. Chang, J.-P. Dodelet, R. Chenitz, *Chem. Rev.* **2016**, *116*, 3594.
[25] F. Lyu, Q. Wang, S. M. Choi, Y. Yin, *Small* **2019**, *15*, 1804201.
[26] C. J. Brinker, Y. Lu, A. Sellinger, H. Fan, *Adv. Mater.* **1999**, *11*, 579.
[27] T. Brezesinski, M. Groenewolt, A. Gibaud, N. Pinna, M. Antonietti, B. Smarsly, *Adv. Mater.* **2006**, *18*, 2260.
[28] C. Sanchez, C. Boissière, D. Grosso, C. Laberty, L. Nicole, *Chem. Mater.* **2008**, *20*, 682.
[29] E. Ortel, A. Fischer, L. Chuenchom, J. Polte, F. Emmerling, B. Smarsly, R. Kraehnert, *Small* **2012**, *8*, 298.
[30] M. Bernicke, D. Bernsmeier, B. Paul, R. Schmack, A. Bergmann, P. Strasser, E. Ortel, R. Kraehnert, *J. Catal.* **2019**, *376*, 209.
[31] M. Frisch, J. Laun, J. Marquardt, A. Arinchtein, K. Bauerfeind, D. Bernsmeier, M. Bernicke, T. Bredow, R. Kraehnert, *Phys. Chem. Chem. Phys.* **2021**, *23*, 3219.
[32] E. Ortel, J. Polte, D. Bernsmeier, B. Eckhardt, B. Paul, A. Bergmann, P. Strasser, F. Emmerling, R. Kraehnert, *Appl. Catal., A* **2015**, *493*, 25.
[33] S. M. George, *Chem. Rev.* **2010**, *110*, 111.
[34] M. Ritala, M. Leskelä, in *Handbook of Thin Film Materials*, Vol. 1, Academic Press, San Diego **2002**, pp. 103–159.
[35] N. Pinna, M. Knez, *Atomic Layer Deposition of Nanostructured Materials*, Wiley-VCH, Weinheim, Germany **2011**.
[36] C. Marichy, M. Bechelany, N. Pinna, *Adv. Mater.* **2012**, *24*, 1017.
[37] K. L. Pickrahn, S. W. Park, Y. Gorlin, H.-B.-R. Lee, T. F. Jaramillo, S. F. Bent, *Adv. Energy Mater.* **2012**, *2*, 1269.
[38] M. H. Raza, K. Movlaee, S. G. Leonardi, N. Barsan, G. Neri, N. Pinna, *Adv. Funct. Mater.* **2020**, *30*, 1906874.

[39] Y. Fan, Y. Wu, G. Clavel, M. H. Raza, P. Amsalem, N. Koch, N. Pinna, *ACS Appl. Energy Mater.* **2018**, *1*, 4554.
[40] G. N. Parsons, S. M. George, M. Knez, *MRS Bull.* **2011**, *36*, 865.
[41] J. Hämäläinen, T. Hatanpää, E. Puukilainen, T. Sajavaara, M. Ritala, M. Leskelä, *J. Mater. Chem.* **2011**, *21*, 16488.
[42] J. Hämäläinen, M. Ritala, M. Leskelä, *Chem. Mater.* **2014**, *26*, 786.
[43] F. Li, L. Li, X. Liao, Y. Wang, *J. Membr. Sci.* **2011**, *385-386*, 1.
[44] S. Schlicht, S. Haschke, V. Mikhailovskii, A. Manshina, J. Bachmann, *ChemElectroChem* **2018**, *5*, 1259.
[45] S. Schlicht, P. Büttner, J. Bachmann, *ACS Appl. Energy Mater.* **2019**, *2*, 2344.
[46] J. Hämäläinen, M. Kemell, F. Munnik, U. Kreissig, M. Ritala, M. Leskelä, *Chem. Mater.* **2008**, *20*, 2903.
[47] V. Pfeifer, T. E. Jones, J. J. Velasco Vélez, C. Massué, R. Arrigo, D. Teschner, F. Girgsdies, M. Scherzer, M. T. Greiner, J. Allan, M. Hashagen, G. Weinberg, S. Piccinin, M. Hävecker, A. Knop-Gericke, R. Schlögl, *Surf. Interface Anal.* **2016**, *48*, 261.
[48] H. Y. Hall, P. M. A. Sherwood, *J. Chem. Soc., Faraday Trans. 1* **1984**, *80*, 135.
[49] H. Cesiulis, N. Tsyntsaru, A. Ramanavicius, G. Ragoisha, in *Nanostructures and Thin Films for Multifunctional Applications: Technology, Properties and Devices* (Eds: I. Tiginyanu, P. Topala, V. Ursaki), Springer, Berlin **2016**, pp. 3–42.
[50] S. Fierro, L. Ouattara, E. H. Calderon, C. Comninellis, *Electrochem. Commun.* **2008**, *10*, 955.
[51] R. Sachse, M. Pflüger, J.-J. Velasco-Vélez, M. Sahre, J. Radnik, M. Bernicke, D. Bernsmeier, V.-D. Hodoroaba, M. Krumrey, P. Strasser, R. Kraehnert, A. Hertwig, *ACS Catal.* **2020**, *10*, 14210.
[52] S. Schlicht, M. K. S. Barr, M. Wu, P. Hoppe, E. Spiecker, W. Peukert, J. Bachmann, *ChemElectroChem* **2018**, *5*, 3932.
[53] D. Bernsmeier, M. Bernicke, E. Ortel, A. Bergmann, A. Lippitz, J. Nissen, R. Schmack, P. Strasser, J. Polte, R. Kraehnert, *ChemElectroChem* **2017**, *4*, 221.
[54] A. Rossi, J. F. C. Boodts, *J. Appl. Electrochem.* **2002**, *32*, 735.
[55] A. G. Hufnagel, S. Häringer, M. Beetz, B. Böller, D. Fattakhova-Rohlfing, T. Bein, *Nanoscale* **2019**, *11*, 14285.
[56] C. Van Pham, M. Bühler, J. Knöppel, M. Bierling, D. Seeberger, D. Escalera-López, K. J. J. Mayrhofer, S. Cherevko, S. Thiele, *Appl. Catal., B* **2020**, *269*, 118762.
[57] W. Hu, S. Chen, Q. Xia, *Int. J. Hydrogen Energy* **2014**, *39*, 6967.
[58] E. Oakton, D. Lebedev, M. Povia, D. F. Abbott, E. Fabbri, A. Fedorov, M. Nachtegaal, C. Copéret, T. J. Schmidt, *ACS Catal.* **2017**, *7*, 2346.
[59] D. Böhm, M. Beetz, M. Schuster, K. Peters, A. G. Hufnagel, M. Döblinger, B. Böller, T. Bein, D. Fattakhova-Rohlfing, *Adv. Funct. Mater.* **2020**, *30*, 1906670.
[60] H. N. Nong, H.-S. Oh, T. Reier, E. Willinger, M.-G. Willinger, V. Petkov, D. Teschner, P. Strasser, *Angew. Chem., Int. Ed.* **2015**, *54*, 2975.
[61] L. Yang, G. Yu, X. Ai, W. Yan, H. Duan, W. Chen, X. Li, T. Wang, C. Zhang, X. Huang, J.-S. Chen, X. Zou, *Nat. Commun.* **2018**, *9*, 5236.
[62] P. E. Pearce, C. Yang, A. Iadecola, J. Rodriguez-Carvajal, G. Rousse, R. Dedryvère, A. M. Abakumov, D. Giaume, M. Deschamps, J.-M. Tarascon, A. Grimaud, *Chem. Mater.* **2019**, *31*, 5845.
[63] P. Lettenmeier, J. Majchel, L. Wang, V. A. Saveleva, S. Zafeiratos, E. R. Savinova, J.-J. Gallet, F. Bournel, A. S. Gago, K. A. Friedrich, *Chem. Sci.* **2018**, *9*, 3570.
[64] E. Ortel, A. Hertwig, D. Berger, P. Esposito, A. M. Rossi, R. Kraehnert, V.-D. Hodoroaba, *Anal. Chem.* **2016**, *88*, 7083.
[65] R. Sachsé, A. Hertwig, R. Kraehnert, V.-D. Hodoroaba, *Microsc. Microanal.* **2018**, *24*, 762.
[66] S. Ardizzone, A. Carugati, S. Trasatti, *J. Electroanal. Chem. Interfacial Electrochem.* **1981**, *126*, 287.

ADVANCED MATERIALS INTERFACES

Supporting Information

for *Adv. Mater. Interfaces,* DOI: 10.1002/admi.202102035

ALD-Coated Mesoporous Iridium-Titanium Mixed Oxides: Maximizing Iridium Utilization for an Outstanding OER Performance

Marvin Frisch, Muhammad Hamid Raza, Meng-Yang Ye, René Sachse, Benjamin Paul, René Gunder, Nicola Pinna, and Ralph Kraehnert**

Supporting Information

ALD-coated Mesoporous Iridium-Titanium Mixed Oxides: Maximizing Iridium Utilization for an Outstanding OER Performance

Marvin Frisch‡, Muhammad Hamid Raza‡, Meng-Yang Ye, René Sachse, Benjamin Paul, René Gunder, Nicola Pinna and Ralph Kraehnert**

Table of Contents

Section-I: Morphological analysis of mp. TiO_2 prior to and after ALD *via* SEM

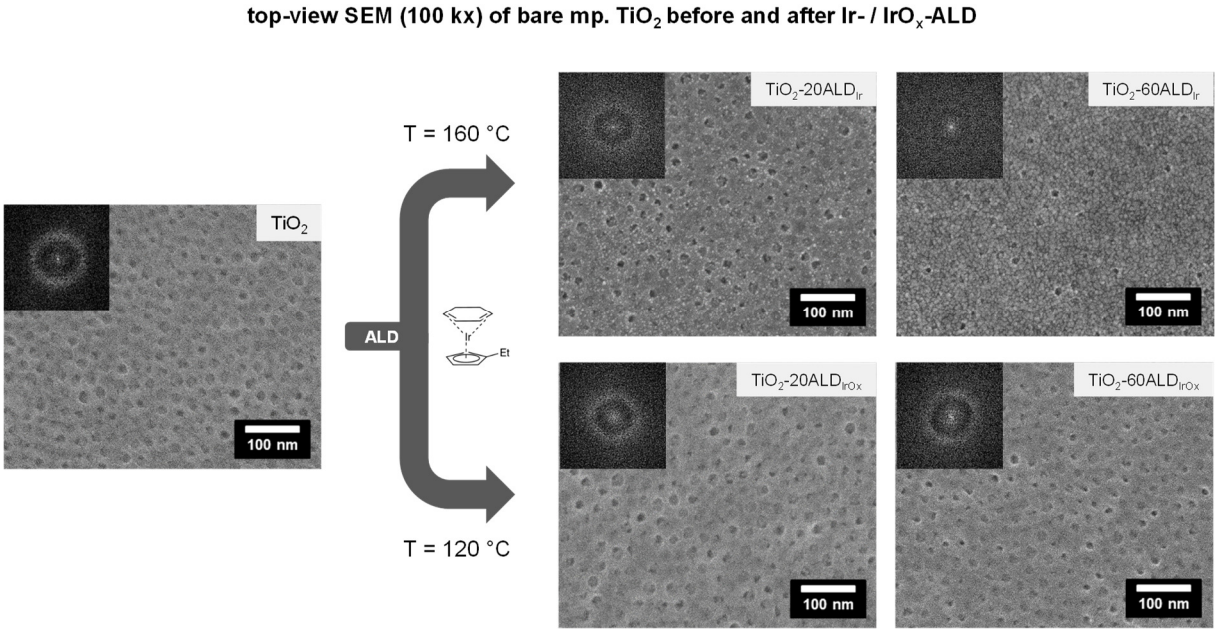

Figure S1. Representative top-view SEM images (100,000x magnification) of mp. TiO_2 films prior to ALD (left) and after ALD at different temperatures (top right: ALD at 160 °C, bottom right: ALD at 120 °C). The images were acquired for films deposited on Si substrates. Corresponding FFT images are shown as insets for each of the top-view SEM images.

Figure S1 illustrates the results from SEM analysis of unmodified, weakly conductive TiO_2 support films prior to ALD (left). The corresponding FFT reveals the formation of a locally ordered mesoporosity after calcination for 20 min at 475 °C in air and a concomitant removal of the polymer template. After 20 ALD cycles at 160 °C, bright spots appear at the surface of the films which indicate the presence of nanoparticulate Ir-rich species. After 60 cycles ALD at 160 °C, these nanoparticles have grown in size and cover almost the entire surface of the film. The mesoporous structure is hence only partially preserved. This is further corroborated by the corresponding FFT inset of TiO_2-60ALD_{Ir}. Contrarily, ALD at 120 °C ensures the deposition of layer-like surface deposits over the range of investigated ALD cycle numbers.

Overall, the results are in good agreement with the observations from the morphological analysis of the mp. $IrTiO_x$ supports presented in **Figure 1** in the main part of this work.

Section-II: Lower magnification SEM of mp. TiO_2 and mp. $IrTiO_x$ prior to and after ALD

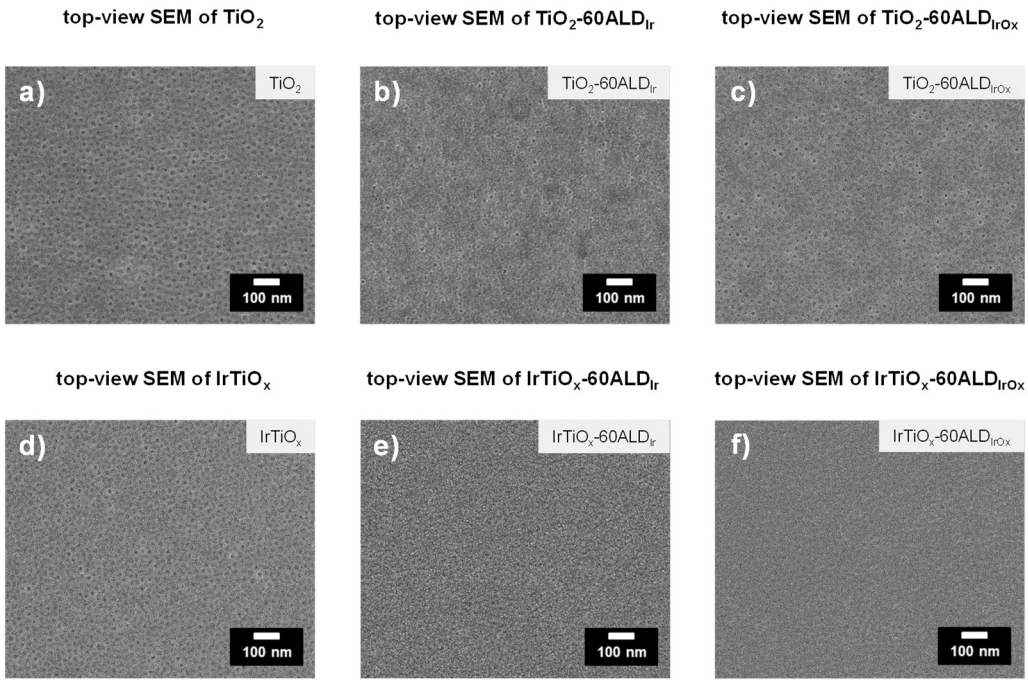

Figure S2. Lower magnification top-view SEM images of mp. TiO_2 (a) prior to ALD, (b) after 60 cycles of Ir-ALD at 160 °C and (c) after 60 cycles of IrO_x-ALD at 120 °C. In (d) – (f), the corresponding images for mp. $IrTiO_x$ prior to and after Ir-/IrO_x-ALD are shown. All images were acquired for films deposited on Si substrates.

Figure S2 shows representative SEM images in a lower magnification of 50,000x for both mp. TiO_2 and mp. $IrTiO_x$ support films prior to ALD (a,d) and after ALD at 160 °C (b,e) as well as after ALD at 120 °C (c,f). The acquired SEM images suggest the predominance of well-defined, crack-free mesoporous structures for all coatings, independent of ALD temperature and cycle number.

Section-III: Structural and phase analysis of mp. TiO_2 prior to and after ALD *via* TEM and SAED

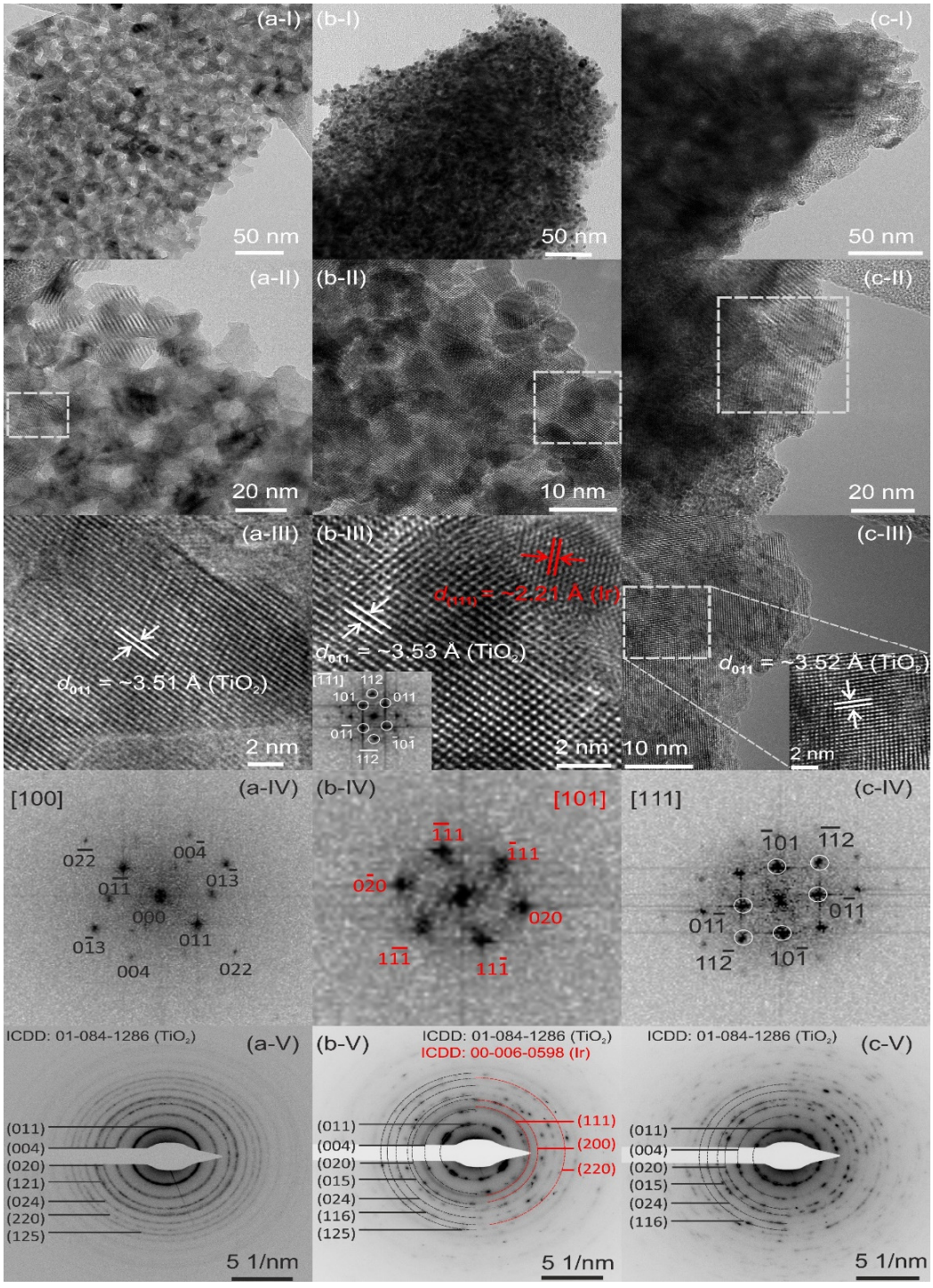

Figure S3. BF-HRTEM images (I-III), power spectra (IV) of the selected regions and SAED patterns (V) for (a) mp. TiO_2, (b) after 60 cycles ALD at 160 °C (TiO_2-60ALD_{Ir}) and (c) after 60 cycles ALD at 120 °C (TiO_2-60ALD_{IrOx}). Patterns are assigned according to the reference ICDD card numbers 01-084-1286 and 00-006-0598 for TiO_2 (anatase) and Ir^0 (cubic), respectively. Red color highlights features corresponding to Ir^0.

The lattice fringes and the PS corresponding to the selected region in the HRTEM image in **Figure S3a, II** are typical for the anatase phase of TiO_2 (**Figure S3a, III-IV**). In addition, the concentric rings in the SAED pattern show reflections corresponding to the anatase planes for TiO_2 (**Figure S3a, V**). This shows that mp. TiO_2 is composed of a nanocrystalline anatase phase after calcination for 20 min at 475 °C in air.

After 60 ALD cycles at 160 °C, the lattice fringes in the HRTEM image and the corresponding PS of the selected areas in **Figure S3b-c, II** clearly reveal the presence of two distinct regions of TiO_2 (marked with white color and the corresponding PS as an inset in **Figure S3b, III**) alongside metallic Ir^0 (highlighted with red color and the corresponding PS in **Figure S3b, IV**), where the interface between the mp. TiO_2 and the ALD-deposited Ir species can be identified as shown in **Figure 3b, III**.

Notably, after 60 ALD cycles at 120 °C, no distinct signals for any metallic Ir^0 surface species introduced *via* ALD can be found (**Figure S3c, II-V**). In fact, weak signals corresponding to IrO_2 (rutile) can be identified in the SAED pattern of ALD-coated $IrTiO_x$ at 120 °C (**Figure S3c, V**).

Section-IV: Elemental mappings of mp. $IrTiO_x$ and mp. TiO_2 films prior to and after ALD

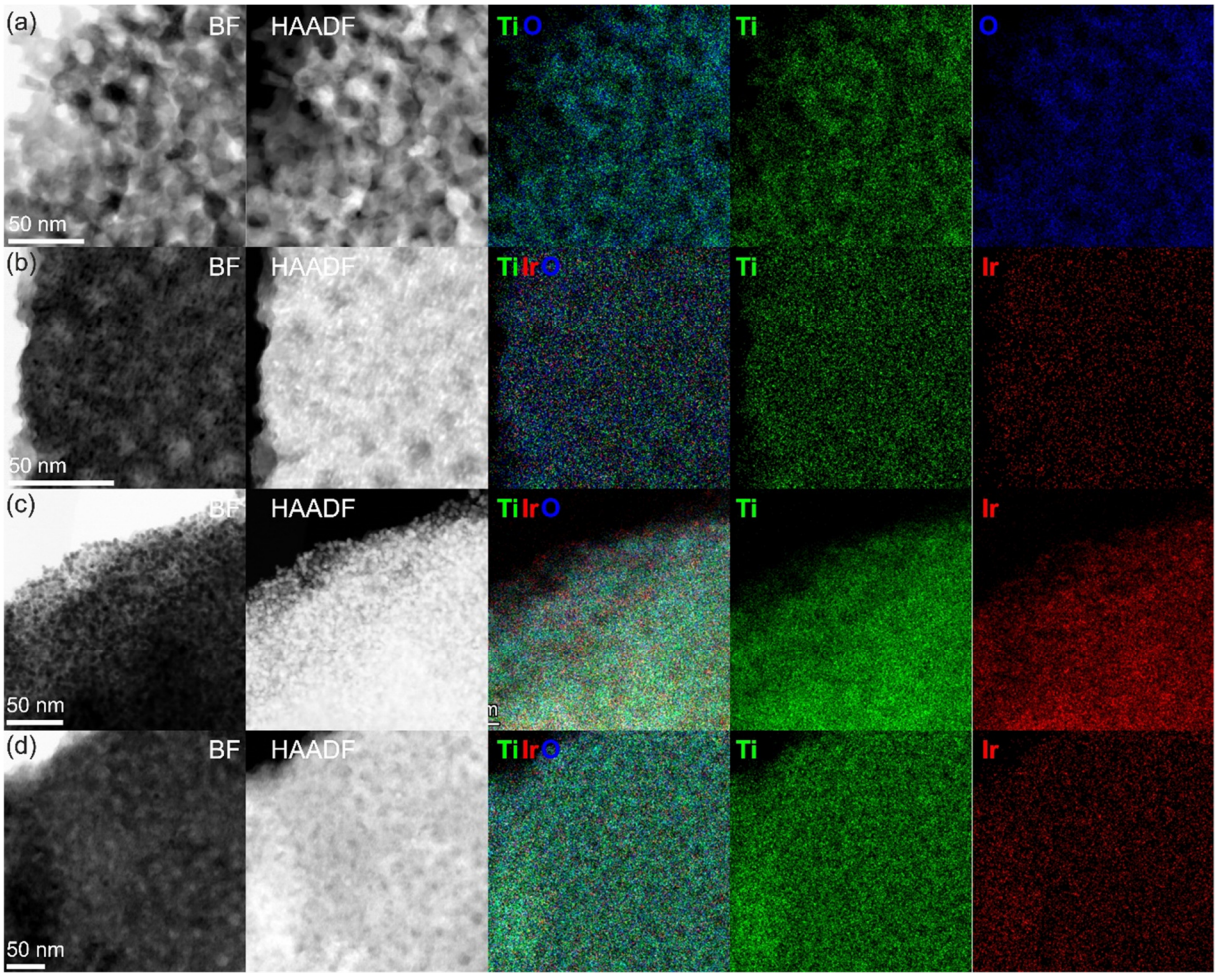

Figure S4-I. BF-STEM, HAADF-STEM images and corresponding EDX mappings for (a) mp. TiO_2 and (b) mp. $IrTiO_x$ prior to ALD, as well as for (c) TiO_2-60ALD_{Ir} and (d) TiO_2-60ALD_{IrOx} after 60 cycles ALD at 160 °C and at 120 °C, respectively.

The BF-STEM images of both TiO_2 and $IrTiO_x$ support films reveal a similar homogeneous mesoporous structure prior to ALD. Regarding the $IrTiO_x$ support, the corresponding elemental mapping underlines a uniform distribution of the Ir species throughout the pore walls.

For the sake of better visibility, the impact of the ALD process and temperature was examined using Ir-free TiO_2 films as support materials. BF-STEM images (c) and (d) clearly indicate the preserved mesoporosity after both ALD processes at 160 °C and at 120 °C. Moreover, the elemental mappings confirm a homogeneous distribution of ALD-introduced Ir / IrO_x species.

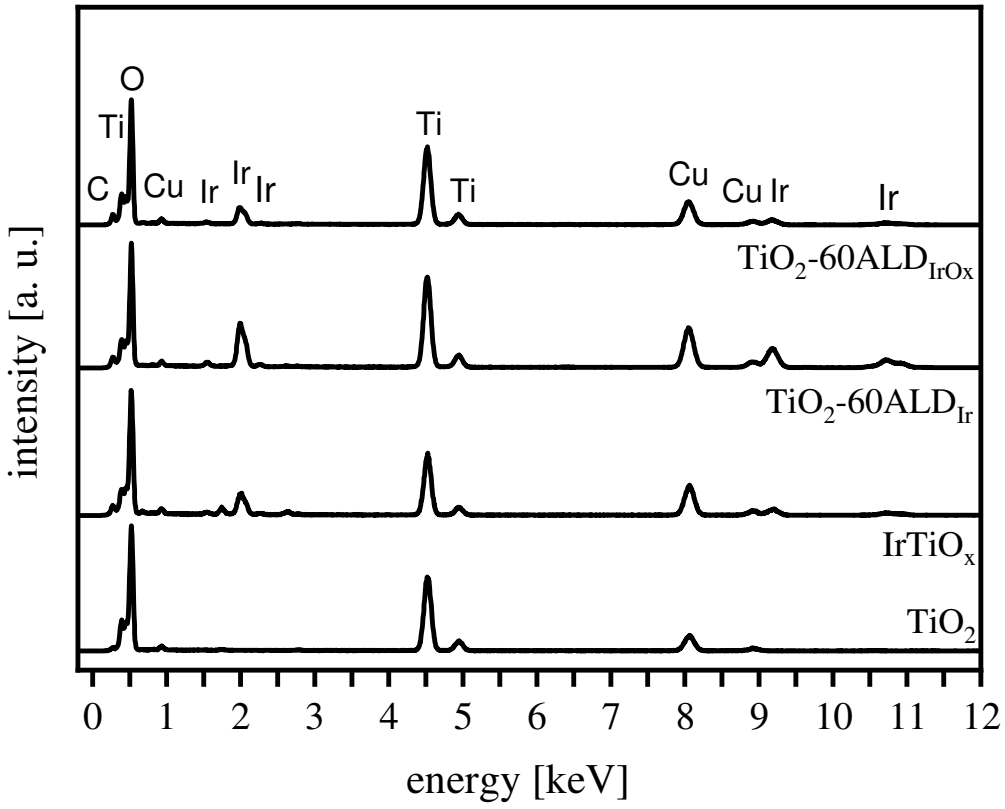

Figure S4-II. TEM-EDX spectra of mp. $IrTiO_x$ (grey) and mp. TiO_2 (black) corresponding to the EDX elemental mapping illustrated in **Figure S4-I**.

Section-V: XPS analysis of fresh and spent mp. $IrTiO_x$ and mp. TiO_2 films prior to and after ALD at 160 °C

In order to study the composition and chemical states of the surface atoms prior to and after ALD at 160 °C, XPS spectra were collected and illustrated in the following (**Figure S5**). Fresh and spent catalyst films on Ti substrates were analyzed to track the influence of OER in acidic electrolyte onto the nature of the surface Ir species. Due to the better signal-to-noise ratio as a consequence of a higher amount of Ir at the surface, the results for supports modified with 60 ALD cycles will be discussed here. In this context, it has to be noted that similar trends regarding the impact of the oxidative conditions during OER catalysis in acidic electrolyte were observed for the 20 cycle modified support films.

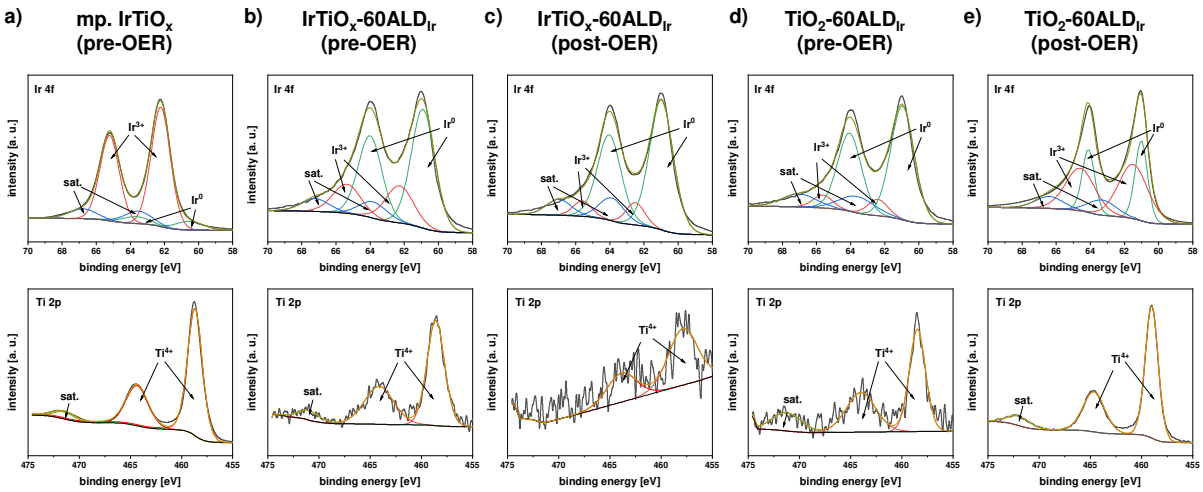

Figure S5. XPS spectra for (a) mp. $IrTiO_x$, (b) $IrTiO_x$-$60ALD_{Ir}$ prior to catalytic testing and (c) $IrTiO_x$-$60ALD_{Ir}$ post-OER in 0.5 M H_2SO_4 as well as (d) TiO_2-$60ALD_{Ir}$ prior to catalytic testing and (e) TiO_2-$60ALD_{Ir}$ post-OER in 0.5 M H_2SO_4. The upper row shows the corresponding Ir 4f spectra with deconvolution of the data and the lower row shows the Ti 2p spectra. All spectra were acquired for films deposited on Ti substrates.

Prior to ALD, the Ir 4f spectrum of mp. $IrTiO_x$ (see **Figure S5a, top**) shows a prominent doublet peak at 62.2 eV corresponding to Ir^{3+} with a characteristic doublet separation of ~ 3.0 eV and broad satellite features corresponding to Ir^{3+}.[1,2] A minor contribution of metallic Ir^0 surface species can be found. As given in **Table S1**, the relative fraction of Ir^{3+} is ten-fold higher than that of Ir^0.

After ALD at 160 °C, however, the most prominent feature can be found at lower binding energies, indicating predominantly Ir^0 species at the surface, since a doublet at 61.0 eV arises for $IrTiO_x$-$60ALD_{Ir}$ (**Figure S5b, top**).[1,2] This is in good agreement with the results from TEM and SAED analyses revealing presence of metallic Ir^0 species for $IrTiO_x$-$60ALD_{Ir}$ (see **Figure 3b** in the main part). Strikingly, after 150 CVs in acidic electrolyte, $IrTiO_x$-$60ALD_{Ir}$ shows a similar surface composition compared to the fresh catalyst (**Figure S5c**). The ALD-deposited nanocrystalline Ir species did not undergo significant oxidation during OER in acid, accordingly. The ratio of Ir^0/Ir^{3+} (**Table S1**) remained similar with 6.3/1 for the fresh $IrTiO_x$-$60ALD_{Ir}$ catalyst and only slightly increased to 6.6/1 for the spent $IrTiO_x$-$60ALD_{Ir}$ catalyst after OER.

For Ir-ALD-modified TiO_2, predominantly metallic Ir^0 surface species can be found according to the XPS data in **Figure S5d**. Analysis of the spent catalyst film after OER, however, indicated a partial conversion of Ir^0 sites to Ir^{3+} after repeated cycling up to a potential of 1.65 V_{RHE}. The ratio drops from 8.3/1 for the fresh TiO_2-$60ALD_{Ir}$ catalyst to 1.6/1 for the spent TiO_2-$60ALD_{Ir}$ film (see **Table S1**). An oxidation of Ir^0 species to Ir species with higher oxidation states has been previously reported in literature[3].

Table S1. Elemental composition at the surface of the catalyst films analyzed *via* XPS prior to and after Ir-ALD at 160 °C as well as prior to and after OER catalytic testings in 0.5 M H_2SO_4.

catalyst	**ratio of Ir^0 / Ir^{3+}**
$IrTiO_x$	0.1 / 1
$IrTiO_x$-$60ALD_{Ir}$ (pre-OER)	6.3 / 1
$IrTiO_x$-$60ALD_{Ir}$ (post-OER)	6.6 / 1
TiO_2-$60ALD_{Ir}$ (pre-OER)	8.3 / 1
TiO_2-$60ALD_{Ir}$ (post-OER)	1.6 / 1

Section-VI: XPS analysis of mp. $IrTiO_x$ and mp. TiO_2 films prior to and after ALD at 120 °C

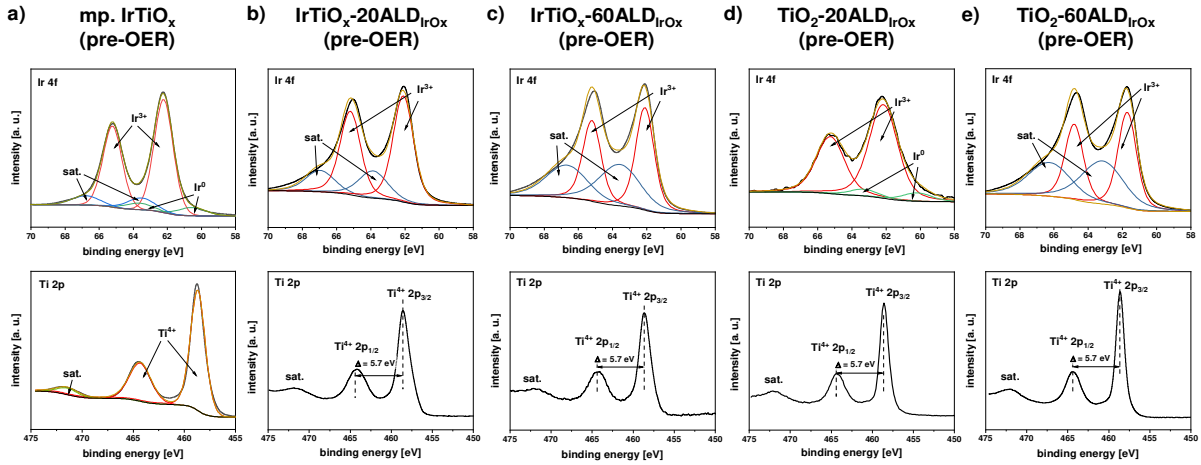

Figure S6. XPS spectra for (a) mp. $IrTiO_x$, (b) $IrTiO_x$-$20ALD_{IrOx}$, (c) $IrTiO_x$-$60ALD_{IrOx}$, (d) TiO_2-$20ALD_{IrOx}$ and (e) TiO_2-$60ALD_{IrOx}$ prior to catalytic OER testing. The upper row illustrates the corresponding Ir 4f spectra with deconvolutions of the acquired data and the lower row shows the Ti 2p spectra. All spectra were acquired for films deposited on Si substrates.

To examine the impact of temperature during the ALD process on the oxidation state of the deposited Ir species, further XPS analyses were performed for low-temperature ALD-modified films. The obtained Ir 4f and Ti 2p spectra are illustrated in Figure S6. In general, all ALD-modified films show a doublet peak at 62.2 eV with broad satellite features centered at 63.5 eV, corresponding to Ir^{3+}.[1,2,4,5] The assignment of Ir^{3+} corresponding to amorphous IrO_x was previously described by a model of IrO_6 octahedra located in the near-surface region of the IrO_x framework. The creation of an Ir vacancy leads to a change in the oxidation state of the surrounding oxygen atoms from –II to the formal oxidation state of -I. This oxidation process produces two additional electrons which are distributed among neighboring Ir^{4+} sites reducing them to Ir^{3+}.[6]

Regarding the surface Ti species, all films show a characteristic signal for Ti^{4+}, *i.e.* a doublet peak at 458.6 eV with a broad satellite feature centered at ~ 472 eV. The distance between the $2p_{1/2}$ and the $2p_{3/2}$ peak lies in the typical range of Δ = 5.7 eV.[7] The O 1s spectra (data not shown) are similar for all films and show three different kinds of contributions. The major

contribution at 530.0 eV corresponds to a Ti-O interaction. Two additional peaks at 531.5 eV and at 532.8 eV, which can be assigned to C=O species and surface –OH groups, respectively, were found. These features are typical for ALD-coated metal oxide surfaces.[7,8] Table S2 provides an overview of the ratio of surface Ti to surface Ir species prior to and after ALD at 120 °C. With an increasing number of ALD cycles, a lower ratio of Ti / Ir is found for both types of supports. This indicates an increasing coverage of the pore wall surface with ALD-deposited IrO_x species of predominantly +III oxidation state.

Table S2. Elemental composition at the surface of the catalyst films analyzed *via* XPS prior to and after IrO_x-ALD at 120 °C.

catalyst	**ratio of Ti / Ir**
$IrTiO_x$	1 / 0.3
$IrTiO_x$-20ALD_{IrOx}	1 / 1.5
$IrTiO_x$-60ALD_{IrOx}	1 / 5.3
TiO_2-20ALD_{IrOx}	1 / 0.7
TiO_2-60ALD_{IrOx}	1 / 1.8

Section-VII: GI-XRD analysis of mp. $IrTiO_x$ and mp. TiO_2 films prior to and after ALD at 120 °C and 160 °C

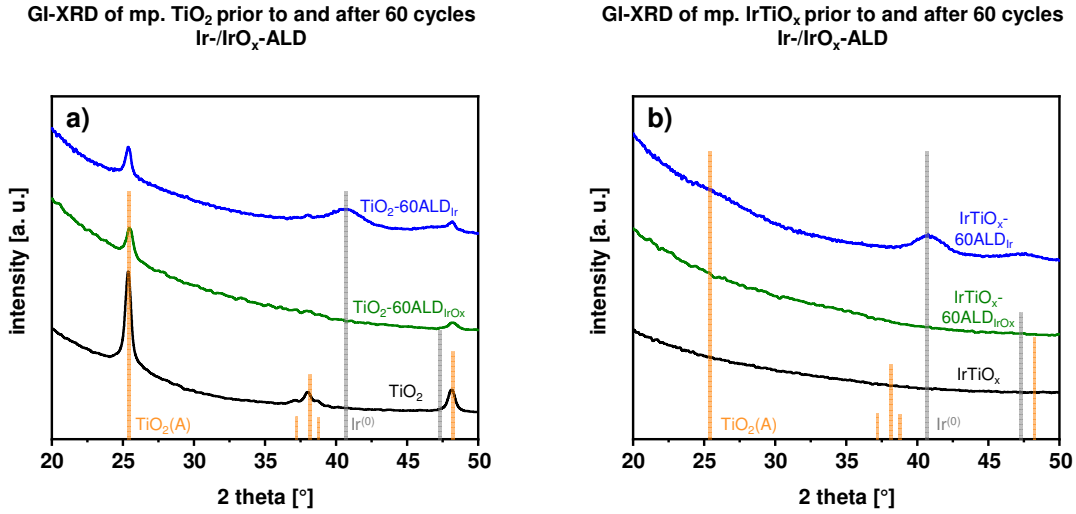

Figure S7. GI-XRD patterns of mp. TiO_2 (a) and mp. $IrTiO_x$ (b) prior to (black) and after 60 cycles ALD at 120 °C (green) and at 160 °C (blue). Reference patterns for anatase-TiO_2 (orange vertical bars) and metallic Ir (grey vertical bars) are given in (a) & (b). The results indicate the formation of a nanocrystalline TiO_2 film with anatase crystal structure (a) and an amorphous material for $IrTiO_x$ prior to ALD (b). After ALD at 160 °C, reflections for metallic Ir species appear for both TiO_2-60ALD$_{Ir}$ and $IrTiO_x$-60ALD$_{Ir}$. After ALD at 120 °C, however, no additional reflections can be found.

Notably, after 60 cycles of ALD at 120 °C, no distinct signals for any metallic Ir^0 surface species introduced *via* ALD can be found (**Figure S7a-b, green graphs**). In addition to the SEM images shown in **Figure 1**, this is another proof for the deposition of thin, layer-like structures *via* ALD at 120 °C, which do not provide sufficient scattering intensities.

Section-VIII: Electrical sheet conductivities of mp. TiO_2 prior to and after ALD

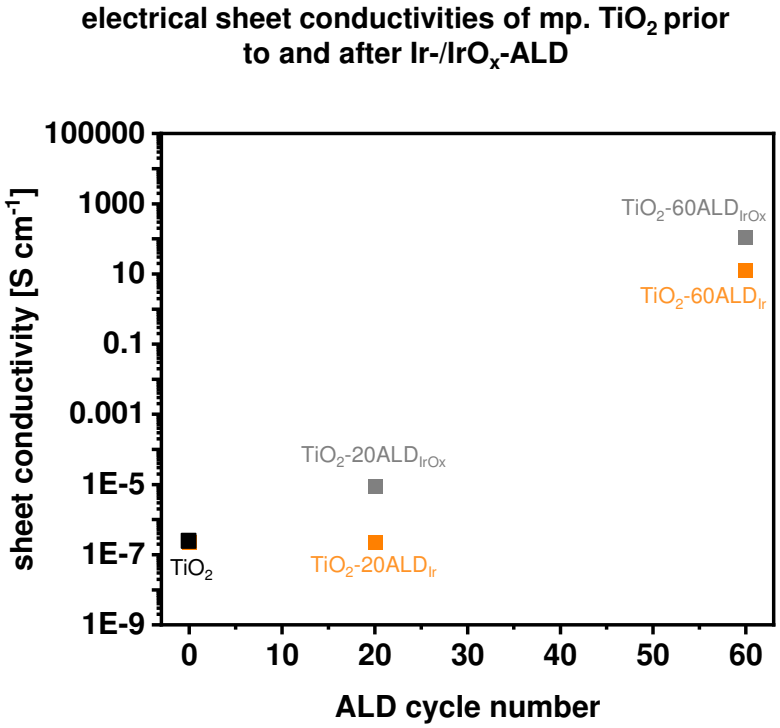

Figure S8. Electrical sheet conductivities assessed *via* impedance spectroscopy of mp. TiO_2 (black square) as well as TiO_2 supports modified *via* ALD at 160 °C (orange) and at 120 °C (grey). All investigated films were deposited on insulating glass substrates.

In accordance with our previous results[9,10] for sheet-thickness-normalized electrical conductivities, mp. TiO_2 films calcined at 475 °C show low conductivities of ~10^{-7} S cm^{-1}.

For low cycle numbers of ALD at 160 °C, *i.e.* 20 cycles, no change in conductivity can be observed. TiO_2-$20ALD_{Ir}$ shows a similar conductivity of ~10^{-7} S cm^{-1} as the bare mp. TiO_2 support. This can be explained by the deposition of nanoparticulate Ir species, rather than conformal surface layers (*cf.* **Figure 1** in the main part). Evidently, the overall sheet conductivity is dominated by the carrier matrix, *i.e.* the semiconducting TiO_2.[11]

For low cycle numbers of ALD at 120 °C, however, a rise in conductivity to ~10^{-5} S cm^{-1} is found, underlining the formation of an ultra-thin surface layer which coats the entire pore wall surface of the support. For a higher ALD cycle number, *i.e.* 60 cycles, a steep increase in sheet conductivities can be seen independent of the temperature during ALD. Accordingly, high loadings of well-conductive surface Ir species lead to a significant rise in film conductivity by

the formation of conductive surface electron pathways.[12,13] Schlicht *et al.*[11] reported similar observations regarding the formation of continuous conduction paths by high ALD cycle numbers for Ir deposited on TiO_2 nanotube arrays.

Section-IX: Cyclic voltammetry and base voltammetry of mp. $IrTiO_x$ prior to and after ALD at 120 °C

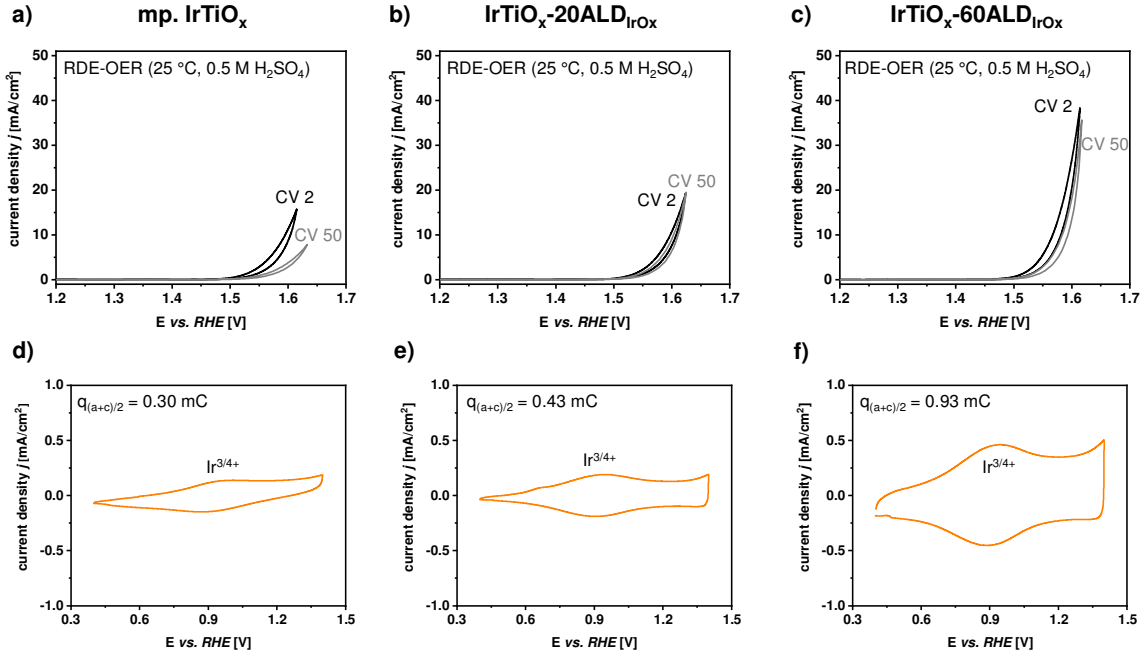

Figure S9. 2nd and 50th CVs from RDE-OER measurements of (a) mp. $IrTiO_x$, (b) $IrTiO_x$-$20ALD_{IrOx}$ and (c) $IrTiO_x$-$60ALD_{IrOx}$ in 0.5 M H_2SO_4 (N_2-sat.) at 25 °C and 1600 rpm rotation of the working electrode. The geometric current densities are plotted vs. potential (vs. RHE). (d) – (f) represent the CVs from base voltammetry at a lower potential for (d) mp. $IrTiO_x$, (e) $IrTiO_x$-$20ALD_{IrOx}$ and (f) $IrTiO_x$-$60ALD_{IrOx}$. $Ir^{3/4+}$ redox transitions at ~ 0.9 V_{RHE} are clearly visible in (d) – (e), which is in accordance with our previous results.

Figure S9 illustrates the results from electrochemical testings in a RDE setup using 0.5 M H_2SO_4 as a supporting electrolyte at 25 °C for mp. $IrTiO_x$ films prior to (**Figure S9a**) and after surface-modification with IrO_x species *via* low-temperature ALD at 120 °C (**Figure S9b-c**). The films show a similar average sheet thickness of ~ 100 nm, which remains essentially unaltered after ALD. For an increasing ALD cycle number, the amount of Ir loaded in the catalyst films rises and, concomitantly, the geometric current densities increase in the OER regime. In **Figure S9d-f**, the anodic and cathodic charge in a lower potential range are given (base voltammetry). Redox peaks of the $Ir^{3/4+}$ couple are clearly visible. For higher ALD cycle numbers, the average anodic and cathodic charge increases, which indicates an increasing number of accessible active metal centers in the films.

Section-X: Geometric current density – potential and corresponding Ir mass-normalized activity plots *via* cyclic voltammetry (RDE-OER) measurements in 0.5 M H_2SO_4

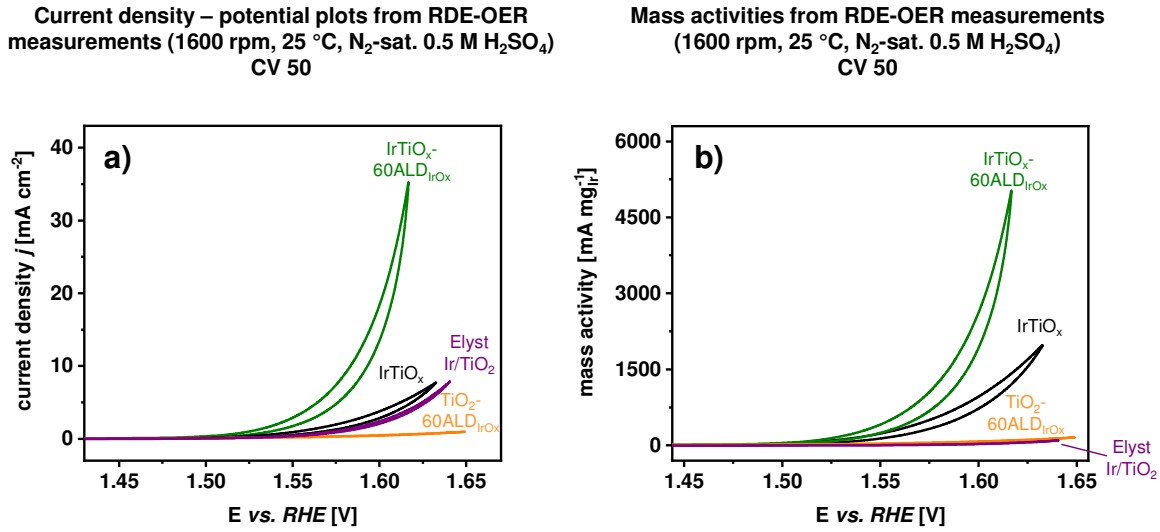

Figure S10. Current density vs. potential plots from RDE-OER measurements in 0.5 M H_2SO_4 (N_2-sat.) at 25 °C and 1600 rpm rotation. The geometric current densities are plotted vs. potential (vs. RHE) in (a). The corresponding potential-dependent Ir-mass-specific activities are given in (b). Selected catalysts are shown, *i.e.* $IrTiO_x$ (black), $IrTiO_x$-$60ALD_{IrOx}$ (dark green), TiO_2-$60ALD_{IrOx}$ (orange) and the commercial reference Elyst Ir/TiO_2 (purple).

Figure S10 shows the results from RDE-OER testings for selected catalyst systems. After normalization of the currents to the respective Ir loadings in the catalyst films (see **Figure S10b**), the significantly improved catalytic OER activity of the top-performing catalyst, $IrTiO_x$-$60ALD_{IrOx}$ (dark green curve), becomes evident. The commercial reference catalyst, Elyst Ir/TiO_2 (purple) shows the lowest mass activities in the investigated potential range.

Section-XI: Evaluation of Tafel slopes *via* RDE-OER in 0.5 M H_2SO_4

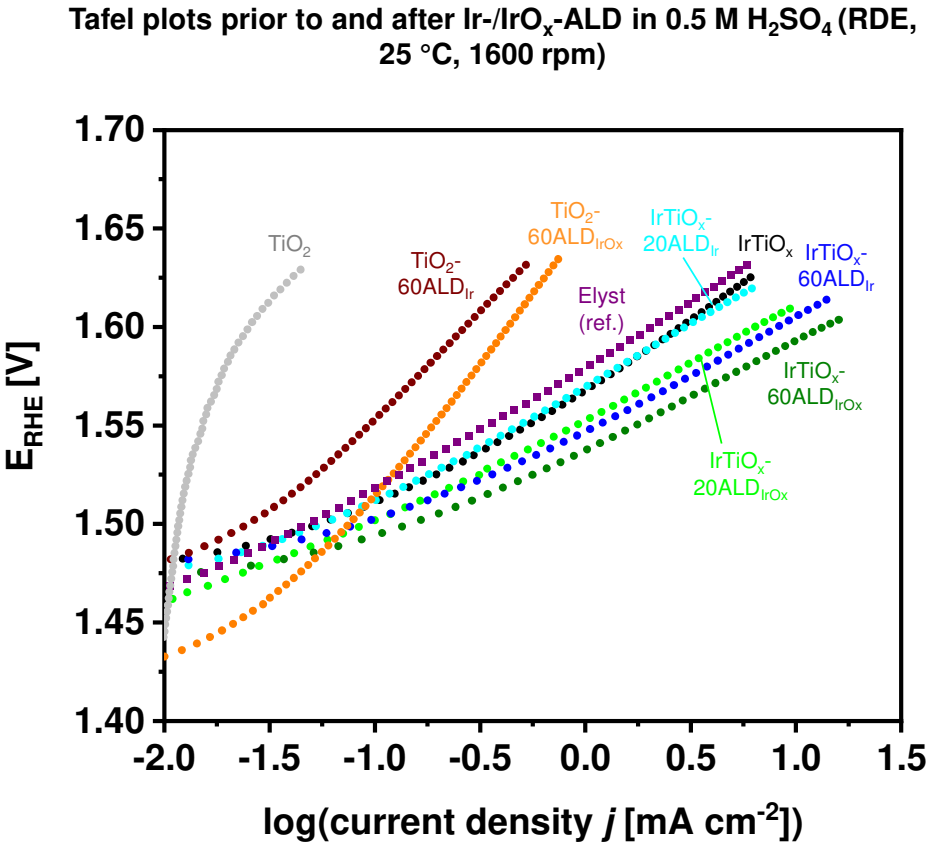

Figure S11. Tafel plots calculated from the 50th CV from RDE-OER measurements of all catalyst films listed in **Table 1** in the manuscript. The corresponding Tafel slopes were calculated in a potential range between 1.55 – 1.60 V_{RHE}.

Next, as a highly relevant indicator for the ongoing reaction kinetics, Tafel slopes of the electrocatalysts were derived from the corresponding CVs. In brief, significantly higher Tafel slopes were found for all surface-modified as well as unmodified films with TiO_2 as a support compared to $IrTiO_x$-supported catalysts. Regarding the latter, slightly smaller values were obtained after both ALD at 120 °C and at 160 °C, indicating faster reaction kinetics compared to the unmodified mp. $IrTiO_x$ support. This enhancement might be related to a higher absolute number of electrochemically accessible metal centers after surface-modification *via* ALD. In this context, ALD at 120 °C leads to the deposition of highly homogeneous IrO_x surface layers with low crystallinity and, thus, promotes OER kinetics as a result of the high intrinsic activity of Ir^{3+} species towards oxygen evolution. Yet, a sufficient electrical bulk conductivity is mandatory for high OER activities, which becomes evident upon comparison of TiO_2-

$60ALD_{IrOx}$ vs. $IrTiO_x$-$60ALD_{IrOx}$. With only 55 mV dec^{-1}, the latter shows the smallest Tafel slope (50^{th} CV, down-cycle), whereas with more than 100 mV dec^{-1}, the former suffers from sluggish reaction kinetics.

In accordance with previous investigations[10,14] regarding potential-dependent changes in the Tafel slopes of Ir-based OER catalysts, all Ir/IrO_x-modified films show a characteristic kink for higher potentials than ~1.50 – 1.55 V_{RHE}. The observed bend in the Tafel slope seems slightly more pronounced for IrO_x-modified catalysts *via* ALD at 120 °C. As nicely discussed by Nong *et al.*[14], this effect can be related to a variation in the coverage of surface holes (h^+) over potential.

Section XII: Impact of ALD on ECSA estimated from base voltammetry

It was shown that the parameters of the ALD process, primarily the temperature during deposition, affect the chemical nature of the Ir species distributed on the surface of the three-dimensional mesoporous network with interconnected porosity.

Base voltammetry in a lower potential range between 0.4 – 1.4 V_{RHE} reveals distinct differences for the average anodic and cathodic charge dependent on the structure and electrical properties of the support. Unmodified mp. TiO_2 shows only a negligible charge calculated from the mean value of the integrated cathodic and anodic scan of the *iR*-corrected CV curve (see **Figure S12b**, grey curve), whereas for mp. $IrTiO_x$ a higher charge $q_{(a+c)/2}$ with small peaks characteristic of redox features of accessible Ir surface sites can be found in the corresponding CV in **Figure S12a** (black curve). After ALD, the charge increases for both $IrTiO_x$-$60ALD_{Ir}$ and $IrTiO_x$-$60ALD_{IrOx}$, confirming their superior OER activities as a consequence of a higher number of accessible catalytically active centers.

In the case of TiO_2-supported catalysts, however, no characteristic $Ir^{3/4+}$ redox peaks can be found in the resulting CVs (see **Figure S12b**). Even though, after ALD, numerous surface Ir species are present, an insufficient bulk electrical conductivity seems to hamper relevant Faradaic currents. Hence, no redox peaks characteristic of active Ir sites can be found in the base voltammograms.

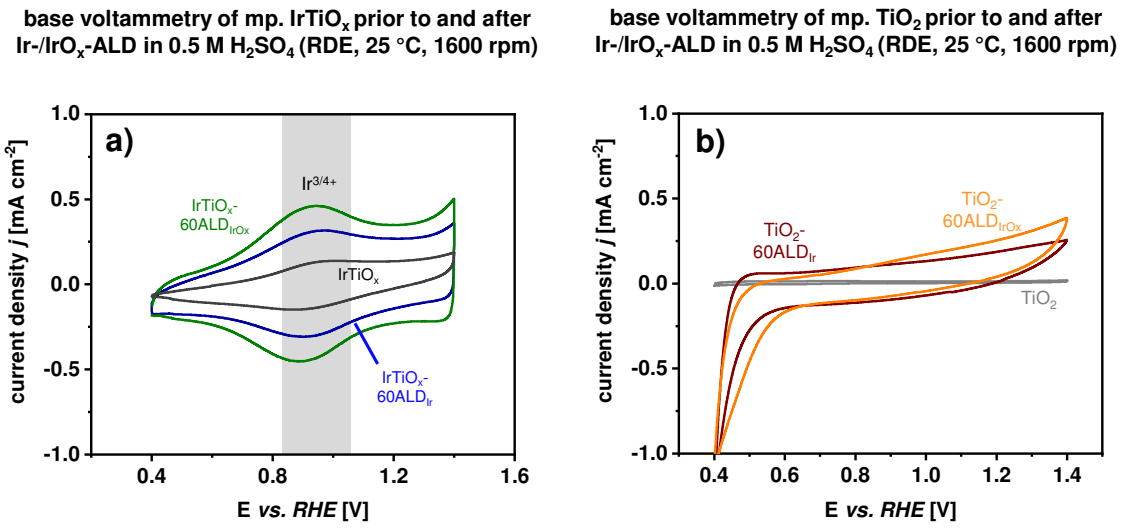

Figure S12. Base voltammetry measurements in a RDE-OER setup of (a) mp. $IrTiO_x$ (black) and (b) TiO_2 (grey) in 0.5 M H_2SO_4. The geometric current densities are plotted vs. potential (vs. RHE). In (a), CVs for $IrTiO_x$-$60ALD_{Ir}$ and $IrTiO_x$-$60ALD_{IrOx}$ are shown in dark blue and green, respectively. $Ir^{3/4+}$ redox transitions at ~ 0.9 V_{RHE} are clearly visible in (a). In (b), CVs for TiO_2-$60ALD_{Ir}$ and TiO_2-$60ALD_{IrOx}$ are illustrated in dark red and orange, respectively. No characteristic Ir redox peaks can be found in (b).

Section XIII: Chronopotentiometric stability tests of mp. $IrTiO_x$ prior to and after IrO_x-ALD

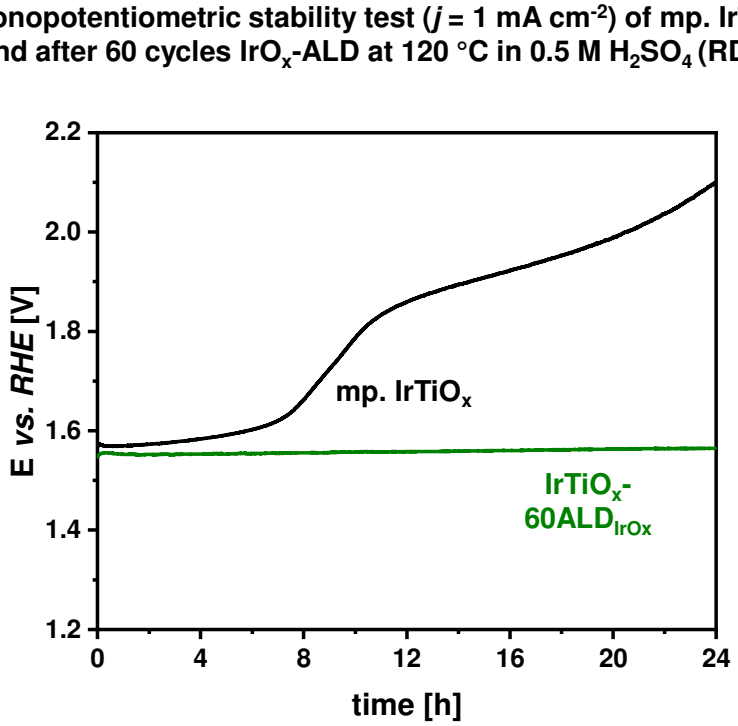

Figure S13. Chronopotentiometric stability tests in an RDE-OER setup of mp. $IrTiO_x$ (black) and $IrTiO_x$-$60ALD_{IrOx}$ (dark green) in 0.5 M H_2SO_4 at 25 °C. The potential (vs. RHE) is plotted over time in electrolyte and j = 1 mA cm^{-2}.

In order to investigate the influence of the ALD process at 120 °C on the electrochemical stability of the films, chronopotentiometry measurements were performed in 0.5 M H_2SO_4 at 25 °C in an RDE setup. As shown in the results in **Figure S13**, surface-modified films are more robust OER catalysts. Prior to ALD, the conductive $IrTiO_x$ reveals an insufficient long-term stability in acid. After approximately 8 hours, pronounced dissolution of the film and a concomitant loss of active sites into the surrounding liquid electrolyte can be observed until the end of the 24-hour stability test.

Contrarily, for the most active herein developed catalyst, $IrTiO_x$-$60ALD_{IrOx}$, a different picture is revealed. Accordingly, the introduction of conformal IrO_x surface layers *via* ALD successfully protects the underlying iridium titania in the mp. $IrTiO_x$ support from an ongoing dissolution under corrosive and oxidative conditions.

Our results serve as a proof-of-principle, highlighting the role of the ALD surface layer in enhancing the durability of the electrocatalyst, as evidenced by the results from static operation conditions on the RDE level. It has to be noted that recent literature[15,16] proposes accelerated degradation/stress tests on the MEA (membrane electrode assembly) level for a more realistic evaluation of catalyst stability. In this context, RDE testings are more appropriate for the determination of catalyst activity. This conclusion has been drawn based on systematic examinations on the influence of anionic species in the electrolytes used in RDE setups on the dissolution of different electrocatalysts.[17] In addition, the impact of accumulated gas bubbles (O_2) during RDE measurements has been thoroughly discussed. A partial shielding of active surface sites by evolving gas bubbles in the catalyst layer, which are not completely removed by the rotational forces, may contribute to a decrease in activity over time rather than degradation of the active material or phase(s).[16,18]

References

[1] V. Pfeifer, T. E. Jones, J. J. Velasco Vélez, C. Massué, R. Arrigo, D. Teschner, F. Girgsdies, M. Scherzer, M. T. Greiner, J. Allan, M. Hashagen, G. Weinberg, S. Piccinin, M. Hävecker, A. Knop-Gericke, R. Schlögl, *Surf. Interface Anal.* **2016**, *48*, 261–273.

[2] H. Y. Hall, P. M. A. Sherwood, *J. Chem. Soc. Faraday Trans. 1 Phys. Chem. Condens. Phases* **1984**, *80*, 135.

[3] E. Özer, Z. Pawolek, S. Kühl, H. Nong, B. Paul, S. Selve, C. Spöri, C. Bernitzky, P. Strasser, *Surfaces* **2018**, *1*, 151–164.

[4] S. J. Freakley, J. Ruiz-Esquius, D. J. Morgan, *Surf. Interface Anal.* **2017**, *49*, 794–799.

[5] F. Claudel, L. Dubau, G. Berthomé, L. Sola-Hernandez, C. Beauger, L. Piccolo, F. Maillard, *ACS Catal.* **2019**, *9*, 4688–4698.

[6] V. Pfeifer, T. E. Jones, J. J. Velasco Vélez, C. Massué, M. T. Greiner, R. Arrigo, D. Teschner, F. Girgsdies, M. Scherzer, J. Allan, M. Hashagen, G. Weinberg, S. Piccinin, M. Hävecker, A. Knop-Gericke, R. Schlögl, *Phys. Chem. Chem. Phys.* **2016**, *18*, 2292–2296.

[7] M. C. Biesinger, L. W. M. Lau, A. R. Gerson, R. S. C. Smart, *Appl. Surf. Sci.* **2010**, *257*, 887–898.

[8] Y. Fan, Y. Wu, G. Clavel, M. H. Raza, P. Amsalem, N. Koch, N. Pinna, *ACS Appl. Energy Mater.* **2018**, *1*, 4554–4563.

[9] D. Bernsmeier, M. Bernicke, R. Schmack, R. Sachse, B. Paul, A. Bergmann, P. Strasser, E. Ortel, R. Kraehnert, *ChemSusChem* **2018**, *11*, 2367–2374.

[10] M. Bernicke, D. Bernsmeier, B. Paul, R. Schmack, A. Bergmann, P. Strasser, E. Ortel, R. Kraehnert, *J. Catal.* **2019**, *376*, 209–218.

[11] S. Schlicht, P. Büttner, J. Bachmann, *ACS Appl. Energy Mater.* **2019**, *2*, 2344–2349.

[12] P. Schmitt, V. Beladiya, N. Felde, P. Paul, F. Otto, T. Fritz, A. Tünnermann, A. V. Szeghalmi, *Coatings* **2021**, *11*, 173.

[13] A. Szeghalmi, M. Arnold, A. Berger, N. Schammelt, K. Fuechsel, M. Knez, E. B. Kley, D. R. T. Zahn, A. Tuennermann, in (Eds.: M. Lequime, H.A. Macleod, D. Ristau), **2011**, p. 81680.

[14] H. N. Nong, L. J. Falling, A. Bergmann, M. Klingenhof, H. P. Tran, C. Spöri, R. Mom, J. Timoshenko, G. Zichittella, A. Knop-Gericke, S. Piccinin, J. Pérez-Ramírez, B. R. Cuenya, R. Schlögl, P. Strasser, D. Teschner, T. E. Jones, *Nature* **2020**, *587*, 408–413.

[15] C. Spöri, C. Brand, M. Kroschel, P. Strasser, *J. Electrochem. Soc.* **2021**, *168*, 034508.

[16] M. Bernt, A. Hartig-Weiß, M. F. Tovini, H. A. El-Sayed, C. Schramm, J. Schröter, C. Gebauer, H. A. Gasteiger, *Chemie Ing. Tech.* **2020**, *92*, 31–39.

[17] C. Van Pham, D. Escalera-López, K. Mayrhofer, S. Cherevko, S. Thiele, *Adv. Energy Mater.* **2021**, *11*, 2101998.

[18] H. A. El-Sayed, A. Weiß, L. F. Olbrich, G. P. Putro, H. A. Gasteiger, *J. Electrochem. Soc.* **2019**, *166*, F458–F464.

A-3 Reprinted Publication [MF-3]:

Mesoporous WC_x Films with NiO-Protected Surface: Highly Active Electrocatalysts for the Alkaline Oxygen Evolution Reaction

M. Frisch*, M.-Y. Ye*, M. H. Raza, A. Arinchtein, D. Bernsmeier, A. Gomer, T. Bredow, N. Pinna, R. Kraehnert

ChemSusChem **2021**, *14*, 4708-4717.

https://doi.org/10.1002/cssc.202101243

Mesoporous WC_x Films with NiO-Protected Surface: Highly Active Electrocatalysts for the Alkaline Oxygen Evolution Reaction

Marvin Frisch[+,a] Meng-Yang Ye[+,a] Muhammad Hamid Raza,[b] Aleks Arinchtein,[a] Denis Bernsmeier,[a] Anna Gomer,[c] Thomas Bredow,[c] Nicola Pinna,[b] and Ralph Kraehnert*[a]

Metal carbides are promising materials for electrocatalytic reactions such as water electrolysis. However, for application in catalysis for the oxygen evolution reaction (OER), protection against oxidative corrosion, a high surface area with facile electrolyte access, and control over the exposed active surface sites are highly desirable. This study concerns a new method for the synthesis of porous tungsten carbide films with template-controlled porosity that are surface-modified with thin layers of nickel oxide (NiO) to obtain active and stable OER catalysts. The method relies on the synthesis of soft-templated mesoporous tungsten oxide (mp. WO_x) films, a pseudomorphic transformation into mesoporous tungsten carbide (mp. WC_x), and a subsequent shape-conformal deposition of finely dispersed NiO species by atomic layer deposition (ALD). As theoretically predicted by density functional theory (DFT) calculations, the highly conductive carbide support promotes the conversion of Ni^{2+} into Ni^{3+}, leading to remarkably improved utilization of OER-active sites in alkaline medium. The obtained Ni mass-specific activity is about 280 times that of mesoporous NiO_x (mp. NiO_x) films. The NiO-coated WC_x catalyst achieves an outstanding mass-specific activity of 1989 A g_{Ni}^{-1} in a rotating-disc electrode (RDE) setup at 25 °C using 0.1 M KOH as the electrolyte.

Introduction

Generating hydrogen through electrocatalytic water splitting is a sustainable way of obtaining clean energy.[1–3] In this reaction, the oxygen evolution half reaction (OER) shows sluggish kinetics due to its four-electron process.[4,5] The exploration of high performance OER electrocatalysts remains one of the major challenges in order to achieve highly efficient electrocatalytic water splitting.[6,7] In recent years, tremendous efforts have been paid in the pursuit of identifying highly active sites in OER electrocatalysis.[8–11] However, developing suitable catalysts and support materials for highly active sites is equally important.[12] The introduction of supporting materials enables a compensation of many limitations of the catalytically active centers, thus culminating in superior catalytic activities.[13–15] Nickel-derived oxides are known to be low-cost, highly active OER electrocatalysts in alkaline electrolyte.[16–18] Beside a high stability, the excellent OER activity of these materials has been attributed to the preoxidized Ni^{3+} on the surface of the NiO electrocatalyst.[18] The surface-exposed oxidic Ni species can be activated during OER.[9,19] However, a previous study by Bernsmeier et al.[20] indicated that a minimum electrical conductivity is often required to enable efficient electrocatalysis. Unfortunately, bulk NiO materials suffer from rather low conductivities, which hinders fast charge transportation during the reaction.[16]

In general, efficient OER catalysis requires a large number of well-accessible, highly active surface species as well as a high electrical conductivity favorable for charge transfer and a sufficient stability of the catalyst against corrosion.[21,22] A maximization of surface-exposed Ni species can be achieved by introducing a mesoporous nanostructure, for instance.[8,23,24] Moreover, the latter also provides short diffusion pathways and facilitates mass transport during catalysis.[25,26] An optimized utilization of weakly conductive NiO is targeted by employing a highly conductive carrier material.[27] Ordered mesoporous carbon or carbides could be used to provide both high electrical conductivity and high porosity, yet they suffer from oxidative corrosion during OER.[28–31] Moreover, the study of powder electrocatalysts mostly relies on the addition of binders such as Nafion.[27,32,33] The latter was shown to partially block active sites and hampers analyses of the spent catalysts.[7]

Tungsten carbides (WC_x) are highly electrically conductive,[34] earth abundant and show a promising behavior in electrocatalysis.[29,35,36] WC_x materials can be prepared by carburization of their corresponding metal oxides,[37–39] which were

[a] M. Frisch,[+] M.-Y. Ye,[+] A. Arinchtein, Dr. D. Bernsmeier, Dr. R. Kraehnert
Department of Chemistry, Technische Universität Berlin
Strasse des 17. Juni 124, 10623 Berlin (Germany)
E-mail: ralph.kraehnert@tu-berlin.de
[b] M. Hamid Raza, Prof. Dr. N. Pinna
Institut für Chemie und IRIS Adlershof, Humboldt-Universität zu Berlin
Brook-Taylor-Strasse 2, 12489 Berlin (Germany)
[c] A. Gomer, Prof. Dr. T. Bredow
Mulliken Center for Theoretical Chemistry
Universität Bonn, Beringstrasse 4, 53115 Bonn (Germany)
[+] These authors contributed equally to this work.

Supporting information for this article is available on the WWW under https://doi.org/10.1002/cssc.202101243

frequently synthesized and analyzed due to their interesting electrochromic properties.[40,41] However, typical syntheses of WC_x powders require high carburization temperatures above 800 °C, which results in pronounced crystallite growth, sintering and low surface area.[37] In contrast, soft-templated mesoporous WO_x (mp. WO_x) films enable a facile diffusion of reactive carbon species into the oxide lattice,[42,43] hence decreasing the carburization temperature and, concomitantly, preserving the mesoporosity in the obtained WC_x films (mp. WC_x).

Herein, we propose a new concept for nanostructured OER catalysts, in which the bulk consists of a Nafion-free, highly conductive, nanostructured tungsten carbide film, and the entire surface of the carbide is uniformly coated with a homogenous thin layer of NiO.

Scheme 1 outlines the overall concept. As a first step, a substrate is coated homogeneously with a nanostructured mesophase by dip-coating from a solution containing an amphiphilic triblock copolymer (PEO-*b*-PB-*b*-PEO) as a structure-directing agent[8], a metal oxide precursor (WCl_6), a complexing agent (citric acid)[44] and suitable solvents (EtOH). This mesophase is dried and then transformed into the corresponding oxide by thermal treatment in nitrogen, which leads to a concomitant removal of the template polymer and finally results in a controlled mesoporosity of the oxide film. Exposing this oxide phase to a mixture of CH_4/H_2/Ar at 700 °C induces the pseudomorphic transformation of the oxide into the respective carbide, while retaining the film integrity and its open porosity, affording a mesoporous tungsten carbide phase (mp. WC_x). ALD is used as a next step to coat the entire internal surface of the porous carbide systems with NiO (ALD-NiO/mp. WC_x).

In order to produce defined reference catalysts, templated mesoporous nickel oxide (mp. NiO_x) films were prepared by a synthesis route previously described in literature.[24] Moreover, the pore system of this mp. NiO_x as well as that of mp. WO_x were coated with a thin conformal NiO layer by a similar procedure as employed for the carbide. All catalyst films were deposited on polished titanium substrates and subsequently tested in alkaline OER (0.1 M KOH) by cyclic voltammetry in a rotating disk electrode (RDE, 1600 rpm) setup to assess activity and stability. DFT calculations were carried out to provide further evidence for the synergistic effects of the carbide carrier and the surface NiO layer. Moreover, electrical conductivity (impedance spectroscopy), crystallinity (GI-XRD, SAED), sample morphology (SEM, TEM) and local composition (EDX) as well as surface area (Kr-physisorption) were assessed.

The herein developed system has several advantages: (a) maximizing the surface exposure of Ni species, while minimizing the content of less conductive NiO, (b) providing protection of the carbide against corrosion and (c) developing a binder-free electrocatalytic system. As a result, the obtained ALD-NiO/mp. WC_x catalyst films show a low overpotential of 360 mV at a current density of 10 mA cm^{-2} in 0.1 M KOH. At a potential of 1.60 V vs. RHE, an outstanding Ni-mass based OER activity of 1989 A g^{-1}, which is ~284-fold higher than that of pristine mesoporous NiO_x films, can be achieved.

Results and Discussion

Physicochemical characterization of mp. WO_x, mp. WC_x, and ALD-NiO/mp. WC_x

We synthesized micelle-templated mesoporous WO_x films in a similar way as previously reported by Brezesinski, Smarsly and co-workers[45,46] (Figure 1a-I–c-I). The synthesis of the initial porous oxide relies on the Evaporation Induced Self Assembly (EISA) process.[47–50] The obtained mp. WO_x films were carburized in a mixture of CH_4, H_2 and Ar for 6 h at 700 °C to afford a homogeneous, macroscopically crack-free mesoporous WC_x film (mp. WC_x) (Figure 1a-II–c-II). The obtained mp. WC_x was then coated with a thin layer of NiO through ALD by alternating cycles of $Ni(Cp)_2$ and ozone (O_3) at 200 °C (Figure 1a-III–c-III). As shown in previous reports,[27,51–53] such an ALD process can ensure the deposition of a homogenous and thin particulate-

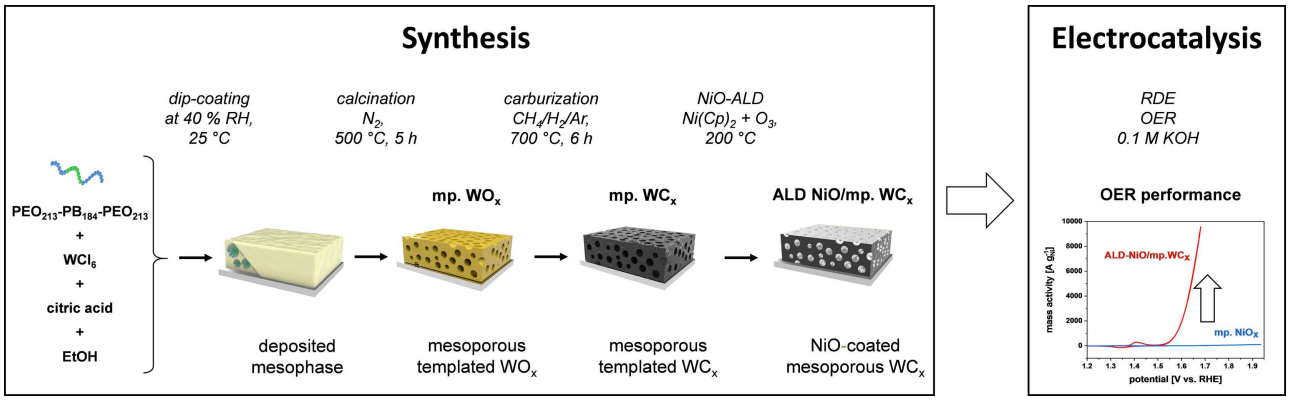

Scheme 1. Developed synthesis route for NiO-coated porous tungsten carbide catalysts. A solution containing the tungsten precursor and a micelle-forming block copolymer is deposited onto a substrate (Si, Ti, glass), dried and then calcined in nitrogen (N_2) to produce mesoporous tungsten oxide (mp. WO_x) with template-controlled porosity. This oxide phase is exposed to a mixture of CH_4/H_2/Ar at 700 °C to induce the formation of a mesoporous carbide (mp. WC_x). The carbide is then exposed in alternating cycles of $Ni(Cp)_2$ and ozone (O_3) to deposit nickel oxide (NiO) over the entire surface of the carbide's pore system to produce the final catalyst. The ALD synthesis was also applied to mp. WO_x as well as mesoporous nickel oxide (mp. NiO_x) as reference systems.

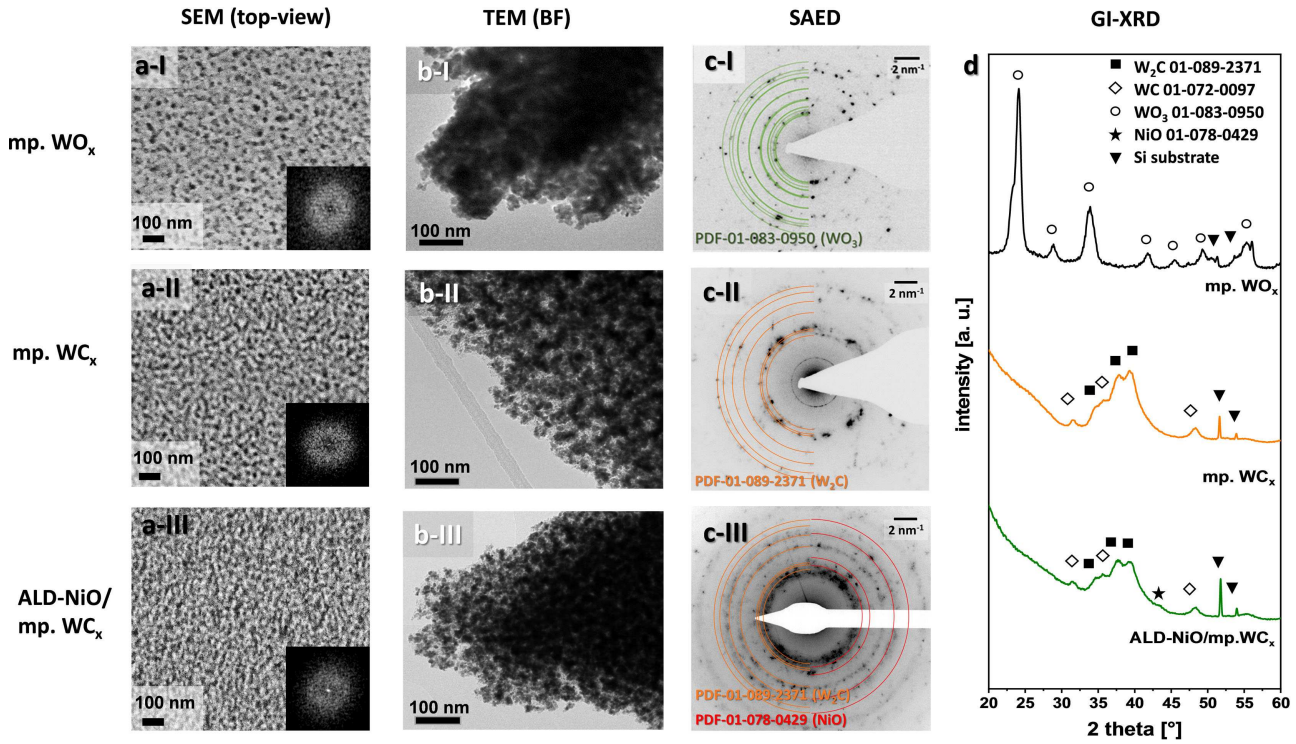

Figure 1. (a) Top-view SEM images with corresponding FFT (inset); (b) TEM images; (c) TEM-SAED patterns of mp. WO_x (I), mp. WC_x (II), and ALD-NiO/mp. WC_x (III). (d) GI-XRD patterns of mp. WO_x, mp. WC_x and NiO-ALD/mp. WC_x acquired on films deposited on Si substrates. In (d), an asterisk indicates the presence of a weak (200) lattice plane reflection of cubic NiO for NiO-ALD/mp. WC_x Electron microscopy (a, b) indicates the formation of similar mesoporous structures for mp. WO_x, mp. WC_x, and NiO-ALD/mp. WC_x. Both SAED (c) and GI-XRD (d) confirm the carburization of mp. WO_x to mp. WC_x with no remaining bulk oxide phases present, as well as the successful loading of NiO by ALD, affording NiO-ALD/mp. WC_x as a last step.

like film onto high-aspect-ratio nanostructured carriers. By changing the number of ALD cycles, the amount and thickness of the NiO coating can be precisely adjusted (for further evidence, see the Supporting Information, Section 1).[27,51,52]

Representative top-view SEM and bright-field (BF) TEM images confirm the homogenous mesoporosity of the synthesized mp. WO_x film (Figure 1a-I, b-I). The surface area of the film amounts to around 120 m^2 per geometric m^2 on average, according to BET evaluations of independent Kr-physisorption measurements.

The FFT image (Figure 1a-I, inset) shows a diffuse ring, indicating a locally ordered mesoporous structure. The SAED and GI-XRD patterns of mp. WO_x can be assigned to the WO_3 phase with minor contributions of non-stoichiometric WO_x phases (Figure 1c-I, d; PDF# 01-083-0950). Broad reflections indicate the formation of a nanocrystalline material. The XPS W4f spectrum (see the Supporting Information, Figure S2a) shows a typical doublet peak centered at 35.7 eV, indicating that the dominating tungsten species in mp. WO_x is W^{6+}, while the corresponding W–O bond centered at 530.2 eV can be observed in the corresponding O 1s spectrum (Figure S2d).[18,27]

After carburization, both top-view SEM and TEM images of the mp. WC_x film clearly portray its homogenous mesoporosity originating from the mp. WO_x precursor (Figure 1a-II, b-II). The surface area of the mp. WC_x film remains high with a value of ~100 $m^2 m^{-2}$ on average. A diffuse ring can be found in the corresponding FFT (Figure 1a-II, inset), indicating a similar structure to the mp. WO_x precursor film. The conversion from mp. WO_x into mp. WC_x can be observed from both SAED and GI-XRD patterns (Figure 1c-II, d) and the reflections can be assigned to WC (PDF# 01-072-0097) as well as W_2C (PDF# 01-089-2371). Importantly, no signs for any remaining WO_x phases are found. Broad reflections underline the preserved nanocrystallinity of the material. Beyond that, the conversion from an oxide into a carbide can be confirmed through XPS analysis of the obtained mp. WC_x after carburization (Figure S2e–h). In the W4f XPS spectrum of mp. WC_x (Figure S2e), the dominating species is indicated by a doublet peak located at 31.9 eV, which can be assigned to tungsten carbides. Only a weak signal of W^{6+} remains, which can be rationalized by a surface oxidation of the WC_x as a result of the passivation step subsequent to carburization.[54]

The deposition of NiO by ALD in the last synthesis step did not show any significant impact on the crystallinity and mesoporosity of the mp. WC_x carrier. As expected, the surface area slightly decreased to ~85 $m^2 m^{-2}$ after the deposition of NiO onto the pore walls of the carrier film, which adds evidence for the preserved mesoporosity in ALD-NiO/mp. WC_x. The GI-XRD pattern looks essentially unaltered, still showing broad reflections of W_2C and WC (Figure 1d), which can also be confirmed by SAED (Figure 1c-III). A weak reflection can be found at 43.4°, which corresponds to the (200) facet of cubic

NiO (PDF#01-078-0429). For a closer investigation of the deposited NiO layer, SAED represents a more sensitive method, clearly underlining the presence of crystalline NiO (Figure 1c-III). The typical morphology of ALD-NiO/mp. WC_x resembles that of mp. WC_x (Figure 1a-II,III, 1b-II, III). The existence of the thin NiO layer can be additionally traced by surface-sensitive XPS analysis (Figure S2i–l). Strong signals appear in the Ni 2p XPS spectrum after the ALD process, which can be addressed to typical Ni^{II} species in NiO.[27,32,55–58] In addition, the corresponding Ni–O interaction was found in the O 1s spectrum (Figure S2k).[24] Notably, Ni took up 17.65 at% of the surface element composition after ALD, while the content of W drastically reduced to 0.13 at% (Table S1), indicating that the NiO layer has covered almost the entire surface of ALD-NiO/mp. WC_x. This conclusion can be further supported by the results from bulk-sensitive WDX/StrataGem analysis, showing a significantly lower overall Ni content of 4.2 at% in the entire film volume. Note that a pronounced surface oxidation of WC_x can be observed in W4f spectrum of ALD-NiO/mp. WC_x, most likely due to the exposure to O_3 at elevated temperatures in the ALD chamber.[18] Still, the existence of WC_x species on the surface of ALD-NiO/mp. WC_x is evident. In addition, the distributions of Ni and W were investigated by using energy dispersive X-ray spectroscopy (EDX) elemental mapping coupled with TEM. A representative BF-TEM image of ALD-NiO/mp. WC_x is given in Figure 2a. The area shown in Figure 2a was analyzed by EDX spectroscopy (see the Supporting Information, Section 3). It can be observed that the signals of both Ni and W homogeneously cover the entire volume of the analyzed film fraction (Figure 2b, c), suggesting that the NiO layer is uniformly distributed over the entire surface of the mp. WC_x carrier. Furthermore, the power spectra of selected regions of a representative high-resolution HR-TEM image of ALD-NiO/mp. WC_x (Figure 2d) are typical of WC in [100] zone axis (Figure 2e) and of NiO in [100] zone axis (Figure 2f). Beyond that, lattice fringes corresponding to the {101} facet of W_2C as well as {111} and {200} facets of NiO can be observed and, importantly, the mesoporous structure of ALD-NiO/mp. WC_x is further corroborated (see the Supporting Information, Section 6).

Evaluation of OER activities, stabilities and Tafel slopes through RDE measurements in 0.1 M KOH (25 °C)

The OER activity of ALD-NiO/mp. WC_x was measured in a RDE setup through cyclic voltammetry (CV) measurements in 0.1 M KOH at RT for all samples listed in Table 1. From the electrochemical testings, Tafel slopes, Ni-based mass activities and electrochemically accessible surface areas (ECSA) of the catalysts were derived. To understand both the impact of the carrier material and the impact of the ALD process on the electrical properties, impedance spectroscopy was used to calculate the electrical sheet conductivities.

Table 1 provides an overview of the calculated electrical properties, Ni loadings and corresponding electrochemical performance data for all investigated catalyst systems. Figure 3a shows the current density-potential plots of the 30th CVs for all developed electrocatalyst systems (for further CV cycles see Figure S4). ALD-NiO/mp. WC_x exhibits by far the highest OER activity. Over 100 cycles of RDE-OER testing, ALD-NiO/mp. WC_x presents an remarkable stability, since the overpotential amounts to 360 mV at 10 mA cm^{-2} in CV 30 and well-preserved in CV 50 (368 mV, Table 1) as well as in CV 100 (372 mV, Table S2). Hence, ALD-NiO/mp. WC_x ranks amongst the state-of-the-art alkaline OER electrocatalysts in terms of overpotential in 0.1 M KOH electrolyte, yet with a significantly enhanced mass activity (Table 2). Importantly, the OER activities of the herein investigated Ni-containing electrocatalysts were normalized by

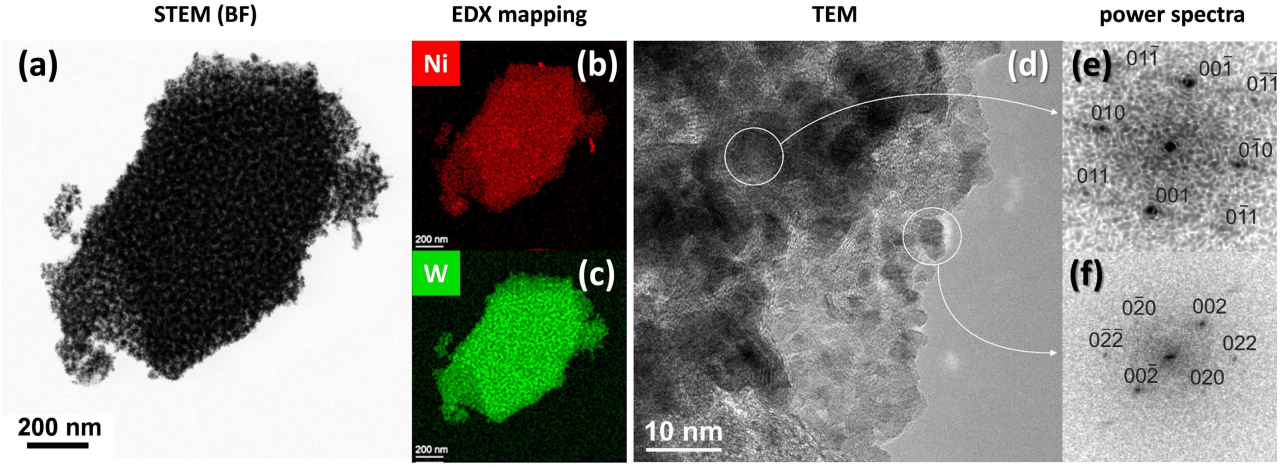

Figure 2. (a) Typical bright field (BF) STEM image of ALD-NiO/mp. WC_x. (b) Ni and (c) W EDX elemental mappings collected in the area shown in (a). (d) Representative TEM image of ALD-NiO/mp. WC_x. (e) Power spectrum of the indicated region shown in (d) typical of WC in [100] zone axis and (f) of NiO in [100] zone axis. The results from electron microscopy (a–d) suggest the formation of a nanostructured material with well-preserved mesoporosity. From the corresponding EDX elemental mappings (b, c), the homogeneous distribution of NiO species inside the pore system of the carbide carrier becomes evident. In (d), lattice fringes for both WC_x and NiO can be found. Notably, NiO is predominant at the outer surface of the material in the form of a surrounding top layer (d). For (e) and (f), two regions with crystallites showing a clear pattern were selected, as indicated by the white circles and corresponding arrows in (d).

Table 1. Electrocatalytic performance of mp. WC_x, mp. WO_x, mp. NiO_x, NiO-ALD/mp. WC_x, NiO-ALD/mp. WO_x, and NiO-ALD/mp. NiO_x.

Sample description	ALD cycle number	Ni loading[a] [µg cm^{-2} geom. area]	Sheet conductivity[b] [S cm^{-1}]	ECSA[c] [cm^2]	Overpotential [mV][d]		Mass activity (1.60 V, CV 30) [A g_{Ni}^{-1}]	Tafel slope (CV 30) [mV dec^{-1}]
					10 mA cm^{-2}, CV 30	10 mA cm^{-2}, CV 50		
mp. WC_x	0	0	$5.4 \cdot 10^{2}$	–	*	*	–	117
ALD-NiO/mp. WC_x	150	7 ± 1	$2.9 \cdot 10^{1}$	11.4	360	368	1989	57
mp. WO_x	0	0	$1.1 \cdot 10^{-1}$	–	–	–	–	–
ALD-NiO/mp. WO_x	150	8 ± 2	$1.1 \cdot 10^{-2}$	4.5	427	550	234	83
mp. NiO_x	0	33 ± 2	$3.0 \cdot 10^{-3}$	2.2	*	*	9	138
ALD-NiO/mp. NiO_x	150	45 ± 4	$1.4 \cdot 10^{-6}$	1.7	*	*	7	154

[a] Ni loading determined by ICP-OES after dissolution of the films via acid digestion. [b] Electrical conductivity investigated by impedance spectroscopy in the dark. [c] ECSA calculated from double layer capacitance C_{dl} (Figure S8). The values are stated in cm^2 per geometric cm^2 film area on extensively polished Ti substrates. [d] Asterisks denote catalysts for which the current density did not reach $j = 10$ mA cm^{-2} within the investigated OER potential window (1.20–1.95 V vs. RHE).

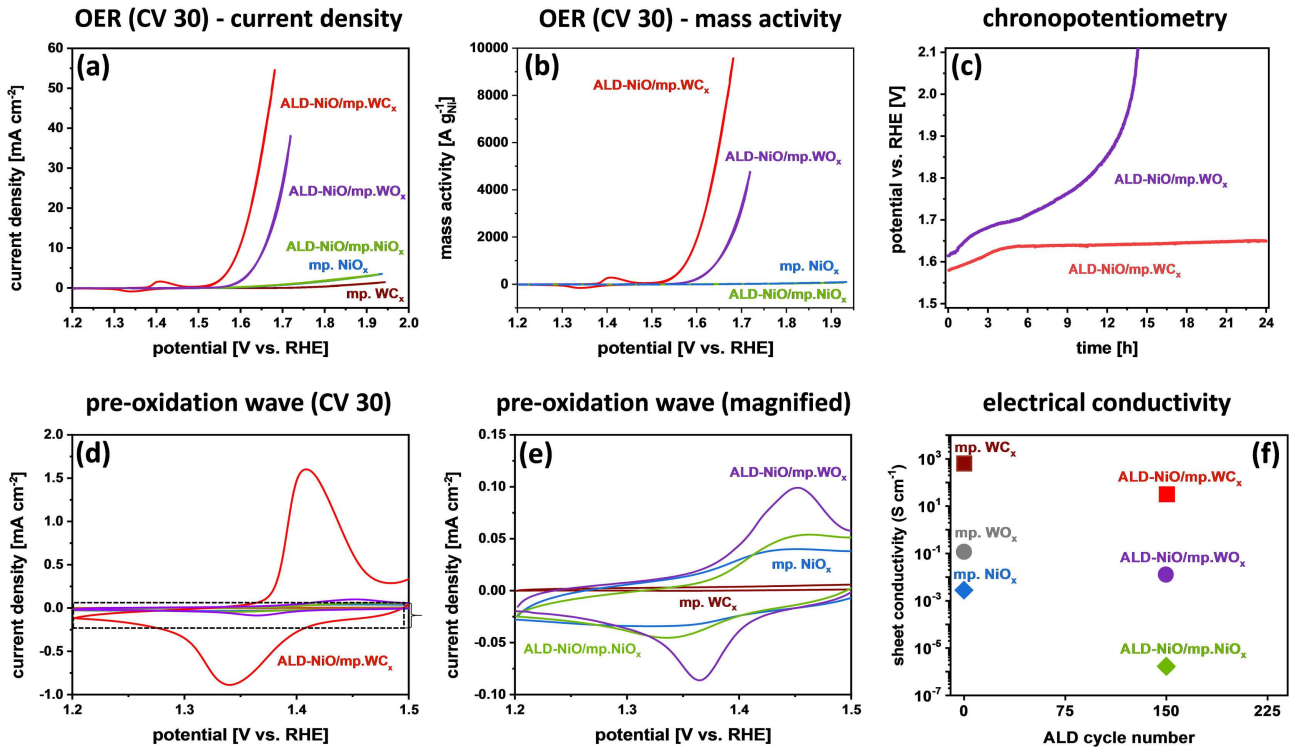

Figure 3. (a) CVs of ALD-NiO/mp. WC_x, bare mp. WC_x carrier, pristine mp. NiO_x, ALD-NiO/mp. WO_x, and ALD-NiO/mp. NiO_x using a RDE setup and N_2-purged 0.1 M KOH at 25 °C. The 30th CV is plotted for each catalyst system. (b) Mass activities of ALD-NiO/mp. WC_x, pristine mp. NiO_x, ALD-NiO/mp. WO_x, and ALD-NiO/mp. NiO_x derived from CVs plotted in (a), normalized by Ni contents. (c) Chronopotentiometric stability test of ALD-NiO/mp. WC_x and ALD-NiO/mp. WO_x for 24 h with a constant current density of 10 mA cm^{-2} in 0.1 KOH at 25 °C. (d) Pre-oxidation wave of $Ni^{2+/3+}$ enlarged from the 30th CVs in (a). (e) Enlarged section of (d) in a lower current density range from −0.075 to 0.012 mA cm^{-2}. Note that the red curve has been removed for the sake of clarity. (f) Electrical sheet conductivities assessed by impedance spectroscopy of bare mp. WC_x, mp. WO_x, mp. NiO_x carriers, and the ALD-NiO/mp. WC_x, ALD-NiO/mp. WO_x, and ALD-NiO/mp. NiO_x. All investigated films were deposited on flat, insulating glass substrates for the impedance spectroscopy measurements at $T = 25$ °C.

the Ni content (Figure 3b). The latter was determined by using inductively coupled plasma optical emission spectrometry (ICP-OES, Table 1). In addition, for the most active catalyst system, StrataGem/WDX analysis was performed to confirm the Ni loading without dissolution of the material. At a potential of 1.60 V vs. RHE, ALD-NiO/mp. WC_x reaches a Ni-mass based OER activity of 1989 A g^{-1}, which is ~9-fold higher than that of ALD-NiO/mp. WO_x, ~221-fold higher than that of pristine mp. NiO_x, and ~284-fold higher than that of ALD-NiO/mp. NiO_x. The outstanding Ni mass-specific activity of the ALD-NiO/mp. WC_x electrocatalyst can be explained by the ultra-low loading and high accessibility of the well-dispersed NiO active centers at the entire surface of the porous carrier film. Beyond that, a comparison of OER activities with state-of-the-art Ni-based catalysts highlights the superior OER activity of ALD-NiO/mp. WC_x (Table 2). In this context, it has to be noted that the herein developed catalyst does not suffer from any blocking of active sites by Nafion binder species.[59]

Moreover, the Tafel slopes (Figure S5) of the electrocatalysts were derived from the CV curves shown in Figure 3a. Pristine

Table 2. RDE-OER performance of highly efficient nickel-based electrocatalysts in alkaline electrolyte at RT reported in literature. Unless otherwise stated, the supporting electrolyte refers to unpurified KOH electrolyte which is expected to contain trace amounts of Fe impurities.

Catalyst	Electrolyte	Electrode type[a]	Binder	Tafel slope [mV dec^{-1}]	Overpotential[b] [V]	Mass activity[c] [A g^{-1}]	Reference
ALD-NiO/mp. WC_x	0.1 M KOH	Ti chip	binder-free	57	0.36	1989 (1.60 V_{RHE})	this work
mp. NiO_x	0.1 M KOH	Ti chip	binder-free	-	0.43 ($j = 1$ mA cm^{-2})	*n. a.*	[24]
NiO-ALD	1.0 M KOH (Fe-saturated)	FTO	binder-free	30	0.48	*n. a.*	[18]
LDH/G/Ni	0.1 M KOH	Ni-foam	binder-free	44	0.33	23 (1.60 V_{RHE})	[59]
NiO-$(La_{0.613}Ca_{0.387})_2NiO_{3.562}$	0.1 M KOH	GC	Nafion	42	0.37	52 (1.63 V_{RHE})	[61]
Ru_3Ni_1NAs	0.1 M KOH	GC	Nafion	152	0.38	*n. a.*	[62]
$NiFe_2O_4$	0.1 M KOH	GC	Nafion	80	0.37	11 (1.70 V_{RHE})	[63]
FeNC sheet/NiO	0.1 M KOH	carbon paper	Nafion	76	0.39	*n. a.*	[64]
ALD-NiO/CNT	1.0 M KOH (Fe-free)	GC	Nafion	50	0.32	*n. a.*	[27]
Ni/WC composite	0.1 M KOH	GC	Nafion	52	0.32	~530[d]	[60]

[a] GC = glassy carbon. [b] Overpotential at a current density of $j = 10$ mA cm^{-2}, unless otherwise stated. [c] Mass activities calculated based on the loading amounts of active species in the catalysts. [d] Mass activity estimated from compositional analysis by EDX (catalyst composition of $Ni_{1.77}WC$ assumed) and LSV curve in 1.0 M KOH.

mp. NiO_x and ALD-NiO/mp. NiO_x feature large Tafel slopes of 138 and 154 mV dec^{-1}, corresponding fairly well to the typical Tafel slope of pristine NiO reported in literature (see Table 2). In contrast, ALD-NiO/mp. WC_x exhibits a significantly reduced Tafel slope of 57 mV dec^{-1}, indicating remarkably faster reaction kinetics. Interestingly, the Tafel slope of ALD-NiO/mp. WC_x resembles that of ALD-NiO/CNT in our previous work,[27] further highlighting that applying a highly conductive substrate can significantly enhance the performance of a NiO-containing electrocatalyst.

Beside a high catalytic activity, a sufficient stability represents a key challenge of carbon-based support materials in OER catalysis under oxidative potentials. Hence, the stability of ALD-NiO/mp. WC_x was examined as a next step (Figure 3c). In the initial phase of the chronopotentiometric stability test, a slight increase in potential is visible, which originates from the oxidation of residual carbon species either from an incomplete decomposition of the polymer template or from the carburization step. In addition, a slight surface oxidation process at the carbide-NiO interface occurs, as described in the following. After reaching a stable state after about 4 h of testing, the catalytic activity of ALD-NiO/mp. WC_x remained stable until the end of the stability test over 24 h, providing strong evidence that the ALD-derived NiO coating is indeed effective in preventing an oxidative degradation of the bulk of the porous tungsten carbide scaffold. Contrarily, ALD-NiO/mp. WO_x did not reach a stable performance during the stability test, which is a consequence of an ongoing loss of active material by means of dissolution into the electrolyte. After about 14 h, most of the active material was dissolved into the surrounding electrolyte, resulting in a steep increase in potential. High-resolution TEM (HR-TEM) images of post-OER ALD-NiO/mp. WC_x scrapped off from the Ti substrate were taken (Figure S6-I). From the representative HR-TEM images, the crystallinity of both mp. WC_x carrier and NiO layer can still be claimed, which is further underlined by SAED analysis (see the Supporting Information, Section 6 for details). Ultimately, the existence of the thin NiO layer is proposed to effectively protect the WC_x carrier from pronounced bulk oxidation during OER, leading to the observed high catalytic stability.

XPS depth profiling of the spent catalyst ALD-NiO/mp. WC_x revealed a surface-oxidation of the WC_x carrier during OER, yet the underlying carbide phase appears to be sufficiently stable against further oxidation (see the Supporting Information, Section 7). Song et al.[60] reported similar observations for Ni/WC composite nanoparticles. The formation of a Ni^0-rich shell was demonstrated to effectively prevent the WC from oxidation during RDE-OER measurements in 1.0 M KOH.

In the present work, highly conformal NiO-ALD (cf. Figure S1) ensures the development of nanostructured catalyst coatings with well-defined mesoporosity that is essentially preserved after OER testing (see the Supporting Information, Section 7).

Electrical properties, estimation of ECSA and DFT calculations

In order to understand the superior OER activity of the ALD-NiO/mp. WC_x electrocatalytic system, the electrical properties of the bare and the NiO-coated carrier materials were investigated (Figure 3f). The sheet conductivities of both mp. WC_x and ALD-NiO/mp. WC_x are several orders of magnitude higher than that of the other materials, leading to significantly enhanced kinetics of the ALD-NiO/mp. WC_x electrocatalyst,[9] which is further proven by its smaller Tafel slope.[9,27,60] Regarding the superior catalytic activity, calculations of the ECSA from the double-layer capacitance (Supporting Information, Section 8) provide deeper insights, as the significantly enhanced ECSA of ALD-NiO/mp. WC_x reveals an excellent active site accessibility, which can be attributed to the mesoporosity introduced by the mp. WC_x carrier. This highlights the excellent suitability of ALD for the introduction of active species onto the porous system of an inactive, yet highly conductive, carrier. Enlarging the CV curves in a lower potential range of 1.20–1.60 V vs. RHE (Figure 3d, e),

the pre-oxidation wave of $Ni^{2+/3+}$ located at approximately 1.42 V vs. RHE becomes evident.[9] Due to the fact that Ni^{3+} has been shown to be the main responsible species for high OER activity, particularly, the pre-oxidation of Ni^{2+} to Ni^{3+} is a crucial process to optimize the electrocatalytic behavior.[9] When comparing with ALD-NiO/mp. WO_x, ALD-NiO/mp. NiO_x and mp. NiO_x, the pre-oxidation wave for ALD-NiO/mp. WC_x is, on the one hand, more pronounced and, on the other hand, shifted to lower potentials. However, it has to be noted that the presence of trace Fe impurities in the KOH electrolyte alters both intensity and position of the reversible $Ni^{2/3+}$ redox peaks (see the Supporting Information, Section 4).[9,23,65] However, our experimental data reveal a significantly increased number of well-accessible active Ni^{3+} sites for ALD-NiO/mp. WC_x that finally lead to the excellent OER activity due to the systematic investigations and similar measurement conditions for all herein studied catalyst systems. In order to highlight the high intrinsic activity of the surface Ni species in ALD-NiO/mp. WC_x, additional electrochemical measurements using an extensively purified Fe-free KOH electrolyte were conducted (Figure S4-II).

To gain deeper insights into the experimentally observed carbide-promoted $Ni^{2+} \rightarrow Ni^{3+}$ transitions, DFT calculations using the Vienna ab initio simulation package (VASP)[66–69] and projector-augmented wave (PAW) approach of Joubert and Kresse[70,71] (see Computational details and Section 9 in the Supporting Information) were performed based on simplified structural slab models of a NiO-coated W_2C (100) surface and a bare NiO (100) surface as a reference. Therefrom, the reaction energies with *OH intermediate species during the initial phases of the OER process were calculated for both NiO-coated W_2C and NiO. The obtained free energies clearly reveal a pronounced beneficial impact of the underlying carbide layers on the adsorption of *OH intermediates on the surface-exposed NiO layer. Our theoretical results provide clear evidence for a more favorable adsorption of *OH intermediate species for the NiO-coated W_2C lattice compared to the NiO reference (Figure S9). Thus, the theoretical findings corroborate the experimentally observed enhanced conversion of Ni^{2+} into Ni^{3+} active sites for ALD-NiO/mp. WC_x. Ultimately, the high number of surface-exposed and well-accessible NiOOH structural motifs in ALD-NiO/mp. WC_x boosts its OER activity in alkaline electrolyte.

Conclusion

In summary, a synthesis route affording macroscopically crack-free, homogeneous mp. WC_x films with interconnected porosity by pseudomorphic carburization of a mp. WO_x precursor film was developed for the first time. A highly efficient ALD-NiO/mp. WC_x OER electrocatalyst was obtained by using highly conformal NiO-ALD on the mp. WC_x carrier. Despite the ultra-low loading, the NiO/WC_x electrocatalyst shows a moderate overpotential of 360 mV in 0.1 M KOH and a remarkably high Ni mass-based OER activity of 1989 $A\,g^{-1}$ as a result of the easily accessible active sites. In this system, the mp. WC_x carrier plays a crucial role in leading to this outstanding activity. On the one hand, the mp. WC_x provides a highly conductive mesoporous scaffold that largely enhances the kinetics of the entire system. On the other hand, the synergetic effects between NiO and mp. WC_x significantly improve the conversion from Ni^{2+} into Ni^{3+}, hence, it provides additional highly active sites for the electrocatalytic OER. In this context, theoretical calculations provide further evidence for a more favorable adsorption energy of *OH intermediate species with respect to bare NiO. All in all, a novel and highly promising mp. WC_x carrier film was developed, offering new approaches for the production of highly active electrocatalysts with excellent electrical properties. The present study serves as a proof-of-concept for the development of highly efficient electrocatalysts with maximized utilization of active species provided by conformal ALD on porous metal carbide scaffolds. Future works will focus on controlled surface modifications of different mesoporous carbide carriers, for example with binary metal oxides such as Co–Ni oxides or noble metal species.

Experimental Section

Synthesis of mesoporous films

Different substrates were used for the deposition of the materials. Single-side polished silicon (Si) wafers obtained from University Wafers with (100) orientation were cleaned with EtOH after a thermal treatment in air for 2 h at 600 °C prior to film deposition. For the electrical sheet conductivity measurements by using impedance spectroscopy, insulating quartz glass (SiO_2) substrates (Science Services GmbH) were used and cleaned using a mixture of KOH and *i*PrOH prior to film deposition. Electrochemical measurements were performed using conductive titanium (Ti) substrates, polished with a 0.02 μm colloidal silica suspension (amorphous; Buehler, MasterMet 2) and cleaned using a 1 : 1 mixture of EtOH and *i*PrOH.

For the synthesis of mesoporous WO_x films, anhydrous tungsten(VI) chloride (WCl_6, > 99.9 % trace metals basis) was purchased from Merck. Citric acid (> 99.5 %, reagent grade) and ethanol (≥ 99.8 %) were purchased from VWR Chemicals. As structure-directing agent, a triblock copolymer PEO-PB-PEO, composed of 20400 $g\,mol^{-1}$ polyethylene oxide (PEO) and 10000 $g\,mol^{-1}$ polybutadiene (PB) was purchased from Polymer Service Merseburg GmbH.[8] All chemicals were used as received without any further purification. In a typical synthesis, the PEO-PB-PEO polymer template (55 mg) was dissolved in EtOH (1.50 mL) at 45 °C (Ar). A clear solution was obtained after stirring for 2 h at 45 °C (**I**). In another vial, WCl_6 (397 mg, 1.0 mmol) was dissolved in EtOH (1.50 mL; Ar) under stirring. Citric acid (384 mg, 2.0 mmol; 2.0 eq.) were added under stirring (Ar) affording a clear dark blue solution (**II**). The addition of citric acid led to a change from a dark green to a dark blue solution, indicating the formation of a metal-ligand complex, as described by Eckhardt et al.[44] for different metal ions in previous works. After stirring for 30 min at 45 °C (Ar), solution (**I**) was added. After stirring for a further 2 h at 45 °C (Ar), the obtained clear dark blue solution (**III**) was transferred into a Teflon cuvette (preheated to 45 °C) and dip-coating was performed in a controlled atmosphere in air (T = 25 °C, relative humidity of 35–40 %) on different substrates with a withdrawal rate of 300 $mm\,min^{-1}$. The films were dried for at least 5 min in the controlled atmosphere. After calcination in nitrogen atmosphere for 5 h at 500 °C with a heating ramp of 2 $K\,min^{-1}$, colored films were obtained.

The obtained mp. WO_x films were converted into mp. WC_x films with well-preserved nanocrystallinity and porous structure by carburization in a ternary gas mixture of CH_4, H_2 and Ar. The ratio of CH_4:H_2 during the carburization step for 6 h at 700 °C in a large tube furnace was set to 6:1. A heating rate of 1 K min^{-1} was used. The films were passivated after reaching RT in a mixture of 1% O_2/Ar for at least 3 h. For the removal of surface coke deposits on the materials, another heat treatment for 2 min at 550 °C in air was performed. Dark grey films were obtained.

For the synthesis of mp. NiO_x films, a previously established method by Bernicke et al.[24] was used. In brief, dip-coating solutions were prepared by dissolving a triblock-copolymer template (PEO_{213}-PB_{184}-PEO_{213}; 60 mg) in EtOH (3.0 mL). The solution was stirred for 2 h at 45 °C. Then, citric acid (144 mg) and $Ni(NO_3)_2 \cdot 6H_2O$ (436.0 mg; NeoLab, 98%) were added. The obtained clear green solution was transferred into a cuvette placed inside a dip-coater at 25 °C and a relative humidity of 40%. After drying, the samples were heated with 2 K min^{-1} to 250 °C and after 1 h at 250 °C, temperature was increased with a ramp of 2 K min^{-1} to 400 °C and again held for 1 h.

NiO-ALD

Nickelocene (Bis(cyclopentadienyl)nickel, $Ni(Cp)_2$, 99%) was purchased from STREM Chemicals Inc. Ozone (O_3) was generated using oxygen (99.99%) at a pressure of 0.5 bar in a BMT803N ozone generator. The estimated concentration of ozone delivered to the ALD system was 60–70 g Nm^{-3}. Argon, nitrogen, and oxygen were provided by Air Liquide (99.99% purity). NiO was directly deposited on the mesoporous WC_x, WO_x and NiO_x films on flat Ti, Si or quartz substrates. Moreover, pre-cleaned single-side polished Si wafers (Siegert Wafer B014002) with a native SiO_2 layer (about 1.2–1.8 nm) were also added into the ALD chamber for calibration of the NiO-thickness by spectroscopic ellipsometry (SE). ALD was performed in a commercial ALD system by ARRADIANCE (GEMStar-6). The comprehensive of the experimental procedure can be found elsewhere.[27,51,52] In brief, nickelocene (contained in a stainless-steel canister at 90 °C) and O_3 (as generated at RT) were used as metal precursor and oxygen source, respectively. The precursors were supplied using two separate manifolds for metal precursor and oxygen source that were maintained at 120 °C and 100 °C, respectively. Ar was used as a carrier and purging gas for the precursors to the reaction chamber, and to remove any of the excess reactants and by-products. Additionally, an Ar booster was used as pulsed-vapor-push method (PVP^{TM}) to carry out nickelocene vapors to the reaction chamber. The ALD system was evacuated (approx. $7.5 \cdot 10^{-3}$ mbar), and the temperature of the ALD reaction chamber was stabilized at 200 °C before starting the deposition. Prior to ALD, all samples were treated in situ with UV-O_3 (5 cycles of 0.5 s O_3 pulse/30 s exposure/15 s purge; total exposure time = 150 s) to remove any residual surface organic impurities and to functionalize the surface, thereby promoting the chemisorption of the nickelocene species. The ALD cycle was adjusted as a sequence of pulse/exposure/purge time as 1.2 s/20 s/30 s and 0.2 s/20 s/30 s for $Ni(Cp)_2$ and O_3, respectively.

Characterization

SEM images were recorded at 20 kV on a JEOL 7401F. The obtained SEM images were evaluated with ImageJ freeware, version 1.48 (www.imagej.nih.gov/ij). Corresponding FFT images were created using this software.

TEM images were taken using a FEI Tecnai G2 20 S-TWIN and a FEI Talos transmission electron microscopes at 200 kV acceleration voltage on scraped-off film fragments deposited on carbon-coated copper grids. A FEI Talos EDX detector was used to collect the elemental mapping for the samples. The EDX elemental mappings were analyzed using FEI Velox software version 2.6. The obtained TEM images and SAED patterns were evaluated with *ImageJ* freeware.

X-ray photoelectron spectra (XPS) were obtained using a Thermo Fisher Scientific ESCALAB 250Xi featuring a spot size of 400 μm, K-alpha X-rays. The peak position of adventitious carbon (284.80 eV) was used in order to correct the binding energy of the obtained spectra. The fitting of the XPS spectra and the quantification of the elemental composition was processed by the software Avantage. The XPS depth profile was measured with 3 cycles of Ar monatomic ion gun etching. The measurement was in low current, single phase etching mode, ion energy for the etching was 4000 eV. Raster size was 1 mm. The sputter rate using Ta_2O_5 as a reference amounts to 0.74 nm s^{-1}.

For the ICP-OES measurements, mesoporous films deposited on Si and on Ti substrates were used after dissolution in acid. Measurements were conducted on a Varian ICP-OES 715 ES (radial configuration). For calibration, aqueous solutions containing both Ni and W (Carl Roth) were prepared. For the calculation of the geometric Ni loading, the geometric areas of the films were evaluated using ImageJ software prior to dissolution of the materials. Each film was digested using a mixture of MilliQ H_2O (1.50 mL) and concentrated HNO_3 (1.50 mL; 65%, Carl Roth) under the application of ultrasound for 4 h at 60 °C. Complete dissolution was indicated by the bare polished wafer surface becoming visible for all investigated samples after the digestion step. Similar geometric Ni loadings were obtained for films deposited on Si and Ti substrates. Alternatively, the evaluation of the geometric loading of the synthesized films, wavelength-dispersive X-ray spectroscopy (WDX) was performed using StrataGem film analysis software (v. 4.8). Five independent measurements were conducted for the most important sample of the study-ALD-NiO/mp. WC_x-using a JEOL JXA-8530F electron microprobe at 10 kV. The mass depth of all components of the analyzed film amounts to an average of 96 ± 1 μg cm^{-2}. Cross-sectional SEM revealed an average sheet thickness of 230 nm (see the Supporting Information Figure S3-II).

The surface areas were measured by Kr-physisorption at 77 K on an Autosorb-iQ (Quantachrome) cooled with liquid N_2. Films were deposited on both sides of double-side polished Si wafers. Prior to the measurements, all samples were degassed for 2 h at 150 °C under vacuum. The geometric areas of the investigated films was analyzed using ImageJ freeware. Finally, the surface areas were calculated by using the well-established Brunauer-Emmett-Teller (BET) method. Note that for the analysis of the NiO-coated samples, the ALD process was applied twice to ensure coating of both sides on the substrate (successful loading was checked for both sides by EDX in a SEM at 20 kV acceleration voltage).

Values for the electrical sheet conductivities were calculated by impedance spectroscopy measurements in a home-built setup in the dark. The measurements were performed using a 8×8 gold pin array as probe head with an altering polarity sequence. A SP-200 potentiostat (Biologic) was used in a range between 100 mHz and 1 kHz. The obtained spectra (Nyquist impedance) were fitted using EIS Zfit software (EC-Lab v. 11.33, Biologic). All values are stated after normalization to the respective film thickness of the investigated material, which was obtained through cross-section SEM. All materials were deposited on insulating quartz glass substrates for the impedance measurements.

Pre-cleaned Si wafers (SSP, Siegert wafer B014002) with a native SiO_2 layer of approximately 1.2–1.8 nm were added into the ALD chamber to calibrate the NiO thickness by spectroscopic ellipsom-

etry (SE). The data were modelled using the software SpectraRay-3 ($Si/SiO_2/NiO$, Cauchy-stack and Lorentz–Lorenz model for SiO_2 and NiO, respectively).

Electrochemistry

Electrocatalytic testing was performed in a three electrode rotating disc setup (RDE) using a reversible hydrogen electrode (Gaskatel, HydroFlex) as a reference and a Pt gauze (Chempur, 1024 mesh cm^{-2}, a wire diameter of 0.06 mm, 99.9% purity) as counter electrode at 25 °C. All potentials are referred to reversible hydrogen electrode (RHE) and are *iR*-corrected to account for Ohmic losses in the setup. For the investigations of the OER activity, mesoporous films coated on a spherical Ti chip of 5 mm diameter were mounted on a rotating disc shaft serving as working electrode. A constant rotation of 1600 rpm was set. 0.1 M KOH was used as supporting electrolyte (Sigma Aldrich, pellets, 99.99% trace metals basis, purity excluding sodium content) and a SP-200 as potentiostat. The electrolyte solution was purged with N_2 for at least 30 min prior to catalytic testing. The OER activity was investigated by cyclic voltammetry (CV) between 1.20 and 1.95 V vs. RHE at a scan rate of 6 mV s^{-1}. It has to be noted that no electrochemical activation of the films has been performed, which is known to increase the observed OER activities for NiO electrocatalysts.[24]

For the evaluation of the double-layer capacitance (C_{dl}) and determination of the ECSA, after 50 CVs in OER regime, cycling with increasing scan rates of 50, 75, 100, 125, and 150 mV s^{-1} was performed in a lower potential range between 0.40 to 1.40 V vs. RHE at 25 °C. At each scan rate, five consecutive CVs were recorded. *iR*-corrections were applied for each scan rate. For the calculation of the double-layer capacitance from CV, the average values of the anodic and cathodic current densities at 0.90 V vs. RHE were used. By dividing C_{dl} by the specific capacitance of the sample (C_s = 0.040 mF cm^{-2} stated by McCrory et al.[72]), the ECSA can be calculated.

For the chronopotentiometric stability testing, mesoporous films coated on a conductive Ti substrate, to which a piece of Ti wire was attached by welding, were used. The relative geometric areas of the mesoporous films were measured using ImageJ software and the current densities were set to 10 mA cm^{-2} OER during chronopotentiometry in 0.1 M KOH at 25 °C.

Computational details

All calculations were carried out with the plane wave Vienna ab initio simulation package VASP,[66–69] version 6.1.1/6.1.2, using the projector-augmented wave (PAW) approach of Joubert and Kresse.[70,71] The PBE functional[73] was applied. London dispersion effects were taken into account by the D3 correction with Becke–Johnson damping.[74–77] The respective PAW parameters were extracted from the VASP POTCAR files library, C 08Apr2002 [4 valence electrons (VE)], W 08Apr2002 (6 VE), Ni 02Aug2007 (10 VE), O 08Apr2002 (6 VE), H 15Jun2001 (1 VE). The energy cutoff was set to 900 eV, except for the adsorbed *OH species on ALD-NiO/mp. WC_x with 600 eV and the gas phase molecules H_2O and H_2 with 450 eV. For the WC_x carrier material, a simplified description using the predominant W_2C phase was established. Preliminary tests for the W_2C bulk revealed that its ground state is non-magnetic. Thus, restricted Kohn–Sham calculations were performed for this system. In all calculations, for NiO an antiferromagnetic state was assumed by defining alternating magnetic moments on the Ni atoms, but without fixing the total magnetic moment during the SCF procedure. The space groups of NiO and W_2C are $Fm\bar{3}m$[78] and $P\bar{3}1m$,[79] respectively. For the antiferromagnetic ground state of NiO, a [(0,1,1),(1,0,1),(1,1,0)] supercell was built. The crystal structure of W_2C, which includes partial occupations of Wyckoff sites 2c and 2d by the carbon atoms, was simplified and all carbon atoms were placed on 2d (1/3, 2/3, 1/2) Wyckoff positions. For the surface optimization, the lattice constants were fixed at the optimized bulk values and only the atomic positions were relaxed. The Monkhorst–Pack k-point grids were set to 4×4×4 for the NiO and W_2C bulk and to 4×4×1 for the surface calculations. To receive the antiferromagnetic order in NiO in the (100) surface, a 2×1-supercell of a (121)-cut of the bulk supercell was set up. The surface models were composed of six stoichiometric layers for NiO and five W_2C layers with one NiO layer at both top and bottom for the NiO-covered W_2C models. The vacuum distance was set to 12 Å, convergence was tested for adsorption of oxygen species for similar systems. Convergence criteria were set to 10^{-6} eV for the chronopotentiometric electronic self-consistent cycle and 0.01 eV $Å^{-1}$ for structure optimization.

Acknowledgements

The authors thank ZELMI (TU Berlin) for access to TEM and SAED analyses and gratefully acknowledge financial support by BMBF (Bundesministerium für Bildung und Forschung) ATO-KAT: Atomar dünn beschichtete poröse Elektroden als neuartige Katalysatoren für die Wasser-Elektrolyse (03EK3052A, 03EK3052C). A.A. and R.K. gratefully acknowledge funding through the DFG SPP 2080 priority program (KR 3920/4-1). Arne Thomas (TU Berlin) is thankfully acknowledged for providing access to XPS analyses. Christoph Erdmann (HU Berlin) is acknowledged for HRTEM, SAED, HAADF-STEM, and elemental mapping measurements. The authors thank Jörg Nissen (TU Berlin, ZELMI) very much for WDX/StrataGem analyses and Astrid Kluge (TU Berlin) for performing ICP-OES measurements and calibration. Benjamin Paul (TU Berlin) is thankfully acknowledged for assistance in building a setup for impedance spectroscopy measurements of thin films in the dark. Open Access funding enabled and organized by Projekt DEAL.

Conflict of Interest

The authors declare no conflict of interest.

Keywords: atomic layer deposition · electrocatalysis · metal carbides · mesoporous materials · nickel

[1] Y. Xu, M. Kraft, R. Xu, *Chem. Soc. Rev.* **2016**, *45*, 3039–3052.
[2] J. Li, Y. Wang, T. Zhou, H. Zhang, X. Sun, J. Tang, L. Zhang, A. M. Al-Enizi, Z. Yang, G. Zheng, *J. Am. Chem. Soc.* **2015**, *137*, 14305–14312.
[3] J. Wang, W. Cui, Q. Liu, Z. Xing, A. M. Asiri, X. Sun, *Adv. Mater.* **2016**, *28*, 215–230.
[4] S. Cobo, J. Heidkamp, P.-A. Jacques, J. Fize, V. Fourmond, L. Guetaz, B. Jousselme, V. Ivanova, H. Dau, S. Palacin, M. Fontecave, V. Artero, *Nat. Mater.* **2012**, *11*, 802–807.
[5] J. Kim, X. Yin, K.-C. Tsao, S. Fang, H. Yang, *J. Am. Chem. Soc.* **2014**, *136*, 14646–14649.
[6] N.-T. Suen, S.-F. Hung, Q. Quan, N. Zhang, Y.-J. Xu, H. M. Chen, *Chem. Soc. Rev.* **2017**, *46*, 337–365.
[7] M. Ye, S. Li, X. Zhao, N. V. Tarakina, C. Teutloff, W. Y. Chow, R. Bittl, A. Thomas, *Adv. Mater.* **2020**, *32*, 1903942.

[8] E. Ortel, T. Reier, P. Strasser, R. Kraehnert, *Chem. Mater.* **2011**, *23*, 3201–3209.
[9] M. Görlin, J. Ferreira de Araújo, H. Schmies, D. Bernsmeier, S. Dresp, M. Gliech, Z. Jusys, P. Chernev, R. Kraehnert, H. Dau, P. Strasser, *J. Am. Chem. Soc.* **2017**, *139*, 2070–2082.
[10] M. Biegun, X. Chen, E. Mijowska, *ChemElectroChem* **2018**, *5*, 2681–2685.
[11] T. Reier, M. Oezaslan, P. Strasser, *ACS Catal.* **2012**, *2*, 1765–1772.
[12] D. V. Esposito, J. G. Chen, *Energy Environ. Sci.* **2011**, *4*, 3900.
[13] Y.-J. Wang, D. P. Wilkinson, J. Zhang, *Chem. Rev.* **2011**, *111*, 7625–7651.
[14] A. S. Aricò, P. Bruce, B. Scrosati, J.-M. Tarascon, W. van Schalkwijk, *Nat. Mater.* **2005**, *4*, 366–377.
[15] X. Li, X. Hao, A. Abudula, G. Guan, *J. Mater. Chem. A* **2016**, *4*, 11973–12000.
[16] J. W. D. Ng, M. García-Melchor, M. Bajdich, P. Chakthranont, C. Kirk, A. Vojvodic, T. F. Jaramillo, *Nat. Energy* **2016**, *1*, 16053.
[17] T. Zhang, M.-Y. Wu, D.-Y. Yan, J. Mao, H. Liu, W.-B. Hu, X.-W. Du, T. Ling, S.-Z. Qiao, *Nano Energy* **2018**, *43*, 103–109.
[18] K. L. Nardi, N. Yang, C. F. Dickens, A. L. Strickler, S. F. Bent, *Adv. Energy Mater.* **2015**, *5*, 1500412.
[19] M. Gong, Y. Li, H. Wang, Y. Liang, J. Z. Wu, J. Zhou, J. Wang, T. Regier, F. Wei, H. Dai, *J. Am. Chem. Soc.* **2013**, *135*, 8452–8455.
[20] D. Bernsmeier, M. Bernicke, R. Schmack, R. Sachse, B. Paul, A. Bergmann, P. Strasser, E. Ortel, R. Kraehnert, *ChemSusChem* **2018**, *11*, 2367–2374.
[21] F. Lyu, Q. Wang, S. M. Choi, Y. Yin, *Small* **2019**, *15*, 1804201.
[22] M. Shao, Q. Chang, J.-P. Dodelet, R. Chenitz, *Chem. Rev.* **2016**, *116*, 3594–3657.
[23] M. Yu, G. Moon, E. Bill, H. Tüysüz, *ACS Appl. Mater. Interfaces* **2019**, *2*, 1199–1209.
[24] M. Bernicke, B. Eckhardt, A. Lippitz, E. Ortel, D. Bernsmeier, R. Schmack, R. Kraehnert, *ChemistrySelect* **2016**, *1*, 482–489.
[25] S. M. Bhaway, P. Tangvijitsakul, J. Lee, M. D. Soucek, B. D. Vogt, *J. Mater. Chem. A* **2015**, *3*, 21060–21069.
[26] D. Chandra, T. Sato, Y. Tanahashi, R. Takeuchi, M. Yagi, *Energy* **2019**, *173*, 278–289.
[27] Y. Fan, Y. Wu, G. Clavel, M. H. Raza, P. Amsalem, N. Koch, N. Pinna, *ACS Appl. Mater. Interfaces* **2018**, *1*, 4554–4563.
[28] S. Lu, J. Wu, H. Hu, X. Pan, Z. Hu, H. Li, H. Zhu, F. Duan, M. Du, *J. Colloid Interface Sci.* **2021**, *585*, 258–266.
[29] Y. Wang, S. Song, P. K. Shen, C. Guo, C. M. Li, *J. Mater. Chem.* **2009**, *19*, 6149.
[30] R. Sachse, D. Bernsmeier, R. Schmack, I. Häusler, A. Hertwig, K. Kraffert, J. Nissen, R. Kraehnert, *Catal. Sci. Technol.* **2020**, *10*, 2057–2068.
[31] D. Bernsmeier, R. Sachse, M. Bernicke, R. Schmack, F. Kettemann, J. Polte, R. Kraehnert, *J. Catal.* **2019**, *369*, 181–189.
[32] H. Jiang, J. Gu, X. Zheng, M. Liu, X. Qiu, L. Wang, W. Li, Z. Chen, X. Ji, J. Li, *Energy Environ. Sci.* **2019**, *12*, 322–333.
[33] J. Zhang, Z. Zhao, Z. Xia, L. Dai, *Nat. Nanotechnol.* **2015**, *10*, 444–452.
[34] J.-M. Giraudon, P. Devassine, J.-F. Lamonier, L. Delannoy, L. Leclercq, G. Leclercq, *J. Solid State Chem.* **2000**, *154*, 412–426.
[35] Z. Wu, Y. Yang, D. Gu, Q. Li, D. Feng, Z. Chen, B. Tu, P. A. Webley, D. Zhao, *Small* **2009**, *5*, 2738–2749.
[36] Y. Wang, C. He, A. Brouzgou, Y. Liang, R. Fu, D. Wu, P. Tsiakaras, S. Song, *J. Power Sources* **2012**, *200*, 8–13.
[37] A. Löfberg, A. Frennet, G. Leclercq, L. Leclercq, J. M. Giraudon, *J. Catal.* **2000**, *189*, 170–183.
[38] Q. Gong, Y. Wang, Q. Hu, J. Zhou, R. Feng, P. N. Duchesne, P. Zhang, F. Chen, N. Han, Y. Li, C. Jin, Y. Li, S.-T. Lee, *Nat. Commun.* **2016**, *7*, 13216.
[39] Z. Chen, W. Gong, S. Cong, Z. Wang, G. Song, T. Pan, X. Tang, J. Chen, W. Lu, Z. Zhao, *Nano Energy* **2020**, *68*, 104335.
[40] D. Chatzikyriakou, N. Krins, B. Gilbert, P. Colson, J. Dewalque, J. Denayer, R. Cloots, C. Henrist, *Electrochim. Acta* **2014**, *137*, 75–82.
[41] G. A. Niklasson, L. Berggren, A.-L. Larsson, *Sol. Energy Mater. Sol. Cells* **2004**, *84*, 315–328.
[42] O. Ostrovski, G. Zhang, *AIChE J.* **2006**, *52*, 300–310.
[43] H. Wang, G. Li, J. Ma, D. Zhao, *RSC Adv.* **2017**, *7*, 3921–3927.
[44] B. Eckhardt, E. Ortel, J. Polte, D. Bernsmeier, O. Görke, P. Strasser, R. Kraehnert, *Adv. Mater.* **2012**, *24*, 3115–3119.
[45] T. Brezesinski, D. Fattakhova Rohlfing, S. Sallard, M. Antonietti, B. M. Smarsly, *Small* **2006**, *2*, 1203–1211.
[46] S. Sallard, T. Brezesinski, B. M. Smarsly, *J. Phys. Chem. C* **2007**, *111*, 7200–7206.
[47] T. Brezesinski, M. Groenewolt, A. Gibaud, N. Pinna, M. Antonietti, B. Smarsly, *Adv. Mater.* **2006**, *18*, 2260–2263.
[48] C. J. Brinker, Y. Lu, A. Sellinger, H. Fan, *Adv. Mater.* **1999**, *11*, 579–585.
[49] D. Grosso, F. Cagnol, G. J. de A. A. Soler-Illia, E. L. Crepaldi, H. Amenitsch, A. Brunet-Bruneau, A. Bourgeois, C. Sanchez, *Adv. Funct. Mater.* **2004**, *14*, 309–322.
[50] T. Fontecave, C. Boissiere, N. Baccile, F. J. Plou, C. Sanchez, *Chem. Mater.* **2013**, *25*, 4671–4678.
[51] M. H. Raza, N. Kaur, E. Comini, N. Pinna, *ACS Appl. Mater. Interfaces* **2020**, *12*, 4594–4606.
[52] M. H. Raza, K. Movlaee, S. G. Leonardi, N. Barsan, G. Neri, N. Pinna, *Adv. Funct. Mater.* **2020**, *30*, 1906874.
[53] X. Tong, Y. Qin, X. Guo, O. Moutanabbir, X. Ao, E. Pippel, L. Zhang, M. Knez, *Small* **2012**, *8*, 3390–3395.
[54] M. C. Biesinger, B. P. Payne, A. P. Grosvenor, L. W. M. Lau, A. R. Gerson, R. S. C. Smart, *Appl. Surf. Sci.* **2011**, *257*, 2717–2730.
[55] H. Wu, J. Geng, H. Ge, Z. Guo, Y. Wang, G. Zheng, *Adv. Energy Mater.* **2016**, *6*, 1600794.
[56] J. Liu, Y. Nan, X. Chang, X. Li, Y. Fang, Y. Liu, Y. Tang, X. Wang, R. Li, J. Ma, *Int. J. Hydrogen Energy* **2017**, *42*, 10802–10812.
[57] X. Wu, X. Han, X. Ma, W. Zhang, Y. Deng, C. Zhong, W. Hu, *ACS Appl. Mater. Interfaces* **2017**, *9*, 12574–12583.
[58] C. Tang, H.-F. Wang, X. Chen, B.-Q. Li, T.-Z. Hou, B. Zhang, Q. Zhang, M.-M. Titirici, F. Wei, *Adv. Mater.* **2016**, *28*, 6845–6851.
[59] H.-F. Wang, C. Tang, Q. Zhang, *J. Mater. Chem. A* **2015**, *3*, 16183–16189.
[60] D. Song, J. Shin, Y. Lee, Y. Kwon, J. Lim, E.-J. Kim, S. Oh, M. Kim, E. Cho, *ACS Appl. Mater. Interfaces* **2019**, *2*, 3452–3460.
[61] R. Liu, F. Liang, W. Zhou, Y. Yang, Z. Zhu, *Nano Energy* **2015**, *12*, 115–122.
[62] J. Yang, Q. Shao, B. Huang, M. Sun, X. Huang, *iScience* **2019**, *11*, 492–504.
[63] C. Mahala, M. D. Sharma, M. Basu, *Electrochim. Acta* **2018**, *273*, 462–473.
[64] J. Wang, K. Li, H. Zhong, D. Xu, Z. Wang, Z. Jiang, Z. Wu, X. Zhang, *Angew. Chem. Int. Ed.* **2015**, *54*, 10530–10534; *Angew. Chem.* **2015**, *127*, 10676–10680.
[65] M. W. Louie, A. T. Bell, *J. Am. Chem. Soc.* **2013**, *135*, 12329–12337.
[66] G. Kresse, J. Hafner, *Phys. Rev. B* **1993**, *47*, 558–561.
[67] G. Kresse, J. Hafner, *Phys. Rev. B* **1994**, *49*, 14251–14269.
[68] G. Kresse, J. Furthmüller, *Comput. Mater. Sci.* **1996**, *6*, 15–50.
[69] G. Kresse, J. Furthmüller, *Phys. Rev. B* **1996**, *54*, 11169–11186.
[70] G. Kresse, D. Joubert, *Phys. Rev. B* **1999**, *59*, 1758–1775.
[71] P. E. Blöchl, *Phys. Rev. B* **1994**, *50*, 17953–17979.
[72] C. C. L. McCrory, S. Jung, J. C. Peters, T. F. Jaramillo, *J. Am. Chem. Soc.* **2013**, *135*, 16977–16987.
[73] J. P. Perdew, K. Burke, M. Ernzerhof, *Phys. Rev. Lett.* **1996**, *77*, 3865–3868.
[74] S. Grimme, J. Antony, S. Ehrlich, H. Krieg, *J. Chem. Phys.* **2010**, *132*, 154104.
[75] S. Grimme, S. Ehrlich, L. Goerigk, *J. Comput. Chem.* **2011**, *32*, 1456–1465.
[76] E. R. Johnson, A. D. Becke, *J. Chem. Phys.* **2005**, *123*, 024101.
[77] E. R. Johnson, A. D. Becke, *J. Chem. Phys.* **2006**, *124*, 174104.
[78] J. Zio'łkowski, L. Dziembaj, *J. Solid State Chem.* **1985**, *57*, 291–299.
[79] T. Epicier, J. Dubois, C. Esnouf, G. Fantozzi, P. Convert, *Acta Metall.* **1988**, *36*, 1903–1921.

Manuscript received: June 18, 2021
Revised manuscript received: August 11, 2021
Version of record online: September 8, 2021

ChemSusChem

Supporting Information

Mesoporous WC_x Films with NiO-Protected Surface: Highly Active Electrocatalysts for the Alkaline Oxygen Evolution Reaction

Marvin Frisch[+], Meng-Yang Ye[+], Muhammad Hamid Raza, Aleks Arinchtein, Denis Bernsmeier, Anna Gomer, Thomas Bredow, Nicola Pinna, and Ralph Kraehnert*

Table of Contents

Results and Discussion

Section 1: Spectroscopic ellipsometry (SE) of NiO-ALD

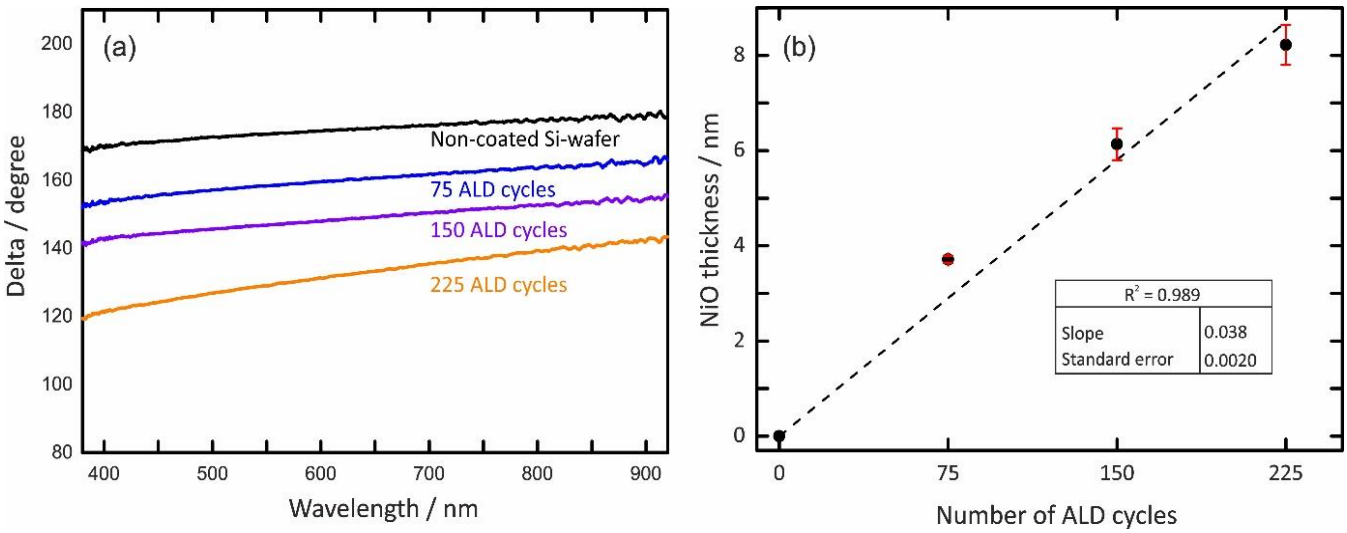

Figure S1. (a) Spectroscopic ellipsometry (SE) data (phase difference, delta Δ(λ)) for different numbers of NiO-ALD cycles (0, 75, 150 and 225) on Si wafers as substrates with a thin, native oxide SiO_2 layer. The plot in (b) reveals a linear correlation of film thickness (nm) and ALD cycle number. The linear fits of the thickness *via* SE provides clear evidence for a linear growth with a growth per cycle of 0.38 Å $cycle^{-1}$.

For the best-performing catalyst film, ALD-NiO/mp.WC_x, an optimum ALD cycle number of 150 in terms of OER activity and stability has been found out in this study. Results from SE on Si wafers reveal an average NiO layer thickness of ~6 nm for NiO layers grown on flat Si wafers as substrates after 150 ALD cycles. In this context, it has to be noted that this value represents only a rough estimate for the thickness of the deposited NiO layers on the pore wall surfaces of the investigated mesoporous carbide and oxide films, since nucleation and growth are affected by the nature of the substrate. For example, the nucleation period is affected by both the morphology and the presence of functional groups at the substrate's surface. This, in turn, has an impact on the thickness of the deposited NiO layer after a certain number of ALD cycles.

Section 2: XPS analysis

In order to follow the changes in chemical states of the surface atoms during the synthesis of ALD-NiO/mp.WC_x, W 4f, Ni 2p, O 1s and C 1s XPS spectra of each key step were collected and illustrated in the following (**Figure S2**). The elemental composition on the surface of each material was quantified and listed in **Table S1**.

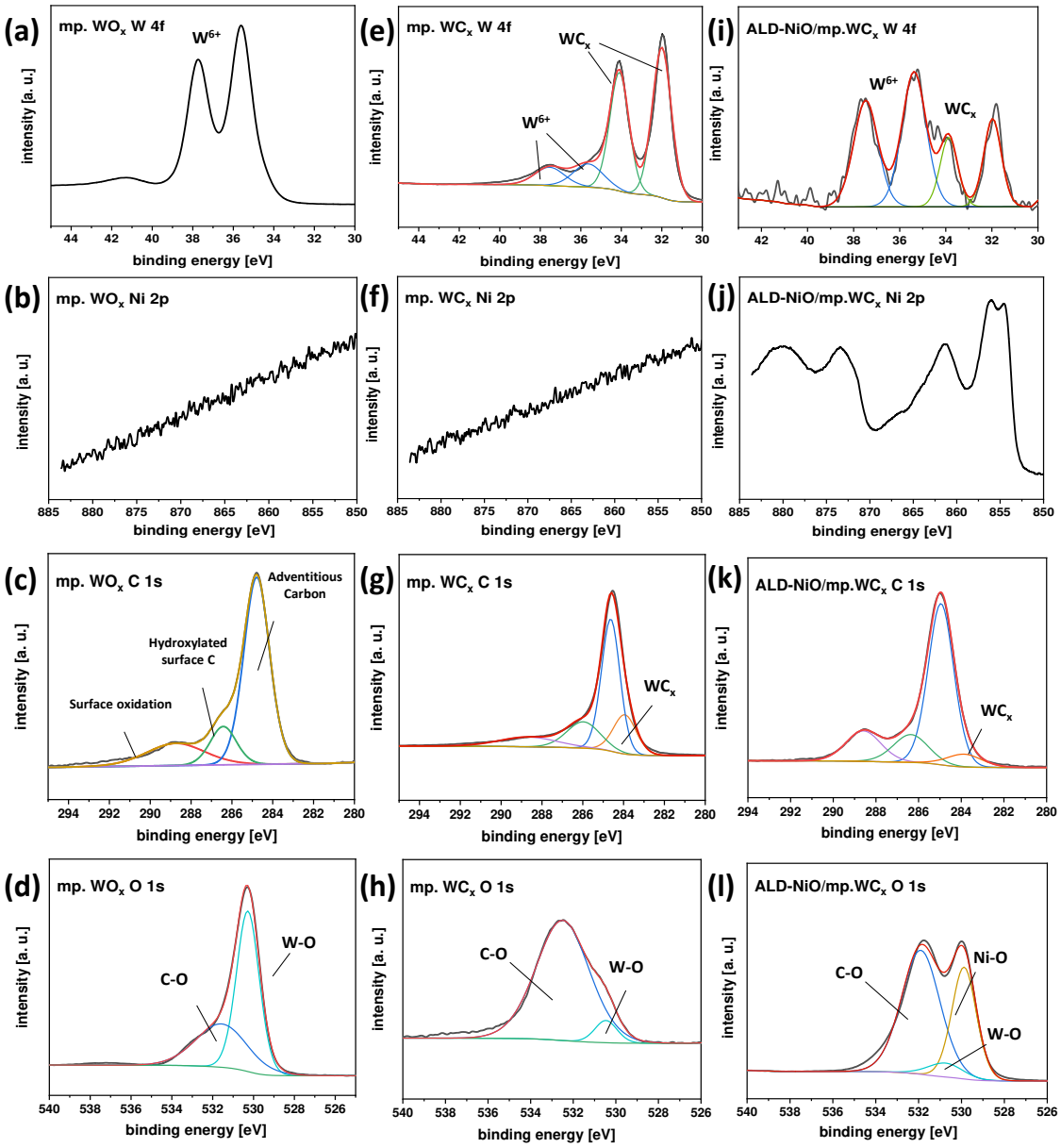

Figure S2. (a) W 4f, (b) Ni 2p, (c) C 1s, (d) O 1s XPS spectra of mp. WO_x. (e) W 4f, (f) Ni 2p, (g) C 1s, (h) O 1s XPS spectra of mp. WC_x. (i) W 4f, (j) Ni 2p, (k) C 1s, (l) O 1s XPS spectra of ALD-NiO/mp.WC_x.

Note that the three peaks in the C 1s spectrum can be assigned to adventitious carbon, hydroxylated surface carbon and oxidized surface carbon, which are often observed in porous samples exposed to air. Moreover, the broad peak in the O 1s spectrum located at ~ 532 eV can also be assigned to presence of oxidized surface carbon species.[1,2] The W 4f spectrum of mp. WO_x (see **Figure S2a-d**) shows a clean doublet peak corresponding to W^{6+}, a corresponding W-O peak can be found in the O 1s spectrum.[1,3]
The conversion from mp. WO_x to mp. WC_x can be confirmed from the analysis of the XPS spectrum of mp. WC_x (**Figure S2e-h**), in which a doublet peak stemming from WC_x can be observed in **Figure S2e** and the corresponding W-C bond is visible in the C 1s spectrum.[4] Importantly, a slight surface oxidation of mp. WC_x becomes evident from both W 4f and O 1s spectra, which is inevitable in the case of transition metal carbides, and usually helps to stabilize the materials from bulk oxidation.[4,5] Remarkably, the coating of NiO *via* ALD significantly alters the surface composition of the materials (see **Figure S2i-l**). A high intensity signal of typical NiO can be observed in the Ni 2p spectrum (17.65 wt% Ni), followed by a pronounced decrease in W 4f intensity (from 4.43 at% in mp. WC_x to 0.13 at% in ALD-NiO/mp.WC_x). The corresponding Ni-O can be spotted in the O 1s spectrum. Besides, the doublet peak as well as the observed multiplet splitting in the Ni $2p_{3/2}$ spectrum reflect the presence of mainly Ni^{2+} species. These features are in good consistency with previous works[6–8]. At the same time, an increase in surface oxidation degree becomes evident, which can be explained by the exposure of the mp. WC_x film to O_3 during the ALD process.

Table S1 Elemental composition at the surface of the films analyzed *via* XPS.

film	W content (at%)	Ni content (at%)	C content (at%)	O content (at%)
mp. WO_x	13.39	-	39.37	47.24
mp. WC_x	4.43		87.34	8.23
ALD-NiO/mp.WC_x	0.13	17.65	36.57	45.65

Section 3: EDX spectrum and cross-sectional SEM of NiO-ALD/mp.WC_x

The original EDX spectrum corresponding to the TEM and EDX mapping in **Figure 2** of the manuscript of this work is provided in the following to prove the material's purity. Only signals for the elements W, Ni, O, C are found in the area presented in **Figure 2a**. Please note that the Cu signals in the spectrum originate from the TEM grid, on which the material was deposited for imaging.

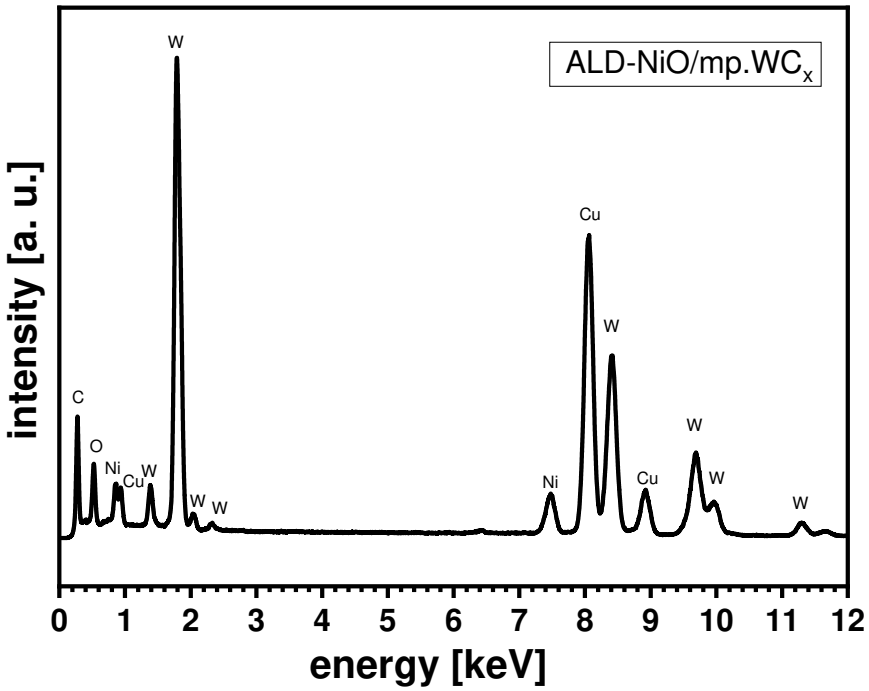

Figure S3-I. EDX spectrum of ALD-NiO/mp.WC_x corresponding to the TEM and EDX elemental mapping presented in **Figure 2** in the main part of this work. The $K_{\alpha1}$, $K_{\alpha2}$ (at 7.47 and 7.46 keV) and $L_{\alpha1}$, $L_{\alpha2}$ (at 8.39 and 8.33 keV) signals were collected for the EDX measurement.

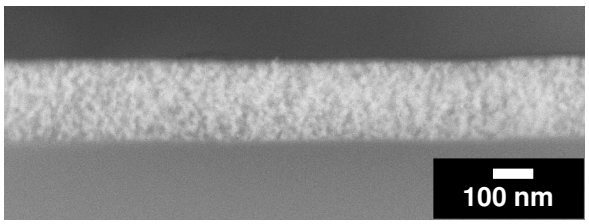

Figure S3-II. Representative cross-sectional SEM image (COMPO mode, 50 kx magnification) of ALD-NiO/mp.WC_x after 150 cycles of NiO-ALD acquired for a film deposited on a flat Si substrate after careful cracking of the coated wafer.

Section 4: Results from RDE-OER testings in 0.1 M KOH at 25 °C and influence of Fe impurities in the electrolyte

To gain further insights into the OER performance of the investigated catalyst systems described in this work, the potential-dependent current density plots of the 3rd, 50th and 100th CVs are given in this section (see **Figure S4-I**). The corresponding values for the overpotential of ALD-NiO/mp.WC_x throughout the different CV cycles are listed in **Table S2** in comparison to the values of ALD-NiO/mp.WO_x (all other catalyst systems were not active enough to reach the current density of 10 mA cm^{-2} within the measured potential range). It can be observed that after several CVs in the alkaline electrolyte, ALD-NiO/mp.WC_x not only shows excellent OER activity, but also presents outstanding stability over time in increasing cycle numbers of the CV measurements. On the contrary, ALD-NiO/mp.WO_x undergoes ongoing deactivation over time, which might be rationalized by slow dissolution effects and concomitant loss of active species.
Please note that main purpose of this work is to understand the role of the mp.WC_x carrier in the catalytic system. Thus, the 0.1 M KOH electrolyte used in all measurements in this work was not extensively purified to remove trace amounts of Fe ions, which were shown to significantly promote the OER activity of Ni-based catalysts.[9–12] Nonetheless, the rudimentary conclusion of our work would not be influenced by the presence of impurities such as Fe.

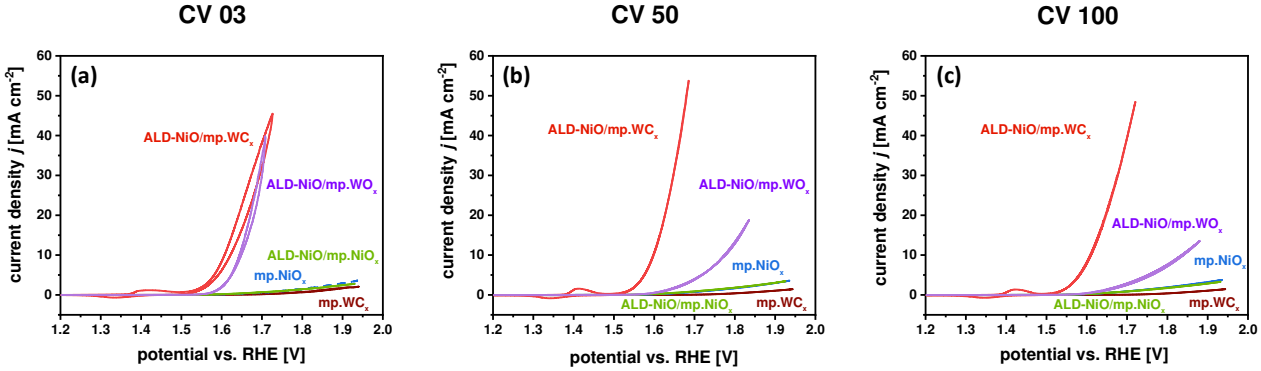

Figure S4-I. (a) CV 3, (b) CV 50, (c) CV 100 of ALD-NiO/mp.WC_x, bare mp. WC_x, pristine mp. NiO_x, ALD-NiO/mp.NiO_x, and ALD-NiO/mp.WO_x using a RDE setup and N_2-purged 0.1 M KOH at 25 °C. All potentials are *iR*-corrected and stated vs. RHE.

Table S2. Overpotential (j = 10 mA cm^{-2}) of ALD-NiO/mp.WC_x, and ALD-NiO/mp.WO_x in different CV cycles.

	overpotential (CV 2) [mV]	overpotential (CV 30) [mV]	overpotential (CV 50) [mV]	overpotential (CV 100) [mV]
ALD-NiO/mp.WC_x	380	360	368	372
ALD-NiO/mp.WO_x	416	427	550	600

In order to investigate the impact of trace amounts of Fe impurities in the KOH electrolyte on the catalytic activity of NiO-based catalysts, further RDE-OER measurements were performed for the most active system, *i. e.* ALD-NiO/mp.WC_x, after purification of the KOH according to a well-established procedure[13,14]. The results are shown in **Figure S4-II**. In brief, the comparison of the activity in purified (Fe-free) vs. as-received KOH (trace amounts of Fe) leads to the conclusion that an enhancement in activity by the incorporation of Fe species at the catalyst's surface occurs. In the case of the purified Fe-free electrolyte, a mass activity of 1545 A/g_{Ni} at a potential of 1.60 V *vs. RHE* can be calculated, which is lower than the one obtained in the case of as-received KOH (1989 A/g_{Ni}). Still, the calculated mass activity in Fe-free KOH electrolyte is significantly higher than that of all herein investigated reference systems and, even more important, than that of literature-reported catalysts in non-purified KOH electrolyte (*cf.* **Table 1** in the main part).
In good consistency with results from our previous work[12], a slight shift in both the position and shape of the $Ni^{2/3+}$ redox peak can be observed. For Fe-free KOH, a shift of the redox peaks to lower potentials is indicated in **Figure S4-II**. Similar to the conclusion drawn in our previous study[12], ALD-NiO/mp.WC_x shows a much higher intrinsic activity than our reference catalysts and literature-reported systems.

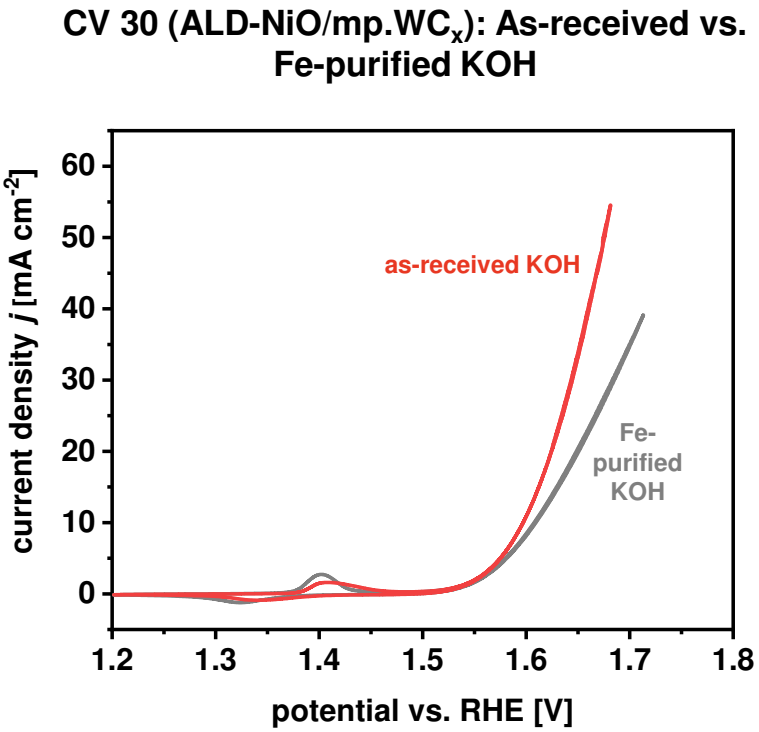

Figure S4-II. Impact of Fe impurities in the KOH electrolyte on the catalytic OER activity of the most active developed catalyst system ALD-NiO/mp.WC_x. Results from CV measurements (CV 30) in an RDE setup and N_2-purged 0.1 M KOH at 25 °C. All potentials are *iR*-corrected and stated vs. RHE.

Section 5: Evaluation of Tafel slopes

As an important indicator to study the reaction kinetics, the Tafel slopes of the presented electrocatalysts were derived from the CV curves shown in **Figure 3a**. From the obtained linear graphs in a semi-logarithmic plot, it can be observed that ALD-NiO/mp.WC_x shows a significantly smaller Tafel slope, indicating a faster reaction kinetics compared to pristine NiO_x or NiO-coated on any other mesoporous carrier. This enhancement might be a consequence of the excellent electrical conductivity of the WC_x carrier. Similar beneficial impacts of a highly conductive support were previously reported by Görlin *et al.*[11], for instance, who found similar Tafel slopes of approx. 60 mV dec^{-1} for Ni-based electrocatalysts in 1.0 M KOH. The introduction of a carbonaceous support led to a decrease in the observed Tafel slopes for both Ni-based and NiFe-based catalysts. Smaller Tafel slopes of less than 40 mV dec^{-1} were reported for the carbon-supported NiFe-based catalysts and assumed to result from an increased number of electrochemically accessible metal centers. Thus, kinetic OER rates are enhanced.

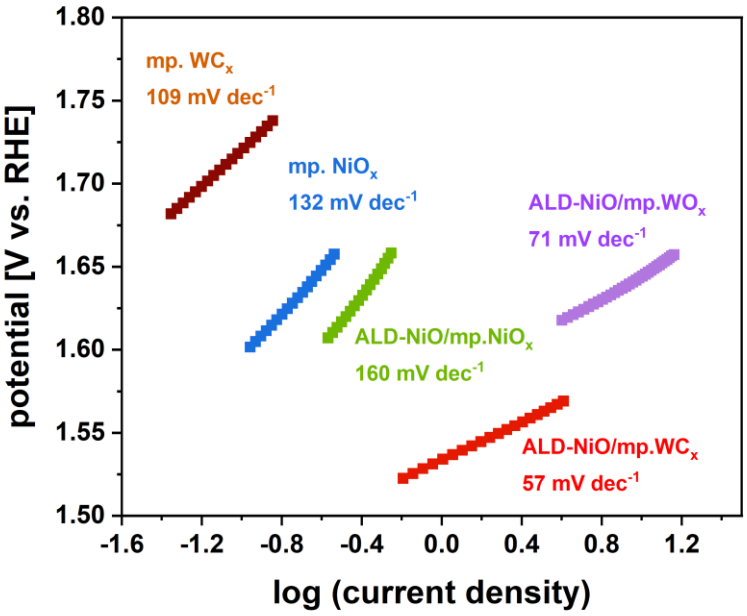

Figure S5. Tafel slopes of ALD-NiO/mp.WC_x, bare mp.WC_x carrier, pristine mp. NiO_x, ALD-NiO/mp.NiO_x, and ALD-NiO/mp.WO_x derived from CVs in **Figure 3a**.

Section 6: TEM & SAED analysis prior to and after OER stability testings

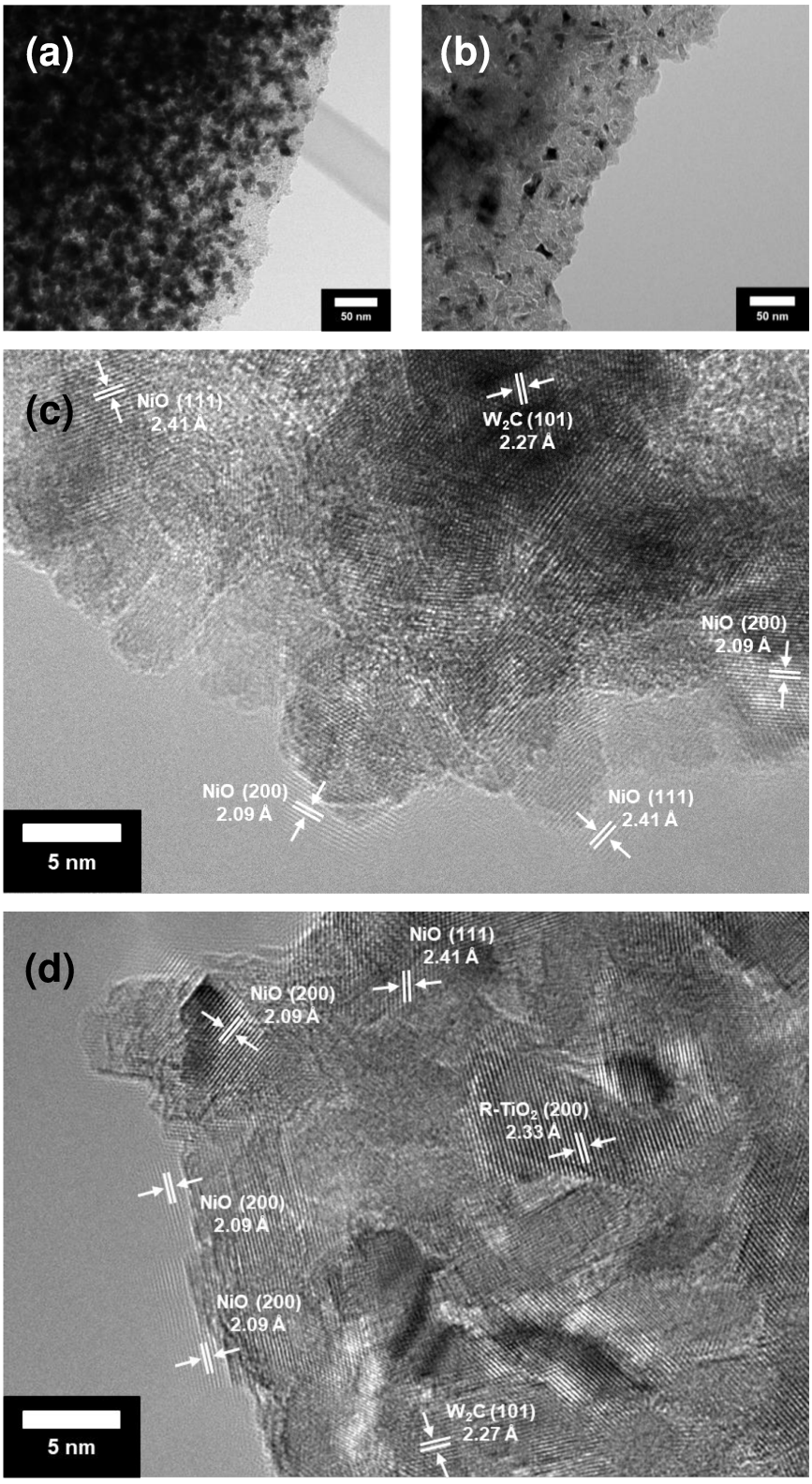

Figure S6-I. (a,c) Representative (HR-)TEM images of the fresh ALD-NiO/mp.WC_x catalyst in different magnifications and (b,d) of the spent catalyst after OER.

In order to investigate the morphological and structural stability of the ALD-NiO/mp.WC_x electrocatalyst, the film was scraped off from the Ti electrode using a diamond scraper after chronopotentiometric stability testing in alkaline electrolyte. Owing to the binder-free system, HR-TEM images can be easily obtained without any interference from organic Nafion binder species. In this section, several representative TEM images of the fresh and the spent catalyst are shown, indicating a high stability of the material during OER in 0.1 M KOH (see **Figure S6-I,II** for TEM and SAED prior to and after OER testing).

The lattice fringes highlighted in **Figure S6-Ic,d** correspond to the {101} facet of W_2C nanocrystals as well as the {200} and {111} facets of NiO. In the SAED pattern of the spent ALD-NiO/mp.WC_x catalyst (**Figure S6-II**), both NiO and W_2C phases can be assigned, further highlighting a well-preserved crystallinity. Note that due to the very high mechanical hardness of the carbide, strong forces must be applied to scrape the ALD-NiO/mp.WC_x electrocatalyst off the Ti electrode. Accordingly, the SAED pattern in **Figure S6-II** reveals the presence of rutile TiO_2, originating from the surface of the substrate peeled off together with the mesoporous film. Corresponding rutile-TiO_2 latticed fringes were found in the HR-TEM images (see **Figure S6-Id**).

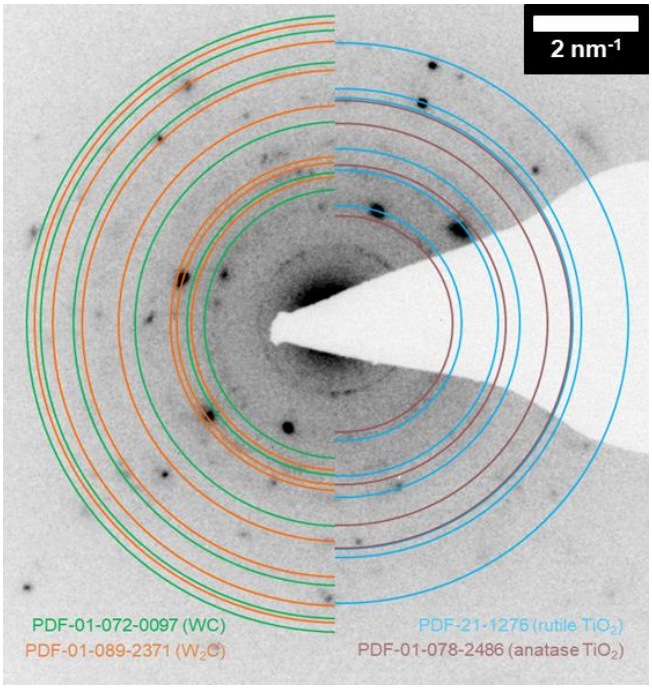

Figure S6-II. SAED pattern of the spent ALD-NiO/mp.WC_x catalyst scraped-off from a partially oxidized Ti substrate after OER catalysis in 0.1 M KOH as the electrolyte.

Section 7: SEM, EDX and XPS analysis of the spent catalysts (post-OER)

top-view SEM image of ALD-NiO/mp.WC$_x$ after RDE-OER in 0.1 M KOH

SEM-EDX spectrum of ALD-NiO/mp.WC$_x$ after RDE-OER in 0.1 M KOH

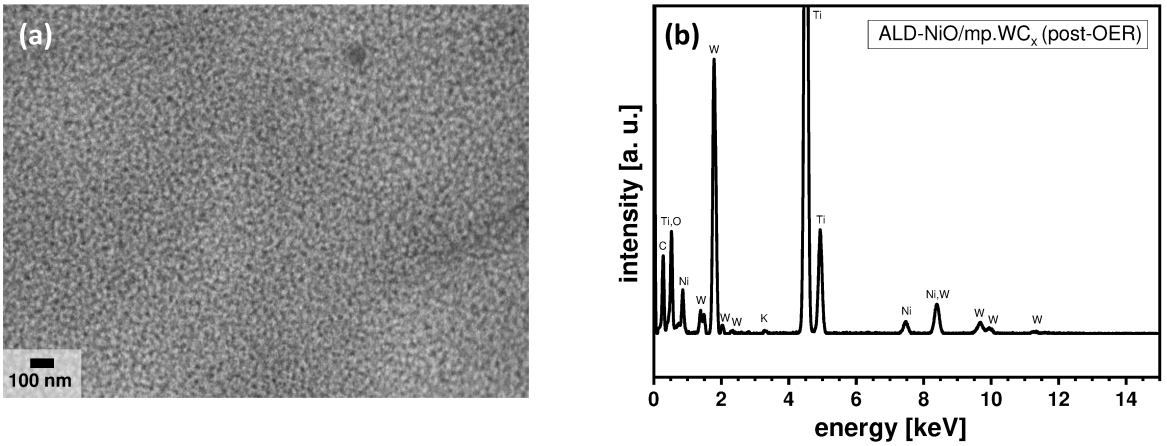

Figure S7-I. (a) Representative top-view SEM image of the spent ALD-NiO/mp.WC$_x$ catalyst after RDE-OER testings (50 kx magnification) and (b) corresponding SEM-EDX spectrum acquired at 20 kV acceleration voltage on a Ti substrate. After RDE testing, the mesoporous structure remains well-preserved. Yet, some pinholes and cracks can be observed as a consequence of gas bubble formation during O_2 generation in OER regime. The formation of cracks and pinholes was observed for all spent catalyst materials, independent of their composition. In the EDX spectrum (b), both Ni and W can be found. This provides further evidence for the high stability of the material during OER in alkaline electrolyte.

XPS analysis of spent ALD-NiO/mp.WC$_x$ after RDE-OER in 0.1 M KOH

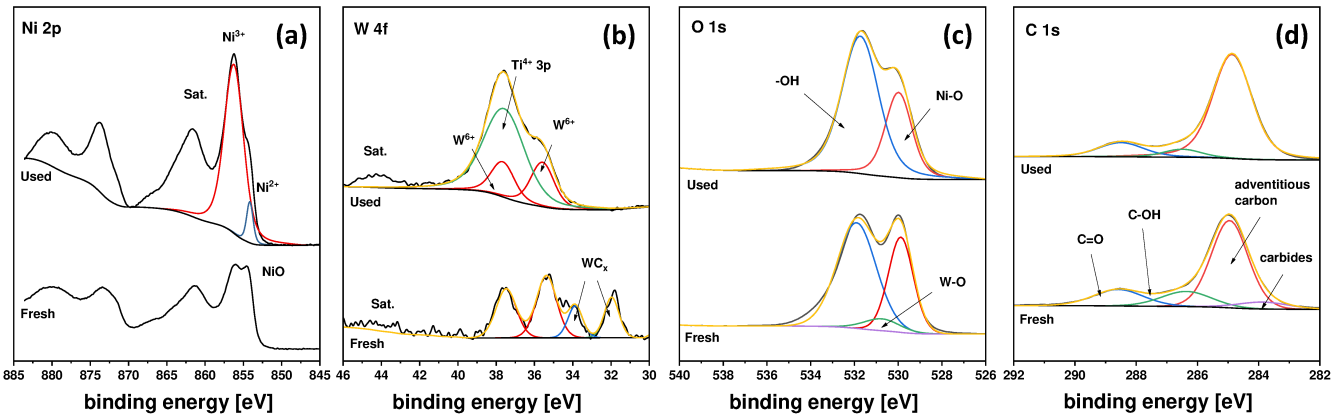

Figure S7-II. (a) Ni 2p, (b) W 4f, (c) O 1s and (d) C 1s XPS spectra of the spent ALD-NiO/mp.WC$_x$ catalyst after RDE-OER testings in 0.1 M KOH. In (a), both Ni^{2+} and Ni^{3+} can be found. Importantly, the fraction of Ni^{3+} is predominant, indicating a pronounced surface oxidation of Ni^{2+} species to Ni^{3+} during OER. The W 4f results (b) indicate a surface oxidation of the WC$_x$ carrier. Moreover, an overlapping Ti^{4+} 3p peak originating from a partial surface oxidation of the Ti substrate can be found. The stability of the ALD-deposited NiO layer is further evidenced by the strong Ni-O peak in the O 1s spectrum in (c). No significant contributions of W-O species can be detected for the spent catalyst film, as the surface is dominated by oxidic Ni^{3+} species. This is in line with XPS results in **Table S1** showing that the surface of ALD-NiO/mp.WC$_x$ is primarily composed of Ni, C and O species after ALD.

XPS depth profile of spent ALD-NiO/mp.WC_x after RDE-OER in 0.1 M KOH

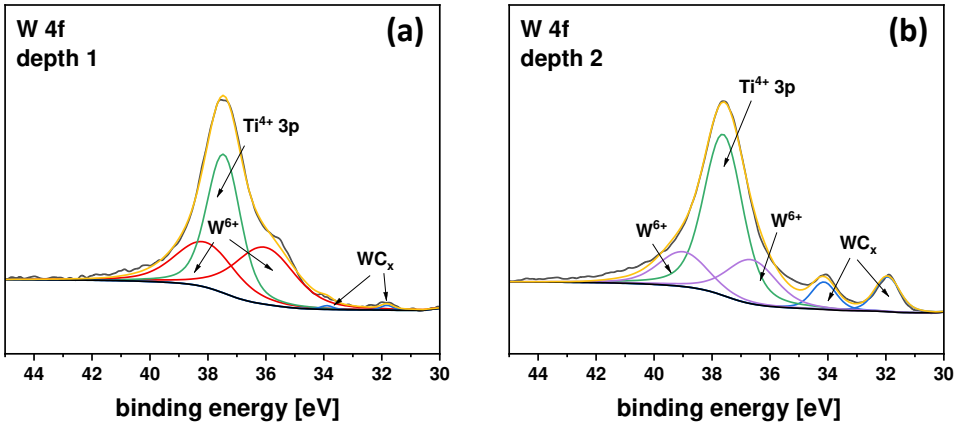

Figure S7-III. XPS depth profile analysis of the spent ALD-NiO/mp.WC_x catalyst after RDE-OER testings in 0.1 M KOH. The W 4f regions are shown in (a) and (b) for increasing depths of analysis. In (a), weak signals corresponding to WC_x can be found, which increase in intensity for an increasing analysis depth in (b). These results indicate a surface oxidation of the WC_x carrier during OER, yet the bulk remaining a highly conductive metal carbide phase. Accordingly, undesired bulk oxidation of the WC_x carrier in ALD-NiO/mp.WC_x during OER can be ruled out.

Section 8: ECSA calculations

The electrochemically accessible surface area (ECSA) was calculated following a well-established procedure reported elsewhere[15]. The current density - potential plots for each investigated catalyst system are given in **Figure S8**, the calculated C_{dl} and ECSA values are listed in **Table S3**. A remarkably higher ECSA value was obtained for ALD-NiO/mp.WC_x, which likely results from the high conductivity of WC_x carrier. Beyond that, the well-defined nanostructure and mesoporosity introduced by the latter show a beneficial impact on both capacitance and ECSA.

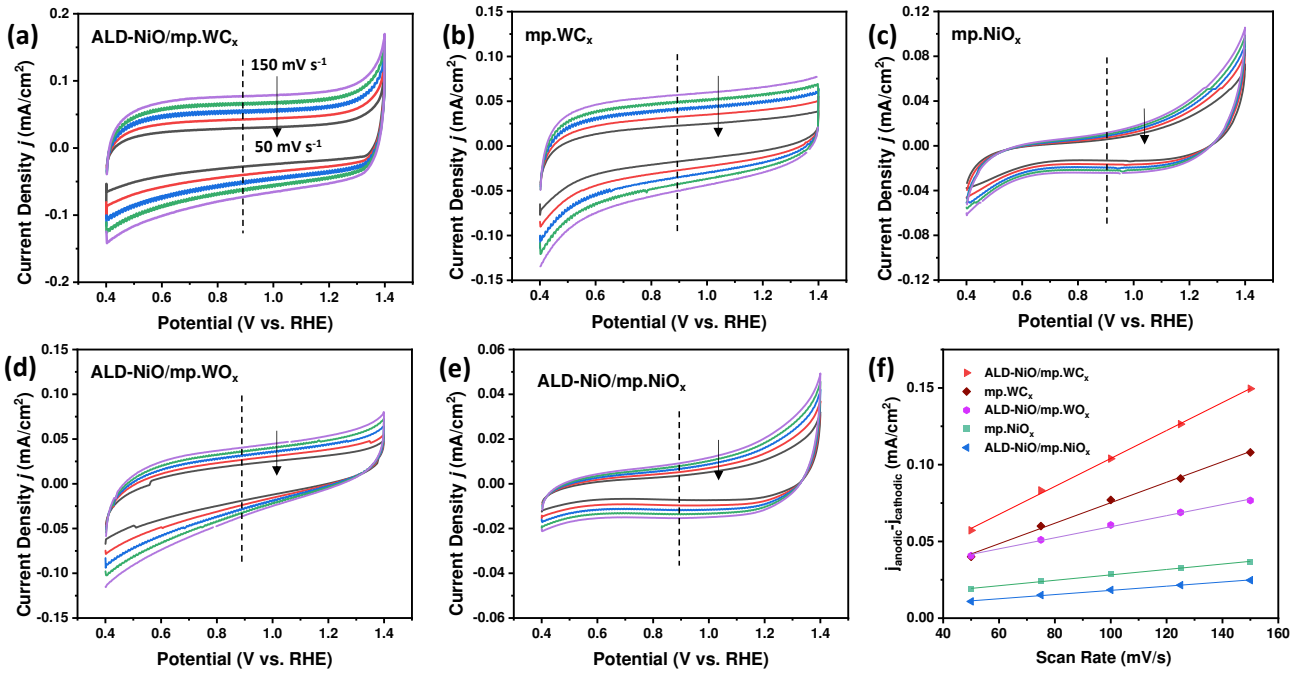

Figure S8. Electrochemical double-layer capacitance evaluations. (a-e) CV curves of the electrocatalysts in 0.1 M KOH between 0.40 and 1.40 V vs. RHE with increasing scan rates of 50, 75, 100, 125 and 150 mV s^{-1}. (f) Linear fits to the extracted summed up values for the anodic and cathodic currents extracted from CVs given in (a-e) at 0.9 V (vs. RHE) plotted vs. scan rate.

Table S3. Double-layer capacitance and ECSA values of the electrocatalysts. In brief, the ECSA was calculated based on non-Faradaic capacitance currents *via* double-layer charging in a lower potential range from 0.4 – 1.4 V vs. RHE. Several CVs at different scan rates between 50 to 150 mV s^{-1} were measured and the obtained values for $\Delta j = j_{anode} - j_{cathode}$ were plotted *vs.* scan rate. From the slope of the linear fit, C_{dl} can be estimated. After dividing C_{dl} by the specific capacitance, an ECSA-estimate can be calculated. A specific capacitance of 0.040 mF cm^{-2} was assumed based on previous literature reports.[15]

sample	C_{dl} [mF]	ECSA [cm^2]
mp. WC_x	0.334	-
mp. NiO_x	0.088	2.2
ALD-NiO/mp.NiO_x	0.068	1.7
ALD-NiO/mp.WO_x	0.180	4.5
ALD-NiO/mp.WC_x	0.456	11.4

Section 9: Results from DFT calculations

Bulk optimizations:

The optimized lattice parameters of NiO and W_2C were calculated as a = 4.1513 Å as well as a = 5.2196 Å and c = 4.7134 Å, respectively. These values are in good agreement with experimental values reported previously in literature with relative errors below 0.7 %.[16–18]
The optimized lattice parameters of W_2C were used to build the (100) surface and a square-planar monolayer of NiO was added on both sides of the slab model in order to avoid artificial dipole moments.

Surface models:

The reaction energy of the *OH intermediate species was calculated by the following equation with H_2 and H_2O as reference, according to Garcia-Mota *et al.*[19]:

$$\Delta E_{OH^*} = E_{OH^*} - E_{slab} - (E_{H_2O} - 0.5\, E_{H_2}) \quad (1)$$

In order to increase symmetry and avoid artificial dipole moments, two adsorbates are added to the upper and lower side of the slab models. Here, *OH represents the adsorbed species on the surface, E_{slab} corresponds to the surface energy of the simplified NiO-W_2C model and the corresponding energies of the gas molecules, normalized to one adsorbed species. The bare NiO surface changed only slightly during the optimization process. The Ni atom, on which the adsorption takes place, is shifted slightly upwards (see upper right inset in **Figure S9**).

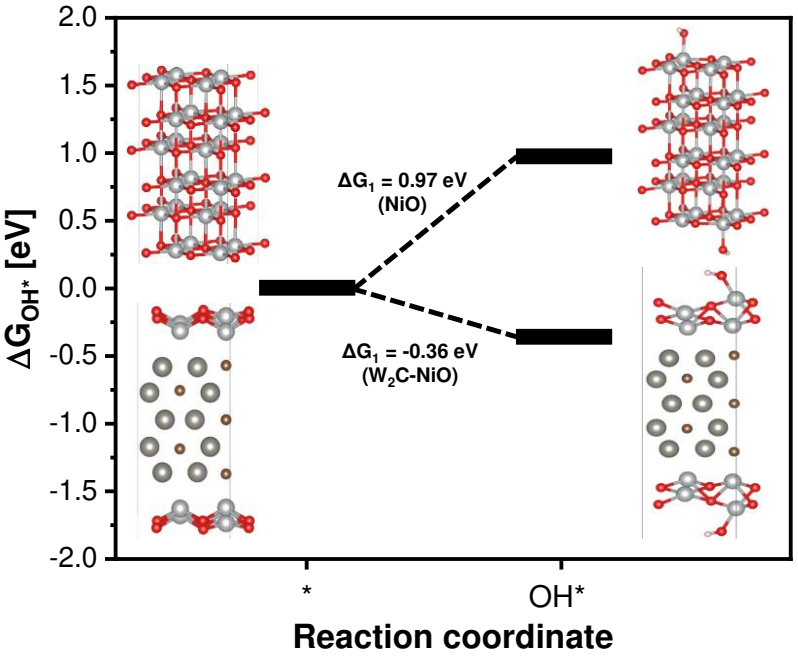

Figure S9. Free energy diagram showing the relative energies for the formation of OH* species adsorbed on a NiO-surface-modified W_2C (100) surface (denoted as W_2C-NiO) and on a NiO (100) surface as a reference (denoted as NiO). The first step of the OER is examined, *i.e.* $\Delta G_{OH^*} = \Delta G_1$. For W_2C-NiO, a more negative ΔG_{OH^*} compared to that of bare NiO reveals a preferred formation of NiOOH-type species at the surface. Surface hydroxylation is promoted by the carbide carrier, which is in accordance with a strongly pronounced pre-oxidation wave intensity for ALD-NiO/mp.WC_x (*cf.* **Figure 3** in the manuscript). O atoms are illustrated in red, Ni atoms in light grey, W atoms in dark grey and C atoms in brown. Fully optimized structures are given in the diagram. Energies are given relative to the bare W_2C-NiO and NiO surfaces at zero potential (U = 0 V).

In contrast, the NiO monolayer deposited on W_2C is strongly reconstructed. The adsorption leads to an even more pronounced distortion. In particular, the Ni atom, on which the *OH species adsorbs, is affected (see lower right inset in **Figure S9**). For the *OH adsorbate, the spin polarization is non-existent.

According to Diaz-Morales *et al.*[20], the free energies were approximated as follows:

$$\Delta G = E_{DFT} + ZPE - TS \quad (2)$$

E_{DFT} denotes the total energy, ZPE represents the zero-point electronic energy calculated *via* DFT and the term TS describes contributions from entropy. TS was assumed to be relevant explicitly for gas phase species. ZPE(H_2), ZPE(H_2O) and ZPE(*OH) were used as given in reference [30] as 0.27, 0.56 and 0.34 eV, respectively. TS corrections for H_2 and $H_2O_{(l)}$ were approximated as 0.40 and 0.67 eV, respectively.[20,21]

References

[1] Y.-J. Ko, J.-M. Cho, I. Kim, D. S. Jeong, K.-S. Lee, J.-K. Park, Y.-J. Baik, H.-J. Choi, W.-S. Lee, *Appl. Catal. B Environ.* **2017**, *203*, 684–691.

[2] J. V. Rojas, M. Toro-Gonzalez, M. C. Molina-Higgins, C. E. Castano, *Mater. Sci. Eng. B* **2016**, *205*, 28–35.

[3] F. Y. Xie, L. Gong, X. Liu, Y. T. Tao, W. H. Zhang, S. H. Chen, H. Meng, J. Chen, *J. Electron Spectros. Relat. Phenomena* **2012**, *185*, 112–118.

[4] D. V. Esposito, J. G. Chen, *Energy Environ. Sci.* **2011**, *4*, 3900.

[5] T. Y. Ma, J. L. Cao, M. Jaroniec, S. Z. Qiao, *Angew. Chemie Int. Ed.* **2016**, *55*, 1138–1142.

[6] P. Dubey, N. Kaurav, R. S. Devan, G. S. Okram, Y. K. Kuo, *RSC Adv.* **2018**, *8*, 5882–5890.

[7] W. Liu, C. Lu, X. Wang, K. Liang, B. K. Tay, *J. Mater. Chem. A* **2015**, *3*, 624–633.

[8] L. Soriano, I. Preda, A. Gutiérrez, S. Palacín, M. Abbate, A. Vollmer, *Phys. Rev. B* **2007**, *75*, 233417.

[9] M. Bernicke, B. Eckhardt, A. Lippitz, E. Ortel, D. Bernsmeier, R. Schmack, R. Kraehnert, *ChemistrySelect* **2016**, *1*, 482–489.

[10] A. S. Aricò, P. Bruce, B. Scrosati, J.-M. Tarascon, W. van Schalkwijk, *Nat. Mater.* **2005**, *4*, 366–377.

[11] M. Görlin, J. Ferreira de Araújo, H. Schmies, D. Bernsmeier, S. Dresp, M. Gliech, Z. Jusys, P. Chernev, R. Kraehnert, H. Dau, P. Strasser, *J. Am. Chem. Soc.* **2017**, *139*, 2070–2082.

[12] Y. Fan, Y. Wu, G. Clavel, M. H. Raza, P. Amsalem, N. Koch, N. Pinna, *ACS Appl. Energy Mater.* **2018**, *1*, 4554–4563.

[13] M. Görlin, J. Halldin Stenlid, S. Koroidov, H.-Y. Wang, M. Börner, M. Shipilin, A. Kalinko, V. Murzin, O. V. Safonova, M. Nachtegaal, A. Uheida, J. Dutta, M. Bauer, A. Nilsson, O. Diaz-Morales, *Nat. Commun.* **2020**, *11*, 6181.

[14] L. Trotochaud, S. L. Young, J. K. Ranney, S. W. Boettcher, *J. Am. Chem. Soc.* **2014**, *136*, 6744–6753.

[15] C. C. L. McCrory, S. Jung, J. C. Peters, T. F. Jaramillo, *J. Am. Chem. Soc.* **2013**, *135*, 16977–16987.

[16] J. Zio´łkowski, L. Dziembaj, *J. Solid State Chem.* **1985**, *57*, 291–299.

[17] T. Epicier, J. Dubois, C. Esnouf, G. Fantozzi, P. Convert, *Acta Metall.* **1988**, *36*, 1903–1921.

[18] B. Lönnberg, *J. Less Common Met.* **1986**, *120*, 135–146.

[19] M. García-Mota, A. Vojvodic, H. Metiu, I. C. Man, H.-Y. Su, J. Rossmeisl, J. K. Nørskov, *ChemCatChem* **2011**, *3*, 1607–1611.

[20] O. Diaz-Morales, I. Ledezma-Yanez, M. T. M. Koper, F. Calle-Vallejo, *ACS Catal.* **2015**, *5*, 5380–5387.

[21] Y. Cheng, Y. Zhang, Y. Li, J. Dai, Y. Song, *J. Mater. Chem. A* **2019**, *7*, 9324–9334.

Author Contributions

M. Frisch† and M.-Y. Ye† contributed equally to this work. MF contributed to all experimental aspects of data analysis, evaluation and interpretation. MF & MYY both contributed to the writing and editing of manuscript. MYY performed XPS measurements and interpretation of the acquired data. MHR conducted NiO-ALD experiments and wrote the relevant experimental part. Besides, MHR contributed to the analysis of HAADF-STEM EDX maps. AA aided in the design of synthesis protocols of the templated mesoporous films. Besides, AA contributed to TEM and SAED analyses. DB contributed to the electrochemical testing of the films and performed BET surface area measurements. AG, TB and MF contributed to the theoretical DFT calculations and data interpretation. NP, RK & MYY conceived the study, contributed to the writing and editing of the manuscript.

B Author Contributions

In the following, the contributions of each co-author to each publication are briefly stated.

[MF-1] M. Frisch*, J. Laun*, J. Marquardt, A. Arinchtein, K. Bauerfeind, D. Bernsmeier, M. Bernicke, T. Bredow, R. Kraehnert, *Bridging Experiment and Theory: Enhancing the Electrical Conductivities of Soft-Templated Niobium-Doped Mesoporous Titania Films*, *Physical Chemistry Chemical Physics* **2021**, *23*, 3219-3224. https://doi.org/10.1039/d0cp06544g

M. F. & J. L. contributed equally. M. F. contributed to all aspects of synthesis and characterization, as well as to the analysis and interpretation of the experimental data. J. L. contributed to all theoretical aspects (theoretical calculations, simulations and data interpretation). Both M. F. & J. L. wrote and revised the manuscript. J. M. conducted Raman spectroscopy and analyzed the spectra. A. A., D. B. and M. B. helped in the development of synthesis protocols of the porous films. Beyond that, A. A. contributed to GI-XRD and TEM analysis. K. B. contributed to the computation of phase stability and Raman spectra. T. B. & R. K. conceived the study and contributed to the editing of the manuscript. All authors have discussed the findings of the study.

[MF-2] M. Frisch*, M. H. Raza*, M.-Y. Ye, R. Sachse, B. Paul, R. Gunder, N. Pinna, R. Kraehnert, *ALD-Coated Mesoporous Iridium-Titanium Mixed Oxides: Maximizing Iridium Utilization for an Outstanding OER Performance*, *Advanced Materials Interfaces* ***2022***, *9*, 2102035. https://doi.org/10.1002/admi.202102035

M. F. & M. H. R. contributed equally to the work. M. F. contributed to the synthesis and characterization of the porous electrodes as well as to the analysis and interpretation of the experimental data (electron microscopy, X-ray analysis, ICP measurements, electrocatalytic tests). M. H. R. performed Ir- and IrO_x-ALD and evaluated data from SE analysis for the determination of ALD layer thickness on bare Si substrates as reference. With the assistance of R. K., N. P. and M. H. R., M. F. wrote and revised the manuscript. M.-Y. Y. conducted XPS analysis and analyzed the obtained spectra together with M. F.

R. S. contributed to the validation of the geometric Ir loadings in the catalytic coatings *via* quantitative EDX analysis in an SEM microscope. B. P. contributed to the analysis of the electrical properties *via* impedance spectroscopy and evaluated the data together with M. F. R. G. contributed to phase analysis *via* GI-XRD. N. P. & R. K. conceived the study and contributed to the editing of the manuscript. All authors agreed with the content of the final version of the paper.

[MF-3] M. Frisch*, M.-Y. Ye*, M. H. Raza, A. Arinchtein, D. Bernsmeier, A. Gomer, T. Bredow, N. Pinna, R. Kraehnert, *Mesoporous WC_x Films with NiO-Protected Surface: Highly Active Electrocatalysts for the Alkaline Oxygen Evolution Reaction*, *ChemSusChem* **2021**, *14*, 4708-4717. https://doi.org/10.1002/cssc.202101243

M. F. & M.-Y. Y. contributed equally to the work. M. F. synthesized the materials and reference catalysts, contributed to all aspects of data analysis, evaluation and interpretation. M. F. & M.-Y. Y. wrote and edited the manuscript together. In addition, M.-Y. Y. contributed to XPS analysis and interpretation of the spectra. M. H. R. performed ALD, contributed to the analysis of HAADF-STEM-EDX mappings, and wrote the relevant experimental sections. A. A. helped in the development of synthesis protocols, and performed TEM/SAED analysis. D. B. conducted BET surface area measurements and performed welding of the working electrodes for the subsequent CP stability tests. A. G., T. B. and M. F. contributed to theoretical calculations *via* DFT and interpreted the data. N. P., R. K. & M.-Y. Y. conceived the study and revised the manuscript together with M. F. All authors have discussed and agreed on the final version for publication.

C Further Works NOT Included in this Thesis

[MF-4] K. C. L. Bauerfeind*, J. Laun*, **M. Frisch**, R. Kraehnert, T. Bredow, *Metal Substitution in Rutile TiO_2: Segregation Energy and Conductivity*, *Journal of Electronic Materials* **2021**. https://doi.org/10.1007/s11664-021-09318-4

[MF-5] **M. Frisch**, R. Kraehnert, *Methode zur Herstellung Mesoporöser Übergangsmetallkarbidschichten mit Definierter Nanostrukturierung sowie deren Anwendung in der Elektrokatalyse,* EPO submission date 18.05.2021, **2021**, EP21174253.

[MF-6] **M. Frisch**, M. H. Raza, N. Pinna, R. Kraehnert, *Methode zur Herstellung Aktiver und Stabiler Titanbasierter Mischoxidkatalysatoren mit Optimierter Edelmetallverteilung durch Oberflächenkonforme Atomlagenabscheidung*, EPO submission date 15.03.2022, **2021/22**, EP22162190.

[MF-7] A. Arinchtein, M.-Y. Ye, M. Geske, **M. Frisch**, R. Kraehnert, *Influence of Phase Composition and Pretreatment on the Conversion of Iron Oxides into Iron Carbides in Syngas Atmospheres, Catalysts* **2021**, *11*, 773. https://doi.org/10.3390/catal11070773

D Experimental Details to the General Discussion

Synthesis of Y^{3+}-doped titania films with templated mesoporosity (section 5.2.1)

For the synthesis of the Y^{3+}-doped titania films with templated porosity discussed in section 5.2.1, 45 mg of a PEO-PB-PEO tri-block copolymer (PEO_{213}-PB_{184}-PEO_{213}) were dissolved in 2.25 mL EtOH *p.a.* under stirring for at least 60 min at 45 °C (air) (**I**). An appropriate amount of $TiCl_4$ was carefully dissolved in a closed vial in 2.25 mL EtOH *p.a.* in an Ar-filled glovebox at rt. (**II**) and after to solution (**I**). A clear solution (**III**) was obtained, to which an appropriate amount of $YCl_3 \cdot 6H_2O$ were added under stirring (air; 45 °C) (**IV**). Dip-coating was performed using (**IV**) after further 10 min of stirring at 45 °C (air) in a controlled atmosphere. Mesoporous templated $YTiO_x$ films were deposited on flat Si, Ti and SiO_2 substrates at 25 °C ambient temperature and 40 % RH, using a pre-heated *Teflon* cuvette (45 °C) at a withdrawal rate of 300 mm/min. After drying of the deposited films for at least 5 min in the controlled atmosphere, films were dried for 60 min at 80 °C in air in a pre-heated drying oven. Calcination in air was immediately performed after the drying step for 30 min at 600 °C in a pre-heated muffle furnace, unless otherwise stated. The total amount of Y and Ti amounted to ~ 0.86 mmol in each synthesis. The molar ratio of Y and Ti was adjusted in order to afford compositions with values of 0 to 50 mol-% Y.

Synthesis of co-doped titania films with templated mesoporosity (section 5.2.2)

In a typical synthesis, 45 mg of a PEO-PB-PEO copolymer (PEO_{213}-PB_{184}-PEO_{213}) were dissolved in 1.00 mL EtOH *p.a.* by stirring for 60 min at 45 °C in air (**I**). 46 mg $NbCl_5$ were dissolved in 1.00 mL EtOH *p.a.* under stirring in an Ar-filled glovebox at 25 °C, affording a clear, colorless solution (**II**) after 10 min of stirring. 46 µL $TiCl_4$ were dissolved in a closed vial in 1.00 mL EtOH *p.a.* and added to solution (**II**) (Ar, 25 °C). A clear, slightly yellow solution (**III**) was obtained.

As a representative example for co-doping, 4.0 mg $ScCl_3$ *anhydr.* were added to solution (**III**) (Ar, 25 °C) under vigorous stirring, affording a clear, slightly yellow solution (**IV**). Afterwards, (**I**) was added to (**IV**) under stirring (air). After 30 min of further stirring at 45 °C (air), a clear, slightly yellow solution (**V**) was obtained.

Dip-coating was performed using precursor solution (**V**) at 25 °C ambient temperature in air, 40 % RH and 300 mm/min withdrawal rate. A pre-heated *Teflon* cuvette (45 °C) was used. For all co-dopants and mentioned ternary oxide compositions, crack-free colored films were obtained on flat Si and SiO_2 substrates, which were subsequently calcined for 30 min at 600 °C in air using a pre-heated muffle furnace.

For the introduction of Fe co-dopants, $FeCl_3$ was used as precursor salt. In the case of Y co-dopants, $YCl_3 \cdot 6H_2O$ was applied as precursor.

Adapted synthesis procedure for mp. WO_x and mp. WC_x films (section 5.4.2)

In section 5.4.2, results for the surface modification of mp. WO_x and mp. WC_x films with templated porosity *via* IrO_x-ALD (according to **[MF-2]**) are discussed. The preparation of the tungsten-based support films has been slightly adapted with respect to the experimental details previously reported in **[MF-3]**. In a typical synthesis, 792 mg WCl_6 (2.0 mmol) were dissolved in 6.0 mL EtOH *p.a.* under inert gas atmosphere (Ar-filled glovebox). After 5 min of stirring, a clear yellow-orange solution was obtained. 575 mg citric acid (3.0 mmol, 1.5 eq.) were added under vigorous stirring at 45 °C (Ar). After 15 min of further stirring (Ar), a clear, dark green solution was formed and, subsequently, 110 mg of a PEO-PB-PEO copolymer (PEO_{213}-PB_{184}-PEO_{213}) were added under stirring at 45 °C (Ar). Afterwards, the reaction mixture was stirred for further 60 min at 45 °C (Ar). A dark bluish-green solution was used for dip-coating on different substrates (flat Si, Ti, SiO_2) in a controlled atmosphere using a withdrawal rate of 300 mm/min at 25 °C ambient temperature and 40 % RH. A pre-heated *Teflon* cuvette was used (45 °C). Dark blue films were obtained after drying for at least 10 min under controlled conditions. After drying for at least 60 min at 80 °C in air in a pre-heated drying oven, films were treated in high-purity N_2 gas, as described in **[MF-3]** & **[MF-5]**, in order to afford tungsten oxide films with templated pore structure (mp. WO_x), which can be subsequently converted into the corresponding carbide films (mp. WC_x).